NASA CR-135106
PWA-5458

NASA

EXPERIMENTAL CLEAN COMBUSTOR PROGRAM – NOISE STUDY

By T. G. Sofrin and N. Riloff, Jr.

PRATT & WHITNEY AIRCRAFT DIVISION
UNITED TECHNOLOGIES CORPORATION

September 1976

Prepared for

NATIONAL AERONAUTICS AND SPACE ADMINISTRATION

NASA Lewis Research Center
Contract NAS3-18544

1. Report No.	2. Government Accession No.	3. Recipient's Catalog No
CR- 135106		

4. Title and Subtitle	5. Report Date
Experimental Clean Combustor Program - Noise Study	September 1976
	6. Performing Organization Code

7. Author(s)	8. Performing Organization Report No.
T. G. Sofrin and N. Riloff, Jr.	PWA-5458
	10. Work Unit No.

9. Performing Organization Name and Address	11. Contract or Grant No.
Pratt & Whitney Aircraft Division United Technologies Corporation East Hartford, Conn. 06108	NAS3-18544
	13. Type of Report and Period Covered

12. Sponsoring Agency Name and Address	13. Type of Report and Period Covered
National Aeronautics and Space Administration Lewis Research Center 21000 Brookpark Road, Cleveland, OH 44135	Contractor Report
	14. Sponsoring Agency Code

15. Supplementary Notes

16. Abstract

Under a Noise Addendum to the NASA Experimental Clean Combustor Program (ECCP) internal pressure fluctuations were measured during tests of JT9D combustor designs conducted in a burner test rig. Measurements were correlated with burner operating parameters using an expression relating farfield noise to these parameters. For a given combustor, variation of internal noise with operating parameters was reasonably well predicted by this expression but the levels were higher than farfield predictions and differed significantly among several combustors. For two burners, discharge stream temperature fluctuations were obtained with fast-response thermocouples to allow calculation of indirect combustion noise which would be generated by passage of the temperature inhomogeneities through the high pressure turbine stages of a JT9D turbofan engine. Using a previously developed analysis, the computed indirect combustion noise was significantly lower than total low frequency core noise observed on this and several other engines.

17. Key Words (Suggested by Author(s))	18. Distribution Statement
	Unclas ified – Unlimited

19. Security Classif. (of this report)	20. Security Classif. (of this page)	21. No of Pages	22. Price*
Unclassified	Unclassified		

* For sale by the National Technical Information Service, Springfield, Virginia 22151

NASA-C-168 (Rev 6-71)

FOREWORD

This report was prepared for the National Aeronautics and Space Administration Lewis Research Center under Contract NAS3-18544, Noise Addendum. Analysis of internal fluctuating pressure data (including data from Phase I) and information about indirect combustion noise generated by interaction of temperature inhomogeneities with a full scale engine turbine pressure drop are presented here.

Appreciation is expressed for the contributions made by Mr. Ronald Huff of the NASA Lewis Research Center, and by Messrs. R. Roberts, R. Dils, A. Peduzzi and G. Vitti of the Combustion Technology Group and G. F. Pickett of the Acoustics Technology Group at P&WA.

TABLE OF CONTENTS

TABLE OF CONTENTS (Cont'd)

LIST OF ILLUSTRATIONS

LIST OF ILLUSTRATIONS (Cont'd)

LIST OF ILLUSTRATIONS (Cont'd)

LIST OF TABLES

1. SUMMARY

Internal measurements for the purpose of studying combustion noise characteristics were made on a variety of JT9D scale experimental combustion designs during the course of the NASA Experimental Clean Combustor Program, and partial results were reported in Reference 1. Tests were conducted on 90 degree combustor segments installed in a special burner rig. Measurements were of two types: 1. fluctuating pressure signals from transducers flush-mounted in the walls of the combustors, and 2. fluctuating temperature signals from an array of fast-response thermocouples located in the exit plane of the combustors.

The objective of the pressure measurement program was to determine how the near field combustion chamber noise characteristics varied with combustor design and rig operating parameters, and to determine if certain operating parameters used to predict farfield core engine noise could also serve to correlate the internal measurements. It was found that a function of these parameters (Equation 9 of NASA TMX 71627, recommended by NASA as an interim prediction procedure for core engine farfield noise) provided a reasonably good description of changes in internal noise of a particular combustor as its operating parameters were varied. It was also found that the levels of internal noise of different combustor designs differed from each other by significant amounts at common operating conditions, and also that the average of the internal levels of the combustors evaluated at common operating conditions was appreciably higher than the corresponding predicted farfield value, as would be expected for information obtained from measurements in the near field of a noise source. Before these results were obtained it was found necessary to edit the internal pressure transducer signatures to reduce the effects of local aerodynamic noise.

The purpose of acquiring fluctuating temperature data downstream of the combustor was to obtain information relating to what has been identified as "indirect combustion noise". As distinct from direct combustion noise which is caused by local fluctuations in the heat release rate, "indirect" noise is produced downstream of the burner zone when hot spots or temperature inhomogeneities in the flow encounter a sharp pressure change, such as is produced by an engine turbine stage. No such sharp pressure drop existed in the operating of the combustor rig, so that no mechanism existed for the actual generation of indirect noise during the tests. The objective of taking the temperature measurements was to obtain information about spectra and length scales of the inhomogeneous flow which was then used as input to a computer program. Calculations were made, using performance characteristics of the JT9D high pressure turbine, to predict the indirect combustion noise that would be generated in a JT9D engine equipped with the experimental combustors. Details of the mathematical model used in the calculations are given in an Appendix to this report.

It was found that the fluctuating temperature levels in one of the two combustors evaluated were appreciably higher than previously experienced with other, production engine combustors. Despite the high temperature fluctuations in this combustor calculated values of indirect combustion noise were on the order of 10 dB lower than total core engine noise levels measured on a variety of engines and predicted by the previously referenced equation used in correlating internal pressure measurements. Therefore, it is expected that indirect combustion noise will not be significant in engines such as the JT9D operating with the experimental clean combustors tested in this program.

2. INTRODUCTION

As aircraft powerplant noise sources from the fan, jet, and turbine are reduced through improved engine design and use of sound-absorbing treatment, noise generated by the combustor could emerge as a significant limitation to further reductions. Compared to other powerplant noise sources, relatively little is known about combustion-generated noise. Noise measurements using combustor rigs have the advantage of allowing studies of the effects of varying operating parameters in a more independent manner than can be obtained in full scale engines. The NASA Experimental Clean Combustor Program involved emissions and performance tests on a variety of experimental combustors designed for reduced emission advanced CTOL aircraft engines. This program, conducted on a burner rig test stand, provided the opportunity to take internal measurements of the noise characteristics of several advanced combustor designs over a range of operating conditions.

In Phase I of the program internal pressure measurements were taken on several combustors, and partial results were reported in Reference 1. During Phase II these data and further data on two other combustors were studied in greater detail. The objectives of this effort were to determine whether the internally measured noise varied with operating parameters in a manner similar to the predicted farfield noise, whether the internally measured noise levels were reasonably consistent with farfield noise information, and whether there were significant differences in the internal noise characteristics of different experimental combustors.

A second type of investigation was also conducted during Phase II, which involved measurements of burner discharge temperature fluctuations. The purpose of this effort was to use these measurements to calculate and evaluate the significance of indirect combustion noise that would be produced by the interaction of the temperature inhomogeneities with a JT9D high pressure turbine.

3. COMBUSTOR EQUIPMENT AND TEST FACILITIES

During Phase I of the NASA Experimental Clean Combustor Program internal pressure data were taken during emissions tests on ten burner configurations which involved variations of three basic combustor types. Detailed descriptions are given in the ECCP Phase I Final Report, NASA-CR-134736, Ref. 3. In the Noise Addendum to Phase II both internal pressure and combustor exit temperature fluctuations were measured on two configurations, designated as H-6 and S-23, the features of which are described fully in the Phase II Final Report, NASA-CR-134969, Ref. 4. The principal design features of all the basic combustor types studied in the Noise Addendum are summarized below:

Swirl-Can Combustor (N-Series)

The swirl-can modular combustor design utilizes concepts developed by the NASA Lewis Research Center. This combustor incorporates a carburetor module array of 40 swirl cans in each of three circumferential rows, on a full annular basis. Each module is constructed with three major components: a carburetor, swirler, and flame stabilizer. The baseline configuration is shown in Figure 1a. Fuel is supplied to the modules through injection tubes centered in the carburetor-cans. The fuel-air mixture passes through the swirlers and is then burned. Dilution air enters the combustion chamber around hexagon shaped flame stabilizers. Fuel is staged to the outer row of carburetor cans at idle and to all the swirl cans at higher power.

Six Swirl-Can Combustor configurations were evaluated during this program. These are listed in Table I and described briefly in the sketches presented in Figures 1b and 1c. Modifications were confined to diffuser inserts, in an attempt to provide more uniform diffuser flow, and carburetor module changes to alter flameholding characteristics and carburetor fuel-air ratio. In one modification, configuration N-11, inner and outer liner dilution holes were provided.

Staged Premix Combustor (P-Series)

The design of the Staged Premix Combustor is based on previous single and two-stage premix combustor developments conducted at Pratt & Whitney Aircraft. Figure 2a presents the baseline design involving use of two combustion zones, denoted as pilot and main. Each zone has a separate fuel injector array, premix passage, flameholder, and combustion volume, as may be seen in Figure 2a. .Two zones are employed with the intent to facilitate emission control over the range of engine operation more readily than can be accomplished with a single zone combustor. The pilot zone is sized to accommodate all heat release for idle operation and is designed for optimum emission control at idle. With appropriate fuel management the combination of both pilot and main systems can be optimized for the high power operating regime.

Two configurations of the basic Staged Premix Combustor were tested in Phase I as indicated in Table I. Both incorporated slotted pilot and main flameholders, as shown in Figure 2b with no liner dilution air. This produced a very lean bulk premix passage equivalence ratio. Configuration P-8 additionally incorporated 2X main zone fuel source density.

TABLE I

COMBUSTOR DESIGN MODIFICATIONS EVALUATED IN ACOUSTICAL PROGRAM

Combustor	Scheme	Configuration	Figure Ref.
Swirl-Can Combustor	*N-7*	*Diffuser Screen; 1.27 cm recessed swirlers*	*1b, 1c*
	N-8	*"V" gutter trip; non-recessed swirlers*	*1b, 1c*
	N-9	*Diffuser screen; outer swirler flame-holder design.*	*1b, 1c*
	N-10	*Diffuser screen; reduced swirl can air.*	*1b, 1c*
	N-11	*Diffuser screen; ID and OD dilution air.*	*1b, 1c*
	N-12	*Diffuser screen; outer swirler flame-holder design; pressure atomizing nozzles.*	*1b, 1c*
Staged Premix Combustor	*P-7*	*No dilution air; slotted flameholders pilot and main.*	*2a, 2b*
	P-8	*No dilution air; slotted flameholders pilot and main; 2X main fuel nozzles.*	*2a, 2b*
Swirl Vorbix Combustor	*S-8*	*No dilution air; high flow main swirlers; pressure atomized pilot fuel nozzles.*	*3*
	S-9	*15 percent pilot swirlers blockage; main fuel nozzles aimed downstream.*	*3*
Swirl Vorbix Combustor (Phase II)	*S-23*	*Pressure atomized pilot nozzles with JT9D-70 swirlers; reduced main zone swirler airflow; increased pilot volume; dilution air in both pilot and main zones.*	*4, 5*
Hybrid Combustor (Phase II)	*H-6*	*Pressure atomized hollow cone primary nozzles; main zone swirler airflow increased 40%; no dilution air.*	*6, 7*

Swirl Vorbix Combustor (S-Series)

The Swirl Vorbix (Vortex Burning and Mixing) Combustor also employs two combustion subsystems, as shown in Figure 3. The pilot zone is a conventional swirl stabilized, direct fuel injection design and is sized to provide all heat release at high efficiency during idle operation. At higher power conditions, main zone fuel is introduced through fuel injectors located downstream of the pilot combustion zone. Main combustion and dilution air is introduced into the main burning zone through 60 swirlers located on each side of the combustor (on an annular basis). The hot exhaust product - fuel vapor mixture is entrained by the swirling air jets and partial premixing occurs prior to auto ignition of the main zone fuel. The main combustion process, in which most of the fuel is consumed at high power conditions, proceeds rapidly at the interface between these jets and the surrounding fuel rich pilot jet mixture.

Two configurations of the Swirl Vorbix Combustor were evaluated in Phase I, S-8 and S-9. Configuration S-8 differed from the baseline design in that pressure atomizing fuel nozzles were substituted for the aerating pilot zone nozzles, and large swirlers were installed at the main throat location. These had somewhat more than twice the effective flow area of the baseline swirlers, and necessitated the elimination of all aft liner dilution holes in order to maintain pressure drop. S-9 incorporated pilot swirler blockage rings to increase pilot zone equivalence ratio, and modified the orientation of the main fuel injectors. The downstream injection of main fuel was intended to minimize combustion prior to mixing with the main swirler airflow.

Swirl Vorbix Combustor S-23 (Phase II)

The basic Swirl Vorbix Combustor design used in the Phase II program (S-11) differed from the configuration evolved during Phase I in that the length of the pilot burner was increased by 3.8 cm (1.5 inch), while the main burner length was reduced by this amount. These changes were made to improve emissions characteristics. The specific model on which acoustic tests were conducted, S-23, differed from the basic Phase II Swirl Vorbix design in using JT9D-70 pilot swirlers and having reduced main burner swirler flow. The pilot zone volume was increased about 30 percent, and dilution air was added to both pilot and main zones. The basic Phase II design features are illustrated in Figures 4a, b, and c. Additional details applicable to configuration S-23 are shown in Figure 5, and a more extensive description is found in the companion main ECCP Final Report NASA CR-134979, Ref. 4.

Hybrid Combustor H-6 (Phase II)

The specific Hybrid Combustor, H-6, on which noise data were acquired in Phase II was a modification of the basic Hybrid Combustor, H-1, shown in Figures 6a and 6b. The combustor employs two burning zones that are separated radially and axially. The design basis for each zone evolved from two potentially good concepts for high and low power emission control that were developed in Phase I. The pilot zone duplicates the geometry of the Premix Combustor P-3 pilot which exceeded the low power emission goals in Phase I. The main burner zone design was based on the Swirl Combustor N-9, which demonstrated significant reductions in high power emissions reduction.

Fuel is introduced into the pilot premix passage through thirty pressure-atomizing fuel injectors (on a full annular basis), where it mixes with air and is partially vaporized. This mixture then passes through holes in the flameholder into the pilot combustion zone. The main burner zone has an arrangement of concentric, counter-rotating swirlers, located downstream and displaced radially from the pilot zone. Fuel enters through low pressure drop injectors in the center of the swirlers.

The specific Hybrid Combustor, H-6, evaluated for noise characteristics in Phase II incorporated modifications that increased the outer swirler airflow about 40 percent and blocked the inner liner dilution air. Details of this configuration are shown in Figure 7.

Test Facility and Combustor Rigs

The combustor noise tests were conducted on X903 stand, a high pressure combustion component test facility located at the Pratt & Whitney Aircraft Experimental Test Department, Middletown, Conn. This facility was fully equipped with the necessary inlet ducting, exhaust ducting, controls and instrumentation for conducting component tests at simulated engine operating conditions. For testing, the combustor test rig containing the combustor was installed at the inlet and outlet flanges of the test stand ducting. Heated non-vitiated compressed air was supplied to the test rig and the discharge pressure was controlled by valves in the exhaust ducting, allowing operation over a range of test conditions.

Different complete 90 degree sector combustor rigs were fabricated for use in this program. A JT9D-7 engine diffuser/burner case was sectioned to provide the same strut orientation in all rigs. Each case was modified to provide the fuel support pads and instrumentation bosses required by the particular combustor design. Stand duct work and flanges were also fabricated to mate the rig to the facility. A schematic diagram of the test rig, showing the location of the performance instrumentation is given in Figure 8, together with a diagram of the overall test facility.

Instrumentation was provided to measure the variables required to determine combustor performance, such as air flow, fuel flow, fuel temperature, static pressure and total temperature at the combustor inlet, and total temperature and pressure of the gases at the exhaust of the combustor. Results of these measurements were used in correlating noise with operating parameters.

4. ACOUSTICS INSTRUMENTATION AND TEST PROCEDURE

Pressure Measurements

Combustor internal pressure measurements were made using Kistler Model 603Al dynamic pressure transducers. The transducers were installed in Kistler water cooling jackets, model 616M135, in order to protect the transducer from the extreme temperatures. The transducer installation is shown schematically in Figure 9. Additionally, in Phase I an inlet transducer was located on the ID wall of the combustor inlet duct, 0.299m upstream of the diffuser case forward mounting flange.

The sidewall combustion compartment transducers were located in the same relative locations in all combustor configurations. The locations were in the combustor sector sideplates, centered radially approximately 0.0859m forward of the combustor rear mount flange. Details of the combustor sidewall transducer installation are shown in Figure 10. Due to procedures required for installing the combustion compartment transducers, it was necessary to install them as the combustor was being assembled. This required at least two separate sets of transducers allowing one combustor to be built up while another was at test.

Use of the pressure transducers requires determination of two different characteristics: (1) sensitivity and (2) frequency response. "Sensitivity" is the output voltage per unit sinusoidal input pressure at a fixed reference frequency. "Frequency response" is the relative change in output voltage as the frequency of a constant amplitude input pressure is varied. During Phase I it was determined (Ref. 1) that the frequency response was essentially constant over the range 30 to 5000 Hz. Small deviations were noted for some of the transducers and were applied in the data reduction procedure. In Phase II for tests of Configurations H6 and S23 it was decided that these corrections were sufficiently small to ignore.

The transducer sensitivity was determined by use of a system involving a pressure source pistonphone, the calibration of which is traceable to NBS standards (Ref. 1), a previously-calibrated reference transducer, and the subject transducer. Both transducers employ charge amplifiers in the system. The reference transducer and charge amplifier system (NBS traceable) is subjected to the pistonphone output, operating at a sound pressure level of 170 dB and a frequency of 15 Hz, and the system output noted. The reference transducer-charge amplifier system is then removed from the pistonphone assembly and replaced by the particular Kistler-amplifier being calibrated. By setting and locking the subject charge amplifier gain to produce the output voltage recorded for the reference system, sensitivity of the subject transducer-amplifier is set equal to standard. No further correction procedures are required in data acquisition of data reduction. After completion of testing, the Kistler systems were re-checked and were found to be operating properly.

The data recording system consisted of: 1) the pressure transducers and their power supplies, and 2) the signal conditioning and recording equipment, which provided calibration and monitoring instrumentation, switching capability, and analog magnetic tape recording capability. Recordings were made at a tape speed of 30 inches per second, using the FM mode of a Precision Instrument, Model 200 Recorder. Figure 11 is a schematic diagram of the data recording system. Recording system response calibration signals were provided by a local oscillator and random noise generator. Gain settings established on each channel at the pre-amplifier, to obtain optimum signal to noise recordings, were noted on the recorder log sheets and announced on the tape voice channel.

The data analysis system is shown in Figure 12. The recorded pressure signals were frequency analyzed using a set of 24, one-third octave band filters having geometric mean frequencies extending from 50 Hz to 10K Hz. These filters complied with the filter characteristics recommended in IEC Publication 225. The system was set up to provide a readout of one-third octave levels for each transducer, time averaged over a minimum time period of 30 seconds for each operating condition. Following this analysis, the data were stored on digital magnetic tape for input to the computer. Recording response and transducer frequency response corrections were applied to the data in the computer from 50 Hz to 5K Hz.

Selected narrow band analyses were performed on a high speed spectral analysis system providing wide-range, high-speed digitization of the narrow band analysis analog data. Resultant spectra were stored and averaged in a local memory before being plotted as narrow band spectrum plots.

Temperature Measurements

Through use of fine wire elements, carefully butt-welded at the junction, thermocouples have been developed that operate reliably in engine combustor environments, and with electronic compensation, will respond to dynamic temperature fluctuations in the stream in the frequency range from 0 to 1000 Hz.

In this program, an array of 16 such elements was used to measure the dynamic temperature field of the discharge from two combustor designs. Details of the thermocouple elements are described here together with features of the 16-element array installation, and the recording, playback, and signal processing techniques used in this investigation.

These Type S thermocouple elements were formed from pairs of .00762 cm (.003 inch) diameter wires, one of platinum and the other of platinum with 10% rhodium. The junction between each wire pair was formed by laser beam butt-welding. The resulting wire element, with the weld at midpoint had a span of .23 cm (.09 inch), and was spot welded at each end to .025 cm (.010 inch) diameter support posts. These posts are .51 cm (.2 inch) long stripped ends of standard Type S thermocouple wires sheathed with MgO insulation.

Four such thermocouple elements, spaced 1.08 cm (.425 inches) apart were installed in a rake assembly which was installed in the combustor rig to measure temperatures at four radial locations in the annular burner discharge station. Figure 13 shows details of the thermocouple elements and the rake construction, which incorporated a steam cooling jacket for increasing the durability of the thermocouple wire insulation and the rake structure itself. (The thermocouple element is not affected.) The fine wire elements can survive environmental temperatures on the order of 2500 to 3000°F long enough for most test purposes, but are subject to the hazards of overtemperature transients during ignition and other changes in setting operating points. To guard against such premature failures, the rake assembly was fitted with another jacket system to provide jets of screening air for the thermocouple elements during the setting of rig operating conditions. These jets were arranged to not actually

impact the wire element but rather to act as aerodynamic windscreens by diverting the burner efflux locally away from the element. After stabilization of the operating point conditions the screening air supply was turned off prior to taking data. Four such rakes, each mounting four fine wire thermocouple elements were mounted in the discharge plane of the annular combustion chamber segment. This array is shown in Figure 14. The circumferential separation between elements on adjacent rakes varied between about 7 to 8 times the 1.08 cm radial separation.

Details of the heat transfer characteristics that determine the dynamic response function of these thermocouples may be found in References 9 and 10. Very briefly, the wire element acts as a low frequency bandpass filter for harmonic components of the unsteady input temperature. The "cutoff frequency" depends upon local steadystate heat transfer characteristics of the wire/gas system and in practice has to be determined (usually in terms of the corresponding "time constant") for each operating point. Roughly, the basic wire cutoff frequency is very low – on the order of 10 Hz. Above this frequency the output voltage response drops at a rate approaching 6 dB per octave. To obtain information on temperature fluctuations beyond about 10 Hz, electrical compensation must be provided. From previous experience a frequency range of zero to 1000 Hz was selected as providing a balance between true temperature fluctuation information and unwanted amplification of electrical system noise. Compensating amplifiers have been developed with the properties of balancing the 6 dB per octave drop above the bare wire cutoff frequency with a transfer function such that the overall system frequency range is extended by a factor of about 100. At high frequencies the overall system response (including the compensating amplifiers) falls at a rate approaching 12 dB per octave. In use, the network has an adjustment which must be set to the wire time constant in order that compensation starts at the correct frequency. This time constant is determined by making a simple calculation involving knowledge of the steady state gas properties at the operating point. Figure 15-a is a diagramatic representation of the thermocouple and compensating amplifier system. Figure 15-b gives the voltage frequency response characteristic of the overall system, and also shows a sample uncompensated thermocouple response. The system "cutoff" frequency, f_c, (defined as that frequency for which the combined system response is down 6 dB) in the response function expression has been set from previous experience at 1000 Hz. (While it might appear desirable to modify the network to provide still higher frequency range, such an alteration would have the effect of amplifying unwanted electronic system noise; the cutoff frequency of 100 Hz has been fixed on the basis of considerable development experience with these instrumentation systems.)

In tests employing relatively few thermocouples, each thermocouple is provided with a compensating amplifier in the tape recording data acquisition process. However, because this test program used a large (16) number of thermocouples, an adequate number of compensating networks could not be provided for recording. Instead, the uncompensated signals were amplified and recorded directly, using the Precision Instrument FM tape recorder previously described in connection with the pressure transducer signals. (The 40 dB dynamic range of the tape recorder allows valid recording to be made without use of compensating amplifiers.) Two records were taken at each operating point, selecting the pressure transducers and some of the thermocouples for one record and the remaining inputs for the second recording.

During playback of the thermocouple information, either one or two compensating amplifiers were inserted between the tape recorder and the signal analyzer. Two essentially different types of signal processing were used for the thermocouple information. One-third octave band voltage spectra were obtained using a single compensating amplifier and the previously described wave analyzer. Values of overall root mean square voltage fluctuation were obtained from a B&K 2425 true rms voltmeter. To obtain the corresponding rms temperature fluctuation the ASTM Standard Temperature-Electromotive Force Tables for Thermocouples, E-230-72 were employed.

The table for type S thermocouples was entered at the mean steady state discharge temperature of the operating point. The local sensitivity computed from the table at this point, when multiplied by the rms voltage fluctuations, gave the corresponding rms temperature fluctuation. This sensitivity was essentially constant over the test operating range with an average value of about 0.15 degrees Fahrenheit per microvolt.

The other mode of signal processing involved correlation, using a Saicor Model 43A correlator. For autocorrelation of selected thermocouple signals a single compensating amplifier was inserted between the tape recorder and the correlator. For cross correlation analysis of selected pairs of thermocouple elements two compensators were provided. The purpose of the correlation processing was to determine axial and transverse length scales of the temperature inhomogeneities in the combustor discharge gas stream. Details of how these scales were obtained from the correlograms are presented in the Results section of this report.

Test Procedures

In Phase I of the program dynamic pressure measurements were taken for the combustors operating at simulated idle and takeoff conditions. Corresponding cold flow (fuel off) conditions were also recorded. In Phase II, tests on Configuration H-6 also included simulated approach operation and the corresponding cold flow point. Tests on Configuration S-23 further added operation at climb conditions. Temperature data were taken only during the H-6 and S-23 tests.

Combustor performance data were also taken to provide information for correlating the fluctuating pressure and temperature information with steady-state performance parameters. Measurements were made to obtain airflow, fuel flow (primary and secondary fuel systems), combustor inlet and total static pressure and total temperature, inlet mass flow parameters, combustor liner pressure drop, and ideal average combustor exit temperature.

In Appendix A-1 are tabulated those parameters of greatest significance from the standpoint of identifying the run conditions and providing a particular correlation between noise and combustor performances. These tables are supplemented by acoustic power level listings that are defined in the Results section of this report. They are listed in Appendix A-1 to provide a convenient reference location. All points recorded in Phase II are given in these tables. However, detailed analysis of the data acquired in Phase I was limited here to certain points for configurations N-8, N-11, P-8 and S-8, and consequently only those corresponding points are tabulated. Performance parameters for the other tests conducted in Phase I are given in Reference 1. Further details of the construction, performance, and emission features of the Phase II configurations may be found in the ECCP Phase II Final Report, NASA-CR-134969.

5. RESULTS AND DISCUSSION

Because of the significant differences in basic phenomena, measurement systems, and analytical procedures, between the internal pressure and combustor exit temperature investigations conducted in this program, the presentation and discussion of the results is divided into two sections: first, the pressure data, and last, the temperature information. Furthermore, background material necessary to understanding the specific quantified results is presented in subsections entitled, "Method of Analysis" which precede the specific "Results" subsections.

5.1 PRESSURE INFORMATION

For convenience in discussing the pressure information, the objectives given in the Introduction to this report are repeated here: These objectives were to determine the characteristics of internally measured noise for a variety of experimental combustors and to note whether there were significant differences in the overall noise among the configurations. It was also sought to study how variations in operating parameters affected the noise, and in particular to determine whether this relation could be quantified by a simple expression recommended for use in predicting farfield core engine noise.

5.1.1 Method of Analysis

Corrected Sound Pressure Levels

For each set of runs at various degrees of burner temperature rise obtained at the same mass flow and burner entrance pressure and temperature, a run was made with no burning and is referred to as the corresponding "cold" point. Cold points were obtained for simulated idle, approach and takeoff conditions for configuration H6, and in addition, at climb for configuration S23. By examining a set of spectra for a particular condition, e.g., idle, together with the cold point in that set (Appendix A-3) it is evident that the effect of burning on increasing the noise is generally limited to a frequency range from about 100 to about 4000 Hz, and is usually evident over a narrower range. A major portion of the pressure transducer signal is due to noise of aerodynamic origin rather than unsteady combustion and does not constitute a valid measure of the process under study. To obtain a better measure of the noise associated with burning, therefore, requires that the "as measured" spectra be corrected in some manner to de-emphasize the aerodynamic noise contribution. The method selected here involved subtracting (logarithmically) the corresponding cold flow spectrum from each of the spectra obtained with the burner operating. Further, where necessary, no contributions to burner noise were assigned below 125 Hz or above 4000 Hz. By summing (logarithmically) these "corrected" 1/3 octave band levels in the 125-4000 Hz range, a "corrected" overall sound pressure level, $OASPL_{cor}$, was obtained. In this manner a single number rather than a spectral distribution function could be used as a measure of the combustion noise signal from the transducer and employed in subsequent calculations. The uncorrected overall value, OASPL, was also employed in a limited way, as will be described presently. Sample spectra, illustrating the correction method are given in Appendix A4 for H6 and S23 and 4 configurations selected from Phase I for analysis.

Power Level Calculation, PWL and PWL_{cor}

Corresponding to values of OASPL and $OASPL_{cor}$, the acoustic power levels, PWL and PWL_{cor} were obtained from the logarithmic form of the expression for power:

$$P = \frac{\overline{p^2}}{\rho c} A (1 + M), \text{ where}$$

P = acoustic power

$\overline{p^2}$ = mean square pressure

ρ = fluid density

c = speed of sound

A = section area

M = Mach number,

where all quantities are evaluated in the plane of the transducer, are in mks system units. In the calculations A was taken as 4 times the 90 degree rig sector area to obtain representative values for a full-scale complete annulus. The Mach number in the plane of the transducers was always less than 0.09 and was therefore ignored since there are much larger uncertainties in the acoustic power determination as explained below.

In the mks system a reference PWL of 10^{-12} watts is used. To obtain PWL values in a system where 10^{-13} watts is taken as reference (see following section on PWL_{pred}) 10 dB must be added. The following expressions give the acoustic power level (re 10^{-13} watts) for the full scale engine where Mach number is ignored. A is the 90° sector rig area (the correction to the full annulus area is included in the constant), and all units (except PWL as noted above) are mks units:

$$PWL = 42 + 10 \log A - 10 \log \rho c + OASPL$$

$$PWL_{cor} = \text{above} + OASPL_{cor}$$

Near Field, Transverse Modes, and Transmission Effects

The preceeding equation for acoustic power is correct only when the acoustic particle velocity and pressure are in phase, and when the direction of wave propagation is locally normal to the element of surface, A. Both restrictions are necessarily violated in the very near field of a source distribution such as was the case with the transducer measurements in this program.

For a discrete frequency or band-limited coherent wave structure, *if* the particle velocity, u, could be determined, the quantity $\overline{p^2}/\rho c$ should be replaced by $p_{rms} u_{rms} \cos \phi$ where

ϕ is the phase angle between pressure and particle velocity. Therefore, by employing $\overline{p^2}/\rho c$ to compute "power" the effect of phase angle, cos ϕ, or "power factor" is necessarily suppressed. For this reason it can be seen that the values of "power" as computed here must be higher than would be measured at some distance from the source region, where the acoustic pressure and particle velocity are actually in phase. Due to the construction of the burner test rig it was impossible to position microphones downstream of the combustor in a region where they would not be impacted by disturbed flow or subjected to other undesirable side effects.

These limitations should not be construed as an argument against the use of combustion chamber pressure transducers, for in an engine there is no other location available for internal measurements that is free from equivalent complications. It would be highly desirable, however, in future combustion noise experiments to provide the test apparatus with a downstream duct location sufficiently far from the combustor so that near field effects could be avoided and such that flow, valve, and vibration noise effects were minimal. This location would be used to obtain true acoustic power measurements which in turn could be used to correlate with the combustion chamber readings.

Another limitation of the data (which would also apply to a downstream duct location free from the above mentioned near field effects) is that one or two transducers in general cannot adequately define the acoustic field structure in a duct whether they are close to or well separated from the source region. Under conditions where frequency is low enough such that only the plane wave can propagate, a single transducer can define the field (if there are no end-reflections). However, where the range of frequencies is such that higher transverse duct modes are above cutoff, the acoustic pressure distribution in a transverse plane of the duct will not be uniform (as it is for the plane wave only). In such cases a plurality of transducers must be employed in an array and their outputs must be specially processed in order that the mode structure and power flux can be computed properly. The dimensions of the test combustors used in this program and the general temperature range of operation were such that the first transverse mode could propagate for frequencies greater than about 500 Hz. Therefore, in addition to the near field effects described previously, the presence of transverse duct modes makes the estimation of acoustic power by means one or two transducers subject to errors of uncertain magnitude.

The expression $P = \overline{p^2}\ A/\rho c$, used here to calculate power, is known to overestimate the true farfield power due to both near field effects and the presence of transverse modes. The near field "power factor" effect has been explained. It can also be shown that a transverse mode (in a rectangular duct) may be synthesized by a pair of plane wave trains propagating at an angle, β, with respect to the duct axis. If the duct cross section area, A is used, the power flux through this area will involve the component of the inclined wave intensity along the duct axis or $P_m = (\overline{p_m^2}\ A/\rho c) \cos \beta_m$ where the m-subscript refers to a particular transverse mode. Since the calculation of "power" in this program has had to be based on assuming both power factor and direction cosines to be unity, the values thus obtained will be overestimates of the correct figures. In an engine, due to the effects of passage through the turbine stages, stream turbulence, and terminal nozzle impedance, not all of the "true" combustion acoustic power is radiated to the far field. These internal losses are a third cause for the

"power" as obtained from the internal transducer readings to overestimate the combustion acoustic power that will, in fact, radiate to the far field.

Aerodynamic Noise Check Procedure

In the above section dealing with corrected sound pressure levels it was stated that the transducer signal spectra indicated significant contributions from aerodynamic noise. (When the burner was ignited, only certain third-octave band levels increased.) For verification steps were taken to determine if: (1) the overall power level, PWL, could vary with rig operating conditions in a way that was consistent with an aerodynamic noise source; and (2) that the corrected power level, PWL_{cor}, had in fact been freed from this influence.

Noise of aerodynamic origin may be characterized in the far field by a super-position of source distributions that are referred to as monopole, dipole, and quadrupole in behavior. If one of these source distributions dominates, the far field acoustic power will vary as the stream velocity raised to an exponent that is 4 for a monopole distribution, 6 for dipoles, and 8 for a quadrupole source field. However, regardless of the far field behavior, the pressure fluctuations in the near field of any aerodynamically generated noise will vary as ρV^2 where V is a characteristic mean velocity.

The "power" P, calculated from the square of the near field pressure, is thus proportional to $\rho^2 V^4$. Therefore, in logarithmic units, this overall power level, PWL, will equal 4 (10 log v) + 20 log ρ + a reference constant if the source is aerodynamic.

When the quantity (PWL - 20 log ρ) is plotted against 10 log V a line with a slope of 4 results. Hence if a plot of these variables is made for a set of test points, and a line with slope of 4 results, there is strong evidence that the pressure transducer is sensing the near field of an aerodynamic source distribution, rather than (as is desired in this program) noise generated by unsteady combustion. Accordingly, to test whether PWL was possibly dominated by flow noise, and especially to confirm that the procedure for computing the "corrected" quantity, PWL_{cor} had removed this influence, plots of the type described were made for tests conducted on Configurations H6 and S23 using average values of stream density and velocity in the discharge plane of the combustor, station 5. This information is presented at the beginning of the "Results" subsection below.

Correlation of Pressure With Rig Operating Parameters

For several reasons, listed below, the task of correlating the internally-measured pressure fluctuations with rig operating parameters was performed by employing equation (9) of Reference 2, "NASA TMX-71627, Interim Prediction Method for Low Frequency Core Engine Noise". When the quantities in the referenced equation are expressed in the notation used here, Eq. (9) becomes:

$$PWL_{pred} = 56.5 + 10 \log W_a \left[(T_5 - T_4) \frac{P_4}{P_o} \frac{T_o}{T_4} \right]^2$$

where PWL_{pred} = overall far-field acoustic power level, dB re 10^{-13} watts

W_a = engine airflow (lbm/s)

T = Total temperature (°R)

P = Total pressure (lb/ft^2)

Station 0 = atmospheric

4 = combustor inlet

5 = combustor exit

In the rig tests, a 90 degree sector of the annular combustor was used, so to obtain corresponding engine predictions 6 dB should be added if rig airflow is used, making the constant 62.5 instead of 56.5.

The method used here for correlating measurements with operating parameters consisted of computing PWL_{pred} (called predicted power level) for the operating points and comparing the measured and predicted power levels. As previously explained, measured power employed a correction for cold flow noise, and the resulting quantity is called PWL_{cor}.

The expression for PWL_{pred} as a correlator function for the internal pressure measurements was selected for these reasons:

1. Eq. 9 is reported (Ref. 2) to do a good job of predicting far field low frequency core engine noise. The constant differs by 16 dB depending on engine type (e.g., turbojet, turbofan, turboprop) but not with engine size.

2. Item 1 is an important reason for determining whether this equation (with a different constant) also is a good predictor of combustion noise measured internally.

3. Eq. 9 has the virtue of being simple to use.

For the above reasons, the combination of rig operating parameters given in Reference Eq. 9 was used as the basis for correlating noise. The mechanics of performing this correlation was extremely simple: at each operating point, PWL_{pred} was calculated by this equation and used as the abscissa of a point having ordinate given by (measured) PWL_{cor}. If the resulting plot of PWL_{cor} vs PWL_{pred} scatters about a line with slope of unity, PWL_{pred} is a good predictor or "correlator" for the measured power. To evaluate the degree of "goodness" the standard error of estimate (standard deviation using N-2 degrees of freedom) was obtained and compared with the corresponding deviation of the data points from a horizontal line through the centroid. The latter quantity is a measure of the null hypothesis -- that the measured quantity PWL_{cor} does not depend on PWL_{pred}.

5.1.2 Results

The following results were obtained by applying the above procedures to the data:

Pressure Data Presentations

Pressure data tabulations and plots for tests conducted on configurations H6 and S23 are presented in Appendix A, and corresponding information for the configurations tested in Phase I is contained in Reference 1. Appendix A-1 tabulates the ECCP rig aerodynamic performance data and may be used to identify the operating conditions corresponding to the point numbers for which acoustic data were taken. In Appendix A2 are found tabulations of 1/3-octave band and overall sound pressure levels for both left and right hand side transducers. Machine-generated plots of 1/3 octave band spectra for the right hand side transducer are contained in Appendix A-3. No plots are given for the left-hand transducer because this information was not used in the subsequent analysis. Although there was not evidence of transducer malfunction during the recording of data for tests on H6 and S23, nor during post-test calibration, examination of the tabulated and plotted spectral information showed serious discrepancies at several operating conditions between the two microphone spectra. Order of magnitude studies were made of possible extraneous transducer response to vibration, heat fluctuations, aerodynamic noise and local flow impact noise. Based on these studies it appeared that the left microphone frequently indicated levels that were inconsistant with changes in rig operating conditions, and was probably more affected by local aerodynamic noise effects than the right hand transducer.

Aerodynamic Noise Checks

Estimation of possible microphone signal domination by aerodynamic noise sources rather than combustion noise was performed for configurations H6 and S23 by computing overall power level corrected for density, obtained by subtracting 20 log ρ_5 from PWL, and plotting the result versus 10 log V_5. Figures 16 and 17 present this information. Least squares fits give lines with slopes of 4.1 for H6 and 0.7 for S23, as shown on the figures. The slope for H6 is uncomfortably close to 4, indicating probable response to noise of aerodynamic origin. Spectra for H6 compared with cold flow spectra show that the high frequency portions (above 4K Hz) are generally similar and of large amplitude, confirming that the overall sound pressure level (from which PWL is obtained) is a poor measure of noise due to unsteady burning. In spectra for configuration S23 the influence of burning predominates over a wide frequency range, accounting for lack of V^4 dependence.

Therefore, overall power level as such cannot be used with confidence as a measure of combustion noise, and a correction procedure must be applied. The procedure used here to obtain a corrected power level, PWL_{cor}, involved logarithmically subtracting the cold flow noise spectrum from the spectra obtained with burning at common values of combustor mass flow and entrance pressure and temperature and truncating the result at 4K Hz. When this corrected value, PWL_{cor}, is used instead of PWL the results are shown in Figures 18 and 19. Slopes of the least squares lines of 5.7 and 2.9 for H6 and S23 suggest that aerodynamic noise has been eliminated as a dominant influence.

Alternative procedures exist for emphasizing the combustion noise component of the internal transducer signal. In full scale engines rather than rig tests no cold flow data acquisition is possible. There is sufficient general evidence in the combustion noise field that noise due to unsteady burning is limited to relatively low frequencies. Therefore if the spectra are arbitrarily truncated at an upper frequency limit such as the 4K Hz employed here the combustion noise contribution will be emphasized.

Configuration H6 Results

As described in the subsection on method of analysis, study of the relation of combustion noise to rig operating parameters was confined to a particular function of the parameters defined by Eq. 9 of TMX-71627. Values of acoustic power predicted by this equation, called PWL_{pred}, were computed for each operating condition and used as the x-coordinate of a point, the corresponding y-coordinate being PWL_{cor} obtained from pressure transducer measurement.

If the points thus obtained define a line with slope of unity, Eq. 9 is established as a perfect predictor of internally measured acoustic power. The standard deviation or standard error of measurement of the actual set of data points is a measure of systematic or random deviations from this predictor, large values indicating poor correlations. To provide a reference value against which this deviation can be compared the standard deviations from a horizontal line through the centroid of the set of points may be used. This procedure is comparable to testing the "null hypothesis" that measured noise is completely uncorrelated with the combination of operating parameters given by PWL_{pred}.

Figure 20 shows values of PWL_{cor} versus PWL_{pred} for the 15 operating conditions tested. Lines with unity and zero slopes are drawn thru the centroid of the distribution. Standard error of estimates for the data with respect to Eq. 9 predictor is 2.75 dB (and 4 dB for the flat line), indicating that Eq. 9 is a reasonably good predictor, 95% of the data falling within ±5.5 dB of the predicted values. It is worth noting that the constant difference, about 16 dB, between the slope 1 line through the data and the line through (0, 0) is compatible with near field and far field differences and to reported differences in the constant among far field data for different engine types (Reference 2).

Limited tests in Phase I indicated that once the burner was ignited at an operating pressure, temperature and flow, changes in temperature rise seemed to have small effects on the spectra. This observation suggested the possibility that noise might correlate better with a parameter in which the temperature rise was suppressed. Accordingly, a quantity called "ΔPWL_{pred}" was computed which simply omitted the 20 log ΔT term. Data for H6 were plotted against this parameter, as shown in Figure 21. This figure makes clear that ΔPWL_{pred} is a poor predictor of measured noise compared to PWL_{pred}.

To determine if the scatter of the data of Figure 20 could be reduced, the points were segregated into groups corresponding to runs at simulated idle, approach and takeoff conditions. Figure 22 shows that the idle data simply scatter about ±2 dB around a constant level as the burner exit temperature is increased by burning richer mixtures. Clearly PWL_{pred} fails completely to describe this behavior.

The approach condition data, Figure 23, have been divided into 3 groups as indicated by the broken lines. The three points on the line with slope of unity correspond to increasing fuel air mixtures, using only the secondary nozzle fuel system. Two points falling on an essentially horizontal line were obtained by supplying all fuel through the primary nozzle system. Completing this picture, the vertical line connects two points that were obtained with both fuel systems operating; the lower point corresponding to supplying 35 percent of the fuel through the primary system, and the upper point representing a 50 percent fuel split. Taken together, these results indicate that the details of how fuel is supplied to the burner may have an important effect on the noise. These details which presumably affect the time derivative of the heat release rate, should on physical grounds be of significance. By the same reasoning it cannot be expected that a simple prediction formula which is a function entirely of steady-state parameters can account for such variations.

The observation that lower noise levels were observed at approach for configuration H6 by exclusive use of the secondary fuel system should not be generalized without having a deeper understanding of the unsteady burning process. For example the data in the cluster at takeoff power, Figure 24, were recorded with a fuel distribution varying between about 10 and 35 percent primary to total flow, and if plotted against percent primary flow indicate more scatter than a trend. Despite the need for caution, it is difficult to avoid spectulating that a special in-flight fuel system selection for use in terminal approach might be developed to offer a measure of combustion noise reduction capability.

The takeoff data, plotted in Figure 24, were taken in such a way that there was very little variation in temperature rise. Most of the points represent different fuel management procedures. Therefore the takeoff data by themselves, as presented in Figure 24, do not provide a good basis for evaluating PWL_{pred}.

Summarizing, for configuration H6, Eq. 9 of TMX 71627 is a reasonably good predictor of the overall variation with operating parameters of internally measured noise "power". More detailed investigation showed that at some conditions the fuel management split produced noise variations that were not predicted by Eq. 9. In addition the acoustic "power" calculated from the internal, near field pressure transducers is on the order of 16 dB higher than the predictions for far field power, a difference which is not unreasonable to expect between internal near field and far field quantities.

Configuration S23 Results

Results for tests on S23, which included runs at simulated idle, approach, climb, and takeoff conditions, may be described briefly as similar to those just described for configuration H6.

A plot including all data of PWL_{cor} vs PWL_{pred}, Figure 25, shows reasonably good correlation, the standard error of estimate being 2.4 dB as compared to a deviation of 3.1 dB from a horizontal line through the centroid. PWL_{cor} averages about 12.6 higher than the far field PWL_{pred}. Suppression of the temperature rise effect in predicting ΔPWL_{pred}, Figure 26, results in somewhat better correlation than obtained in H6, but offers no advantage over use of the more straightforward quantity PWL_{pred}.

Breakout of the data for idle, approach, etc. conditions is not as revealing as was the case for H6. In the idle data plot, Figure 27, the trend determined by the pair of right hand points is violated by the extreme left hand point. Examination of the spectrum at this point, in comparison with the idle cold flow spectrum indicates a very slight noise increase with burning, making calculation of PWL_{cor} relatively unreliable. This point, being dominated by aerodynamic noise should probably be discarded, in which case the two remaining points indicate good correlation between predicted and measured power.

The approach condition data, Figure 28, do not span a sufficient range of either PWL_{pred} or PWL_{cor} to establish information about conformity with or departures from predicted behavior. Attempts to relate PWL_{cor} to fuel management, as was done for H6 are of questionable value due to the small range of PWL_{cor}.

Three points at different fuel-air ratios for the climb condition, Figure 29, show no variation as burner temperature rise is increased, although the change in the prediction parameter (about 1.5 dB) is probably too small to allow giving much significance to this observation.

At takeoff, Figure 30, the three data points spread out in both coordinates sufficiently well to allow observing that a slope 1 line would give a much better fit than a null effect or horizontal line.

A general summary relating to test results for configuration S23 is that, as with H6, PWL_{pred} is a reasonably good predictor of the overall variation of noise with operating characteristics. The average difference between internally measured "power" and predicted far field power is about 12.6 dB. Based on the data for the particular test points that were run, no information is available about the effects of other variables, such as fuel systems management.

Results for Configurations P-8, S-8, N-8, and N-11

These configurations were tested in Phase I of the ECCP program at simulated idle and takeoff condition only. Comments about the spectral characteristics of the internal pressure transducer signals are given in Reference 1.

Since the detailed testing and analysis performed for configurations H6 and S23 and reported immediately above have disclosed the general conformity of data trends with predictions and also possible departures therefrom, the current analysis of the Phase I data was limited to obtaining sample results. Specifically the four configurations listed above were selected from the Phase I program, and for each of these one idle point and one takeoff point were used in calculating power levels. The test points were selected to obtain comparable values of PWL_{pred} among the configurations at idle and comparable values at takeoff conditions.

Power levels for the above data are presented in Figure 31. Despite the fact that only the two points for configuration P8 define a line having a slope close to unity, it should not be concluded that the other three configurations demonstrate systematic departures from applicability of PWL_{pred} as a prediction of variation of PWL_{cor} with operating parameters. It will be seen that the difference in PWL_{pred} from idle to takeoff is smaller (due to test procedures) than was the case for H6 and S23. Further, the plots for these two configurations (Figures

20 and 25) show that due to data scatter, slopes very much different from unity could be obtained by selecting just two points.

The most significant information revealed in Figure 31 is probably the general differences in mean levels among the configurations, an observation that was made in Ref. 1 on the basis of examining all the available spectra. These differences are discussed in the next subsection.

Comparison Among Configurations

From the relatively large number of data points available for configurations H6 and S23 it has already been noted that the variations of PWL_{cor} with operating conditions is reasonably well predicted by PWL_{pred}. It has just been seen that insufficient data are presented for the other four configurations to either support or refute this observation. However, using the 2-point mean values for the Phase I configurations, as well as the more reliable mean values for H6 and S23 it is possible to infer overall level differences among all the configurations. Table II below gives the differences between corrected (observed) power level, PWL_{cor} and predicted far field values, PWL_{pred}:

TABLE II

MEASURED AND PREDICTED POWER LEVEL DIFFERENCES

Configurations	Difference: PWL_{cor}-PWL_{pred}
H6	16.2
S23	12.6
P8	23.3
S8	13.4
N8	10.2
N11	6.3
Average	13.7

Table II shows that the level of PWL_{cor} is significantly higher for all combustors than the far field noise predicted by referenced Equation (9). It is also seen that some combustors are appreciably quieter than others, assuming that PWL_{cor}, derived from internal measurements, can be used to rank combustors for far field noise. Thus, while the variation of internal noise for a given burner was seen to be reasonably well described by the specific combination of operating parameters giving PWL_{pred}, the levels of internal noise are appreciably higher than given by PWL_{pred} and there are large differences in level among various combustor designs.

These results are consistent with the previously discussed property of near field measurements in producing high estimates of far field noise. Furthermore, while PWL_{pred} predicts the same noise for all combustors at a common operating condition, the measured results indicate large differences among configurations. These differences are hardly surprising, for a simple expression involving only steady state parameters that does not account in some way for a variety of combustion chamber designs and fuel system details ignores the aero-thermodynamic details that govern the unsteadiness of the heat release rate – – the basic source of combustion noise.

For background information a comparison of one-third octave band sound pressure spectra is presented in Figure 32. These spectra, which were used in computing PWL_{cor}, are representative of takeoff conditions for the six configurations of Table II and are the corrected spectra obtained by subtracting corresponding cold flow spectra from the takeoff point raw spectra. It may be noticed that the general decrease in spectrum levels conforms to the sequence of power levels given in Table II. An interesting feature is that all spectra contain significant energy in the frequency range from about 400 Hz to 2000 Hz, which is appreciably higher than the range usually associated with combustion noise. A similar observation applies to the spectra at lower power conditions as may be inferred from the additional curves in Appendix A-3 and those for other configurations tested in the Phase I program, contained in Reference 1. This frequency shift, which amounts to at least a full octave above previous data, cannot be attributed solely to general peculiarities of internally-measured pressure because these previous data also include results of internal measurements. At this point no satisfactory explanation has been evolved to account for this result.

A final pair of curves, Figures 33 and 34 completes the presentation of the pressure data. Although these figures pertain to data for configurations H-6 and S-23 their introduction has been deferred in order to facilitate presentation of results. These curves give for Configurations H-6 and S-23, respectively, plots versus PWL_{pred} of the uncorrected or raw power levels, denoted simply by PWL. It is evident from these figures that total "power", PWL, uncorrected for flow effects, does not correlate with PWL_{pred}, since the data distribution is best described as scattering about an essentially constant value. Without giving statistical information about these distributions, the relatively poor correlation can be further appreciated by comparing these figures with the corresponding plots using corrected power, PWL_{cor}, Figures 20 and 25. These last curves support the decision to avoid use of raw power level as a measure of combustion noise in this program.

Internal Pressure Measurements and Far Field Combustion Noise

Until a reasonable number of tests of a different type are conducted, the relation of internal pressure measurements to far field combustion noise will remain a matter of speculation. Even after correcting the data to reduce the influence of aerodynamic noise (using PWL_{cor}), a basic remaining problem is that transducers such as were used in this program, being positioned directly inside the source volume, measure the so-called hydrodynamic field rather than just a propagating acoustic field. In the area of fan and compressor noise, where the details are comparatively well understood, it is known that pressure measurements taken very close to the rotating or stationary blades are meaningless as predictors of far field noise. On the other hand, measurements taken in the inlet and discharge ducts, at some distance from the blade rows can indeed be used to predict far field results (although the measurement procedures and subsequent calculations are quite complicated).

These facts suggest that future combustion rig tests should employ transducer arrays in a discharge duct sufficiently downstream of the zone of combustion so that the resulting measurements would give information about the propagating acoustic field. Such tests should also employ combustion chamber transducers, as were used in this program, to determine the degree of correlation between the combustion chamber measurements and the propagating combustion noise. (In the test arrangement used in the program reported here, it was not possible to install duct-mounted transducters in a location where reliable measurements could be obtained, due to the plumbing geometry and control valve locations employed in the combustion rig setup.) The objective of such tests would be to determine the degree of reliability of combustion chamber measurements systems in predicting far field noise, so that burner rig results could be used with confidence to develop combustion noise reductions, study the detailed mechanisms involved, and predict far field combustion noise for full-scale engines.

5.2 TEMPERATURE INFORMATION

As stated previously the objective of the fluctuating temperature investigation conducted in this program was to evaluate the potential for generating "indirect" combustion noise in a JT9D engine equipped with the test combustors, as a result of the interaction of the temperature inhomogeneities in the combustor discharge stream with the pressure drop across a JT9D turbine.

5.2.1 Method Of Analysis

"Indirect" combustion noise, or "entropy" noise results from a mechanism whereby temperature fluctuations or inhomogeneities in a stream that encounters a strong pressure gradient produce acoustic waves. It may be helpful to regard this mechanism in terms of local momentum fluctuations associated with the acceleration of fluid volumes of different densities imbedded in the mean flow undergoing a change in velocity. This mechanism was first identified in the context of aircraft gas turbine noise by Candel (Ref. 5), although it is implied by the generalized unsteady flow analysis of Kovasznay and Chu (Ref. 6). Additional work disclosing the importance of this source in core engine noise was performed and reported by Cumpsty and Marble, (ref. 7) and by Pickett (Ref. 8). The analysis used in this investigation assumes the pressure change to take the form of a sharp jump across an actuator disk, and was implemented by a computer program developed by Pickett based on Reference 8, which is enclosed as Appendix B1.

The required inputs to the program, in addition to the steady-state turbine characteristics, are simply the mean square temperature fluctuations and the transverse and axial length scales of the temperature distribution. These temperature field quantities were found for a total of 17 operating points in the ECCP program by processing the signals from a fast response thermocouple system developed by Dils, References 9 and 10.

Temperature Field Characteristics

Mean square temperature fluctuations were obtained from the thermocouple system voltages by means of the conversion procedure described in the section on Acoustics Instrumentation. Although not required for input to the indirect noise calculation, 1/3 octave band thermocouple voltage spectra were also obtained for general information and to obtain occasional checks of the overall mean square levels. In addition to the mean square intensity of temperature fluctuations, axial and transverse length scales are required in order to predict indirect combustion noise. The axial length scale, L_x, was obtained from the autocorrelation function of the sampled thermocouple output voltages. In conformity with the mathematical model of the indirect noise analysis, the characteristic length (or corresponding delay time) is defined as the point where the normalized correlation function has a value of $1/e = 0.37$. Thus, for the axial length scale, the delay time corresponding to a normalized autocorrelation of 0.37 was read from the autocorrelogram and multiplied by the stream velocity to give L_x. Several values of L_x were determined from different thermocouples in the array at different rig operating conditions.

Transverse length scales were obtained by cross-correlating paired outputs from transducers on 4 radial rakes. By cross correlating successive radial thermocouples with the end element of a rake and plotting the normalized cross correlation coefficients at zero time delay versus probe separation distance, the radial length scale was determined by entering the curve drawn through these points at a value of 1/e and reading out the corresponding distance. The transverse length scale could be determined by a similar procedure using corresponding elements of different radial rakes. However, it was found early in the data reduction that the cross correlation between elements on the closest rakes was insignificant, due to the relatively large distance between rakes, as compared with the comparatively small separation between thermocouple elements on a common rake. Therefore the only inference that could be drawn was that the circumferential length scale was significantly less than the rake spacing (order of 6 to 7 cm). In the absence of further information, for purposes of calculation the circumferential and radial length scales were taken as equal.

It should be remarked that the temperature data were first examined for evidence of a possible fluctuating structure that would not produce indirect noise. It has been reported (Ref. 9) that some combustors operate with long streams of relatively cool air issuing from the chamber cooling wall holes, that wander randomly in the position where they penetrate the burner exit plane. Such motion will not produce indirect noise. Thermocouples in the exit plane would exhibit time-varying fluctuations as a result of such streams sweeping across the elements. If the interpreter of the thermocouple outputs were unaware of the actual fluid motion involved he could impute the fluctuation to the passage of hot spots in a purely axial direction, in the manner postulated for the indirect noise temperature input field, and would proceed to use the inferred intensities and length scales to compute indirect noise associated with a turbine pressure drop when, in fact, no such noise would be generated.

Accordingly, the temperature data were examined for the possible presence of temperature streaks sweeping transversely in random directions across the thermocouple array. Their presence would be indicated by cross correlation functions between pairs of thermocouples that peaked at delay times that would be related to the streak transverse velocity and the separation between thermocouples. If, for example such a streak were moving radially, the delay times for the peaks of the voltage cross correlations between an element at one end and successively distant elements would progressively increase or decrease, depending on the direction of motion. A similar succession of progressively delayed peak cross correlations between circumferentially displaced thermocouples would indicate the presence of circumferentially moving streams of hot or cold fluid.

On the other hand, if in fact the temperature non-uniformities were in the form of globules convecting along steady streamlines, the peak cross correlation between adjacent thermocouples would occur at zero delay time, for the arrival of such globules at adjacent elements would be synchronous. In this test program, it turned out that such indeed was the case, so that the input temperature fields had the globular structure for which the indirect combustion noise model applies.

Prediction of Indirect Combustion Noise

The downstream indirect acoustic intensity flux was evaluated in each of the standard third octave bands for the passage of stream hot spots through the successive blade rows of the JT9D 2-stage high pressure turbine: first stator, first rotor, second stator and second rotor. Total intensity was obtained by adding the downstream contributions from each of the four rows, and no attenuation was applied for the multi-stage low pressure turbine or the transmission loss through the exhaust nozzle. The low pressure turbine generates insignificant indirect noise due to the much lower pressure drops involved.

Calculations were performed by IBM S/370-168, programmed to evaluate the triple integrals (over frequency and the two transverse wavenumbers) in Equation (8) of Appendix B-1. This equation, which is too lengthy to reproduce here gives the intensity between specified frequency limits which are taken as applicable to the standard 1/3 octave bands. The transverse wave numbers are involved because they enter into the spatial distribution of the acoustic fields and account only for the portions of the energy that are in propagating modes, as distinct from decaying modes.

Some appreciation of the significant factors governing indirect combustion noise may be discerned if this equation is rewritten as follows:

$$\left[I_x\right]_{\omega'_1}^{\omega'_2} = \text{const.}\,(\Delta P)^2\,\overline{\theta'^2_c}\int_{\omega'_1}^{\omega'_2}\int_{k'_{z1}}^{k'_{z2}}\int_{k'_{y1}}^{k'_{y2}} F\, d\omega'\, dk'_z\, dk'_y$$

In this abbreviated form it is readily seen that the acoustic intensity is proportional to the square of the pressure drop, ΔP, across a row, and also to the mean square value of the (non dimensional) entering stream temperature fluctuations, θ'_c, root mean square (r.m.s.) fluctuating temperature divided by steady state average temperature. Thus, doubling either the stage pressure drop or the r.m.s. fluctuating temperature each produces a factor of four change in acoustic intensity or 6 dB in power level.

The effects of the other variables affecting noise are much harder to extract since these variables are combined as complicated functions in both the integrand, F, of the above expression and also in the limits of the two integrations with respect to wave number. However, some insight is provided by considering the special case where the axial length scale L_x is sufficiently long such that most of the resulting noise will be restricted to frequencies that are low enough for only the plane wave mode to propagate. In this case, the intensity in a bandwidth $2\Delta\omega'$, centered at the frequency of peak intensity, ω'_m, is given by Equation 12, Appendix B-1. Writing this equation in simplified form gives:

$$\frac{1}{2\Delta\omega'} \left[I\right]_{\omega'_m - \Delta\omega}^{\omega'_m + \Delta\omega} = \text{const.} (\Delta P)^2 \, \overline{\theta'^2_c} \; L'_y \; L'_z$$

This expression shows the previously demonstrated effects of pressure drop and temperature level (which are exact) and further reveals that the intensity is proportional to $L'_y L'_z$ or to the transverse correlation area of the "hot spots".

The principal effect of axial length scale is to establish together with the axial stream velocity, the frequency of peak intensity, ω_m, which is on the order of the ratio of velocity to axial length scale. However L'_x also enters into determination of intensity in several more complicated ways. Let equation (11) of Appendix B-1 for the intensity of a plane wave in a frequency band be simplified to the form:

$$\left[I\right]_{\omega'_1}^{\omega'_2} = \text{const} (\Delta P)^2 \; \overline{\theta'^2_c} \; L'_y L'_z \; \frac{1}{L'_x} \left[\exp - \left(\frac{L'_x \omega'}{2}\right)^2\right]_{\omega_1}^{\omega_2} .$$

The overall intensity is obtained by taking $\omega'_1 = 0$ and $\omega'_2 \to \infty$. Evaluation of the exponential between these limits is just (minus) unity, giving

$$I \text{ (overall)} = \text{const} (\Delta P)^2 \; \overline{\theta'^2_c} \; L'_y L'_z \; \frac{1}{L'_x}$$

It is now seen that the overall acoustic intensity in the plane wave mode varies inversely with axial length scale. The inverse nature of this dependence may be appreciated qualitatively by recognizing that as L_x increases the momentum fluctuations across the blade row become progressively slower, thus diminishing the source strength. In the limit of $L_x \rightarrow \infty$ the change in momentum across the row is constant (independent of time) and no sound is produced, which is evidently the case for steady hot or cold streaks of unlimited length.

Going in the other direction, as L_x decreases, the overall intensity increases by virtue of the above described $1/L_x$ dependence. In addition, however, because the characteristic frequencies increase, acoustic energy begins to propagate in higher modes as well as in the plane wave. Mathematically, the more complex Equation 8 of Appendix B-1 must be employed, and it is not productive to try to trace the effect of decreasing L_x beyond remarking that the double integral over wave number in Equation 8 reflects the cumulative energy contributions of successively larger numbers of higher propagating modes.

Thus, as axial length scale is reduced the overall effects are to increase both frequency of peak acoustic intensity and the overall intensity as well. There will then come a point where a basic assumption of the analysis begins to break down as length scale is reduced, because the analysis assumes existence of an "actuator disk" where the pressure drop occurs over an infinitisimal distance. This assumption is well suited to the case of shock waves or to a choked cascade, but is otherwise increasingly violated as the length scale of the hot spots becomes less than a substantial multiple of the axial extent of the blade row. If in fact the temperature axial length scale and the blade row thickness are comparable the calculation will over-predict the indirect noise because the actual time for the hot spot momentum to change will be longer as a consequence of the finite distance over which the local momentum changes occur.

The high pressure turbine stages (two stators and two rotors) of the JT9D operate unchoked and are not much thinner than the axial length scales that were measured and will be described presently. Therefore it can be expected that the results of the analysis performed here will tend to overpredict indirect combustion noise in this installation.

5.1.2 Results

Applying the methods described above to the measured data the following results were obtained:

Measured Temperature Characteristics

Fast response thermocouple information was obtained from rig tests on combustors H6 and S23 at a total of 17 operating points. These points are identified in the listing of rig performance data, Appendix A-1. The majority of the temperature data were obtained for S23 because this combustor is closely related to the "final" configuration evolved in the main Experimental Clean Combustor Program and also because high thermocouple mortality severely limited the information available from the H6 combustor test program.

Although they are not used as specific input for calculation of indirect combustion noise, 1/3 octave band thermocouple voltage spectra were obtained and are presented in Appendix B-2. Sample spectra for H6 and S23 are shown in Figures 35 and 36. It is worth noting that the spectral shapes are quite similar for all operating conditions. In the appendical plots occasional high frequency prominences are exhibited, but these are chargeable to spurious electrical system noise since the amplifier system response characteristic falls at a 12 dB per octave rate beyond 2000 Hz.

The general peaking of the spectra in the frequency range from 500 to 1000 Hz and subsequent decline should be interpreted with some care because of the frequency response characteristic of the thermocouple and the compensating amplifier used in playback of the tape-recorded signals. As seen in Figure 15b the system response function begins to roll off at about 400 Hz and is 6 dB down at 1000 Hz. Therefore the true peaks of the temperature spectra will be at somewhat higher frequencies than indicated in the spectra presented here. Naturally, the system response characteristic also influences the length scale determinations which are obtained from correlation functions. The impact of this response characteristic on the length scales and on the calculated indirect combustion noise will be mentioned after the following description of the measured length scales and temperatures levels. It turns out that this high frequency roll off is of little practical significance because the calculated indirect noise spectra have peak frequencies that are already higher than normal for core engine noise.

To obtain predictions of indirect combustion noise the temperature information requirements are the axial and transverse correlation length scales, and the mean square or root mean square (rms) levels of temperature fluctuation.

The axial length scale L_x is determined from the autocorrelation function of the thermocouple output voltage. Figures 37 and 38 present sample autocorrelograms at approach and takeoff conditions for configurations H6 and S23. These figures show the characteristic delay time corresponding to a value of the normalized autocorrelation of 0.37 (= 1/e) and the subsequent translation to length scale by use of the stream velocity. A complete set of autocorrelograms is included in Appendix B-3. The effect of the system function high frequency roll off discussed previously is to make the axial length scale obtained from the correlograms somewhat longer than the true value, since correlation delay time and frequency are inversely related.

As previously described the transverse length scales, L_y and L_z, are obtained from plots against thermocouple separation distance of the normalized cross correlation function at zero delay time for pairs of thermocouple output voltages. Figures 39 and 40 show for configurations H6 and S23 sample plots at approach and takeoff of the radial cross correlation, from which the radial length scales were determined. Since there are insufficient data points to justify fitting a Gaussian distribution function a simple decreasing curve drawn through the data is entered at an ordinate of 1/e, determining the radial scale L_z with sufficient accuracy.

All the basic auto and cross-correlograms are presented in Appendix B-3. The cross correlograms between adjacent pairs of circumferentially distributed thermocouples show normalized cross correlations on the order of less than 0.05, as may be seen from the appropriate curves in Appendix B-3. Since the closest circumferential spacing is on the order of seven times the radial thermocouple spacing (≈ 1 cm) and the radial cross correlation at 2 cm spacing is down to about 0.05, it is clear that the circumferential length scale is very much less than the closest circumferential spacing. In the absence of further information it was assumed as a matter of convenience that the circumferential and radial length scales were equal. Length scale information is summarized in the following tables, III and IV.

The final item of temperature information needed for indirect combustion noise is the magnitude of the temperature fluctuations. Root-mean-square values were obtained by true rms voltmeter during the correlation portion of the data reduction. A normalized temperature (rms fluctuation/steady mean absolute temperature) is used as a multiplier to the output of the computer program, the input to which assumes for convenience a normalized value of one percent. Generally, several thermocouple voltages were read at each of the selected operating points corresponding to simulated idle, approach, climb, and takeoff conditions. Tables III and IV summarize this information for configurations H6 and S23. Point weighted average values normalized to burner exit temperature are listed. Although not used for calculating noise the ratios of fluctuating temperature to temperature rise, ΔT, across the burner, are also tabulated for comparison with some previously acquired data.

TABLE III

COMBUSTOR H-6
SUMMARY OF AVERAGE FLUCTUATING TEMPERATURE CHARACTERISTICS

	Length Scales		Normalized RMS Temp.	
Condition	Axial L_x cm (ft)	Transverse L_y, L_z cm (ft)	% of Burner Exit Temp. $\theta'c$	% of Burner Temp. Rise (1)
Idle (2)	5.2 (.171)	1.3 (.043)	20.5%	39.0%
Approach	4.9 (.159)	1.2 (.039	6.2	15.8
Climb (3)	4.7 (.155)	1.0 (.034)	3.9	6.9
Takeoff	4.7 (.154)	1.0 (.033)	3.9	6.9

(1) For reference only; not used in noise prediction

(2) Noise prediction not made for idle condition

(3) Data not taken at this point. Interpolated values used for noise.

TABLE IV

COMBUSTOR S-23
SUMMARY OF AVERAGE FLUCTUATING TEMPERATURE CHARACTERISTICS

Condition	Axial L_x cm (ft)	Transverse L_y, L_z cm (ft)	% of Burner Exit Temp. $\theta'c$	% of Burner Temp. Rise (1)
Idle (2)	3.7 (.121)	1.6 (.052)	11.7%	21.0%
Approach	4.45 (.146)	1.6 (.052)	7.85	16.7
Climb (3)	3.65 (.120)	1.35 (.044)	19.2	40.4
Takeoff	3.9 (.128)	1.45 (.048)	18.7	41.1
Avg. of last 3 pts (3)	4.0 (.131)	1.47 (.048)	---	---

(1) For reference only; not used in noise prediction
(2) Noise prediction not made for idle condition
(3) Average of length scales at takeoff, climb, and approach used for noise predictions

Commenting briefly on the temperature information in Tables III and IV, the following observations can be made:

1. The axial and transverse temperature length scales are relatively insensitive to operating conditions and are generally similar in the two combustors measured. Measurement system response characteristics previously described have the effect of overestimating the true axial length scales. The effect of attenuation of high frequency information upon the transverse length scales is not so easily obtained. However, it is reasonable to expect that the true transverse length scales will either be unaffected or, as with the axial scale will be somewhat smaller than the indicated values. In any event, there is no basis to expect the transverse scales to be greater than the indicated values.

2. On the other hand, the levels of the temperature fluctuations vary significantly with operating conditions, and this variation is quite different in the two combustors tested. For simplicity the idle data will be overlooked since this condition is of no practical concern from the noise standpoint. In configuration H6 the temperature fluctuations, normalized to burner exit temperature, drop from about 6% at approach to about 4% at takeoff. This change represents a reduction of about 4 dB in acoustic power. However, for S23 the normalized temperature rises from about 8% to 20% in this power change, which is equivalent to about a 7.5 dB noise increase.

3. The last column in the temperature tabulations expresses the rms fluctuation as a percentage of the burner temperature rise in order to afford a comparison with some previously acquired data. These data, presented in Reference 10, were acquired on combustors of three current production engines, and show fluctuations ranging from 7 to 25 percent of the burner temperature rise. Apart from the idle condition, combustor H6 falls well inside the range of previously acquired data. On the other hand the 40% fluctuations measured from S23 at high powers are on the order of twice the values previously measured. These high levels have been ascribed to the relative proximity of the temperature measurement station in the burner exit plane to the combustion zone in S23, and have been judged to be consistent with more limited previous data taken upstream of the discharge plane in conventional burners.

4. In terms of indirect combustion noise power the temperature differences between H6 and S23 amount to only about 2 dB at approach but at high power conditions S23 should generate about 15 dB more noise than H6. The effects of the shorter axial length scales and larger transverse scales of S23 are such as to further increase its noise generating characteristics relative to H6.

Before discussing results of the noise calculation it should be mentioned that Appendix B-3, containing the temperature correlograms also includes several cross correlations (see pages 181 and 182) between outputs of a sample thermocouple and a Kistler pressure transducer flush mounted upstream in the combustor S23. (See sections on pressure information.) These correlations were made to see if the internal pressure fluctuations and discharge temperature fluctuations were causally related. The trivial values of the normalized cross correlation function of these quantities indicate that the time-variation of burner internal pressure and discharge temperature at the measurement locations are independent of each other.

Predicted Indirect Combustion Noise

Using the temperature information for combustors H6 and S23 summarized in Tables III and IV, the noise power generated by the interaction of the temperature inhomogeneities with the high pressure turbine of a JT9D engine was calculated from Equation 8 of Appendix B-1. As described previously, the downstream noise contributions of each of the 4 stages (2 stator and 2 rotor) were evaluated and summed. After passing through a stage the axial length scale was stretched in the ratio of exit to entrance axial velocities to establish the corresponding entrance length scale for the next stage in a manner that would conserve the time flux of the temperature eddies.

Figure 41 presents the results of the indirect noise calculation for configuration H6 at approach, climb, and takeoff conditions listed in Table III. Downstream propagating power levels in 1/3 octave bands are shown for each of the four high pressure turbine blade (or vane) rows, together with the resulting spectral sum of these contributions. Similar results for S23 are given in Figure 42. In both cases the length scales listed in Tables III and IV were used. However, a common constant value of the normalized fluctuating temperature of one percent was used both as a matter of convenience and to illustrate the effects of variations in length scale

and turbine characteristics. Actual power levels corresponding to measured values of normalized fluctuating temperature, $\theta'c$, also listed in these tables, are obtained by merely adding 20 log $\theta'c$ to the one percent levels. On the basis of a common 1% temperature variation the overall power levels (integral of the resultant spectrum) of S23 range from about 3.5 to 5 dB higher than those of H6 as a result of its larger transverse and smaller axial length scales, in conformity with the background discussion in the previous section.

As seen in Figures 41 and 42 the second stator contributes on the order of 2 to 3 dB more than the next important stage, the first stator. The second and first rotors, in turn, are progressively lesser contributors to the total power. These differences are a consequence of the detailed interstage variations of the turbine parameters entering into equation 8, Appendix B-1 and do not incorporate any assumptions for attenuation by downstream stages of noise generated upstream. In practice, of course, upstream noise will be progressively attenuated in its transmission through successive downstream stages, and the total resulting high pressure turbine noise also will be significantly attenuated by the 8 blade (or vane) stages in the low pressure turbine. Calculation of these attenuations and the further transmission loss at the exhaust nozzle is beyond the scope of the program, but rough estimates place the probable total attenuation between 5 and 10 dB.

When the 20 log $\theta'c$ effect of the measured temperature fluctuations is added to the overall power levels obtained on a one percent basis the results listed in Table V are obtained for combustors H6 and S23.

TABLE V

CALCULATED INDIRECT COMBUSTION NOISE
JT9D ENGINE WITH CONFIGURATIONS H6 AND S23
(OVERALL POWER LEVEL: dB re 10^{-13} WATTS)

	H6	S23
Approach	129.6	135.5
Climb	127.4	145.8
Takeoff	127.7	145.9

The H6 noise levels decrease slightly with engine power as a result of the decline in levels of temperature fluctuations. For S23, on the other hand, the small increase with power on a constant one percent temperature basis is augmented by the large rise of input temperature fluctuation to net about 10 dB more noise at high power than at approach.

Evaluation of Indirect Noise Results

Before evaluating the significance of the calculated levels of overall indirect noise some remarks on the spectral distribution of this energy should be made. Examination of the spectra in Figures 41 and 42 shows that the indirect combustion noise power is a maximum in the range from 1000 to 1250 Hz, for both combustors over the power range from approach to takeoff.

However, the class of phenomena called core engine noise, of which combustion noise is considered an outstanding contributor, is characterized by spectra peaking well below 1000 Hz, usually in the 300 to 600 Hz range. This observed feature, common to several different types of aircraft turbine powerplants, is well documented in References 2 and 11 and in the literature cited therein.

For this reason, if the indirect combustion noise calculated for combustors H6 and S23 were to be actually generated in a JT9D engine undergoing acoustic tests, it would probably fail to be recognized as a core noise phenomena, assuming in the first place that its spectral levels were high enough to stand out from the broadband fan discharge noise spectrum. The cause of the higher than normal peak frequency of the predicted indirect noise is, of course, the relatively short axial temperature length scales measured for configurations H6 and S23. As in the case of the relatively high amplitudes of temperature fluctuation an explanation may be advanced that they are presumably a consequence of the detailed differences in combusto. design, with the relatively shorter than conventional length of the combustors probably being the most significant parameter.

It may also be recalled that the burner internal fluctuating pressure measurements gave spectra (both as measured and when corrected for cold flow noise) having significant energy well beyond the 300 to 600 Hz range. While these were characteristics of the very near field and it is not known how to transform them to obtain far field power spectra, it is of some interest to note that both the calculated indirect combustion noise and the measured internal pressure spectra differ significantly from the conventional spectral representation of core engine noise.

Finally, the probable significance of indirect combustion noise in the operation of a JT9D engine with the test combustors will be estimated by comparing the computed power levels with certain other core engine information items.

Table VI gives farfield power levels of total low frequency core noise measured on several turbofan engines, including a JT9D, and also the values obtained by the recommended interim prediction formula, Equation 9 of Reference 2. Also listed are rounded-off values of the computed indirect combustion noise for burner configurations H6 and S23 operating in a JT9D engine. No low pressure stage turbine or exhaust nozzle attenuations have been applied to these two items, copied from Table V, but the measured and predicted levels do incorporate such attenuation.

TABLE VI

APPROXIMATE TOTAL CORE NOISE POWER LEVELS PWL dB re 10^{-13} WATTS

Item	Approach Power Range	High Power Range
Engine C1	143	155
C2	143	(n.a.)
C3	140	(n.a.)
B	140	152 (est)
A1	144	(n.a.)
A2	145	(n.a.)
Eq. 9, Ref. 2 (turboshaft)	(153)	(162)
turbofan	145	154
Calculated, config. H6	130	128
Calculated, config. S23	136	146

The unavailable (n.a.) figures at high power operation for several of the above entries reflect the inability to detect or extract a spectral prominence in the expected frequency range. Levels from Equation 9 of Reference 2 for turboshaft engines are shown, together with corresponding values that are 8 dB lower, reportedly applicable to turbofan type engines.

From Table VI it appears that a representative total core noise power level for turbofan engines at approach powers is about 143 dB and at high power is about 153.

Using these figures as representative standards for comparison it follows that:

1. The corresponding calculated levels for configuration H6 of 130 and 128 are at least 13 dB lower, so indirect combustion noise would not be significant for this burner.

2. Calculated indirect combustion noise levels for configuration S23 are about 7 dB lower than representative total core noise. If only 3 dB low turbine and exhaust nozzle attentuation is assumed the indirect noise from S23 will be 10 dB less than total representative core noise. Therefore, for configuration S23 as well, indirect combustion noise is unlikely to be detected in the JT9D engine signature.

Combining these evaluations of the overall levels of indirect combustion noise with the remarks about the higher than normal peak frequency of their spectra it follows that indirect combustion noise is unlikely to be of practical significance for the JT9D and similar engines equipped with either of these experimental combustors.

6. SUMMARY OF RESULTS

1. Signals from transducers measuring pressure fluctuations inside combustion configurations were found to require special processing to provide a measure of combustion-generated noise. The overall sound pressure level indicated without such processing was significantly affected by sound generated aerodynamically.

2. A measure of the near field of combustion noise was obtained by using only the portions of the transducer spectra in which combustion noise dominates. The relevent spectral bands were found by comparing spectra for flows with and without combustion. In applications where cold flow cannot be produced in the combustor (as in an operating engine rather than a test rig), use of the spectra between about 100 Hz and an upper bound of 4K Hz would probably serve as a reasonable general guide.

3. The resulting spectra were found to contain significant energy in frequency bands on the order of an octave higher than the spectra usually associated with combustion noise. This property applied essentially to all configurations and operating points.

4. The sound pressure level determined as described above, and designated as $OASPL_{cor}$ (overall sound pressure level, corrected) was used to calculate a hypothetical combustion noise level (PWL_{cor}) using the relation $P = \overline{p^2}\ A/\rho\ c$, where P, p, ρ, c, and A are values in the plane of the transducer of "Power" pressure, density, sound speed, and section area, when the local Mach number is relatively low. This "Power" is referred to as hypothetical because the equation from which it is computed implies that the acoustic field pressure and particle velocity are in phase, a situation that exists only in the "far field" (at large distances from the source). Due to neglect of this phase angle factor, calculations based on internal measurements overestimate the true acoustic power.

5. For this reason, future experiments to measure combustion noise should provide pressure transducer stations downstream of the actual combustor, insofar as it is practicable to so locate them. In such cases, sufficient transducers should be employed to insure that higher duct modes as well as the plane wave are identifiable and taken into account when computing acoustic power.

6. Extensive pressure data taken on configuration H6 and S23 were processed as described above to compute an acoustic power level called PWL_{cor}, and these values were related to rig operating parameters by using Eq. 9 of TMX-71627. This equation predicts acoustic power level, called here PWL_{pred} by the expression:

$$PWL_{pred} = 56.5 + 10 \log_{10} \dot{m}_a \left[\Delta T \frac{P}{P_{amb}} \quad \frac{T_{amb}}{T}\right]^2$$

where $\dot{m}_a$ is weight flow through the combustor, ΔT is combustion temperature rise, P&T are total Pressure and Temperature at the combustor entrance and the subscript amb refers to ambient or standard atmosphere values.

A test of PWL_{pred}, as a predictor of measured power was obtained by comparing "measured" acoustic power (PWL_{cor}, obtained from the transducers) with values determined from Eq. 9 above.

7. It was found that the referenced Eq. 9 provides a reasonable prediction of acoustic power for Configurations H6 and S23, apart from the constant. The measured power varies with mass flow, temperature rise, and combustor entrance pressure and temperature in the manner described by referenced Eq. 9. However, measured power levels were appreciably higher than predicted, which is consistent with the above remarks that the near field transducer levels lead to overestimates of acoustic power radiated to the far field.

8. Sample data at simulated idle and takeoff conditions for 4 combustors tested in Phase I of this program, were insufficient to provide a valid judgement of the ability of Eq. 9 to predict noise for these configurations. For the limited data used, measured power levels had a range of about 17 dB from the "loudest" to the most quiet, corrected to common rig operating parameters.

9. Despite the general ability of PWL_{pred} to provide estimates of acoustic power variation, important deviations from predicted behavior were observed. For example, at idle conditions, little systematic change in measured noise was noted for some configurations as the temperature rise was increased by adding fuel. As another example, data taken on configuration H6 at approach conditions showed significantly different behavior as a function of temperature rise depending on how the fuel supply was proportioned between primary and secondary nozzle systems.

10. The deviations noted in the above paragraph are not anomalous since no simple prediction formula that fails to provide inputs in the form of aero-thermodynamic field microstructure can account adequately for combustion noise. One of the outstanding source terms of such noise is the time rate of change of heat release rate. This quantity is certainly affected by details of how the fuel is injected and burned, and the turbulence structure of the flow, and no provisions exist in any simple formula for quantifying these crucial parameters.

11. Using fast response thermocouples in the burner discharge stream, fluctuating temperature characteristics were determined for combustors H6 and S23 in order to compute indirect combustion noise. The required temperature parameters were axial, radial, and circumferential length scales of the temperature inhomogeneities and the root mean square (rms) amplitude of the fluctuation. In addition, sample one-third octave temperature spectra and a limited number of cross correlations between a thermocouple and an internal pressure transducer were obtained.

12. For both configurations the temperature length scales remained essentially constant over the operating range from simulated idle to takeoff. Also, corresponding length scales of both combustor streams were comparable. The axial length scale was about 5 cm for H6 and about 4 cm for S23. Radial transverse length scales were approximately 1 cm and 1.5 cm for H6 and S23 respectively. Circumferential length scale could not be directly measured since the spacing between adjacent thermocouples was substantially larger in the circumferential direction than radially; it was taken equal to the radial length scale for input to the noise calculations.

13. Thermocouple voltage spectra are generally similar in shape for both combustors over the operating range. However the maximum one third octave band levels occur at frequencies that are on the order of an octave higher than are usually associated with combustion noise or low-frequency core engine noise. This characteristic is reflected in the magnitude of the axial length scales and subsequently in the spectra of the computed indirect combustion noise.

14. To determine if the discharge temperature fluctuations were causally related to the combustion chamber pressure variations, sample cross correlations were made between signals from a hot wire and from one of the flush-mounted pressure transducers. Essentially zero normalized correlation coefficients were noted at all sampled operating points, indicating that the temperature and pressure fluctuations were completely independent processes.

15. To facilitate discussion of the root mean square (rms) amplitude of the temperature fluctuations, this amplitude is expressed as a percentage of the steady-state burner temperature rise. Excluding the idle operating point, which has little significance from the noise standpoint, combustor H6 temperature levels decreased from about 16% at approach power to about 7% of the burner temperature rise at high power operation. These figures are well within the 5% to 25% range previously measured for three different production engine burners. Configuration S23 behaved quite differently, increasing from about 17% temperature fluctuation at approach to 41% at takeoff power. Thus at low power (approach) H6 and S23 develop comparable temperature fluctuations that fall within the range of other, production type burners. At high powers, however, the temperature fluctuations of S23 are significantly higher than those of H6 and other production engine burners.

16. Calculations were made to estimate the indirect combustion noise that would result from the passage of the temperature fluctuations described above through the high pressure turbine of a JT9D engine. The *shapes* of the resulting acoustic power spectra for combustors H6 and S23 were quite similar and did not change significantly from approach to takeoff power conditions. The one third octave band spectra peaked in the range of 1000 Hz to 1250 Hz, which is on the order of an octave higher than spectra usually associated with combustion noise or low frequency core engine noise.

17. *Levels* of calculated indirect acoustic power, however, differed significantly between the two combustors and also varied with operating conditions in different ways. For H6 the overall acoustic power level was about 130 dB (re 10^{-13} watts) at approach and dropped slightly to 128 dB at takeoff power, primarily as a consequence of the reduced temperature fluctuation. In configuration S23 the calculated indirect noise power level at approach was about 136 dB and increased to 146 dB at high power, reflecting the increase in temperature fluctuation.

18. Significance of these levels was evaluated by comparison with previously determined *total* engine low frequency core noise obtained from measurements on turbofan engines and from the interim prediction procedure discussed in the section of this report on internal pressure measurements. Representative total core noise power levels were taken as 143 dB for approach and 153 dB at high power.

    If the noisier of the two configurations, S23, is considered, and if it is assumed that only 3 dB of attenuation of indirect noise is provided by transmission through the multi-stage low pressure turbine and the exhaust nozzle, farfield indirect noise power levels of 133 dB at approach and 143 dB are projected.

19. Comparing these projected levels for S23 with representative figures for turbofan engine low-frequency core noise it is seen that they are about 10 dB lower than *total* core noise levels from all sources of typical turbofan engines. Levels for the other combustor, H6, will be significantly lower yet. Since the input measured temperature fluctuations for S23 were appreciably higher than indicated by previous experience, it appears that indirect combustion noise for any of the experimental clean combustors can be ruled out as a significant component of JT9D engine core noise.

7. CONCLUSIONS

1. Pressure fluctuations inside a combustor, when corrected for the effects of aerodynamic noise, may be used to compute a rough estimate of acoustic power due to unsteady burning. The effects of near field transducer location and neglect of transverse mode structure are such as to lead to an overestimate of the true acoustic power.

2. For a given combustor, the changes in internally measured acoustic power with variations in burner operating parameters are reasonably well predicted by Equation 9 of NASA TMX 71627.

3. For the combustors tested, the average of the internally measured power is about 14 dB more than predicted by this equation for the far field, a difference which is consistent with the complications of internal near field measurements noted in item 1 above and neglect of turbine and nozzle transmission losses.

4. Differences in noise level of up to 15 dB were observed among different combustors, indicating that design details not specified in a simple expression such as referenced Equation 9 have important effects. Further, in a particular burner design, the effects of such variables as fuel supply system management may cause the variation of noise with operating parameters to depart significantly from the predicted variation.

5. Measurements indicate that the Swirl Vorbix Combustor, S23, produces discharge temperature fluctuations that are significantly higher than those previously observed on several production burners. The Hybrid Combustor H6 produced lower levels of fluctuation that were more in line with previous experience.

6. For both combustors, however, indirect combustion noise produced by interaction of the temperature fluctuations with the high pressure stages of a JT9D turbine was calculated to be significantly (10 dB) lower than observed values of total low-frequency core engine noise from all sources.

7. Since these low sound power levels included the projection for an experimental burner with higher than normal discharge temperature fluctuations, and also since the resulting noise spectra peaked more than an octave above typical core noise spectra, it is unlikely that indirect combustion noise could be detected in the operation of engines such as the JT9D.

REFERENCES

1. Sofrin, T. G. and Ross, D. A., "Noise Addendum, Experimental Clean Combustor Program, Phase I Final Report." NASA CR-134820, October, 1975.

2. Huff, R. G., Clark, B. J. and Dorsch, R. G., "Interim Prediction Method For Low Frequency Core Engine Noise." NASA TMX-71627, November, 1974.

3. Roberts, R., Peduzzi, A. and Vitti, G. E., "Experimental Clean Combustor Program, Phase I Final Report." NASA CR-134736, October, 1975.

4. Roberts, R., Peduzzi, A. and Vitti, G. E., Experimental Clean Combustor Program, Phase II Final Report." NASA CR-134969, 1976.

5. Candel, S. M., "Analytical Studies of Some Acoustic Problems of Jet Engines", Ph. D. Thesis, California Institute of Technology, 1972.

6. Chu. B. T. and Kovasznay, L. S. G., "Non-Linear Interactions in a Viscous Heat-Conducting Compressible Gas," J. Fluid Mech., 3, 1958.

7. Cumpsty, N. A. and Marble, F. E., "The Generation of Noise By the Fluctuations in Gas Temperature Into a Turbine." University of Cambridge, Dept. of Eng. Report CUED/A TURBO/TR57, 1974.

8. Pickett, G. F., "Turbine Noise Due to Turbulence and Temperature Fluctuations," Proceedings of the Eighth International Congress on Acoustics, London England, July 23-31, 1974.

9. Dils, R. R., "Dynamic Gas Temperature Measurements in a Gas Turbine Transition Duct Exit," ASME Journ. of Eng. for Power, July, 1973.

10. Dils, R. R., "Wideband Gas Temperature Measurements in Combustor and Combustor Exhaust Gases," Technical Paper Presented at 22 International Instrumentation Symposium of the Instrument Society of America, San Diego, Calif., May 25-27, 1976.

11. Mathews, D. C. and Peracchio, A. A., "Progress in Core Engine and Turbine Noise Technology," AIAA Paper No. 74-948, August, 1974.

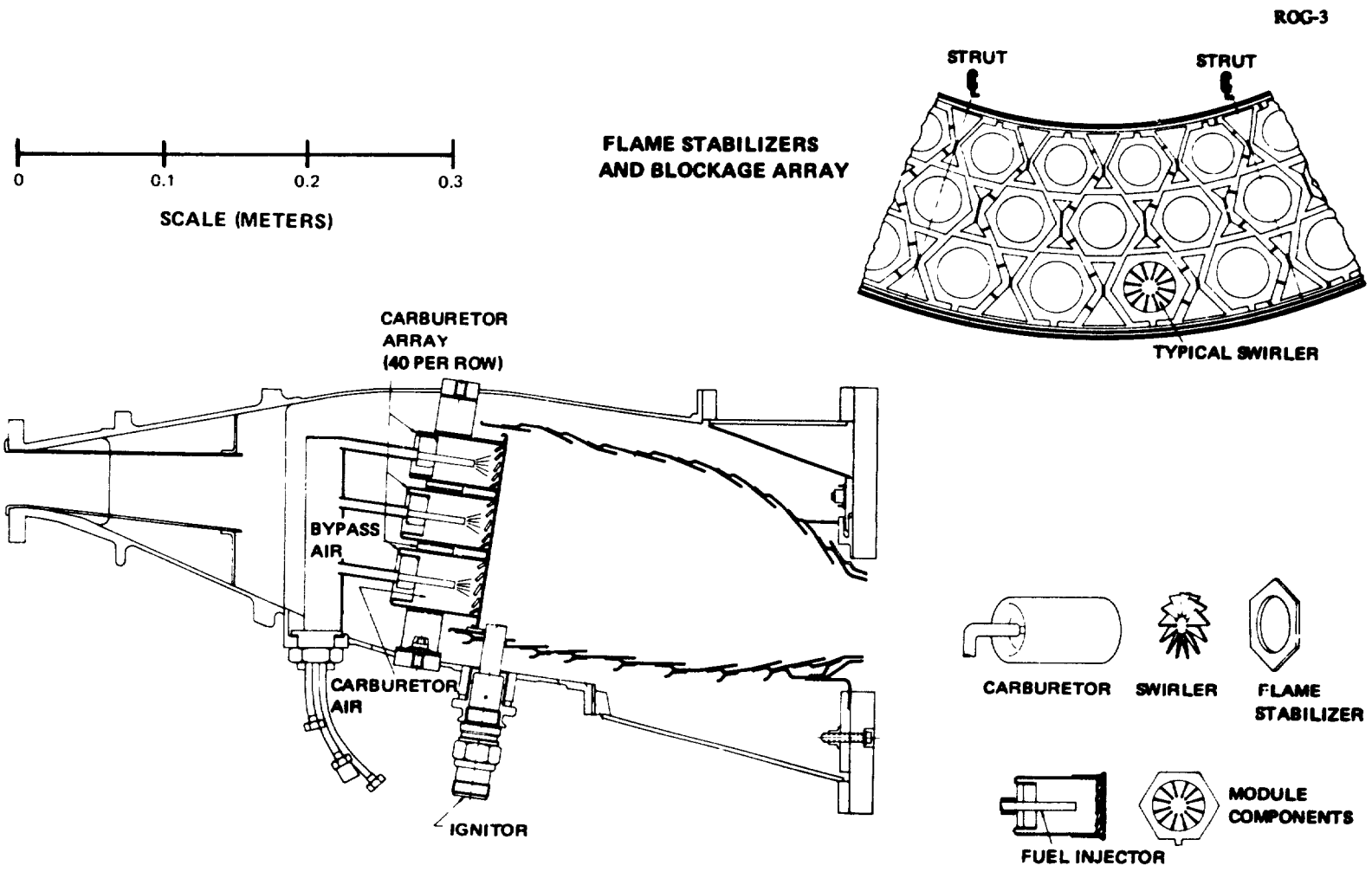

Figure 1a Swirl Can Combustor – Baseline Configuration (N-Series)

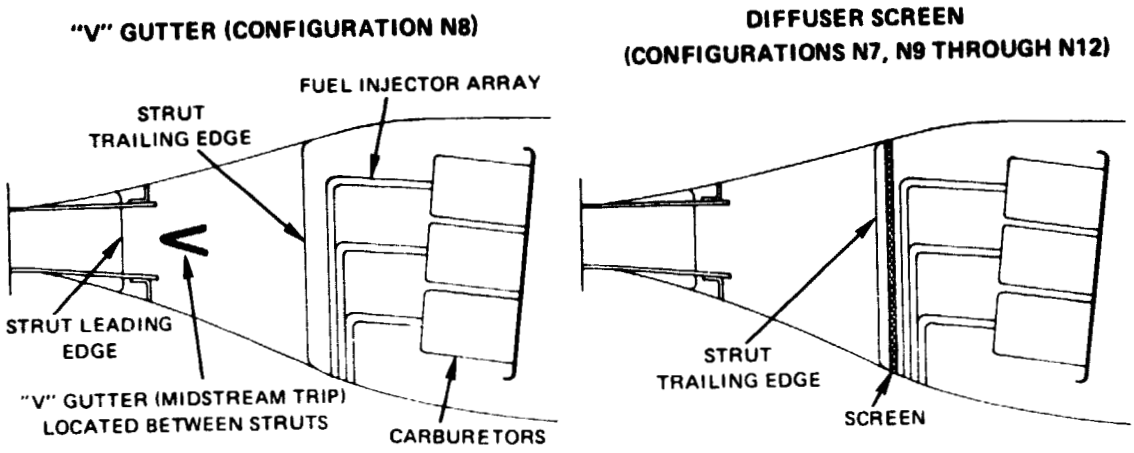

Figure 1b Swirl Can Combustor – Diffuser Modifications (Ref. Figure 1a)

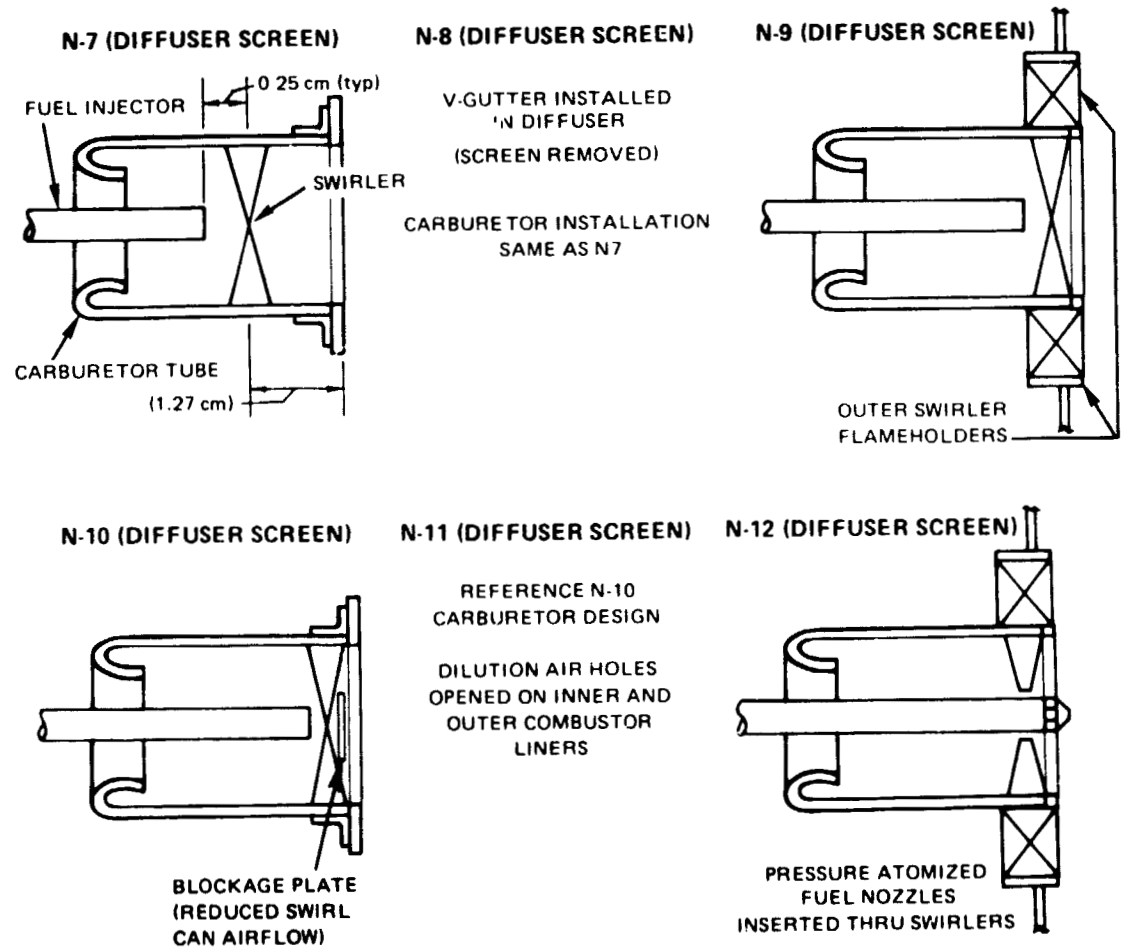

Figure 1c Swirl Can Combustor – Combustor Modifications (Ref. Figure 1a)

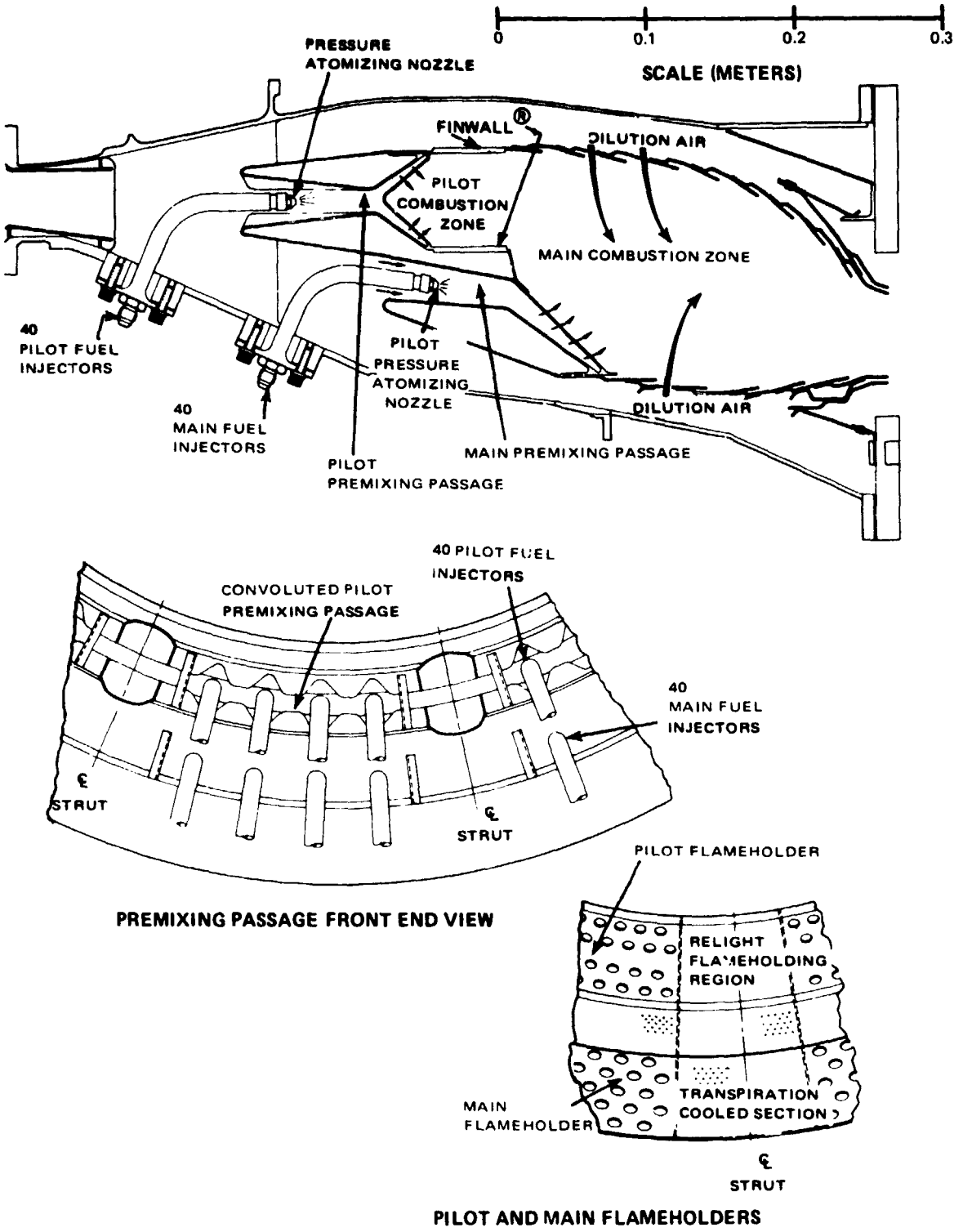

Figure 2a Staged Premix Combustor – Baseline Configuration (P-Series)

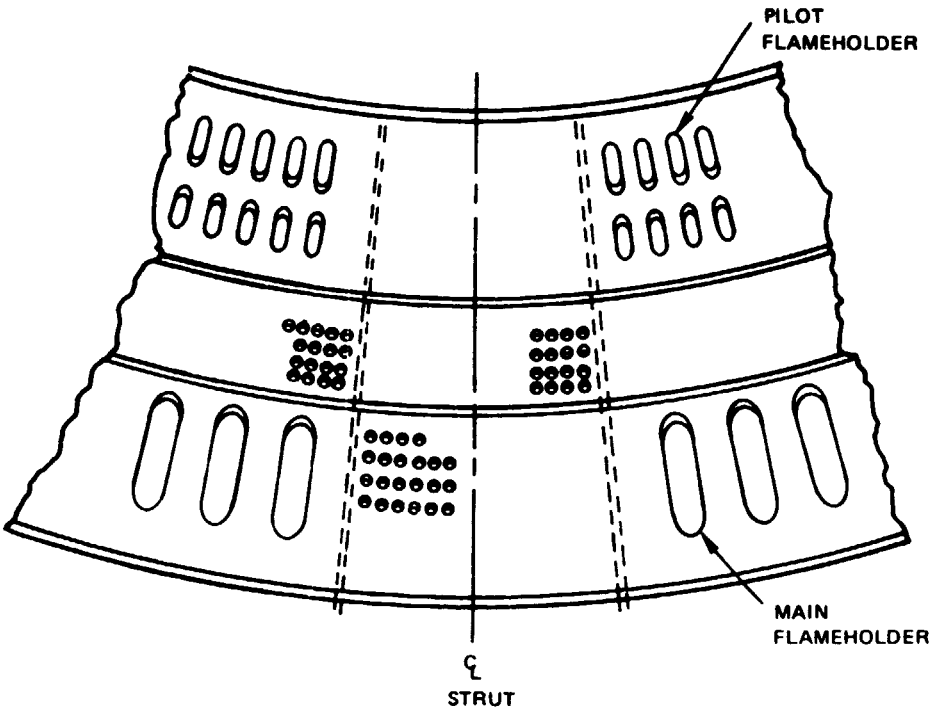

NOTE: INNER AND OUTER LINER DILUTION AIR HOLES NOT USED WITH SLOTTED FLAMEHOLDERS

Figure 2b *Staged Premix Combustor – Slotted Flameholder Configurations P7 and P8 (Ref. Figure 2a)*

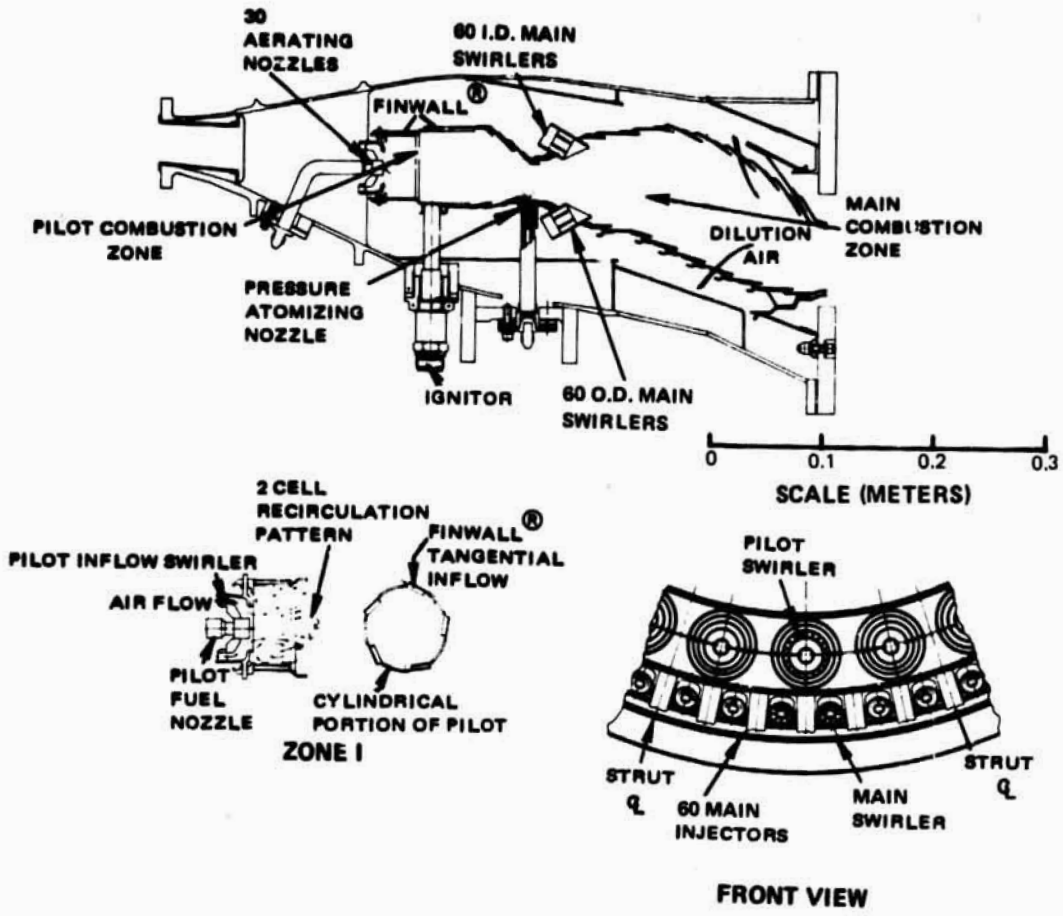

Figure 3 Swirl Vorbix Combustor – Baseline Configuration (S-Series)

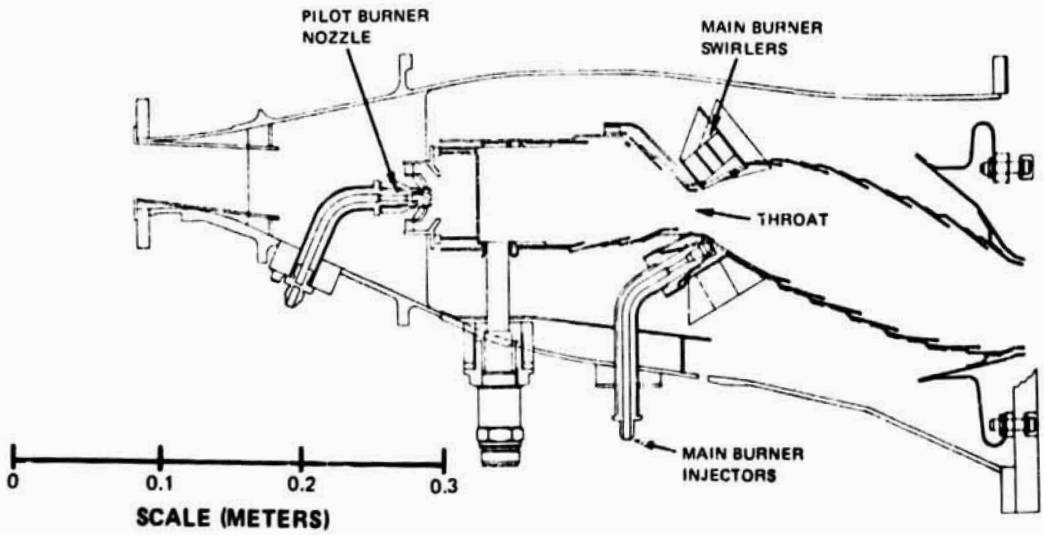

Figure 4a Swirl Vorbix Combustor S-11 (Phase II)

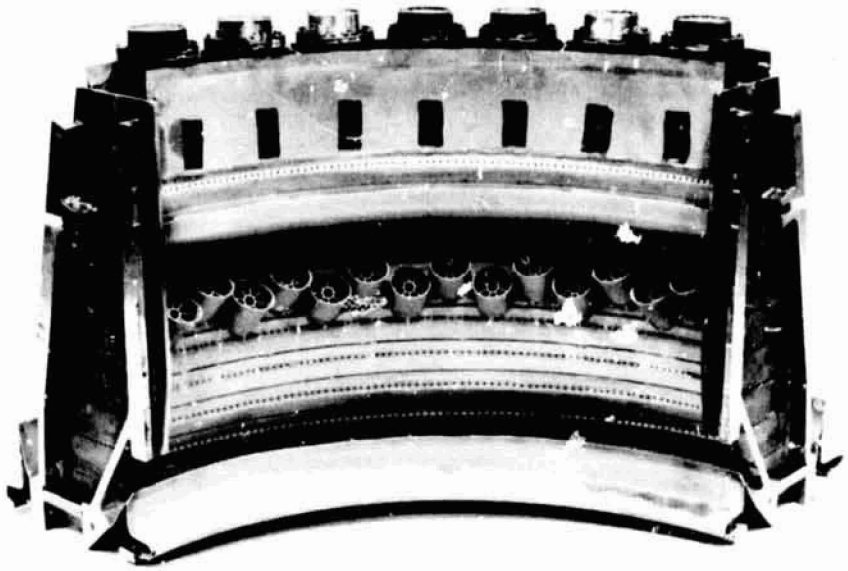

Figure 4b Exterior View of Vorbix Configuraion S-11

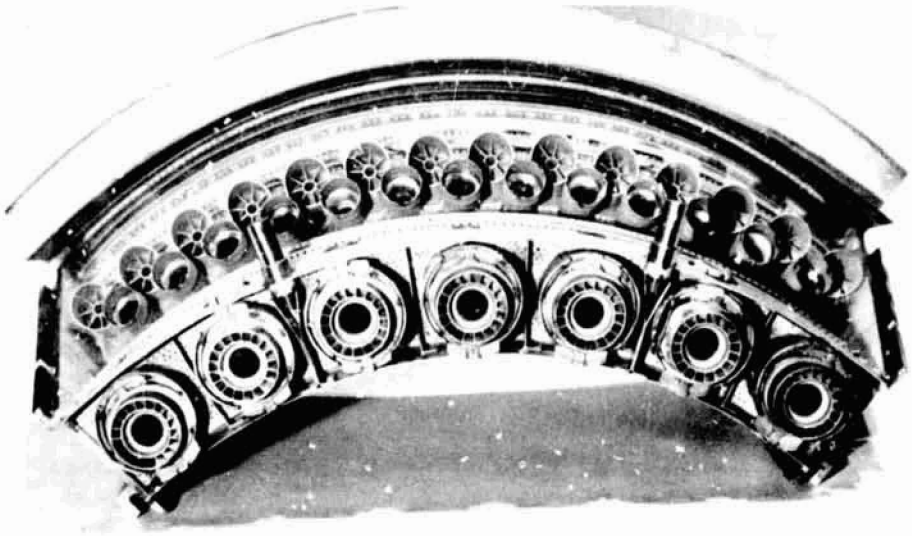

Figure 4c Front-End View of Vorbix Configuration S-11

CONFIGURATION S23

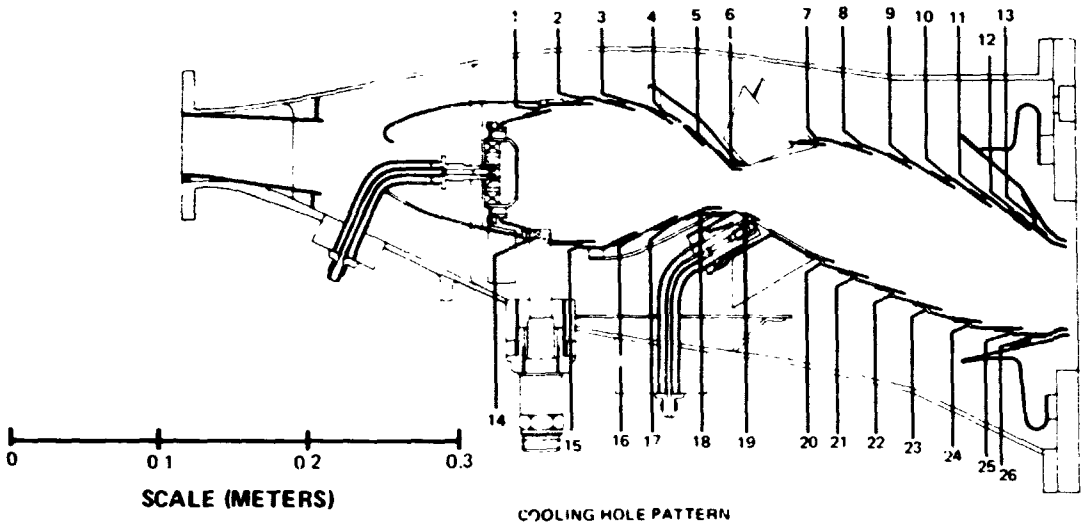

SCALE (METERS)

COOLING HOLE PATTERN

INNER LINER				OUTER LINER			
LOUVER	DIA $m \times 10^{-3}$	#HOLES	AREA $m^2 \times 10^{-4}$	LOUVER	DIA $m \times 10^{-3}$	#HOLES	AREA $m^2 \times 10^{-4}$
1	1 63	84	1 74	14	2 34	84	3 61
2	1 63	84	1 74	15	1 63	84	1 74
3	1 63	84	1 74	16	1 63	84	1 74
4	1 63	84	1 74	17	1 63	84	1 74
5	1 96	84	2 52	18	1 80	84	2 15
6	2 27	84	3 45	19	2 08	130	4 43
7	1 93	85	2 49	20	1 63	99	2 05
8	1 32	85	1 17	21	1 63	99	2 05
9	1 32	85	1 17	22	1 32	118	1 62
10	1 32	85	1 17	23	1 32	95	1 30
11	1 32	85	1 17	24	32	106	1 45
12	1 32	85	1 17	25	1 79	85	2 11
13	1 32	85	1 17	26	1 32	110	1 51

		AREA $m^2 \times 10^{-4}$
PILOT BURNER SWIRLER (INCLUDING SLOTS IN CENTER TUBE OF SWIRLER)	7 LEFTHAND SWIRLERS	27 46 A_{CD} (EFFECTIVE AREA)
BULKHEAD COOLING	140 @ 0 234 X 10^{-2}m DIAMETER	6 09
MAIN BURNER NOZZLE COOLING	52 @ 0 254 X 10^{-2}m DIAMETER	2 63
PILOT BURNER DILUTION (INNER WALL ROW 1)	7 @ 1 63 X 10^{-2}m DIAMETER	14 62
PILOT BURNER DILUTION (OUTER WALL ROW 14)	7 @ 1.63 X 10^{-2}m DIAMETER	14 62
MAIN BURNER SWIRLERS	28 RIGHTHAND SWIRLERS	81 48 A_{CD} (EFFECTIVE AREA)
SIDEWALL COOLING	5% W_{A4} (TOTAL AIRFLOW – STATION 4)	
TURBINE COOLING (INNER WALL)	7 5% W_{A4} (TOTAL AIRFLOW – STATION 4)	
TURBINE COOLING (OUTER WALL)	8 4% W_{A4} (TOTAL AIRFLOW – STATION 4)	
PILOT BURNER NOZZLE	DLN 27700-13, 7 LOCATIONS	
MAIN BURNER NOZZLE	DLN 27700-11, 13 LOCATIONS	
MAIN BURNER DILUTION OUTER WALL	LOUVER 22	15 22
MAIN BURNER DILUTION OUTER WALL	LOUVER 21	25 74

Figure 5 Vorbix Combustor Configuration S-23 (Phase II)

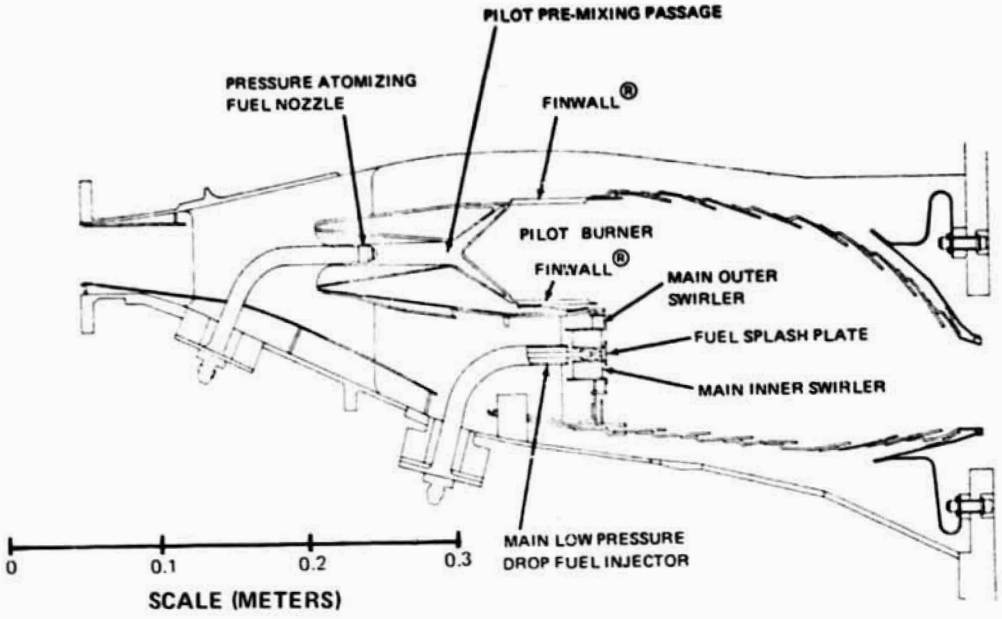

Figure 6a Basic Hybrid Combustor Design (H-Series) (Phase II)

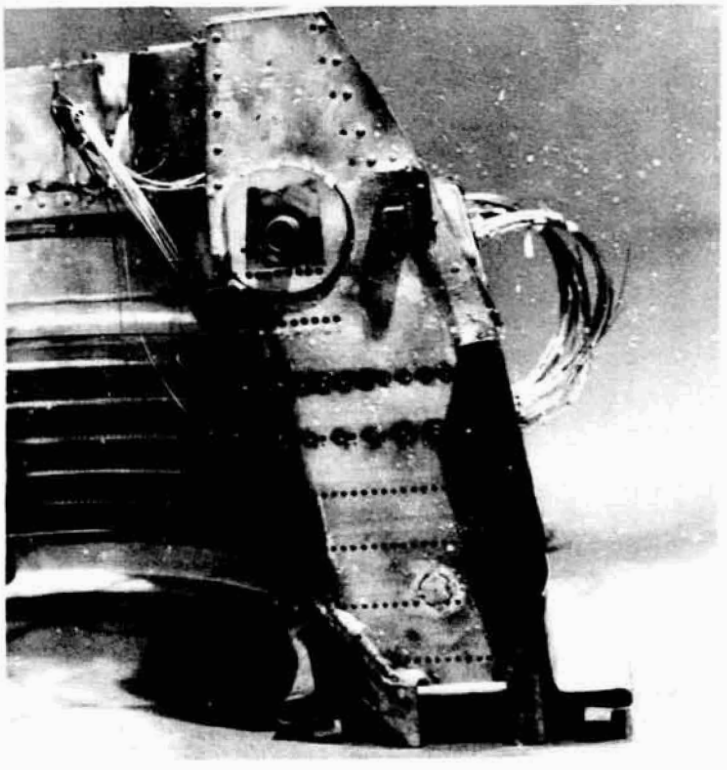

Figure 6b Exterior View of Basic Hybrid Combustor

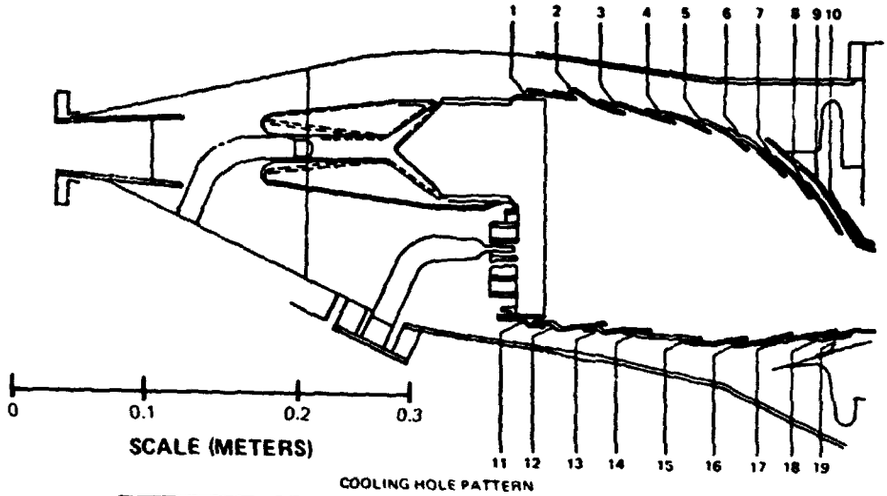

COOLING HOLE PATTERN

INNER LINER				OUTER LINER			
LOUVER	DIA $m \times 10^{3}$	# HOLES	AREA $m^2 \times 10^{4}$	LOUVER	DIA $m \times 10^{3}$	# HOLES	AREA $m^2 \times 10^{4}$
1	1.32	85	1.17	11	1.32	110	1.51
2	1.32	85	1.17	12	1.32	110	1.51
3	1.32	85	1.17	13	1.32	110	1.51
4	1.32	85	1.17	14	1.32	110	1.51
5	1.32	92	1.26	15	1.93	60	1.75
6	1.32	81	1.11	16	2.16	60	2.19
7	1.32	92	1.26	17	2.31	60	2.52
8	1.32	122	1.67	18	2.36	60	2.63
9	1.59	85	1.68	19	1.59	110	2.17
10	1.59	85	1.68				

		AREA $m^2 \times 10^{-4}$
PILOT BURNER FLAMEHOLDER	94 @ 0.80 × 10^{-2} DIAMETER	47.26 A_{CD} (EFFECTIVE AREA)
PILOT BURNER FLAMEHOLDER WEEP		7.43 A_{CD} (EFFECTIVE AREA)
MAIN BURNER OUTER SWIRLER	11 LEFT HAND SWIRLERS	62.31 A_{CD} (EFFECTIVE AREA)
MAIN BURNER INNER SWIRLER	11 RIGHT HAND SWIRLERS	54.42 A_{CD} (EFFECTIVE AREA)
BULKHEAD COOLING	172 @ 0.411 X 10^{-2}m DIAMETER	22.87
FLAMEHOLDER COOLING (ON OUTER WALL)	39 @ 0.254 X 10^{-2}m DIAMETER	1.97
FLAMEHOLDER COOLING (ON INNER WALL)	38 @ 0.254 X 10^{-2} m DIAMETER	1.92
FINWALL® (INNER WALL)	1.01% W_{AB} (BURNER AIRFLOW)	
FINWALL® (OUTER WALL)	1.23% W_{AB} (BURNER AIRFLOW)	
SIDEWALL COOLING	5.00% W_{A4} (TOTAL AIRFLOW – STATION 4)	
TURBINE COOLING (INNER WALL)	7.5% W_{A4} (TOTAL AIRFLOW – STATION 4)	
TURBINE COOLING (OUTER WALL)	8.4% W_{A4} (TOTAL AIRFLOW – STATION 4)	
PILOT BURNER NOZZLE – P/N	DLN 27700-11 10 LOCATIONS	
MAIN BURNER NOZZLE – P/N	LOW ΔP 11 LOCATIONS	

Figure 7 Hybrid Combustor Configuration H-6 (Phase II)

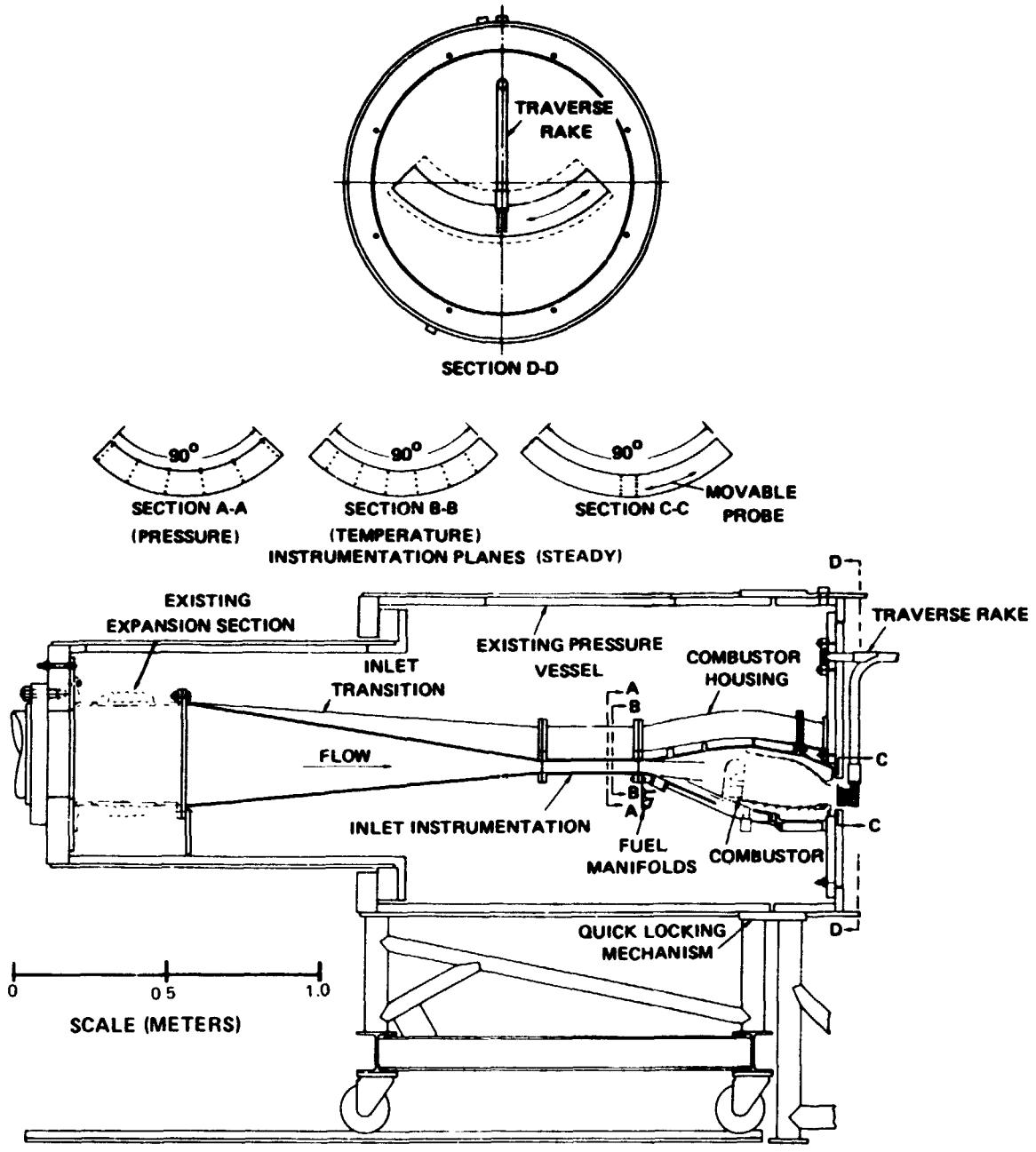

Figure 8a Schematic of Combustor Rig

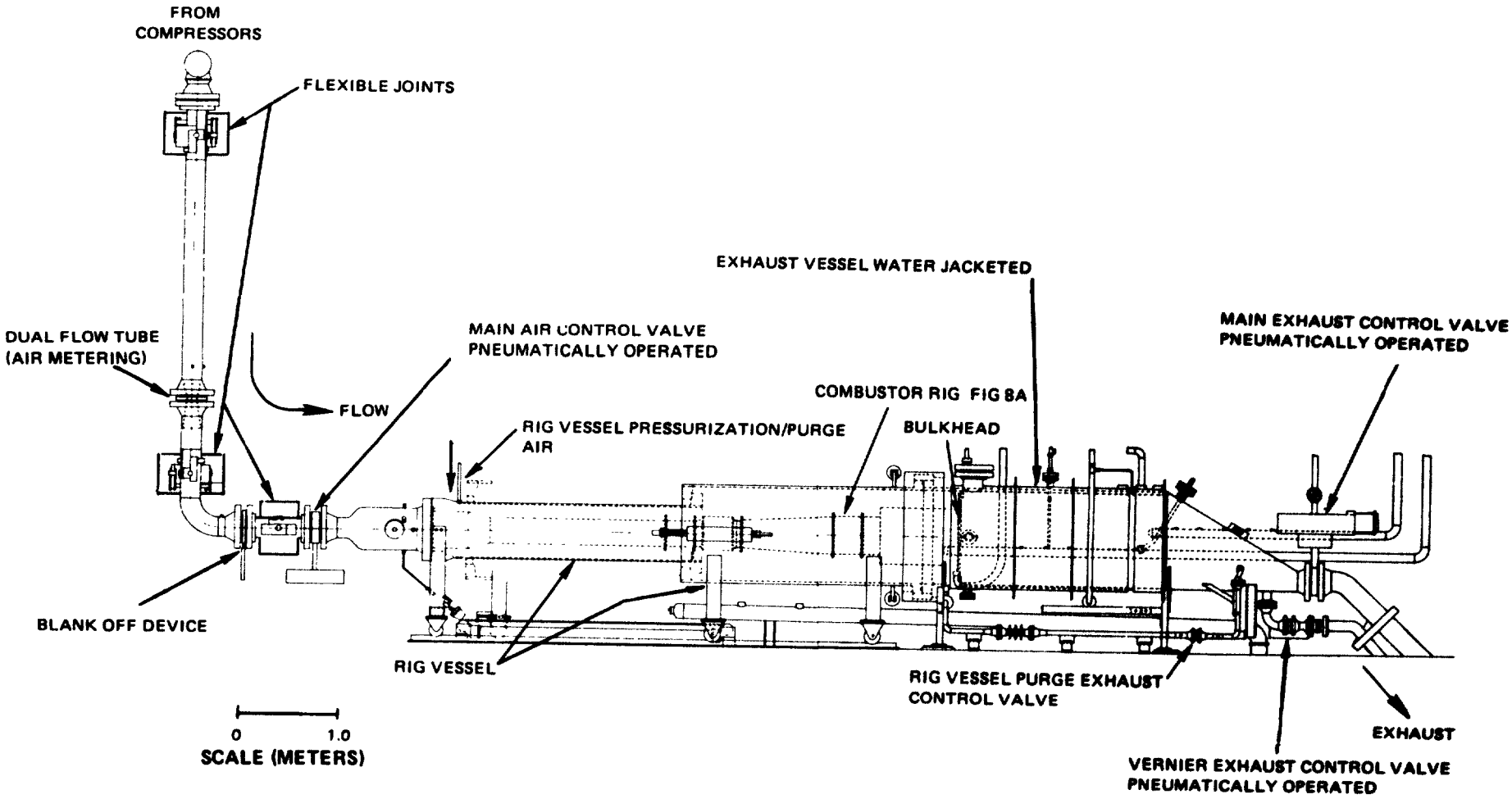

Figure 8B *Schematic of Test Facility*

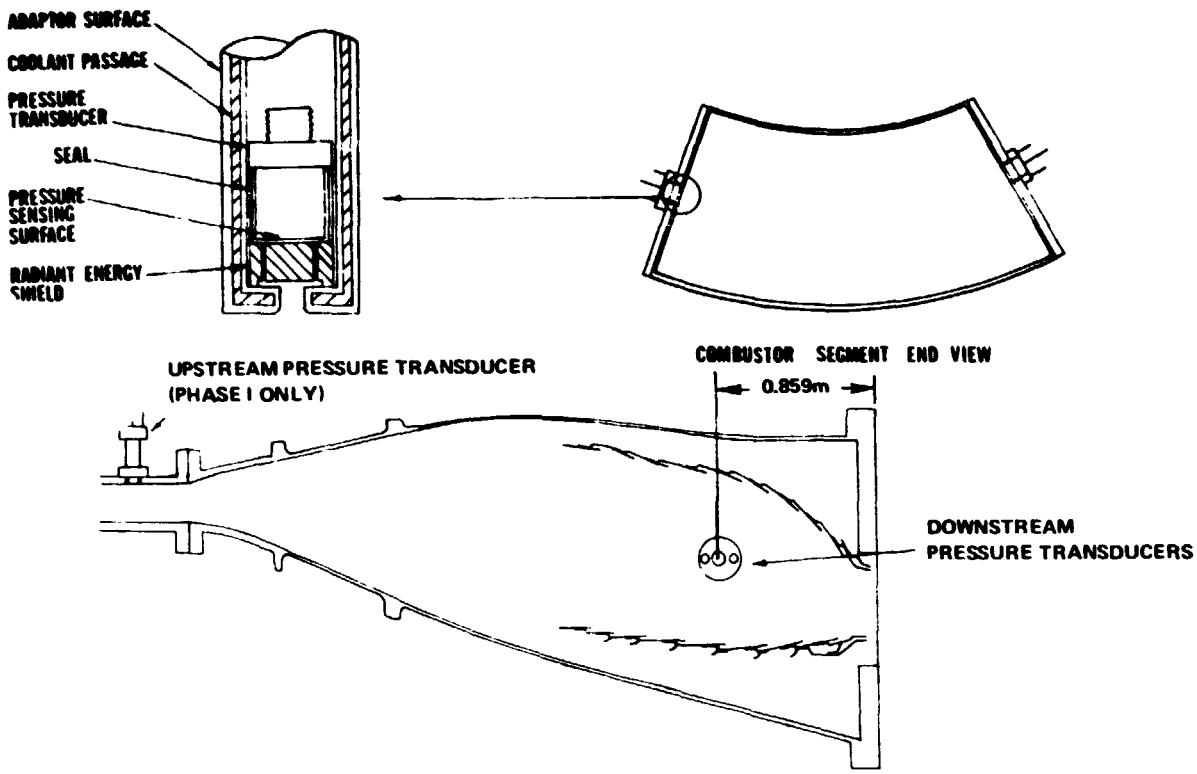

Figure 9 Typical Pressure Transducer Installation in Combustor Rig

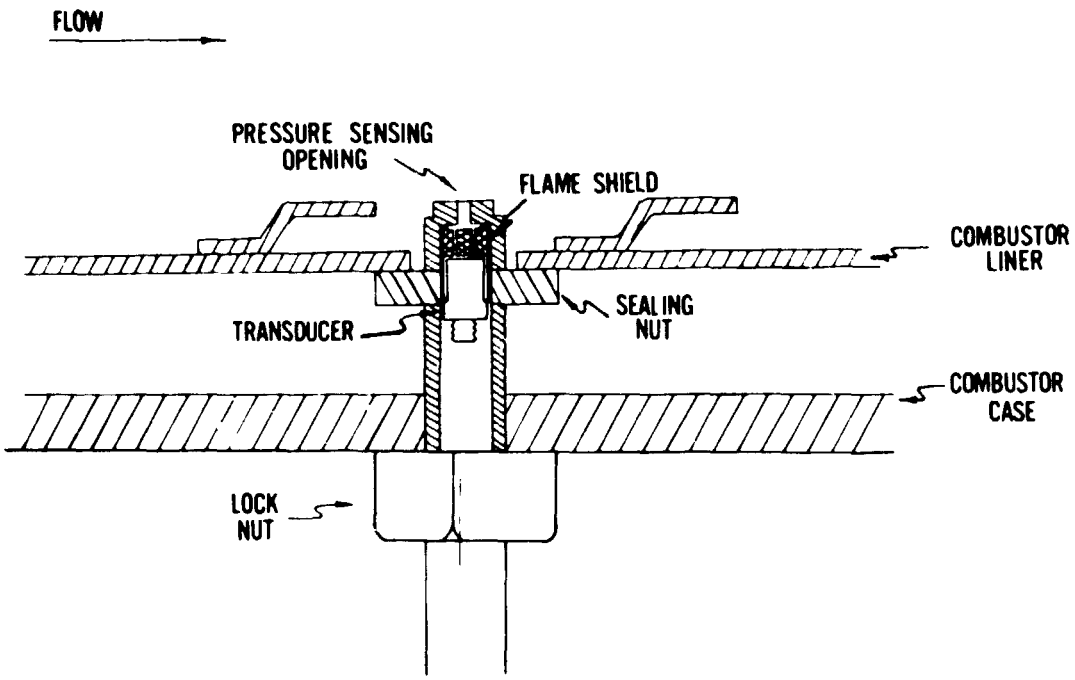

Figure 10 Typical Transducer Installation (detail)

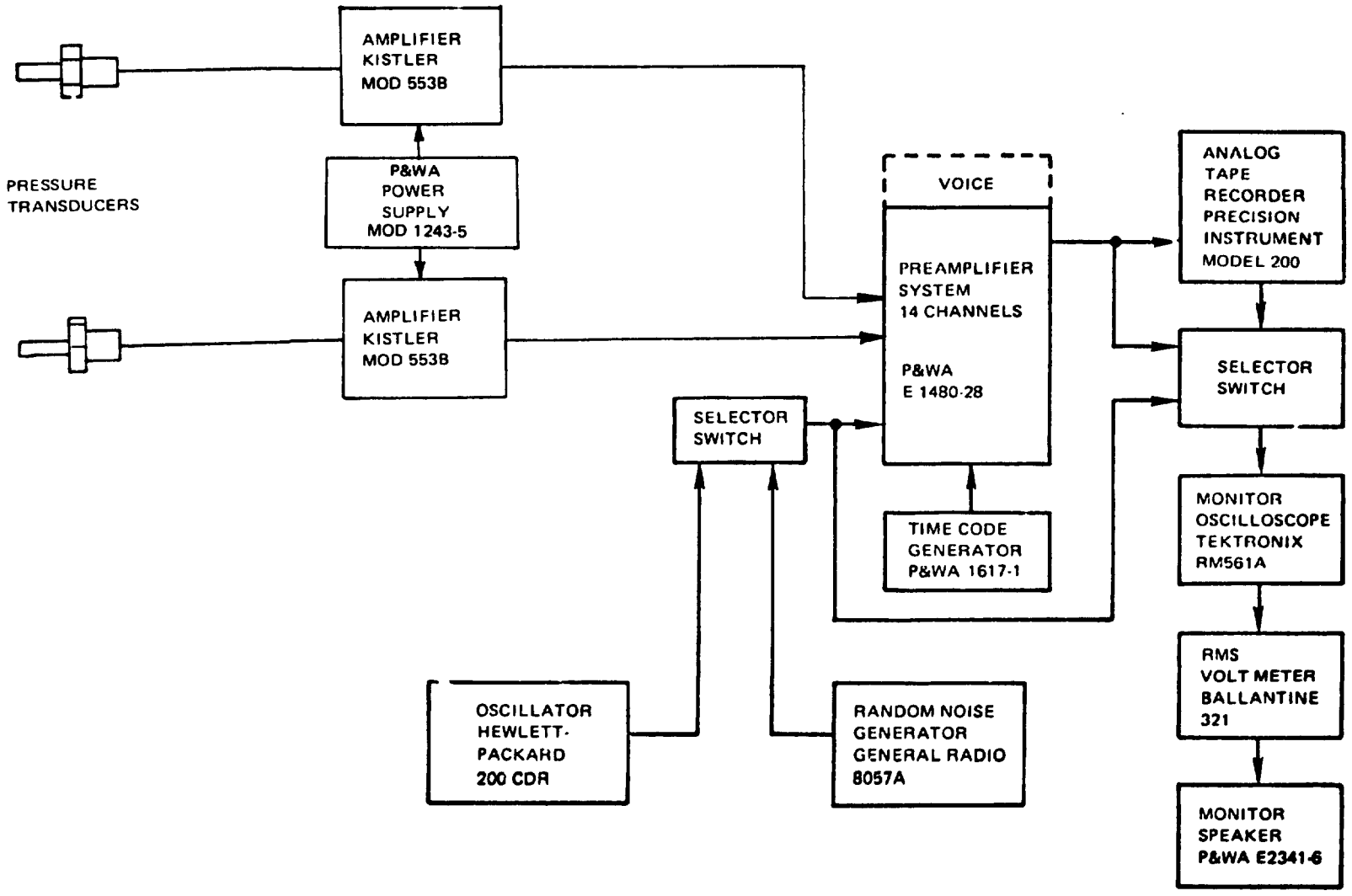

Figure 11 *P&WA Combustor Dynamic Pressure Recording System*

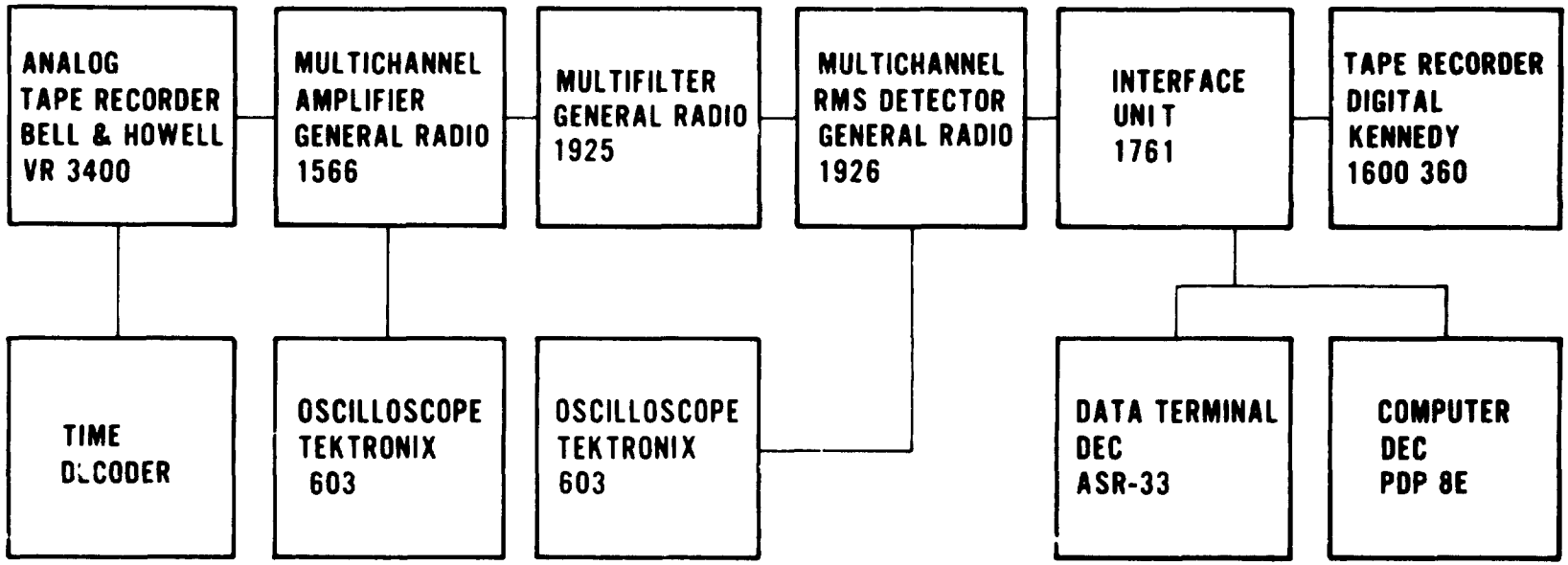

Figure 12 P&WA 1/3 Octave Pressure Analysis System

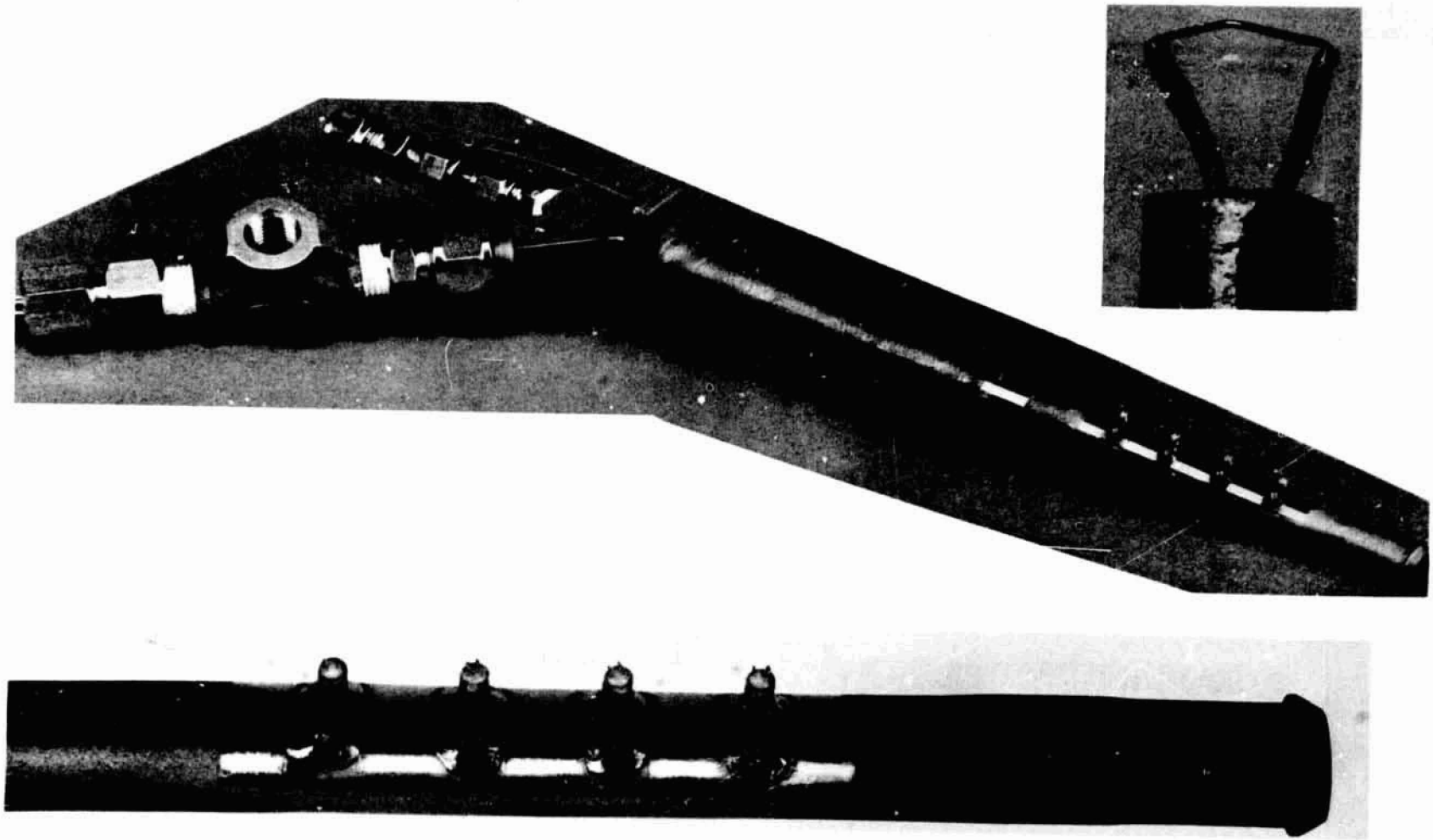

Figure 13 Fast Response Thermocouple and Rake

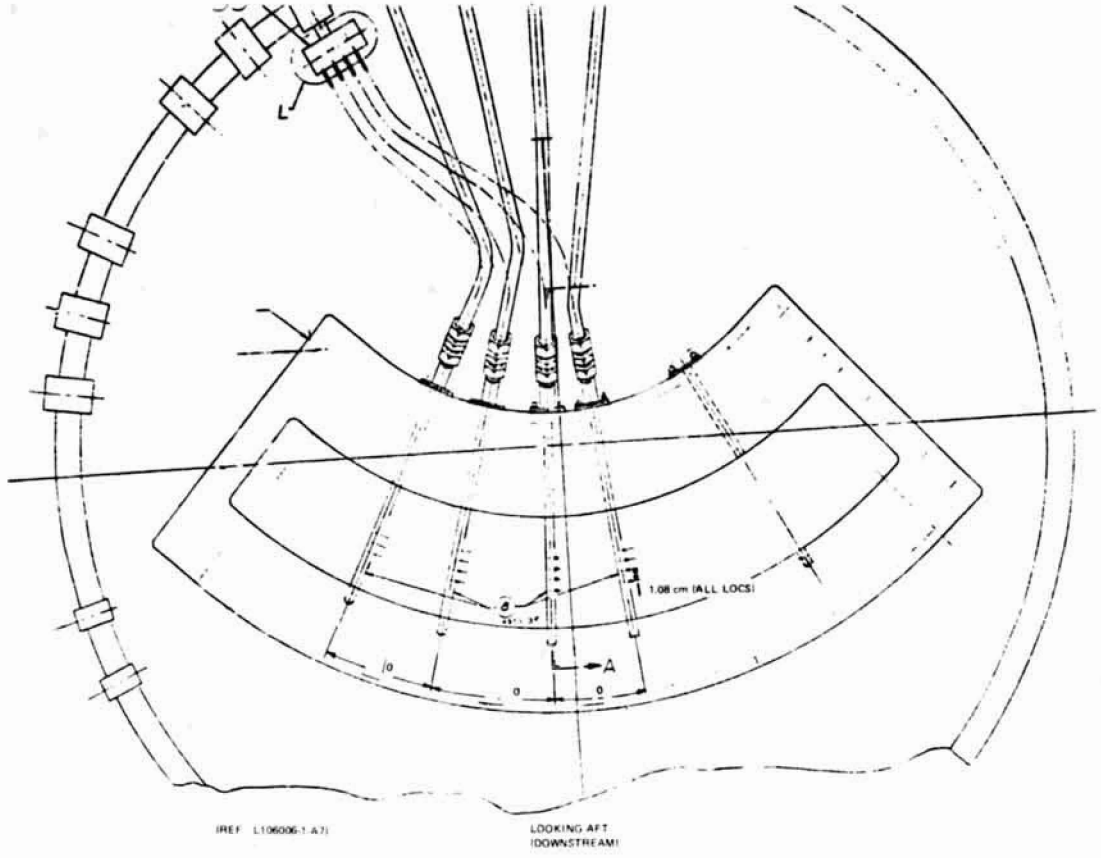

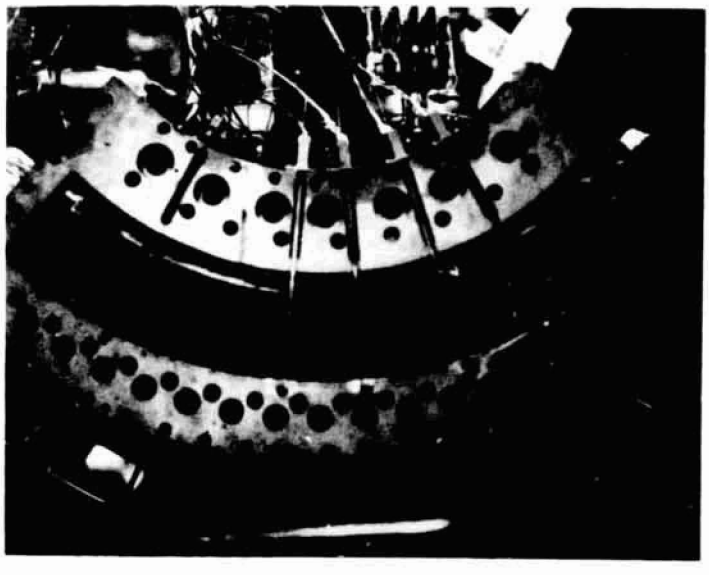

Figure 14 Fast Response Thermocouple Installation

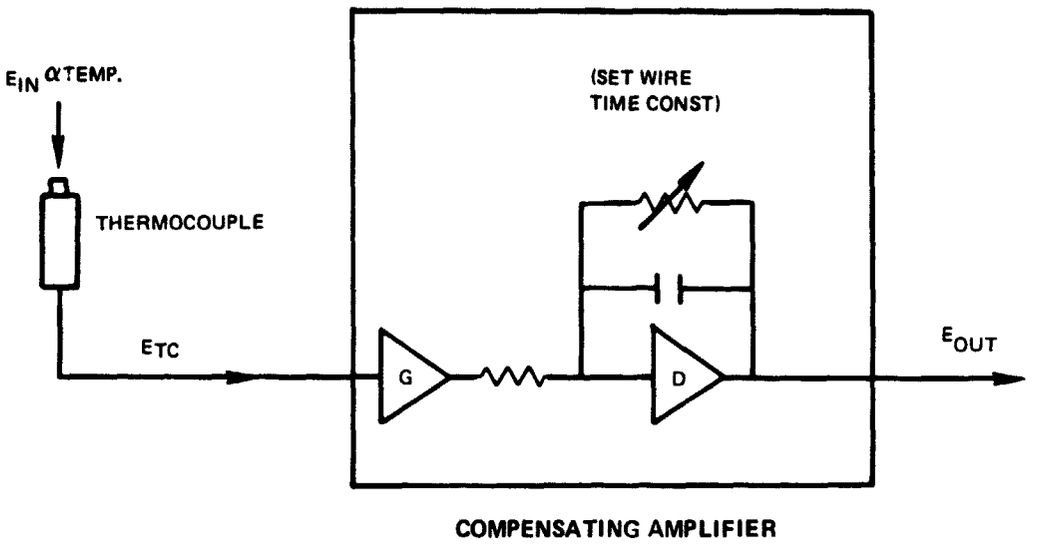

Figure 15a *Schematic Diagram of Thermocouple System Circuit*

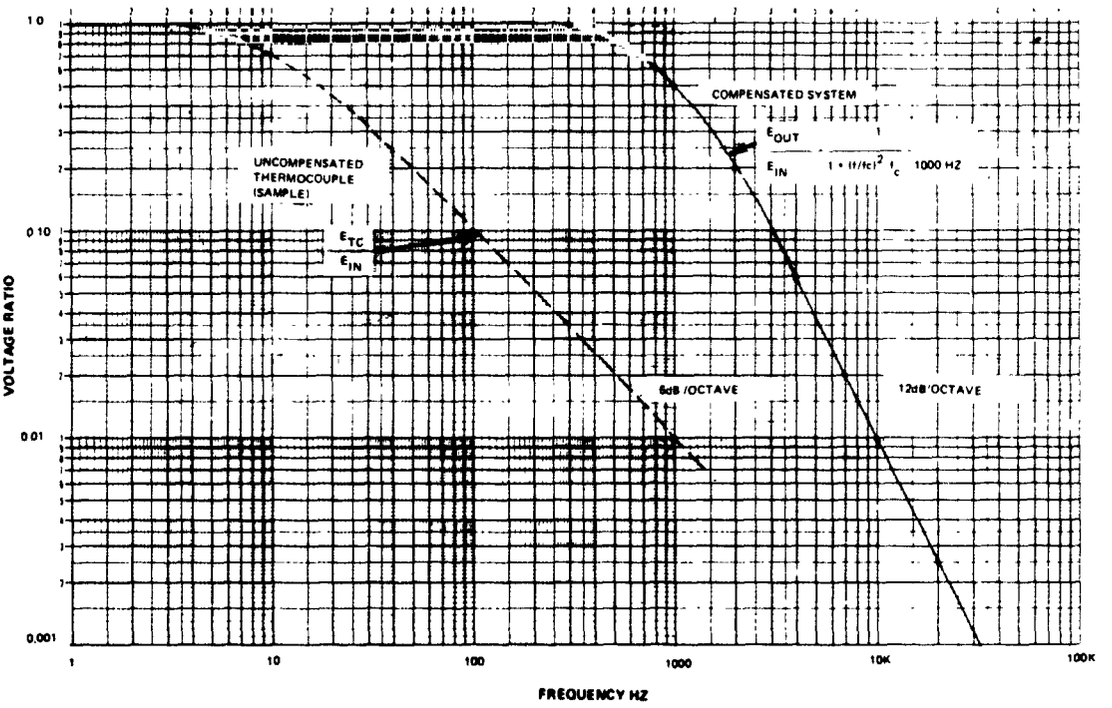

Figure 15b *Overall Frequency Response of Thermocouple and Compensating Amplifier System (Also Showing Sample Uncompensated Thermocouple Response)*

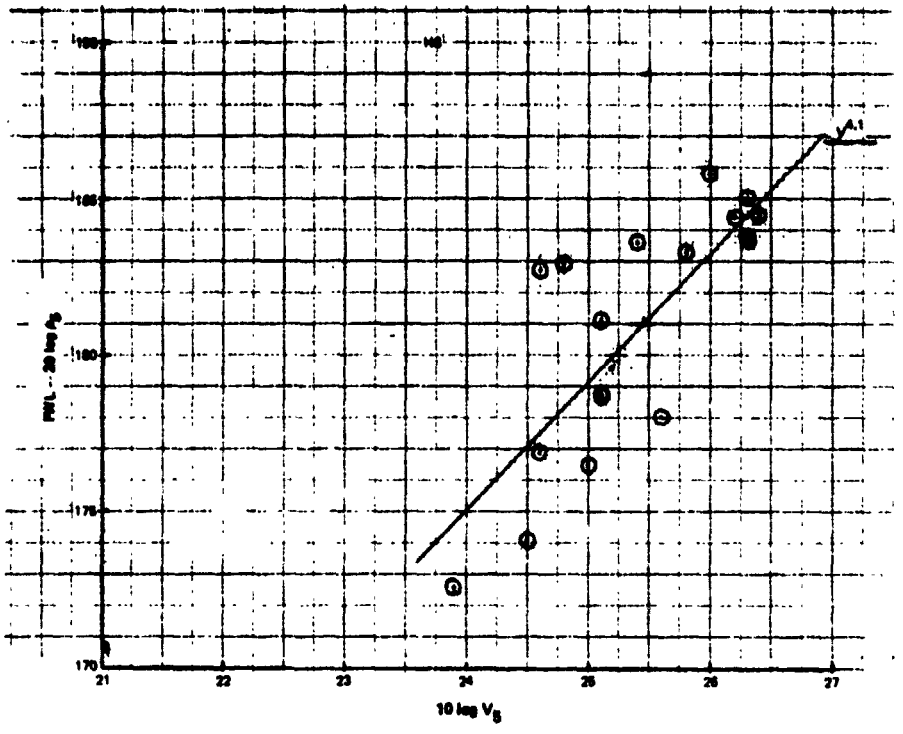

Figure 16 *Aerodynamic Noise Check: H-6*

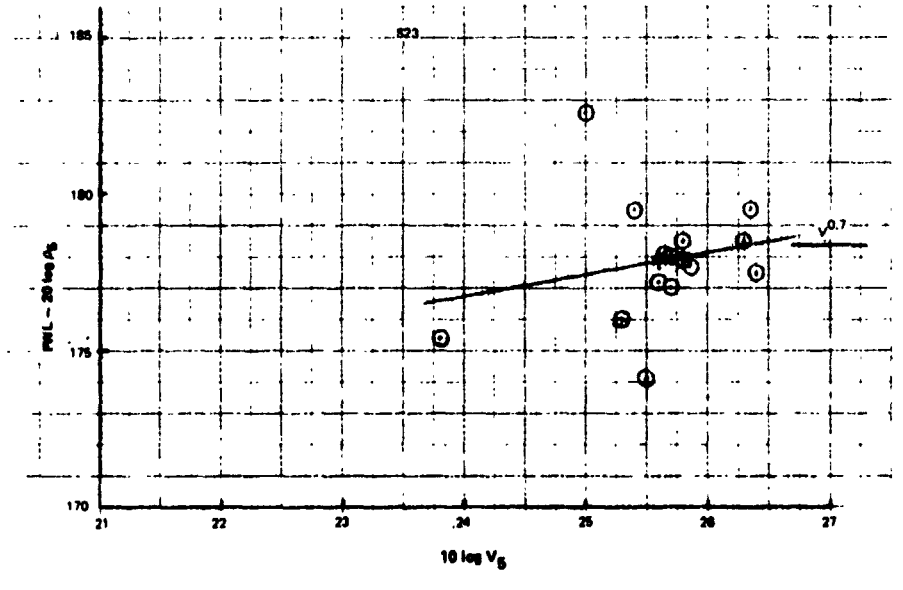

Figure 17 *Aerodynamic Noise Check: S-23*

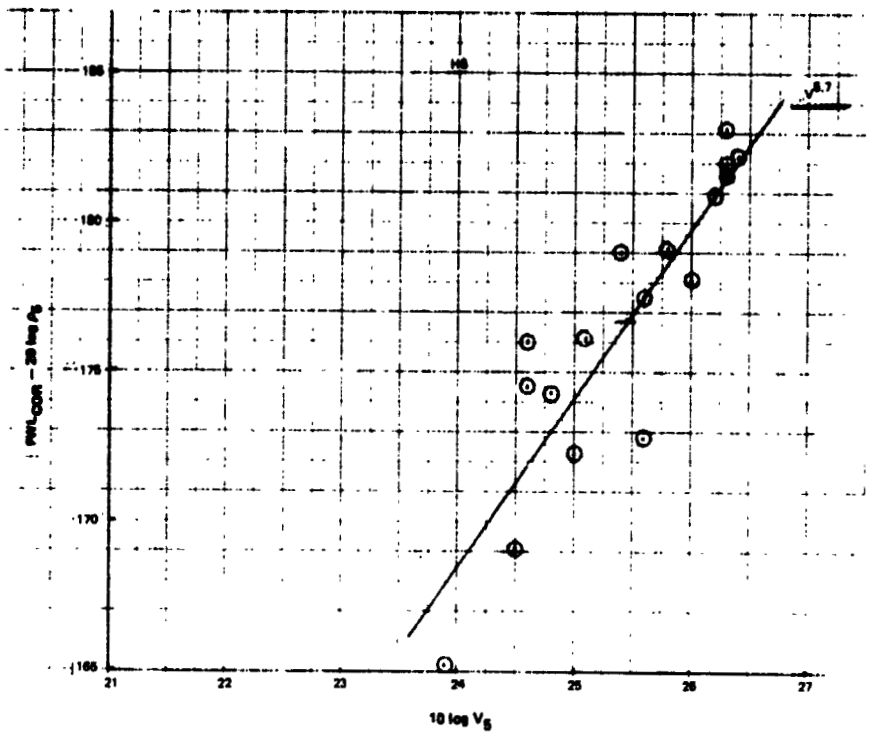

Figure 18 *Aerodynamic Noise Check With PWL_{cor}: H-6*

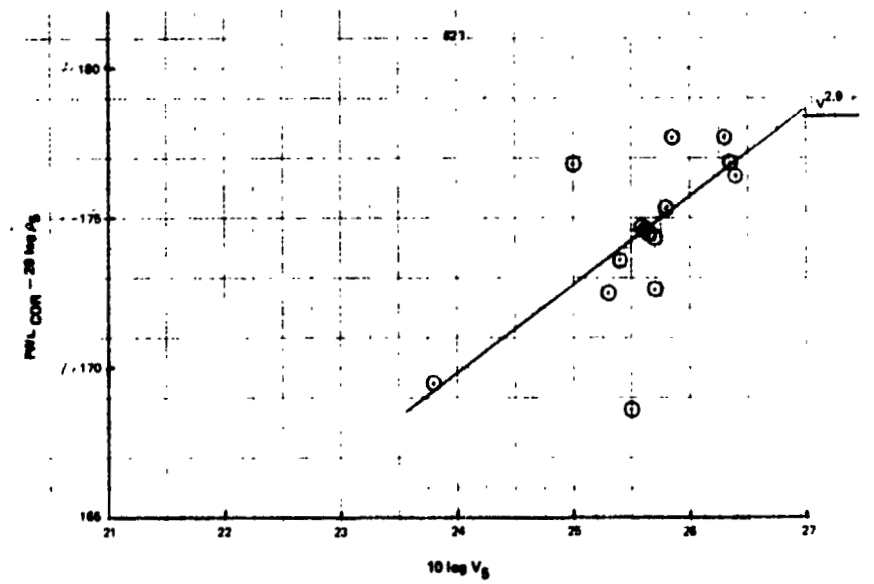

Figure 19 *Aerodynamic Noise Check With PWL_{cor}: S-23*

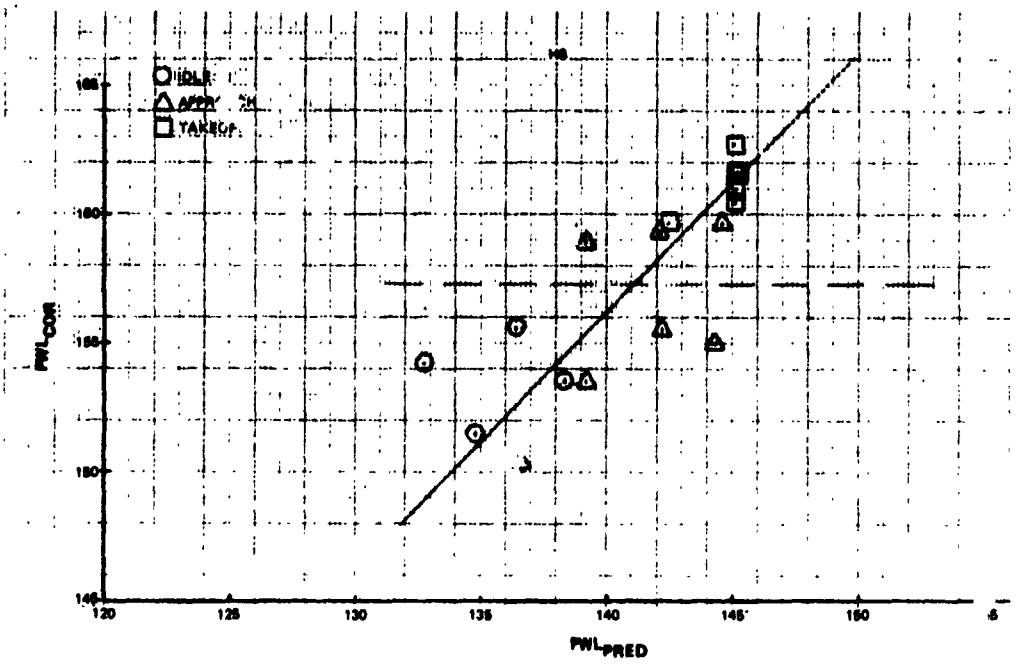

Figure 20 *Relation Between PWL_{cor} and PWL_{pred} (All Points): H-6*

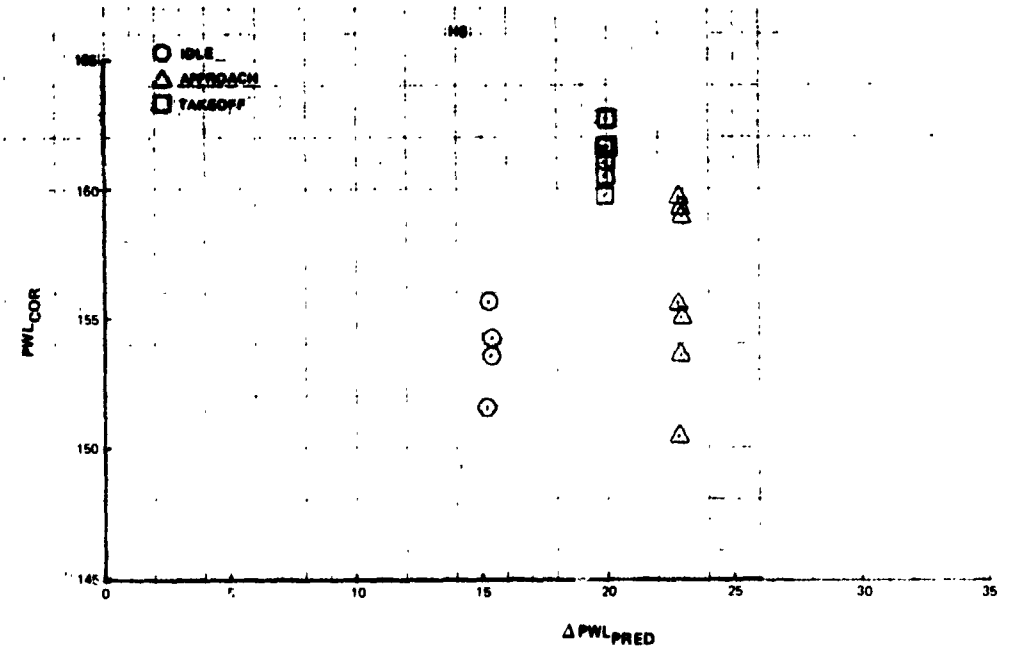

Figure 21 *Relation Between PWL_{cor} and ΔPWL_{pred} (All Points): H-6*

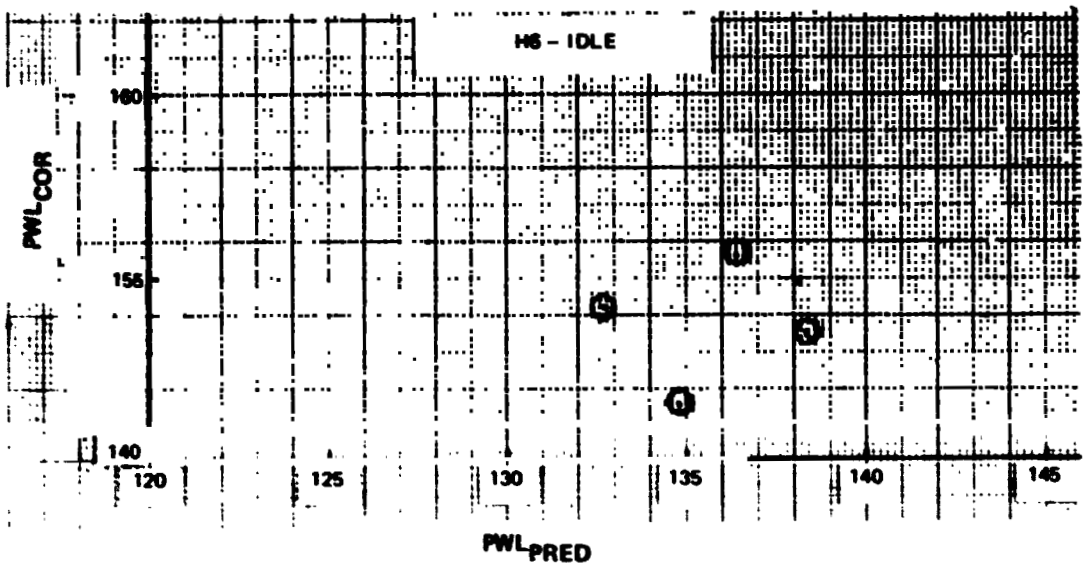

Figure 22 *Relation Between PWL_{cor} and PWL_{pred}: H-6, Idle*

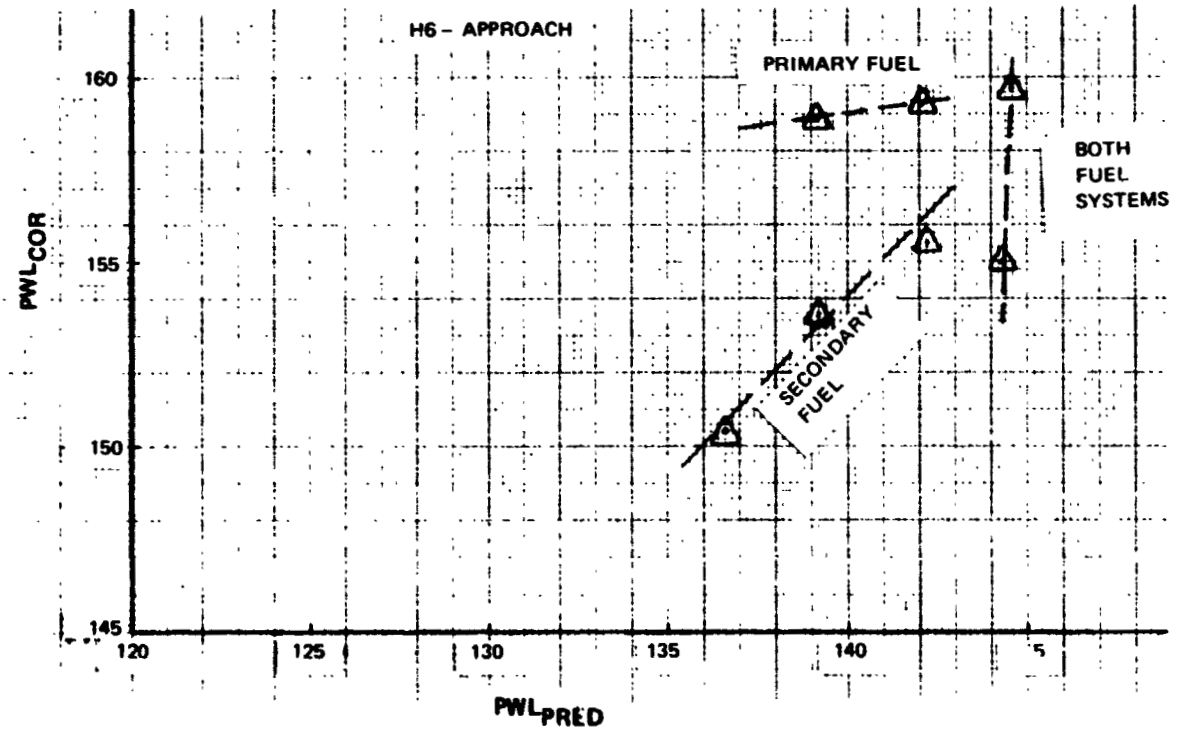

Figure 23 *Relation Between PWL_{cor} and PWL_{pred}: H-6, Approach*

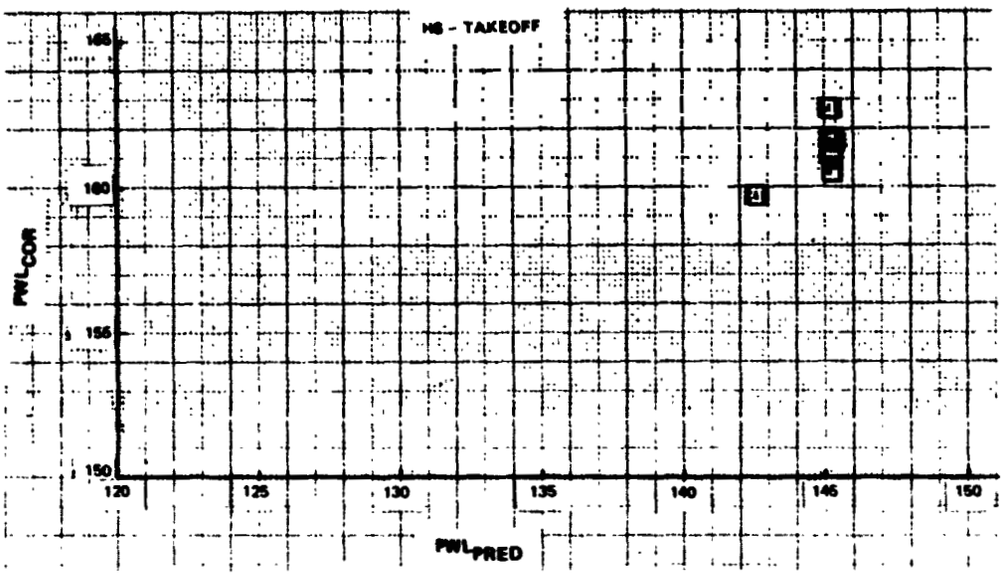

Figure 24 Relation Between PWL_{cor} and PWL_{pred}: H-6, Takeoff

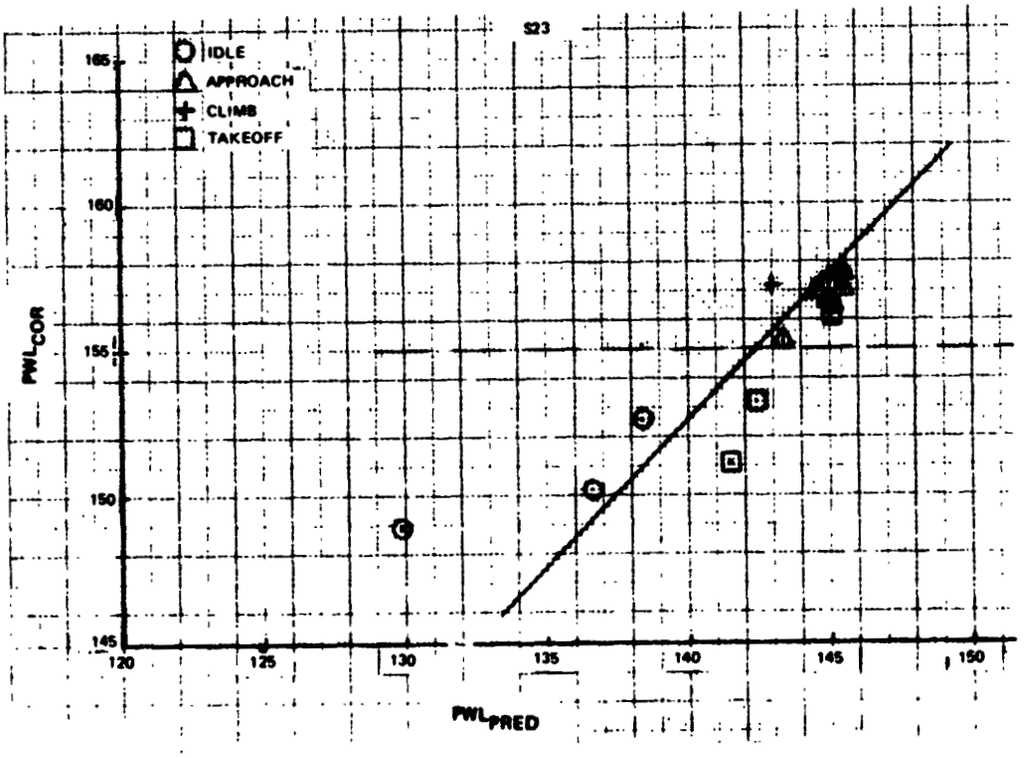

Figure 25 Relation Between PWL_{cor} and PWL_{pred} (All Points): S-23

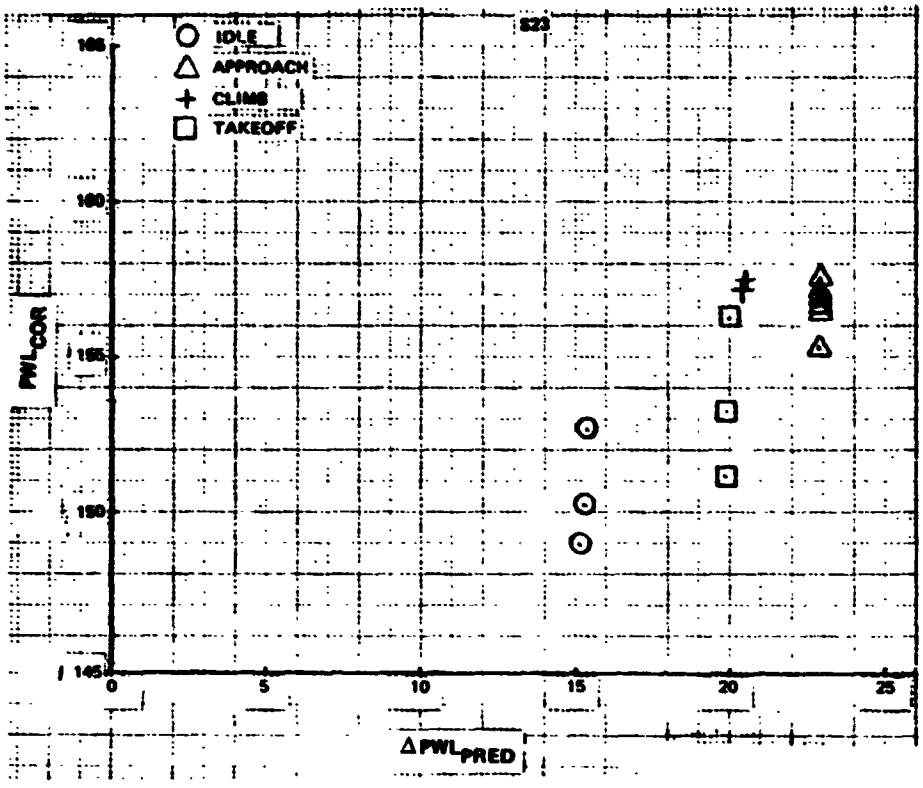

Figure 26 Relation Between PWL_{cor} and ΔPWL_{pred} (All Points): S-23

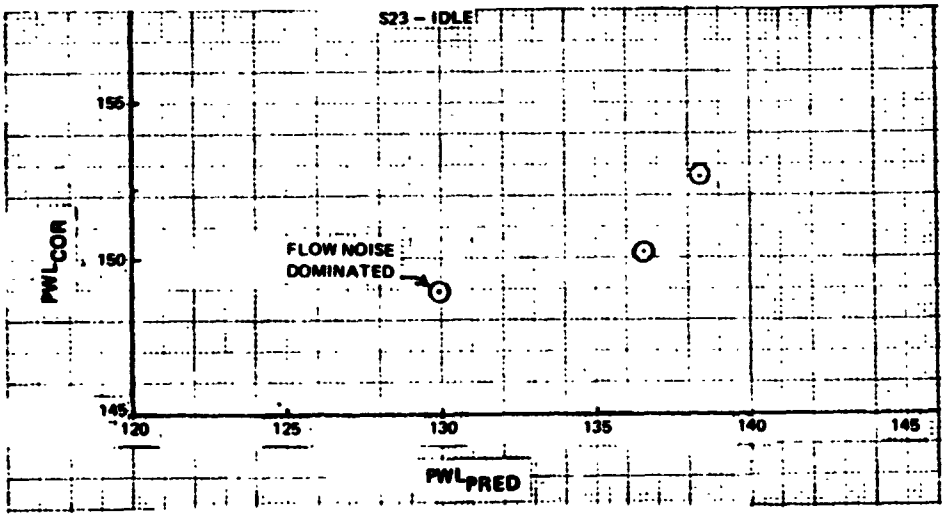

Figure 27 Relation Between PWL_{cor} and PWL_{pred}: S-23, Idle

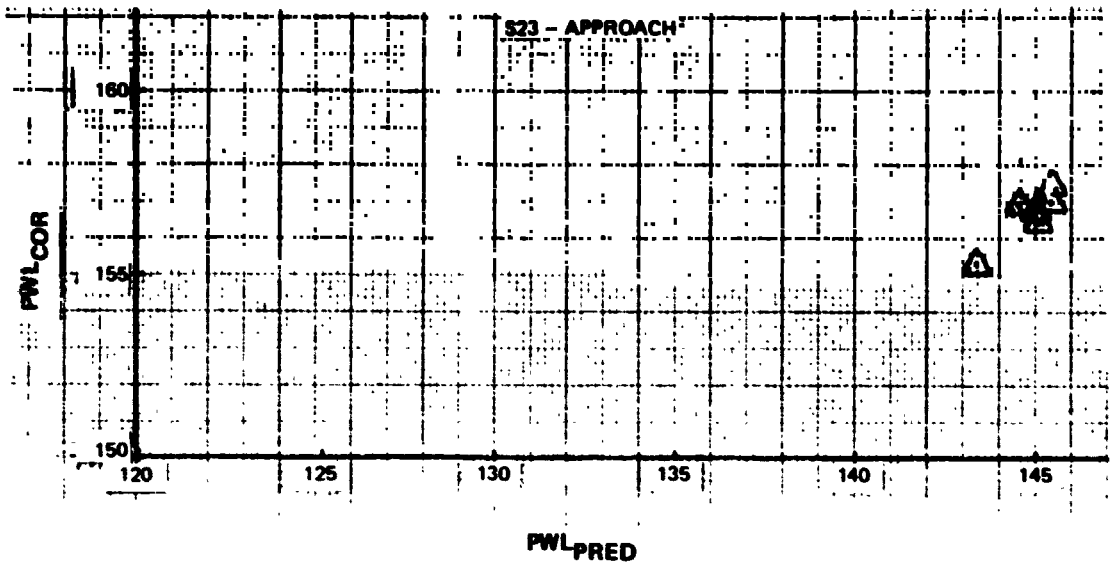

Figure 28 *Relation Between PWL_{cor} and PWL_{pred}: S-23, Approach*

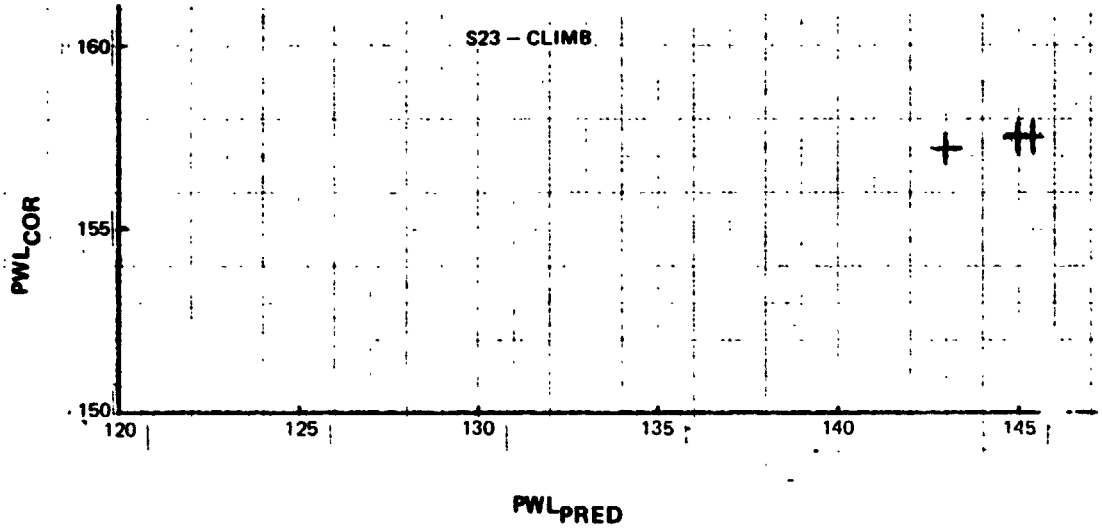

Figure 29 *Relation Between PWL_{cor} and PWL_{pred}: S-23, Climb*

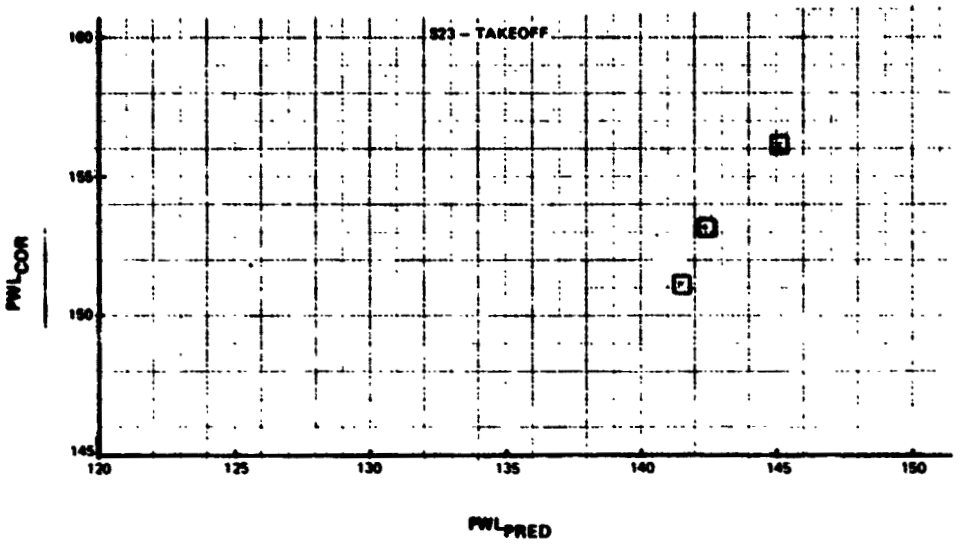

Figure 30 *Relation Between PWL_{cor} and PWL_{pred}: S-23, Takeoff*

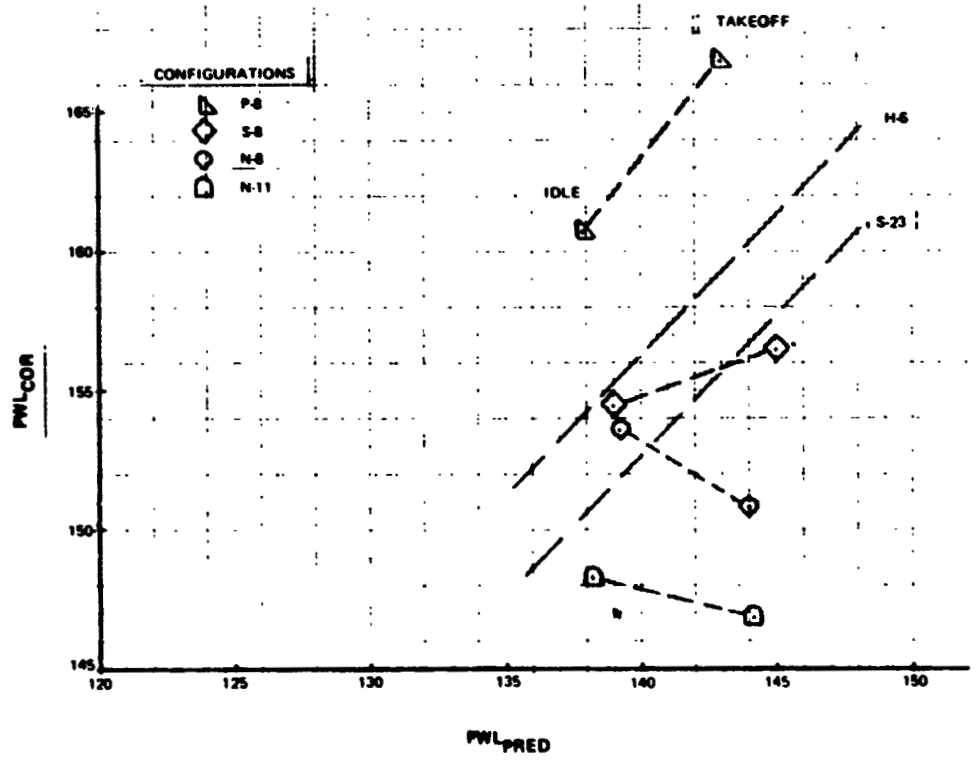

Figure 31 *Configurations P-8, S-8, N-8, N-11, H-6, S-23: PWL_{cor} vs. PWL_{pred}*

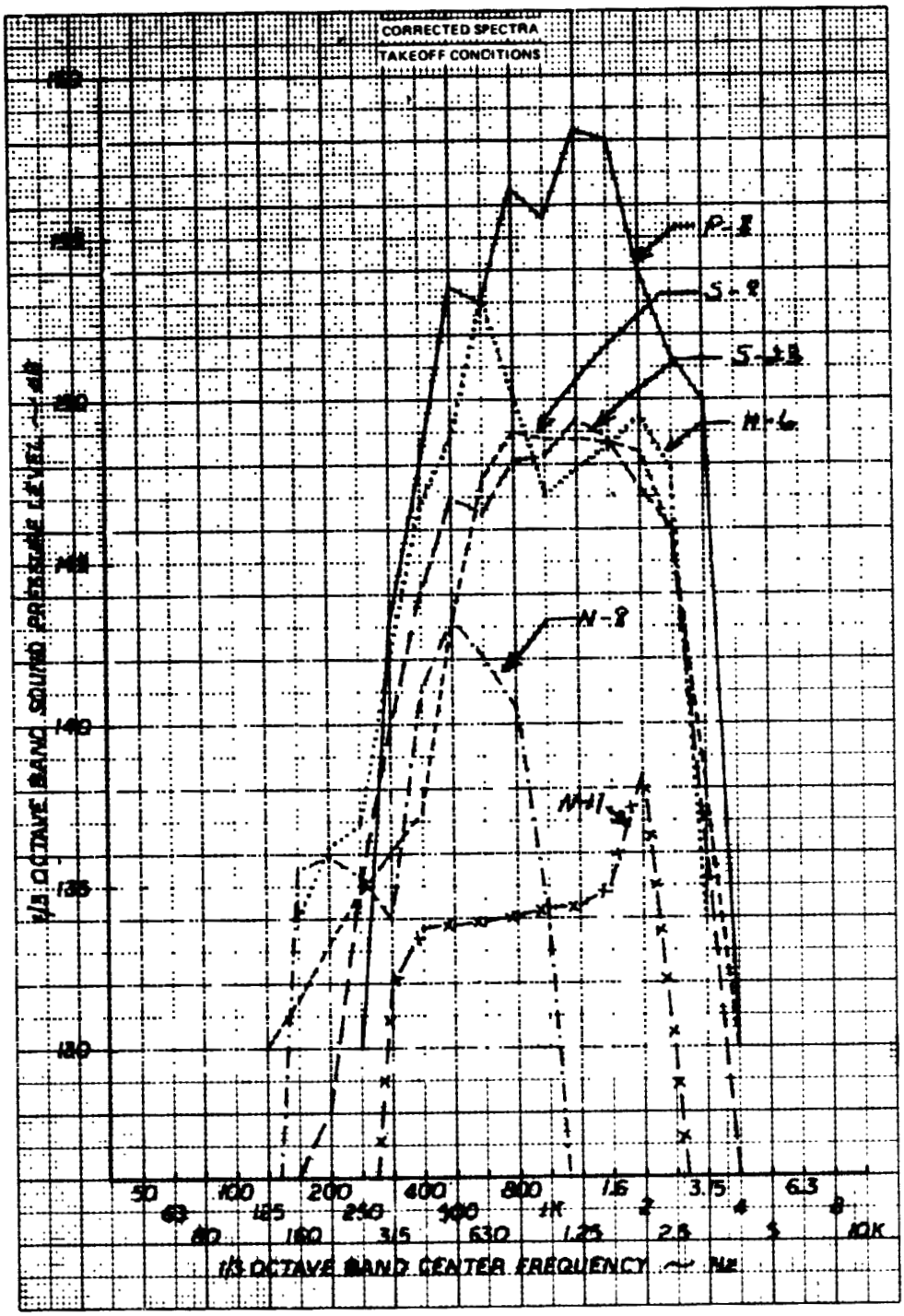

Figure 32 *Corrected Pressure Spectra Used For PWL_{cor} (Takeoff)*

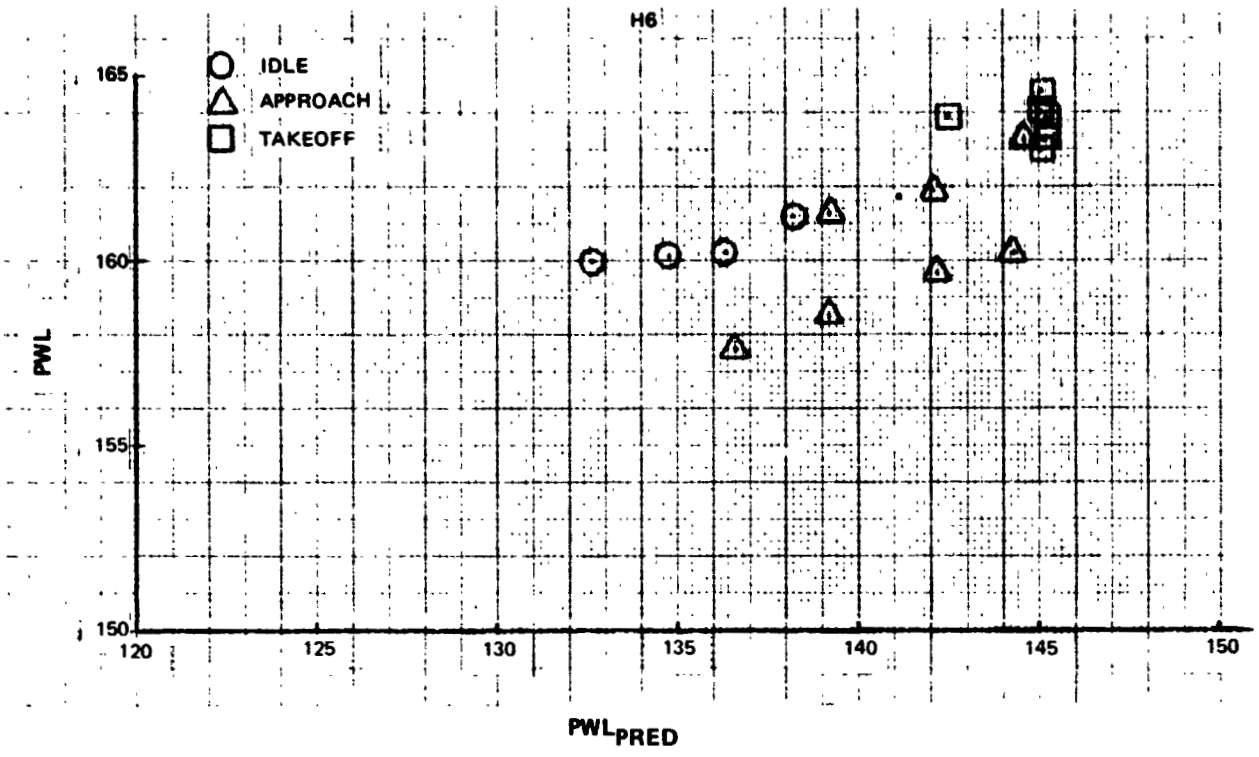

Figure 33 Relation Between PWL and PWL_{pred} (All Points): H-6

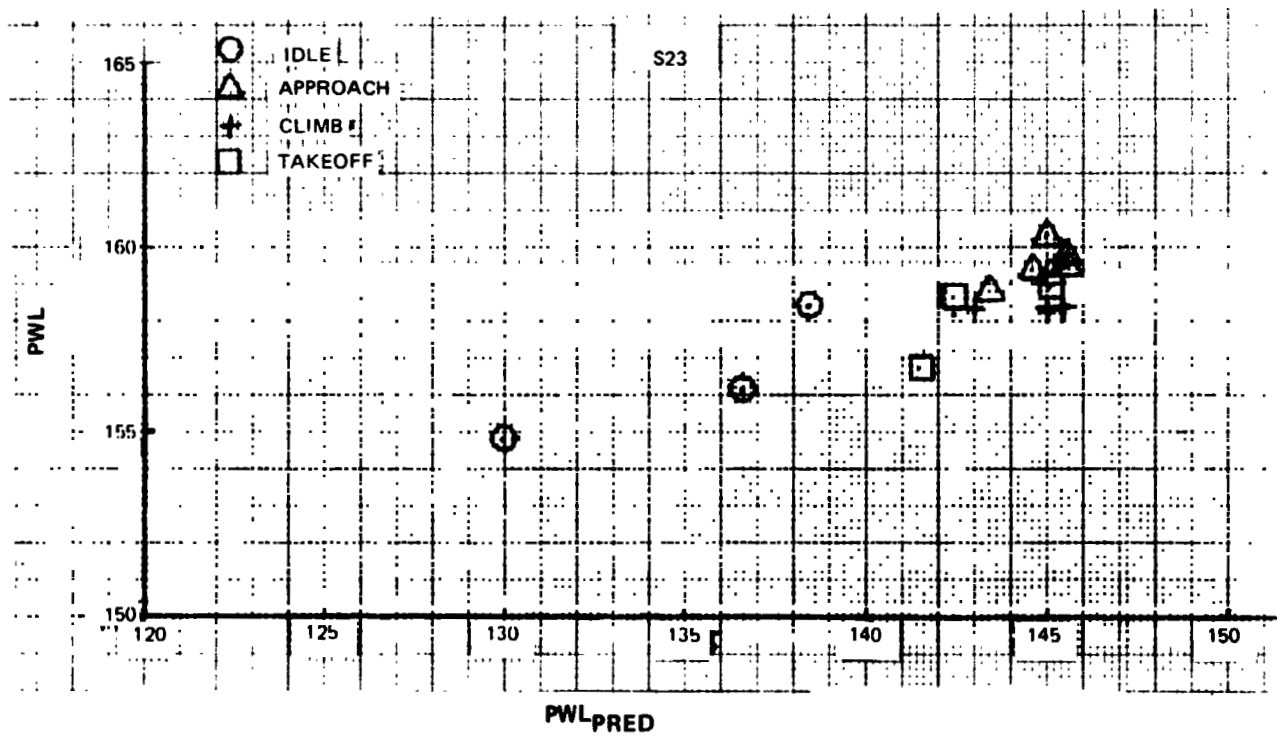

Figure 34 Relation Between PWL and PWL_{pred} (All Points): S-23

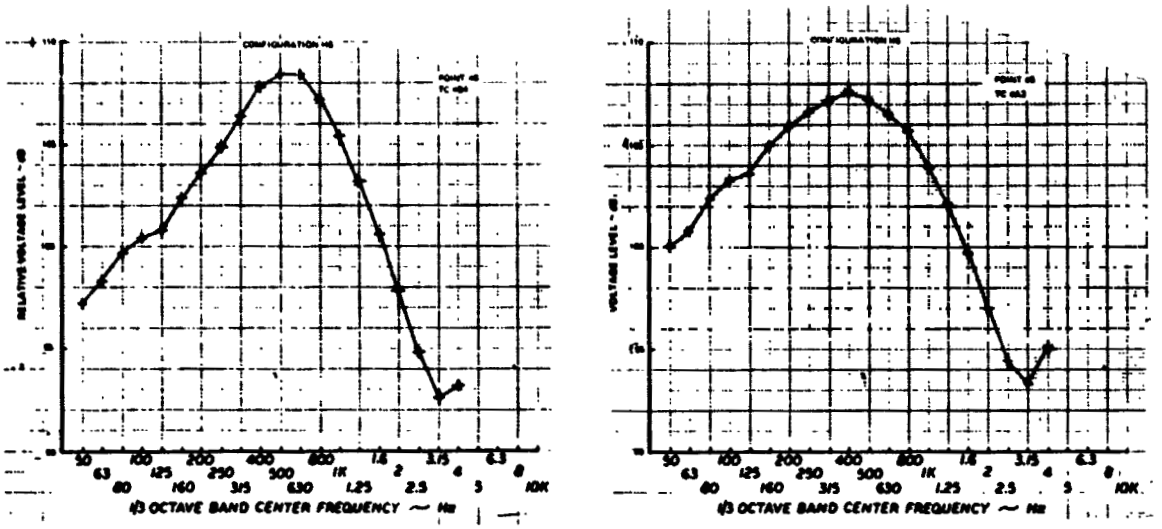

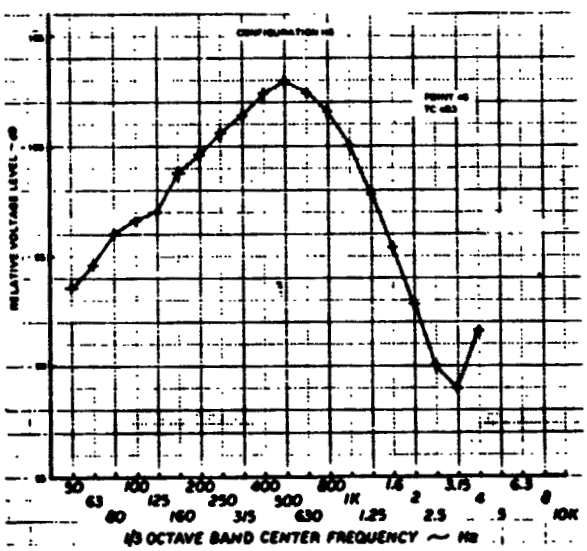

Figure 35 Illustrative Thermocouple Voltage Spectra: H-6

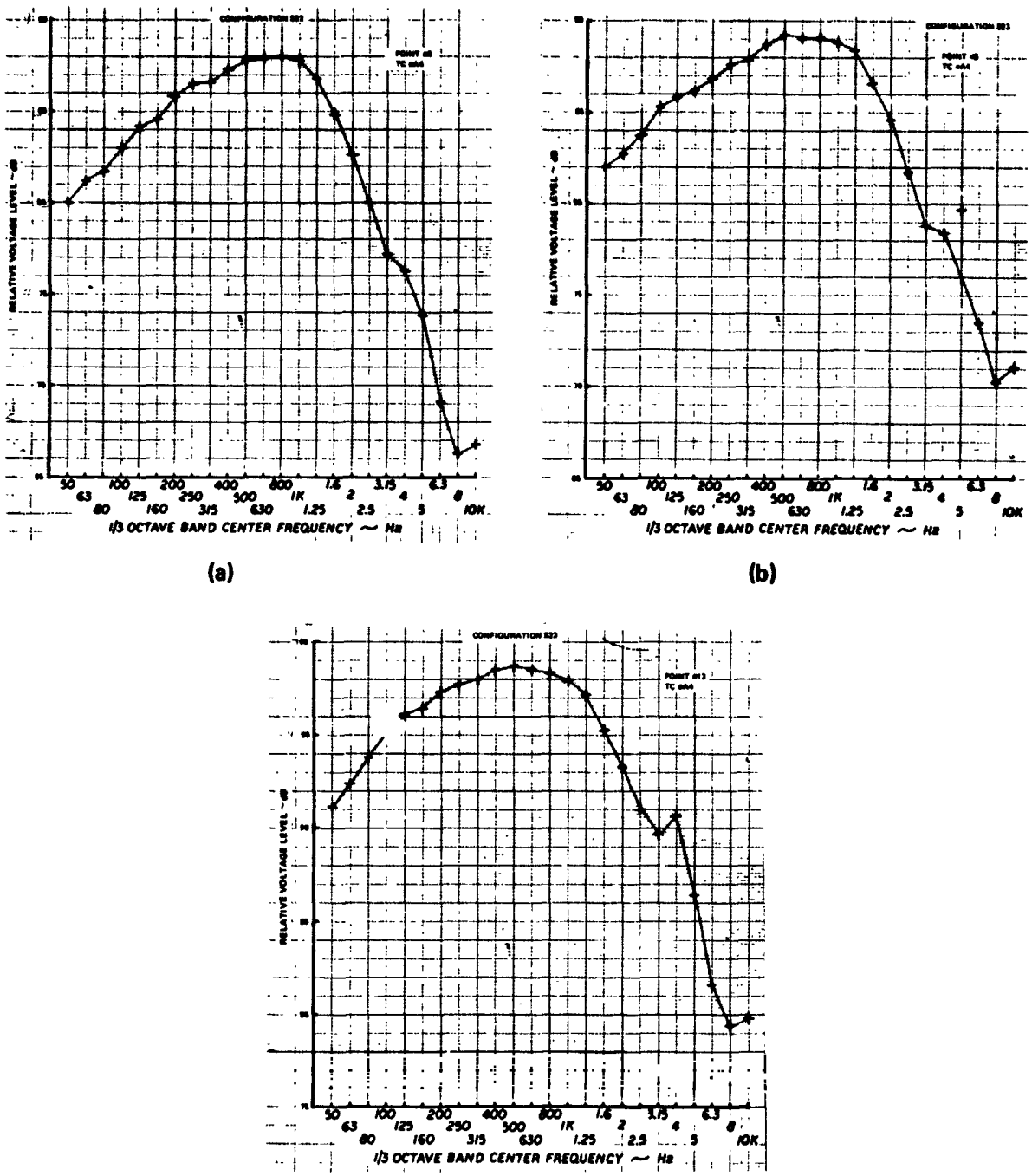

Figure 36 *Illustrative Thermocouple Voltage Spectra: S-23*

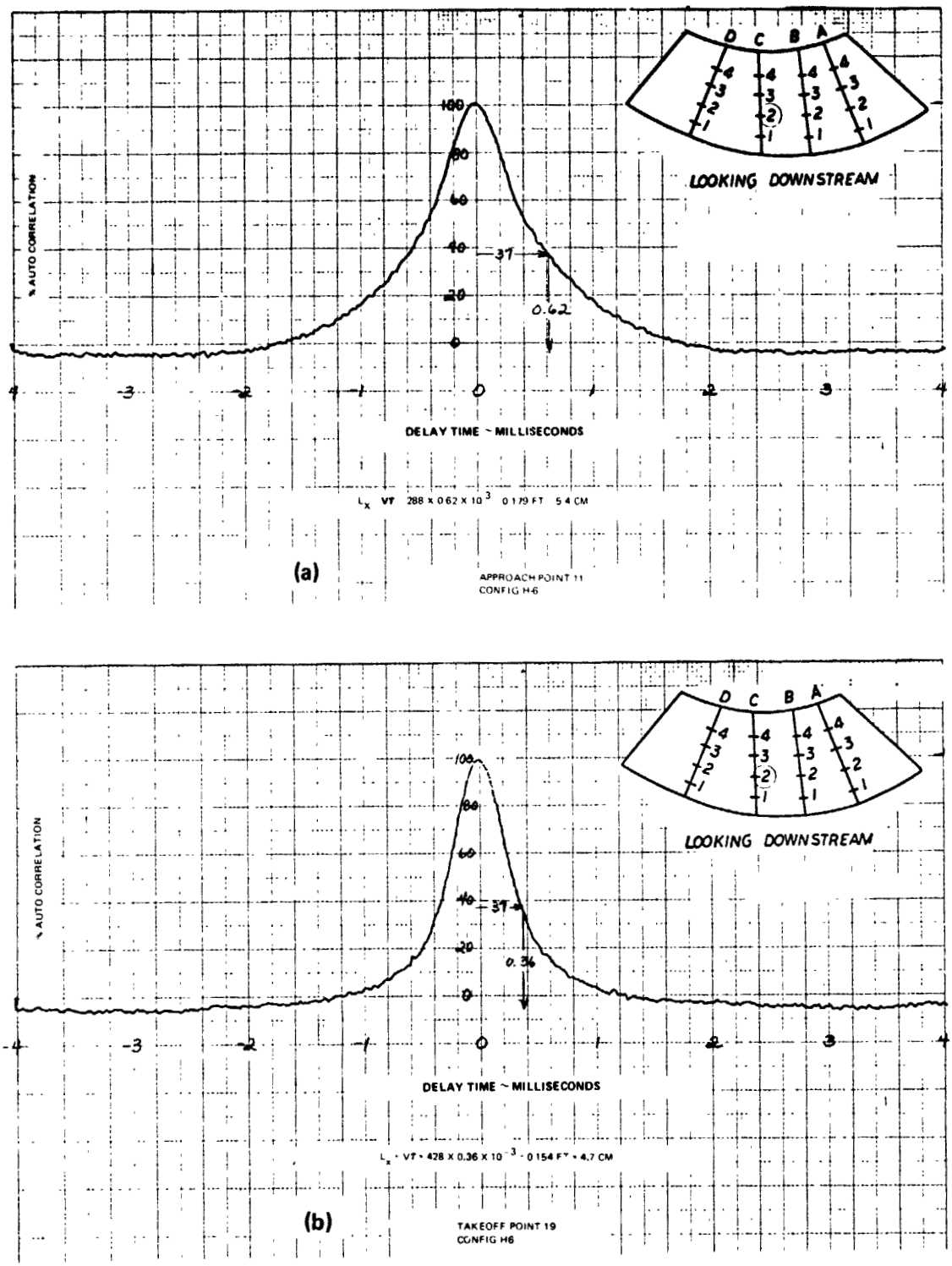

Figure 37 *Temperature Axial Length Scales From Auto Correlograms: H-6*

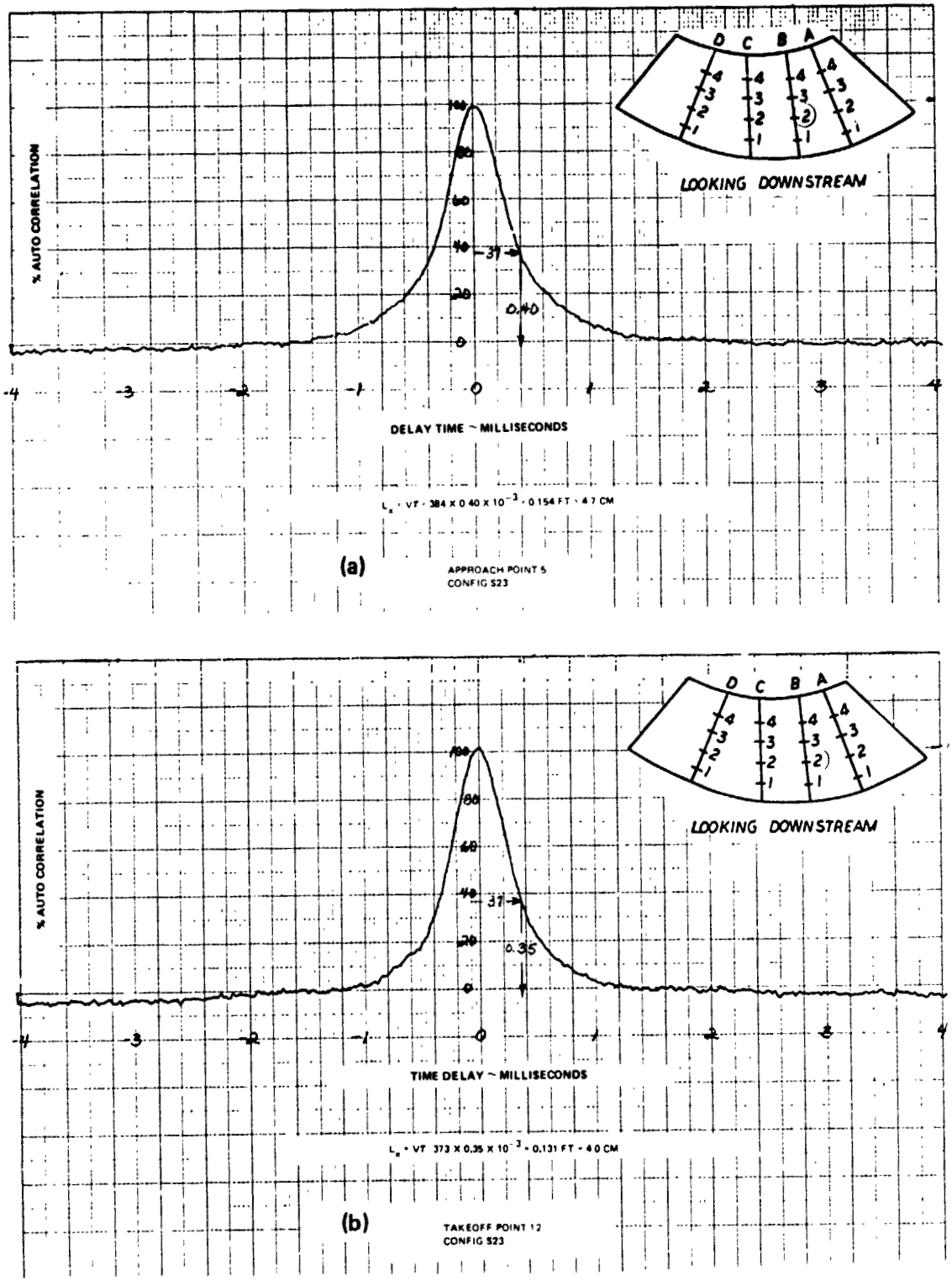

Figure 38 Temperature Axial Length Scales From Auto Correlograms: S-23

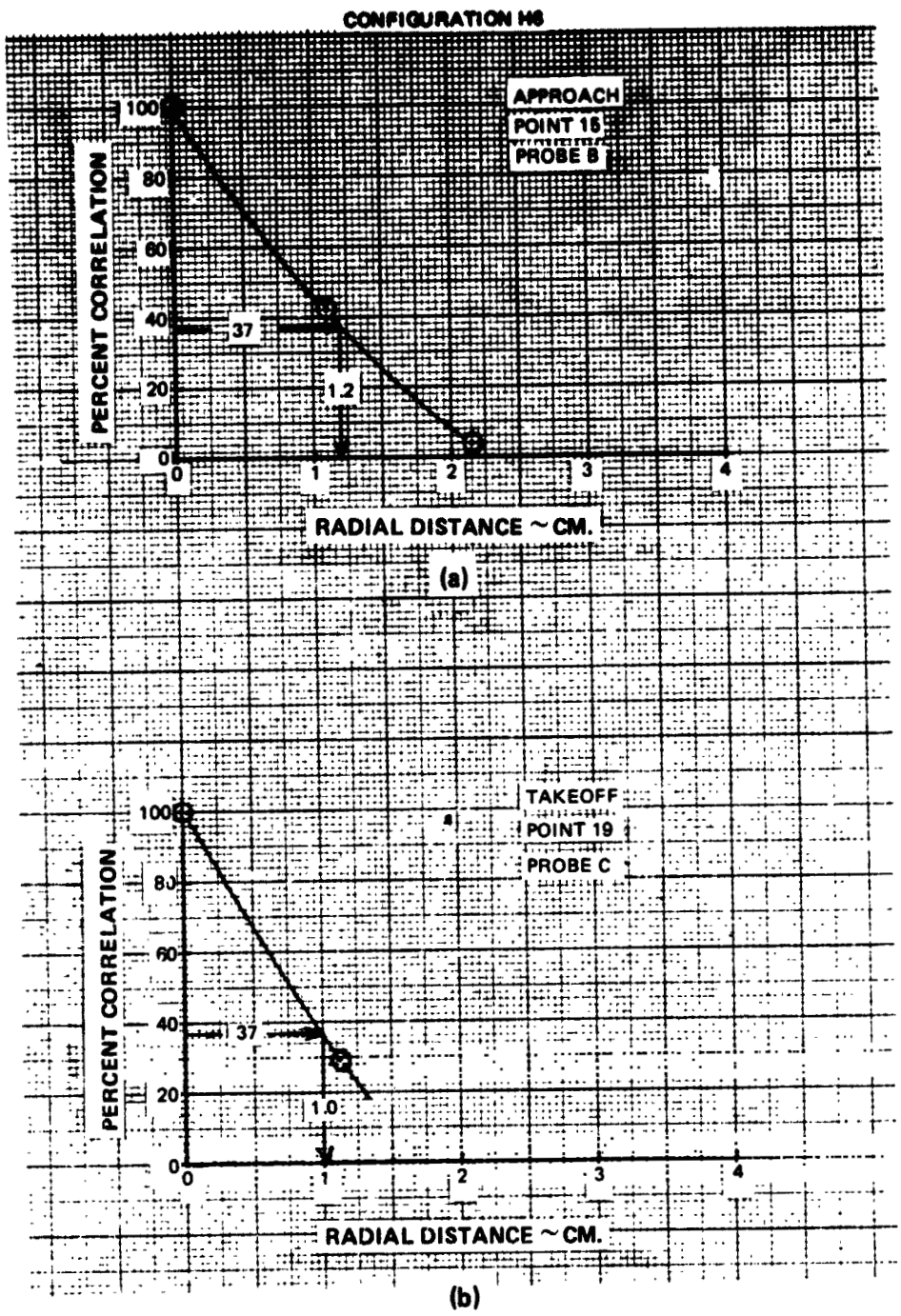

Figure 39 *Temperature Radial Length Scales From Cross Correlograms: H-6*

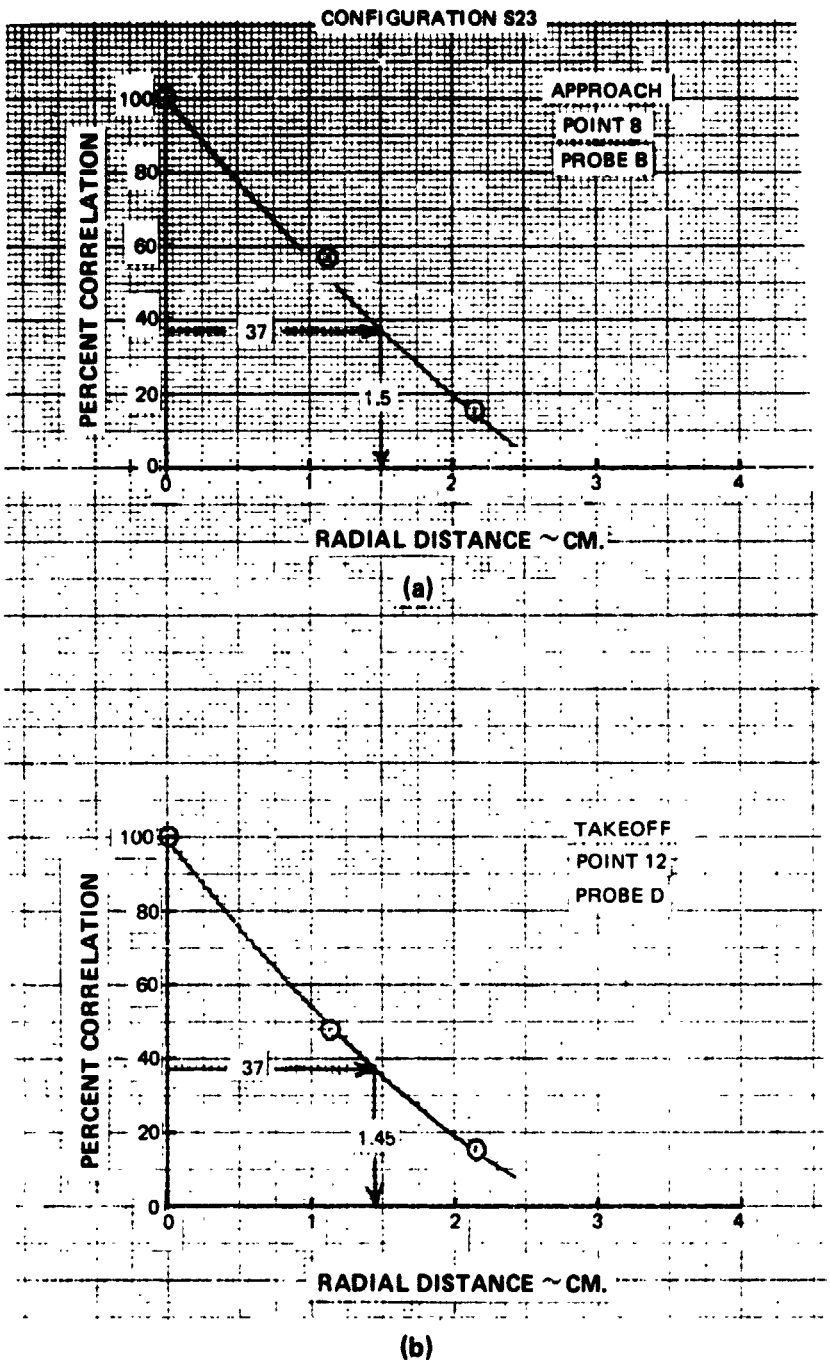

Figure 40 *Temperature Radial Length Scales From Cross Correlograms: S-23*

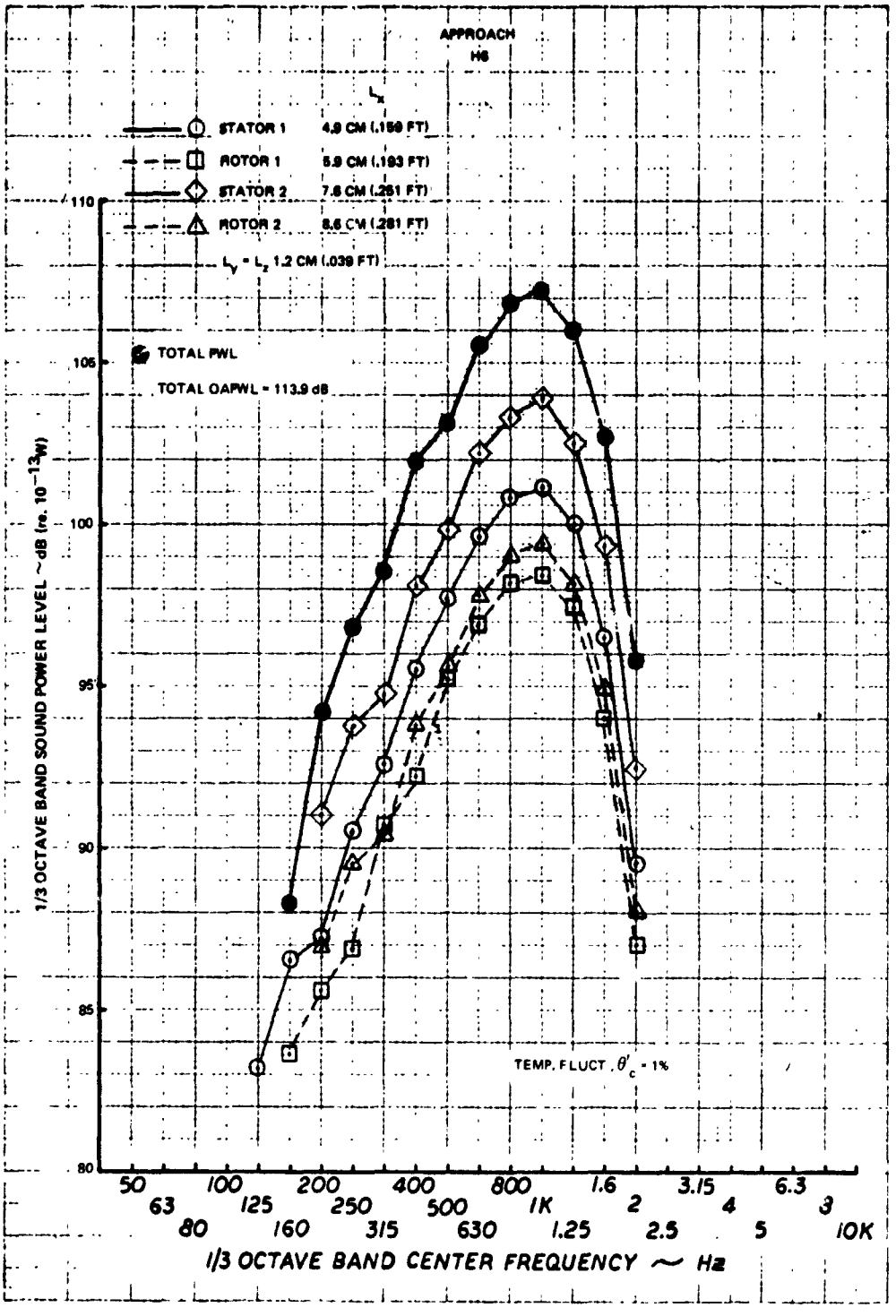

Figure 41a Calculated Indirect Combustion Noise Spectra: H-6

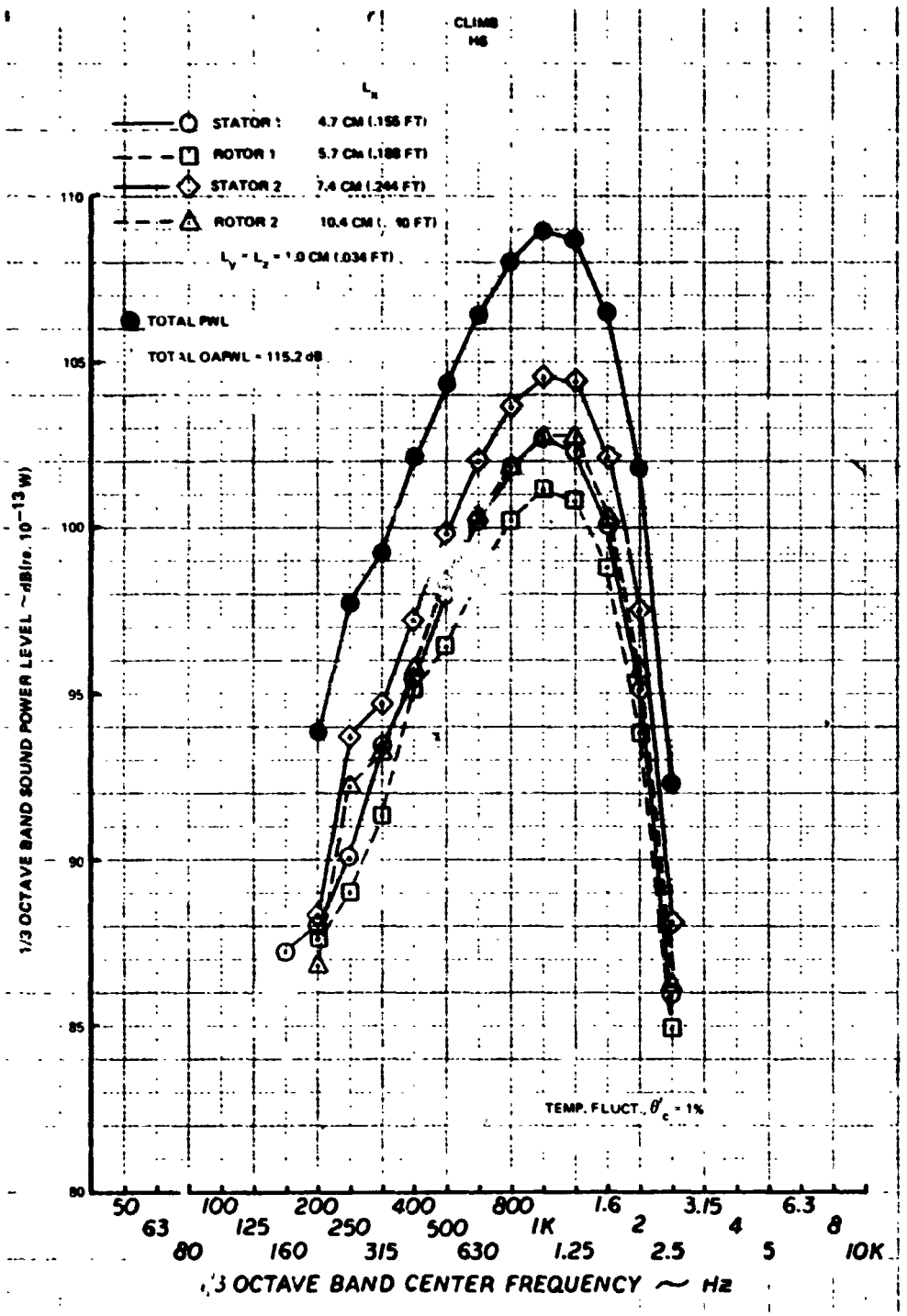

Figure 41b Calculated Indirect Combustion Noise Spectra: H-6

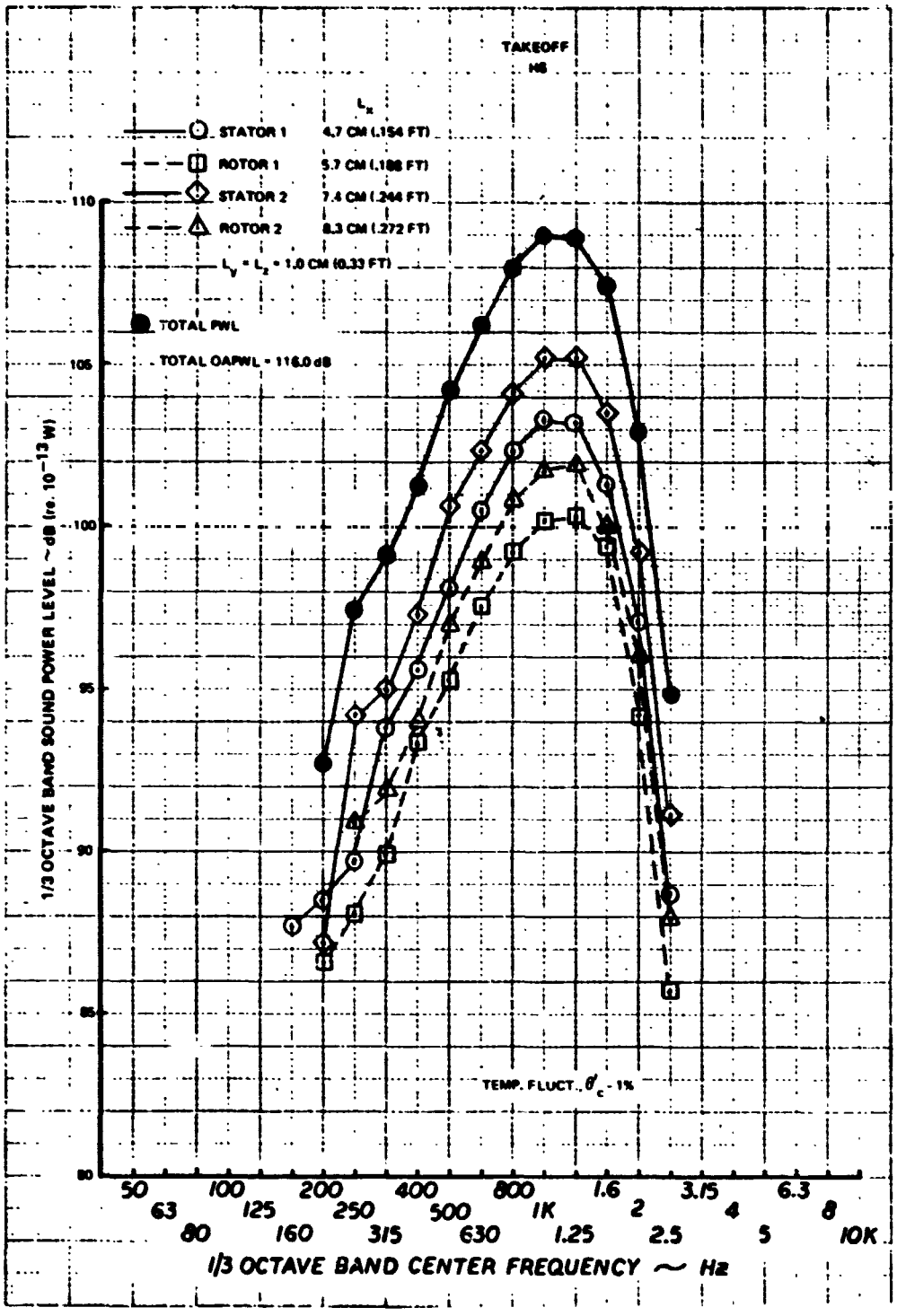

Figure 41c Calculated Indirect Combustion Noise Spectra: H-6

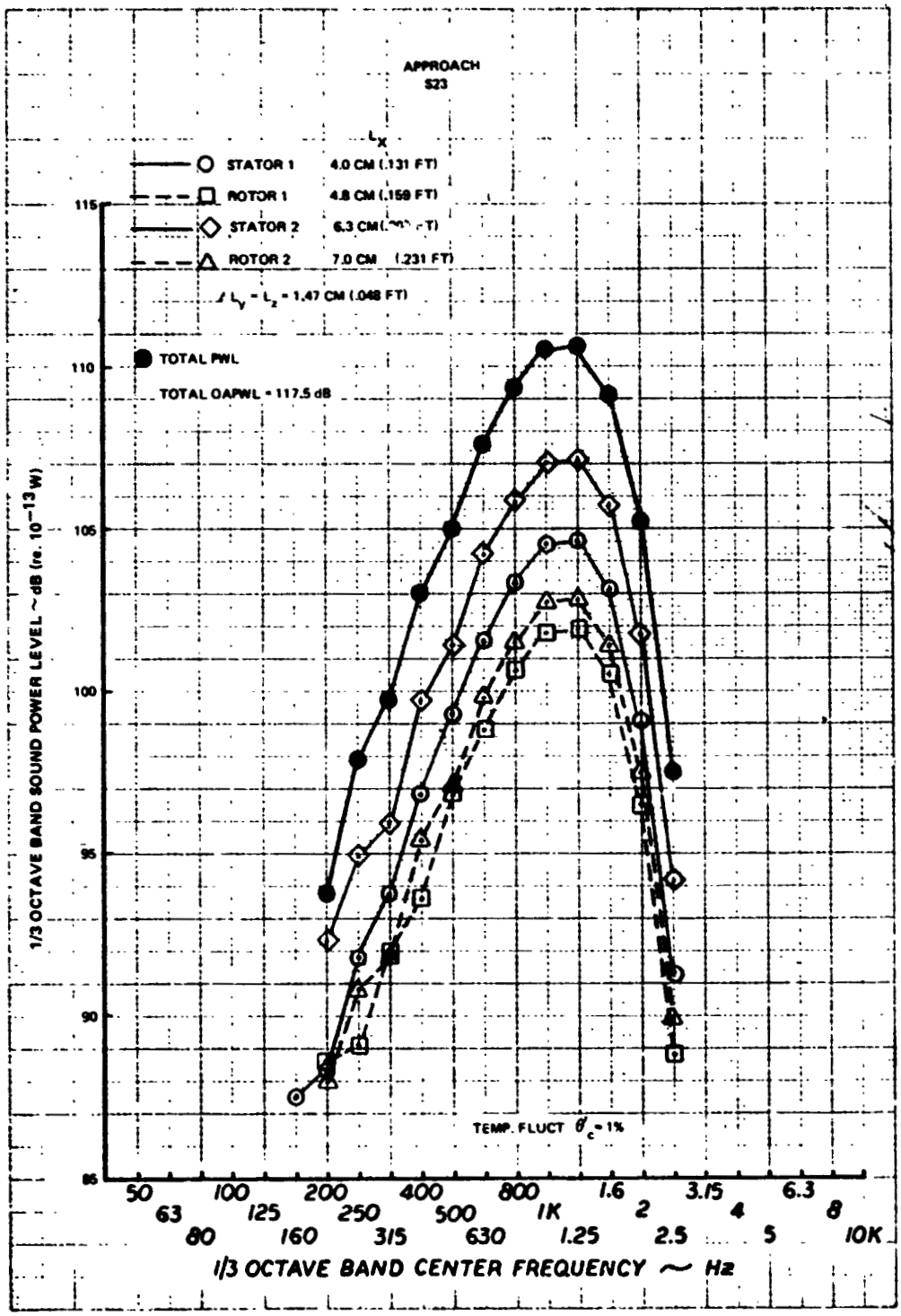

Figure 42a Calculated Indirect Combustion Noise Spectra: S-23

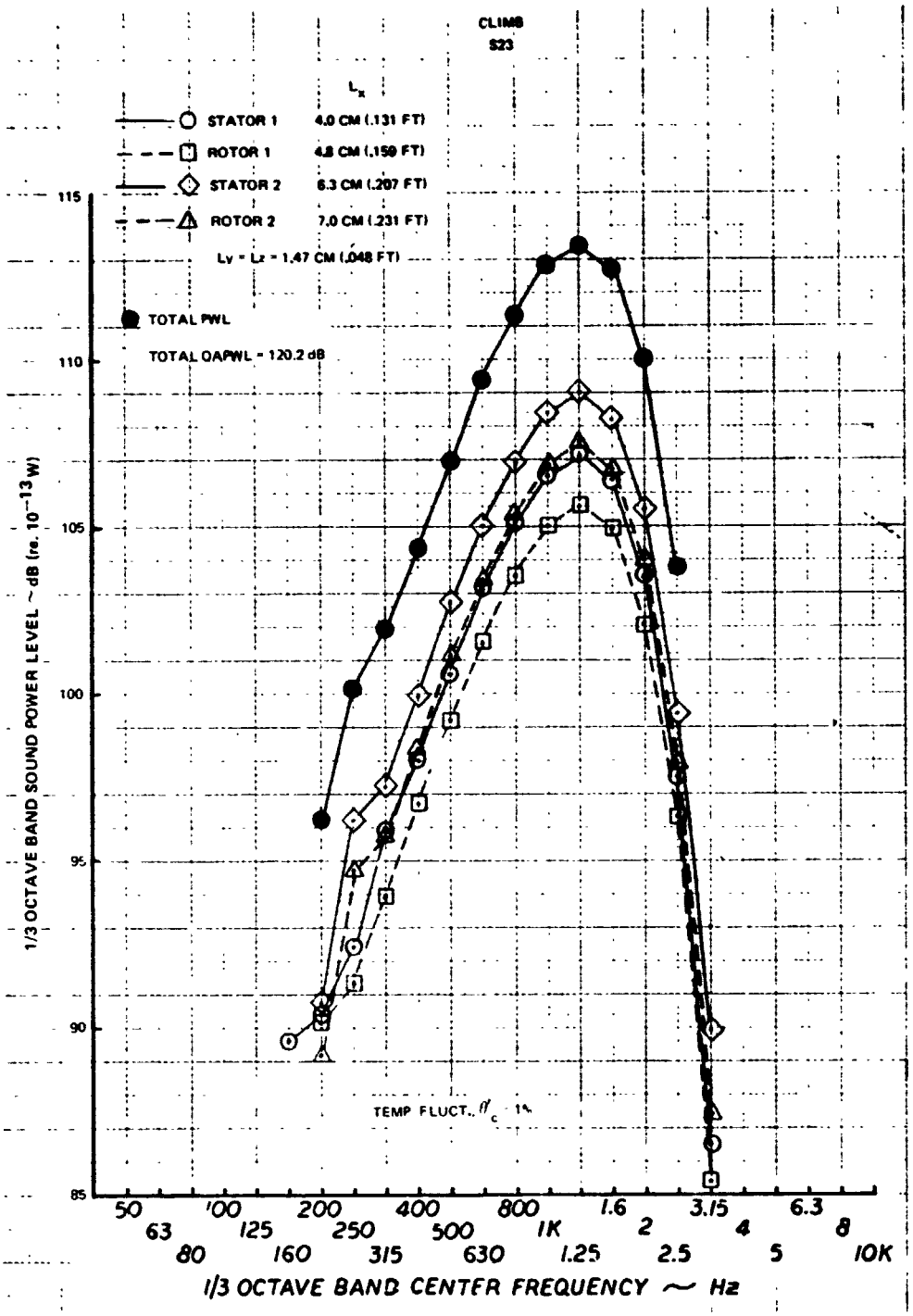

Figure 42b Calculated Indirect Combustion Noise Spectra: S-23

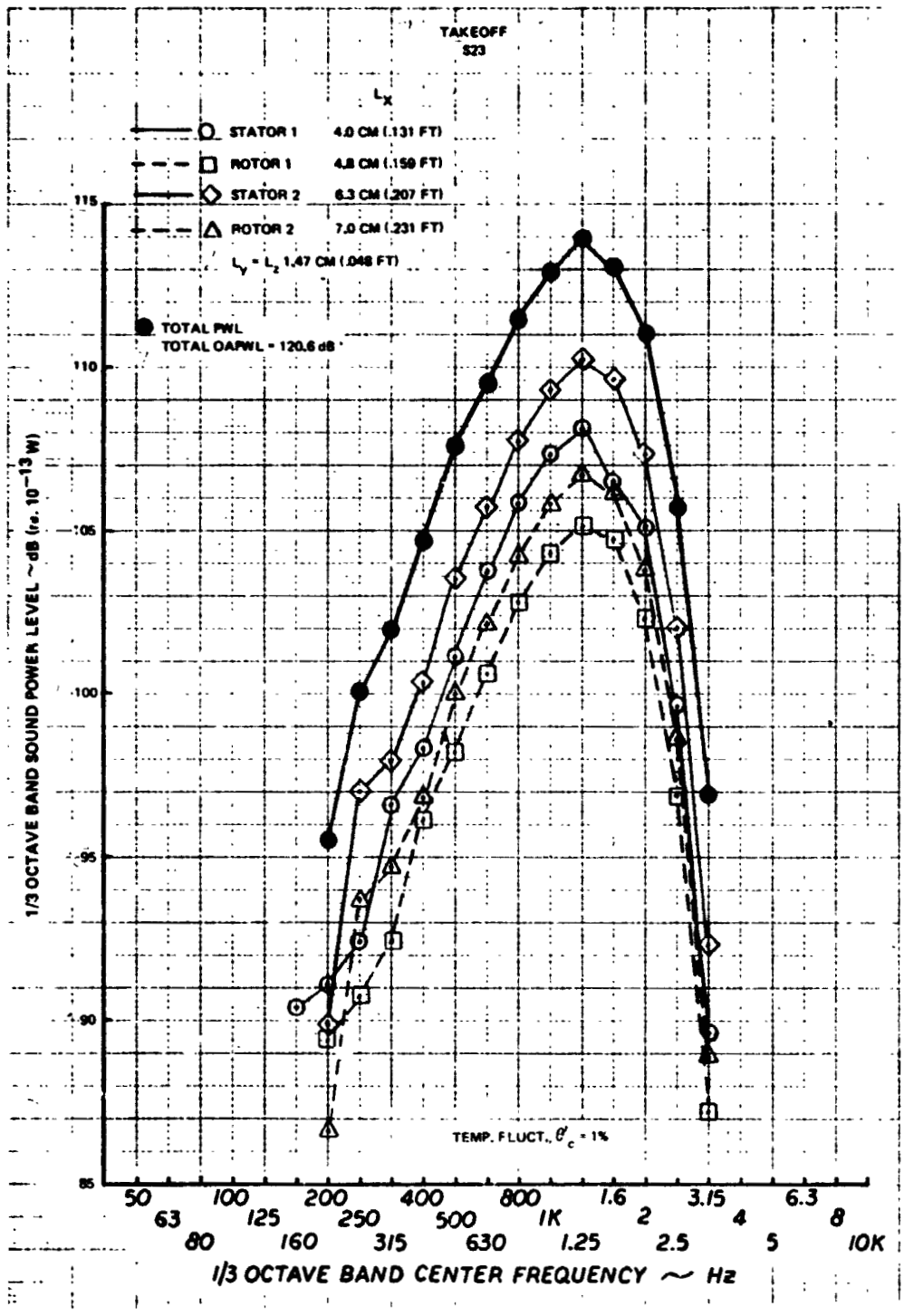

Figure 42c Calculated Indirect Combustion Noise Spectra: S-23

APPENDIX A-1

RIG PERFORMANCE AND POWER LEVEL DATA

This Appendix contains tabulations of rig performance parameters from Phases I and II of the Experimental Clean Combustor Program, and identifies configurations and operating point numbers. Acoustic power levels are also tabulated.

RIG PERFORMANCE DATA - REF 1

List of Symbols

SUBSCRIPTS

4	station upstream of burner.
5	station downstream of burner
t	total condition
s	static condition
i	ideal
b	burner
pri	primary zone
sec	secondary zone

SYMBOLS		UNITS
P	pressure	ATM
T	temperature	°K
Wa	mass flow rate of air	kg/sec
Wf	mass flow rate of fuel	kg/sec
f/a	fuel-air ratio	
$\bar{M}$ ①	mass flow parameter	$\frac{kg\sqrt{K^\circ}}{sec - m^2 - ATM}$

NOTES:

① $\bar{M} = \frac{W_{a4}\sqrt{T_{t4}}}{A_4 P_{t4}}$, where A_4 is defined as 0.02002 m^2 for a 90 sector JT9D burner.

PHASE I

ECCP RIG PERFORMANCE (Sheet 1)

Config.	Point No.	Condition	W_{a4} (kg/sec)	W_{ab}[1] (kg/sec)	W_f pri (kg/sec)	W_f sec (kg/sec)	f/a[2] Carbon Balance	P_{s4} (ATM)	P_{t4} (ATM)	T_{t4} (°K)	P_{t5}[3] (ATM)	T_{t5i}[4] (°K)	$\frac{\sqrt{M}}{\text{kg}\cdot{}^{\circ}\text{K}^{1/2}/\text{sec-m}^2\cdot\text{ATM}}$	$\frac{P_{t4}-P_{t5}}{P_{t4}}$ (%)	$T_{t5i}-T_{t4}$ (°K)
N-7	3	Idle-Cold	10.69	8.42	–	–	–	3.70	3.86	448	–	–	2927	–	–
	43	Idle	8.35	6.13	.0637	–	.0142	3.44	3.79	463	3.21	828	2368	15.4	363
	21	Idle	8.35	6.16	.0494	–	.0109	3.42	3.74	461	3.16	561	2394	15.6	100
	32	Idle	8.45	6.16	.0783	–	.0173	3.45	3.78	463	3.18	1350	2403	15.8	887
N-8	1*	Idle-Cold	7.64	5.93	–	–	–	2.74	3.10	433	2.70	–	2562	12.9	–
	21	Idle	7.64	5.92	.0502	–	.0120	3.51	3.77	455	3.42	738	2159	9.2	283
	32	Idle	7.67	6.03	.0405	–	.0090	3.50	3.77	460	3.42	622	2180	9.4	162
	43	Idle	7.73	5.91	.0671	–	.0143	3.46	3.74	460	3.38	896	2214	9.6	436
	810	TO	8.76	6.93	.0357	.0527	.0145	6.55	6.86	766	6.44	1266	1765	6.1	500
	79	SLTO	8.80	6.93	.0498	.0677	.0191	6.61	6.93	768	6.51	1416	1758	6.1	648
	68	SLTO	8.74	6.89	0601	.0856	.0249	6.55	6.86	767	6.43	1592	1773	6.2	825
	0*	SLTO Cold	8.63	6.90	–	–	–	6.46	6.80	769	6.38	–	1758	6.1	–
N-9	1	Idle Cold	7.79	6.26	–	–	–	3.48	3.74	457	3.28	–	2224	12.2	–
	21	Idle	7.83	6.18	.0502	–	.0109	3.46	3.74	459	3.28	561	2240	12.3	102
	33	Idle	7.90	6.17	.0699	–	.0148	3.44	3.79	457	3.33	828	2226	12.2	374
	42	Idle	7.87	6.21	.0570	–	.0097	3.44	3.71	456	3.24	715	2263	12.6	259
	69	SLTO	8.77	6.99	.0499	.0687	.0220	6.40	6.73	770	6.19	1505	1806	8.0	735
	710	SLTO	8.75	7.04	.0358	.0490	.0161	6.42	6.74	770	6.21	1311	1799	7.9	541
	58	SLTO	8.75	6.97	.0575	.0825	.0257	6.46	6.80	770	6.27	1614	1784	7.8	844
	88	AST	8.69	7.04	.0579	.0823	.0265	6.43	6.78	843	6.20	1699	1859	8.5	856
	99*	SLTO-Cold	8.63	6.90	–	–	–	6.46	6.80	771	6.28	–	1760	7.6	

*Estimated Condition

NOTES:

1. Wab = Wa4 – measured turbine cooling air bleed – estimated rig sidewall cooling airflow
2. fuel-air ratio computed from a carbon balance on the measured exhaust gas species concentration
3. computed values
4. computed from carbon balance fuel-air ratio, corrected for unreacted species (CO, THC) present in exhaust gas.

PHASE I

ECCP RIG PERFORMANCE (Sheet 2)

Config.	Point No.	Condition	W_{a4} (kg/sec)	W_{ab} [1] (kg/sec)	W_f pri (kg/sec)	W_f sec (kg/sec)	f/a [2] Carbon Balance	P_{s4} (ATM)	P_{t4} (ATM)	T_{t4} (°K)	P_{t5} [3] (ATM)	T_{t5i} [4] (°K)	$\frac{\overline{M}}{kg \cdot {}^\circ K^{1/2}}{Sec\text{-}m^2\text{-}ATM}$	$\frac{P_{t4}-P_{t5}}{P_{t4}}$ (%)	$T_{t5i}-T_{t4}$ (°K)
N-10	1*	Idle-Cold	7.80	5.98	–	–	–	3.44	3.80	457	3.25	–	2192	14.4	–
	21	Idle	7.80	5.98	.0502	–	0074	3.50	3.78	459	3.23	675	2208	14.6	216
	33	Idle	7.86	5 99	.0672	–	.0103	3.48	3.76	454	3.20	800	2225	14.9	346
	42	Idle	7.74	5.90	.0569	–	.0090	3.44	3.72	458	3 17	737	2224	14.8	279
	69	SLTO	8.66	6.88	.0499	.0709	.0186	6.51	6.82	775	6.18	1410	1766	9.4	635
	710	SLTO	8.70	6 92	.0356	.0507	0125	6.48	6 80	772	6.16	1204	1776	9.4	432
	58	SLTO	8.73	6.94	.0605	.0787	.0216	6.48	6.80	773	6.15	1499	1783	9.6	726
	88	AST	8 68	6 90	.0606	.0831	.0220	6 53	6.75	847	6.04	1573	1863	10.5	726
	89*	SLTO-Cold	8.63	6.90	–	–	–	6.46	6.80	771	6.17	-	1760	9.3	–
N-11	1*	Idle-Cold	8.01	6 08	–	–	–	3 74	3.74	456	3.13	–	2285	16.3	–
	21	Idle	8 01	6 08	–	.0504	.0074	3 46	3.13	458	3.00	675	2359	17.4	217
	42	Idle	8.03	6.07	–	.0572	.0092	3 43	3.73	458	3.11	783	2301	16.6	325
	33	Idle	8.05	6 07	–	.0675	.0108	3 44	3.75	454	3.14	841	2285	16.4	387
	69	SLTO	7.93	6.28	.0451	0639	.0195	5.80	6.11	766	5.49	1416	1794	10.1	650
	710	SLTO	7.88	6.29	.0321	.0443	.0134	5.85	6.14	765	5.53	1234	1773	9.9	469
	58	SLTO	7.95	6.32	.0543	.0750	.0232	5 87	6 16	769	5.54	1543	1788	10.0	774
	88	SLTO	6 22	4 91	.0424	.0584	.0228	4.54	4.77	767	4.28	1529	1804	10.2	762
	60*	SLTO-Cold	7.95	6.36	–	–	–	5.87	6.19	769	5.58	–	1779	9.9	–

*Estimated Conditions

NOTES:

1. Wab = Wa4 – measured turbine cooling air bleed – estimated rig sidewall cooling airflow.
2. fuel-air ratio computed from a carbon balance on the measured exhaust gas species concentration.
3. computed values.
4. computed from carbon balance fuel-air ratio, corrected for unreacted species (CO, THC) present in exhaust gas.

PHASE I

ECCP RIG PERFORMANCE (Sheet 3)

Config.	Point No.	Condition	W_{a4} (kg/sec)	W_{ab}[1] (kg/sec)	W_{f}pri (kg/sec)	W_{f} sec (kg/sec)	f/a[2] Carbon Balance	P_{s4} (ATM)	P_{t4} (ATM)	T_{t4} (°K)	P_{t5}[3] (ATM)	T_{t5i}[4] (°K)	$\frac{\overline{M}}{kg \cdot {}^{\circ}K^{1/2}}$ / Sec-m^2-ATM	$\frac{P_{t4}-P_{t5}}{P_{t4}}$ (%)	$T_{t5i}-T_{t4}$ (°K)
N-12	1*	Idle-Cold	7.99	6.26	–	–	–	3.57	3.74	478	3.08	–	2333	13.6	–
	21	Idle	7.99	6.26	.0505	–	.0087	3.50	3.78	454	3.30	724	2250	12.7	270
	42	Idle	7.99	6.17	.0571	–	.0090	3.48	3.81	459	3.35	734	2244	12.1	275
	33	Idle	8.09	6.22	.0670	–	.0103	3.44	3.74	454	3.25	752	2302	13.2	298
	69	SLTO	8.73	6.85	.0500	.0727	.0192	6.48	6.83	766	5.97	1428	1767	7.8	662
	710	SLTO	8.70	6.98	.0358	.0494	.0132	6.42	6.76	765	5.91	1235	1778	7.9	470
	58	SLTO	8.75	6.96	.0598	.0826	.0224	6.51	6.84	769	6.00	1520	1772	7.8	751
	88	SLTO	8.76	6.92	.0508	.0184	.0220	6.37	6.73	768	5.85	1560	1802	8.1	792
	60*	SLTO-Cold	8.63	6.90	–	–	–	6.46	6.80	769	6.96	–	1758	7.7	–
P-7	2*	Idle-Cold	7.38	5.47	–	–	–	3.51	3.75	454	3.42	–	2095	8.9	–
	43	Idle	7.61	5.29	.0772	–	.0128	3.46	3.71	462	3.35	943	2202	9.8	485
	32	Idle	8.06	5.64	.0833	–	.0131	3.41	3.76	457	3.36	952	2289	10.7	495
	58	SLTO	8.74	6.60	.0634	.0967	.0312	6.53	6.84	766	6.40	1760	1766	6.4	994
	69	SLTO	8.78	6.48	.0547	.0818	.0257	6.68	6.99	767	6.55	1412	1738	6.3	645
	88	SLTO	8.75	6.62	.0468	.1091	.0300	6.59	6.84	767	6.40	1630	1770	6.4	863
	99*	SLTO-Cold	8.63	6.90	–	–	–	6.43	6.80	768	6.02	–	1757	6.3	–
P-8	0*	Idle-Cold	6.38	4.36	–	–	–	3.46	3.74	768	3.07	–	2361	11.3	–
	11	Idle	6.38	4.36	.0609	–	.0120	3.49	3.69	459	3.44	917	1850	6.9	458
	28	SLTO	7.87	6.59	.0615	.0963	.0312	6.51	6.83	773	6.47	1763	1600	5.2	990
	39	SLTO	8.74	6.65	.0675	.1076	.0348	6.49	6.81	775	6.37	1869	1784	6.4	1094
	410	SLTO	8.24	6.54	.0553	.0848	.0268	6.45	6.81	773	6.42	1382	1680	5.8	608
	88	AST	8.71	6.59	.0616	.0961	.0320	6.48	6.83	843	6.35	–	1849	7.0	–
	102	SLTO-Cold	8.67	6.94	–	–	–	6.38	6.78	770	5.97	–	1772	6.4	–

*Estimated conditions.

Notes:

1. Wab - Wa4 – measured turbine cooling air bleed – estimated rig sidewall airflow.
2. fuel-air ratio computed from a carbon balance on the measured exhaust gas species concentration.
3. computed values.
4. computed from carbon balance fuel-air ratio, corrected for unreacted species (CO, THC) present in exhaust gas.

PHASE I

ECCP RIG PERFORMANCE (Sheet 4)

Config.	Point No.	Condition	W_{a4} (kg/sec)	W_{ab}[1] (kg/sec)	W_f pri (kg/sec)	W_f sec (kg/sec)	f/a[2] Carbon Balance	P_{s4} (ATM)	P_{t4} (ATM)	T_{t4} (°K)	P_{t5}[3] (ATM)	T_{t5i}[4] (°K)	$\frac{\overline{M}}{kg\cdot °K^{1/2}/Sec\cdot m^2\cdot ATM}$	$\frac{P_{t4}-P_{t5}}{P_{t4}}$ (%)	$T_{t5i}-T_{t4}$ (°K)
S-8	1	Idle-Cold	6.81	5.45	–	–	–	3.11	3.53	313	3.28	–	932	7.0	–
	21	Idle	6.99	5.29	.0527	–	.0120	3.52	3.73	450	3.46	907	1986	7.3	457
	32	Idle	7.14	5.49	.0422	–	.0094	3.57	3.88	4.72	3.59	831	1997	7.4	359
	43	Idle	7.20	5.42	.0607	–	.0127	3.57	3.80	456	3.51	897	2021	7.6	441
	58	SLTO	8.79	6.86	.0489	.0888	.0261	6.53	6.82	750	6.42	1621	1763	5.8	871
	69	SLTO	8.81	6.91	.0442	.0788	.0232	6.52	6.83	752	6.43	1529	1767	5.9	777
	810	SLTO	8.65	6.73	.0123	.1141	.0229	6.53	6.84	748	6.46	1481	1728	5.6	733
	128	AST	8.92	6.84	.0250	.1055	.0216	6.46	6.81	826	6.36	1544	1880	6.6	718
	2222	SLTO-Cold	8.75	7.00	-	–	–	6.54	6.93	773	6.53	–	1754	5.7	–
S-9	1*	Idle-Cold	7.62	5.80	–	–	–	3.53	3.77	–	3.54	–	–	–	–
	21	Idle	7.62	5.80	.0525	–	.0110	3.44	3.70	458	3.37	875	2202	9.0	417
	32	Idle	7.79	5.97	.0389	–	.0085	3.42	3.71	459	3.36	778	2247	9.4	319
	43	Idle	7.73	5.98	.0661	–	.0148	3.47	3.75	456	3.41	1005	2199	9.0	549
	69	SLTO	8.65	6.96	.0445	.0810	.0222	6.53	6.84	772	6.45	1501	1755	5.7	729
	1145	SLTO	8.70	6.84	.0567	.0682	.0221	6.51	6.82	772	6.43	1514	1770	5.7	742
	1050	SLTO	8.69	6.75	.0375	.0873	.0219	6.51	6.82	771	6.42	1507	1767	5.8	736
	710	SLTO	8.67	6.89	.0318	.0578	.0152	6.53	6.85	771	6.45	1299	1755	5.8	528
	58	SLTO	8.70	6.82	.0381	.0695	.0185	6.49	6.80	772	6.41	1403	1776	5.8	631
	128	AST	8.85	7.11	.0249	.1013	.0216	6.55	6.91	845	6.47	1559	1860	6.4	714
	712	SLTO-Cold	8.71	6.97	–	–	–	6.41	6.79	772	6.39	–	1780	5.9	1008

*Estimated Conditions

NOTES.

1. Wab = Wa4 – measured turbine cooling air bleed – estimated rig sidewall cooling airflow.
2. fuel-air ratio computed from a carbon balance on the measured exhaust gas species concentration
3. computed values
4. computed from carbon balance fuel-air ratio, corrected for unreacted species (CO, THC) present in exhaust gas.

TEST RESULTS FOR HYBRID COMBUSTOR CONFIGURATION H5 FROM REF 4

Point Number	Airflow - Total kg/s	Airflow - Combustor kg/s	Fuel Flow - Pilot kg/s	Fuel Flow - Main kg/s	Fuel Flow - Total kg/s	Fuel Temperature K	Inlet Total Temperature K	Inlet Total Pressure - atm	Fuel-Air Ratio Metered (M)	Fuel-Air Ratio Carbon Balance (CB)	$\frac{\text{Fuel-Air (CB)}}{\text{Fuel-Air (M)}}$	Ideal Combustor Exit Temperature K	Maximum Combustor Exit Temperature K	Pattern Factor	Reference Velocity - m/s	CO_2 - % Volume	O_2 - % Volume	CO (EI)	THC (EI)	NO_X(EI)	Gas Sample Combustion Efficency	Humidity (g H_2O/kg air)	SAE Smoke Number	Comments
1	4.84	3.85	0.0477	0.0	0.0472	362.	429.	2.93	0.0122	0.0	0.0	902.	1621.	1.93	17.9	0.0	0.0	0.0	0.0	0.0	0.0	1.0		IDLE
4	4.97	3.95	0.0495	0.0	0.0465	361.	427.	2.93	0.0119	0.0000	0.0	901.	0.	0.0	18.3	1.84	18.0	7.9	4.4	4.1	99.3	1.0		IDLE
6	4.94	3.93	0.0612	0.0	0.0612	361.	427.	2.90	0.0156	0.0117	0.75	1015.	0.	0.0	18.3	2.31	17.1	56.6	4.4	4.9	98.2	1.0		IDLE
7	5.04	4.02	0.0307	0.0	0.0307	361.	427.	2.91	0.0076	0.0029	0.38	732.	0.	0.0	18.8	0.56	20.2	98.5	0.0	1.0	99.4	1.0		IDLE
15	9.99	7.96	0.0	0.0803	0.0803	360.	492.	6.80	0.0102	0.0120	1.18	980.	0.	0.0	21.9	2.34	17.4	58.5	30.5	6.6	95.1	1.3	4 SEC	APPR
14	9.99	7.95	0.0	0.0801	0.0801	360.	492.	6.81	0.0071	0.0085	1.20	863.	0.	0.0	22.0	1.55	18.5	87.0	89.0	4.6	87.7	1.2	4 SEC	APPR
131	9.93	7.90	0.0	0.0411	0.0411	360.	490.	6.89	0.0042	0.0060	1.15	794.	0.	0.0	21.5	0.99	19.3	138.9	165.0	3.2	77.7	1.5	4 SEC	APPR
9	6.50	5.17	0.0532	0.0	0.0532	360.	450.	3.74	0.0103	0.0099	0.78	860.	0.	0.0	20.2	1.61	18.1	3.9	2.9	3.1	94.6	1.5	UNLED	IDLE
17	9.93	7.90	0.0545	0.0551	0.1096	360.	493.	6.76	0.0219	0.0232	0.87	1101.	0.	0.0	21.9	2.23	17.2	90.0	83.2	3.9	88.1	1.7	PRI/SEC	APPR
16	10.13	8.05	0.0	0.0586	0.0586	360.	490.	6.79	0.0073	0.0078	1.07	869.	0.	0.0	22.3	0.64	20.0	82.9	64.3	1.1	17.8	1.5	11 SEC	APPR
161	10.14	8.07	0.0	0.0751	0.0751	362.	492.	6.93	0.0093	0.0100	1.09	963.	0.	0.0	21.9	1.07	19.3	90.3	59.2	1.6	35.6	1.4	11 SEC	APPR
18	10.08	8.02	0.0377	0.0	0.0377	361.	490.	6.73	0.0047	0.0118	1.51	775.	0.	0.0	22.4	1.22	18.9	22.5	17.8	1.2	17.3	1.3	PRI/SEC	APPR
181	10.09	8.01	0.0385	0.0705	0.1090	361.	492.	6.71	0.0136	0.0125	0.92	1091.	0.	0.0	22.5	0.98	19.5	81.6	97.0	1.0	17.5	1.5	PRI/SEC	APPR
19	8.71	6.93	0.0526	0.1019	0.1545	360.	767.	6.92	0.0223	0.0215	0.96	1514.	0.	0.0	24.4	4.33	13.9	17.9	2.1	11.2	98.4	1.3		SLTD
20	8.60	6.85	0.0303	0.1250	0.1553	360.	764.	6.85	0.0228	0.0220	0.96	1530.	0.	0.0	24.3	4.45	13.5	47.8	31.3	12.8	97.6	1.3	SN=2	SLTD
21	8.63	6.87	0.0316	0.1321	0.1637	360.	772.	6.85	0.0233	0.0230	1.00	1570.	0.	0.0	24.7	4.35	13.7	67.5	41.5	13.3	93.7	1.1	SN4	SLTD
22	8.64	6.89	0.0154	0.1519	0.1673	360.	763.	6.80	0.0226	0.0234	1.04	1523.	0.	0.0	24.3	4.51	13.3	49.9	26.4	14.6	95.8	1.1		SLTD
23	8.61	6.87	0.0517	0.1352	0.1869	360.	767.	6.91	0.0199	0.0189	0.95	1445.	0.	0.0	24.2	3.77	14.6	26.8	5.7	10.4	99.7	1.1		SLTD
221	8.56	6.81	0.0634	0.1510	0.2144	360.	775.	6.95	0.0275	0.0217	0.96	1520.	0.	0.0	24.1	4.34	13.7	19.6	2.1	13.2	99.3	1.3	SN=3	SLTC
24	8.63	6.86	0.0532	0.1072	0.1604	361.	773.	6.80	0.0159	0.0	0.0	1377.	1447.	0.40	24.8	0.0	0.0	0.0	0.0	0.0	0.0	1.3	T/C TRAV	SLTC
25	8.60	6.84	0.0524	0.0965	0.1489	360.	770.	6.79	0.0159	0.0150	0.94	1353.	0.	0.0	24.7	2.92	16.0	73.8	9.6	7.5	97.2	1.5	SN=5	SLTC
26	9.01	7.17	0.0543	0.1041	0.1584	361.	765.	6.80	0.0203	0.0197	0.97	1438.	0.	0.0	25.1	3.93	14.6	30.4	3.7	8.7	98.9	1.7		CLIMB
28	9.05	7.20	0.0543	0.1041	0.1584	360.	738.	6.76	0.0220	0.0211	0.96	1413.	0.	0.0	25.0	4.21	14.0	25.0	3.0	9.6	99.1	1.6		CLIMB
30	8.91	7.08	0.0544	0.0956	0.1500	360.	714.	6.84	0.0212	0.0197	0.93	1438.	0.	0.0	23.5	3.92	14.6	32.6	5.8	7.8	98.6	1.6		CRUISE
31	9.03	7.19	0.0594	0.0794	0.1388	361.	708.	6.82	0.0158	0.0146	0.92	1364.	0.	0.0	23.7	2.70	16.5	61.9	80.6	5.3	88.8	1.7		CRUISE
32	9.04	7.14	0.0544	0.1068	0.1613	360.	702.	6.78	0.0224	0.0214	0.96	1466.	0.	0.0	23.7	4.37	14.1	22.3	5.0	8.3	98.9	1.7		CRUISE
12	10.04	7.99	0.0807	0.0	0.0807	299.	589.	6.76	0.0101	0.0070	0.69	960.	0.	0.0	22.2	1.43	18.8	1.5	0.6	6.4	99.9	1.0	PRIM ONLY	APPR
11	10.12	8.05	0.0501	0.0	0.0501	299.	594.	6.80	0.0070	0.0048	0.69	862.	0.	0.0	22.4	0.97	19.4	15.8	1.3	2.9	99.5	1.0	PRIM ONLY	APPR
8	4.81	3.87	0.0390	0.0	0.0390	360.	430.	2.94	0.0102	0.0074	0.73	829.	0.	0.0	17.7	1.50	18.7	11.3	11.7	2.7	98.4	0.9		IDLE

TEST RESULTS FOR VORBIX COMBUSTOR CONFIGURATION #23 FROM REF 4

Point Number	Airflow - Total kg/s	Airflow - Combustor kg/s	Fuel Flow - Pilot kg/s	Fuel Flow - Main kg/s	Fuel Flow - Total kg/s	Fuel Temperature K	Inlet Total Temperature	Inlet Total Pressure – atm	Fuel-Air Ratio Metered (M)	Fuel-Air Ratio Carbon Balance (CB)	Fuel Air (CB) / Fuel-Air (M)	Ideal Combustor Exit Temperature K	Maximum Combustor Exit Temperature K	Pattern Factor	Reference Velocity - m/s	CO_2 - % Volume	O_2 - % Volume	CO (EI)	THC (EI)	NO_x(EI)	Gas Sample Combustion Efficiency	Humidity (g H_2O/kg air)	SAE Smoke Number	Comments
1	0.788	0.772	0.0000	0.0	0.0000	298.	298.	0.99	0.0000	0.0	0.0	1046.	0.	0.00	31.7	0.0	0.0	0.0	0.0	0.0	0.0	2.5	I/A Idle	Idle
21	0.788	0.772	0.0000	0.0	0.0000	298.	298.	0.99	0.0000	0.0	0.0	990.	0.	0.00	31.8	0.0	0.0	0.0	0.0	0.0	0.0	2.5	I/A Idle	Idle
34	0.788	0.772	0.0000	0.0	0.0000	298.	298.	0.99	0.0000	0.0	0.0	990.	0.	0.00	31.7	0.0	0.0	0.0	0.0	0.0	0.0	2.5	I/A Idle	Idle
23	0.787	0.771	0.0000	0.0	0.0000	298.	298.	0.99	0.0000	0.0	0.0	990.	0.	0.00	31.5	0.0	0.0	0.0	0.0	0.0	0.0	2.5	I/A Idle	Idle
4	10.030	9.829	0.0000	0.0000	0.0000	298.	298.	0.99	0.0000	0.0	0.0	1046.	0.	0.00	31.8	0.0	0.0	0.0	0.0	0.0	0.0	2.5	I/A Idle	Idle
45	8.233	8.068	0.0000	0.0000	0.0000	298.	298.	0.99	0.0000	0.0	0.0	1046.	0.	0.00	31.8	0.0	0.0	0.0	0.0	0.0	0.0	2.5	I/A Idle	Idle
43	6.233	6.108	0.0000	0.0000	0.0000	298.	298.	0.99	0.0000	0.0	0.0	1046.	0.	0.00	31.8	0.0	0.0	0.0	0.0	0.0	0.0	2.5	I/A Idle	Idle
229	4.233	4.148	0.0000	0.0000	0.0000	298.	298.	0.99	0.0000	0.0	0.0	1046.	0.	0.00	31.8	0.0	0.0	0.0	0.0	0.0	0.0	2.5	I/A Idle	Idle
42	2.233	2.188	0.0000	0.0000	0.0000	298.	298.	0.99	0.0000	0.0	0.0	1046.	0.	0.00	31.8	0.0	0.0	0.0	0.0	0.0	0.0	2.5	I/A Idle	Idle
27	8.87	8.693	0.0000	0.0000	0.0000	298.	298.	0.99	0.0000	0.0	0.0	1018.	0.	0.00	32.4	0.0	0.0	0.0	0.0	0.0	0.0	2.5	I/A Idle	Idle
28	10.030	9.829	0.0000	0.0000	0.0000	298.	298.	0.99	0.0000	0.0	0.0	1046.	0.	0.00	39.9	0.0	0.0	0.0	0.0	0.0	0.0	2.5	I/A Idle	Idle
24	9.42	9.232	0.0000	0.0000	0.0000	298.	298.	0.99	0.0000	0.0	0.0	1046.	0.	0.00	39.9	0.0	0.0	0.0	0.0	0.0	0.0	2.5	I/A Idle	Idle
26	8.63	8.457	0.0000	0.0000	0.0000	298.	298.	0.99	0.0000	0.0	0.0	1046.	0.	0.00	39.9	0.0	0.0	0.0	0.0	0.0	0.0	2.5	I/A Idle	Idle
30	7.11	6.968	0.0000	0.0000	0.0000	298.	298.	0.99	0.0000	0.0	0.0	1046.	0.	0.00	39.9	0.0	0.0	0.0	0.0	0.0	0.0	2.5	I/A Idle	Idle
31	10.030	9.829	0.0000	0.0000	0.0000	298.	298.	0.99	0.0000	0.0	0.0	1046.	0.	0.00	39.9	0.0	0.0	0.0	0.0	0.0	0.0	2.5	I/A Idle	Idle
44	10.030	9.829	0.0000	0.0000	0.0000	298.	298.	0.99	0.0000	0.0	0.0	1046.	0.	0.00	39.9	0.0	0.0	0.0	0.0	0.0	0.0	2.5	I/A Idle	Idle
32	8.80	8.624	0.0000	0.0000	0.0000	298.	298.	0.99	0.0000	0.0	0.0	1046.	0.	0.00	39.9	0.0	0.0	0.0	0.0	0.0	0.0	2.5	I/A Idle	Idle
33	7.70	7.546	0.0000	0.0000	0.0000	298.	298.	0.99	0.0000	0.0	0.0	1046.	0.	0.00	39.9	0.0	0.0	0.0	0.0	0.0	0.0	2.5	I/A Idle	Idle
34	6.60	6.468	0.0000	0.0000	0.0000	298.	298.	0.99	0.0000	0.0	0.0	1046.	0.	0.00	39.9	0.0	0.0	0.0	0.0	0.0	0.0	2.5	I/A Idle	Idle
35	5.50	5.390	0.0000	0.0000	0.0000	298.	298.	0.99	0.0000	0.0	0.0	1046.	0.	0.00	39.9	0.0	0.0	0.0	0.0	0.0	0.0	2.5	I/A Idle	Idle
36	4.40	4.312	0.0000	0.0000	0.0000	298.	298.	0.99	0.0000	0.0	0.0	1046.	0.	0.00	39.9	0.0	0.0	0.0	0.0	0.0	0.0	2.5	I/A Idle	Idle
321	3.30	3.234	0.0000	0.0000	0.0000	298.	298.	0.99	0.0000	0.0	0.0	1046.	0.	0.00	39.9	0.0	0.0	0.0	0.0	0.0	0.0	2.5	I/A Idle	Idle
37	2.20	2.156	0.0000	0.0000	0.0000	298.	298.	0.99	0.0000	0.0	0.0	1046.	0.	0.00	39.9	0.0	0.0	0.0	0.0	0.0	0.0	2.5	I/A Idle	Idle
38	0.79	0.774	0.0000	0.0000	0.0000	298.	298.	0.99	0.0000	0.0	0.0	1046.	0.	0.00	39.9	0.0	0.0	0.0	0.0	0.0	0.0	2.5	I/A Idle	Idle
39	0.79	0.774	0.0000	0.0000	0.0000	298.	298.	0.99	0.0000	0.0	0.0	1046.	0.	0.00	39.9	0.0	0.0	0.0	0.0	0.0	0.0	2.5	I/A Idle	Idle
40	0.79	0.774	0.0000	0.0000	0.0000	298.	298.	0.99	0.0000	0.0	0.0	1046.	0.	0.00	39.9	0.0	0.0	0.0	0.0	0.0	0.0	2.5	I/A Idle	Idle
41	0.79	0.774	0.0000	0.0000	0.0000	298.	298.	0.99	0.0000	0.0	0.0	1046.	0.	0.00	39.9	0.0	0.0	0.0	0.0	0.0	0.0	2.5	I/A Idle	Idle
371	0.80	0.784	0.0000	0.0000	0.0000	298.	298.	0.99	0.0000	0.0	0.0	1046.	0.	0.00	39.9	0.0	0.0	0.0	0.0	0.0	0.0	2.5	I/A Idle	Idle

TABULATIONS FOR POWER LEVEL – 360° ANNULUS
(UNITS AS SPECIFIED BY NASA TMX – 71627)

Config.	Point No.	Condition	Wa (90°) lbm/sec	T_5 T_4 °R	P_4/P_0	T_4/T_0	$PWL_{pred.}$ dB re 10^{-13} watts	PWL_{cor}	PWL
N-8	1	Cold Idle	13.07	0	3.10	1.50			143.8
	32	Idle	13.03	793	3.77	1.58	139.2	153.6	154.8
	0	Cold T/O	15.21	0	6.80	2.67			154.4
	79	T/O	15.28	1167	6.93	2.66	144.0	150.8	156.2
N-11	1	Cold Idle	13.40	0	3.74	1.58			151.9
	33	Idle	13.38	697	3.75	1.57	138.2	148.3	154.4
	60	Cold T/O	14.02	0	6.19	2.67			149.5
	58	T/O	13.93	1395	6.16	2.67	144.1	146.9	153.3
P8	0	Cold Idle	9.61	0	3.74	2.66			153.1
	11	Idle	9.61	824	3.69	1.59	137.9	160.7	162.5
	102	Cold T/O	15.30	0	6.78	2.67			158.9
	410	T/O	14.42	1096	6.81	2.68	143.0	166.8	167.6
S8	1	Cold Idle	12.01	0	3.53	1.08			149.3
	21	Idle	11.66	823	3.73	1.56	139.0	154.5	156.0
	2222	Cold T/O	15.43	0	6.93	2.68			149.9
	810	T/O	14.84	1319	6.84	2.60	145.0	156.5	158.9
H6	1	Cold Idle	8.75	0	2.927	1.484			158.0
	6	Idle	8.67	1063	2.927	1.484	138.3	153.5	161.2
	5	Idle	8.72	854	2.927	1.484	136.4	155.6	160.2
	7	Idle	8.83	550	2.927	1.484	132.7	154.2	159.9
	8	Idle	8.43	723	2.927	1.484	134.8	151.5	160.1
	2	Cold App	17.50	0	6.807	2.050			155.4
	12	App	17.61	681	6.807	2.050	142.1	159.3	161.9
	11	App	17.74	490	6.807	2.050	140.2	158.9	161.3
	15	App	17.43	700	6.807	2.050	142.2	155.5	159.7
	14	App	17.52	490	6.807	2.050	139.2	153.5	158.5
13 or	131	App	17.41	365	6.807	2.050	136.6	150.4	157.6
	17	App	17.41	920	6.807	2.050	144.6	159.7	163.3
	18	App	17.68	881	6.807	2.050	144.3	155.0	160.2
	4	Cold T/O	15.12	0	6.807	2.667			153.9
23 or	221	T/O	15.02	1370	6.807	2.667	145.1	160.5	164.0
	24	T/O	15.13	1006	6.807	2.667	142.5	159.7	163.9
	24	T/O	15.13	1006	6.807	2.667	142.5	159.7	163.9
	19	T/O	15.28	1347	6.807	2.667	145.1	161.6	164.8
	20	T/O	15.11	1373	6.807	2.667	145.2	161.6	163.9
	21	T/O	15.15	1355	6.807	2.667	145.1	161.6	163.0
	22	T/O	15.20	1359	6.807	2.667	145.1	162.7	163.3

TABULATIONS FOR POWER LEVEL – 360° ANNULUS
(UNITS AS SPECIFIED BY NASA TMX – 71627)

Config.	Point No.	Condition	$W_a(90^\circ)$ lbm/sec	T_5-T_4 °R	P_4/P_o	T_4/T_o	PWL_{pred} dB re 10^{-13} Watts	PWL_{cor}	PWL
S23	1	Cold Idle	8.60	0	2.927	1.484			153.6
	2	Idle	8.92	1059	2.927	1.484	138.4	152.6	158.4
	3	[illegible]	8.70	868	2.927	1.484	136.6	150.2	156.1
	4	[illegible]	8.57	405	2.927	1.484	130.0	148.9	154.8
	181	Cold App	17.58	0	6.807	2.050			152.1
	5	App	17.66	1013	6.807	2.050	145.5	157.0	159.7
	6	App	17.62	918	6.807	2.050	144.6	156.9	159.4
	7	App	17.68	795	6.807	2.050	143.4	155.3	158.8
	8	App	17.60	1014	6.807	2.050	145.5	157.5	159.5
	9	App	17.72	953	6.807	2.050	145.0	156.7	160.3
	10	App	17.77	961	6.807	2.050	145.1	156.5	159.2
	17	Cold Climb	15.68	0	6.807	2.563			152.7
	14	Climb	15.83	1325	6.807	2.563	145.4	157.5	158.3
	15	Climb	15.81	1265	6.807	2.563	145.0	157.5	158.3
	16	Climb	15.79	998	6.807	2.563	143.0	157.2	158.3
	175	Cold T/O	15.29	0	6.807	2.667			153.3
	13	T/O	15.17	1358	6.807	2.667	145.1	156.2	158.9
	12	T/O	15.12	997	6.807	2.667	142.4	153.2	158.6
	11	T/O	15.08	900	6.807	2.667	141.5	151.1	156.7

APPENDIX A-2

TABULATED PRESSURE SPECTRA

Pressure transducer one-third octave band spectrum levels are tabulated in this Appendix for configurations H-6 and S-23.

TABULATED 1/3 OCTAVE BAND TRANSDUCER PRESSURE LEVELS

CONFIGURATION H-6

Point Numbers Identified in Appendix A-1
(Use values for transducer shown - disregard other readings)

1/3 Oct Frequency (Hz)	Pt 1 Cold Idle (use) 1	Pt 1 Cold Idle (ng) 2	Pt 5 Idle (use) 1	Pt 5 Idle (ng) 2	Pt 6 Idle (use) 1	Pt 6 Idle (ng) 2	Pt 7 Idle (use) 1	Pt 7 Idle (ng) 2	Pt 8 Idle (use) 1	Pt 8 Idle (ng) 2	Pt2 Cold Appr. (use) 1	Pt2 Cold Appr. (ng) 2	1/3 Oct Frequency (Hz)
50	125.7	139.3	127.9	138.8	128.7	140.0	129.4	138.1	128.0	138.7	130.3	139.6	50
63	127.2	139.4	129.0	139.2	129.3	139.5	131.9	139.6	128.9	138.9	131.0	139.0	63
80	126.9	139.3	133.0	140.7	134.0	141.8	134.4	141.3	133.0	140.3	137.4	139.7	80
100	127.5	139.2	129.3	138.2	131.0	139.7	131.1	138.3	129.6	137.9	136.1	138.6	100
125	129.6	139.0	130.7	138.4	130.9	139.1	133.5	140.0	131.4	138.6	136.9	139.0	125
160	131.3	140.1	132.1	139.5	132.7	140.3	134.1	140.5	132.2	139.4	136.9	139.9	160
200	133.1	141.2	135.1	141.4	134.4	141.3	136.3	142.4	134.7	141.5	137.1	139.5	200
250	136.1	143.4	136.0	144.3	137.7	144.2	138.9	144.8	138.7	144.8	138.6	139.4	250
315	135.6	142.2	140.5	146.5	140.6	146.2	138.1	144.1	140.8	146.6	140.3	140.6	315
400	134.3	141.6	139.8	146.1	140.6	147.8	138.3	145.1	139.3	145.1	138.7	139.6	400
500	133.8	141.3	139.7	144.6	140.0	145.3	139.6	145.5	138.3	145.1	137.1	137.2	500
630	133.1	141.6	139.3	146.2	139.5	146.6	137.4	144.9	139.8	146.6	138.1	137.1	630
800	134.4	141.7	138.8	144.9	139.8	145.5	135.7	143.3	137.7	144.5	137.7	137.4	800
1000	134.9	142.6	139.3	146.4	139.9	146.6	137.7	144.5	138.6	145.5	138.6	139.2	1000
1250	138.0	146.4	144.4	151.0	145.4	151.3	140.6	148.1	142.3	149.3	140.2	141.8	1250
1600	137.6	147.4	141.7	148.9	142.6	149.8	140.2	147.6	140.8	148.6	141.8	140.4	1600
2000	138.7	146.3	140.0	147.9	140.9	148.6	138.8	148.0	139.1	146.1	143.3	140.1	2000
2500	143.7	151.9	141.6	151.1	142.6	151.6	142.6	151.4	141.0	151.3	138.0	142.4	2500
3150	144.2	151.5	144.2	150.6	145.0	150.9	144.2	151.5	143.6	151.0	141.7	141.1	3150
4000	149.2	160.8	148.8	160.7	149.7	161.1	149.6	161.8	149.2	161.8	143.3	146.2	4000
5000	147.8	151.9	145.4	152.3	146.1	152.6	143.2	152.7	144.7	153.0	137.9	140.2	5000
6300	146.5	150.2	144.7	150.4	145.6	150.9	147.0	151.0	146.5	151.1	141.3	141.7	6300
8000	148.1	156.1	146.7	156.1	147.5	157.2	148.0	156.8	148.1	156.8	149.7	149.9	8000
10000	139.5	148.8	139.6	149.3	140.3	150.7	139.3	149.1	139.4	149.7	144.2	144.2	10000
OASPL	155.0	164.1	155.6	164.4	156.3	165.0	155.7	165.0	155.7	165.1	155.4	155.8	OASPL

TABULATED 1/3 OCTAVE BAND TRANSDUCER PRESSURE LEVELS

CONFIGURATION H-6

Point Numbers Identified in Appendix A-1
(Use values for transducer shown - disregard other readings)

1/3 Oct Frequency (Hz)	Pt 11 Appr. (use)	Pt 11 Appr. (ng)	Pt 12 Appr. (use)	Pt 12 Appr. (ng)	Pt 13 Appr. (use)	Pt 13 Appr. (ng)	Pt 14 Appr. (use)	Pt 14 Appr. (ng)	Pt 15 Appr. (use)	Pt 15 Appr. (ng)	Pt 17 Appr. (use)	Pt 17 Appr. (ng)	Pt 18 Appr. (use)	Pt 18 Appr. (ng)	1/3 Oct Frequency (Hz)
50	135.8	140.0	134.4	139.9	137.6	140.2	137.7	140.7	137.9	140.3	140.7	141.3	139.7	139.9	50
63	136.7	139.1	134.9	139.6	136.4	140.0	138.7	140.5	136.5	140.7	141.1	141.6	141.7	141.5	63
80	136.8	139.6	137.5	139.5	139.4	140.6	139.4	140.5	140.5	141.0	143.6	142.3	142.1	141.3	80
100	136.4	138.6	135.0	138.5	137.5	139.6	137.9	139.7	137.8	139.7	140.7	140.9	139.4	139.9	100
125	136.8	138.7	135.8	138.6	138.9	140.1	138.6	140.0	138.6	140.2	139.6	141.4	139.5	139.2	125
160	137.7	139.2	137.3	139.4	139.6	141.0	138.6	140.2	138.1	140.2	140.0	142.9	140.2	140.1	160
200	138.8	140.2	139.0	140.5	139.6	140.6	139.6	141.0	140.1	141.4	140.1	140.6	139.7	141.7	200
250	141.3	141.3	141.0	141.3	140.6	141.4	140.7	141.4	140.8	141.6	141.6	142.6	141.4	141.7	250
315	143.8	143.8	142.7	143.3	143.1	142.6	143.6	143.6	144.2	144.1	144.8	145.3	145.6	143.2	315
400	145.1	143.5	144.9	143.7	142.9	142.4	143.4	142.0	144.6	142.9	147.6	146.7	145.6	143.6	400
500	146.6	143.2	146.1	142.9	142.3	141.3	143.1	142.2	144.8	144.0	146.8	146.3	142.8	142.4	500
630	145.9	143.9	146.1	143.8	142.1	141.4	143.1	142.1	147.1	146.3	146.9	147.9	143.1	141.6	630
800	147.6	143.4	147.2	143.6	141.7	141.6	142.1	142.1	144.2	144.4	147.2	147.9	143.9	141.2	800
1000	148.1	145.3	147.9	145.0	142.5	142.0	142.8	143.5	144.5	144.4	146.7	149.1	144.4	141.9	1000
1250	151.5	147.5	150.1	146.4	143.6	141.7	143.6	143.1	144.9	144.5	149.1	148.1	145.4	141.9	1250
1600	151.7	149.6	152.8	150.3	144.1	142.6	145.6	144.6	145.6	145.1	150.8	149.6	145.5	142.6	1600
2000	148.9	145.3	149.4	146.6	144.6	142.0	141.6	143.0	146.3	142.8	149.5	149.5	145.5	142.7	2000
2500	144.4	146.4	144.6	146.1	140.6	143.4	141.6	142.9	142.2	143.9	146.1	144.3	141.7	144.1	2500
3150	146.7	143.7	146.6	143.9	142.0	142.1	142.5	142.2	142.4	141.9	146.9	145.1	144.8	144.3	3150
4000	150.8	152.2	150.7	152.1	145.9	144.1	141.2	144.2	141.2	146.7	150.9	149.0	144.5	151.6	4000
5000	144.7	144.3	147.5	144.9	140.4	141.6	140.9	142.2	141.1	142.2	145.5	142.7	141.5	144.1	5000
6300	146.5	144.1	148.0	145.5	142.1	143.0	142.7	143.4	143.1	143.7	149.1	145.5	143.9	141.1	6300
8000	151.3	150.2	152.4	151.2	149.3	151.6	150.2	152.5	151.4	153.2	155.6	154.9	152.8	149.9	8000
10000	144.7	149.2	146.6	150.7	149.2	145.8	149.6	146.1	150.1	147.0	152.1	149.9	149.9	152.1	10000
OASPL	160.5	159.5	160.8	159.8	157.0	157.5	157.7	158.3	158.6	158.9	161.9	161.4	158.6	158.5	OASPL

TABULATED 1/3 OCTAVE BAND TRANSDUCER PRESSURE LEVELS

CONFIGURATION H-6

Point Numbers Identified in Appendix A-1
(Use values for transducer shown - disregard other readings)

1/3 Oct Frequency (Hz)	Pt 4 Cold T.O. (use) 1	Pt 4 Cold T.O. (ng) 2	Pt 19 T.O. (use) 1	Pt 19 T.O. (ng) 2	Pt 20 T.O. (use) 1	Pt 20 T.O. (ng) 2	Pt 21 T.O. (use) 1	Pt 21 T.O. (ng) 2	Pt 22 T.O. (use) 1	Pt 22 T.O. (ng) 2	Pt 23 T.O. (use) 1	Pt 23 T.O. (ng) 2	Pt 24 T.O. (use) 1	Pt 24 T.O. (ng) 2	1/3 Oct Frequency (Hz)
50	150.6	0.0	140.1	141.1	140.6	140.1	137.6	139.6	138.6	138.6	140.6	144.6	141.2	142.9	50
63	153.2	0.0	141.1	141.6	140.3	141.1	137.9	141.1	138.6	139.6	140.2	142.6	141.9	142.6	63
80	154.9	0.0	141.7	141.7	140.9	140.6	139.9	139.9	139.6	139.9	141.6	142.6	142.6	142.6	80
100	153.0	0.0	141.6	141.4	141.4	141.1	141.0	141.1	141.0	140.7	141.1	142.4	141.2	142.4	100
125	153.6	0.0	139.3	139.3	138.7	138.6	137.6	138.6	138.9	137.7	138.7	140.6	139.7	141.2	125
160	155.3	0.0	140.0	139.8	139.1	139.2	138.4	138.6	138.6	138.6	139.2	141.2	139.6	140.8	160
200	155.2	0.0	139.4	139.3	139.1	139.2	138.7	138.7	138.5	138.6	138.6	140.3	139.3	140.3	200
250	156.7	0.0	141.4	141.9	140.7	140.9	140.3	140.1	139.3	139.6	139.6	141.2	140.4	141.9	250
315	159.6	0.0	142.0	142.4	141.2	142.1	140.1	142.4	142.1	142.1	141.4	143.9	141.4	144.4	315
400	159.1	0.0	144.3	144.3	144.4	145.1	144.7	145.0	145.1	144.6	145.3	147.3	145.4	146.6	400
500	158.7	0.0	144.1	144.1	144.1	144.1	141.8	144.6	144.6	144.9	144.4	146.5	144.6	146.3	500
630	159.0	0.0	141.4	141.9	141.6	141.3	139.2	141.7	141.1	141.2	141.4	143.2	141.9	144.4	630
800	158.6	0.0	144.5	144.6	144.1	144.9	140.1	144.6	144.1	144.7	144.4	146.1	144.7	146.7	800
1000	158.4	0.0	144.7	144.7	144.3	144.3	144.1	144.4	144.1	144.7	144.2	146.1	144.9	146.8	1000
1250	158.7	0.0	145.3	145.4	144.3	144.5	143.6	145.6	143.7	144.2	143.7	146.2	143.9	146.4	1250
1600	159.9	0.0	145.3	145.4	145.2	145.4	145.4	145.1	145.1	145.2	145.6	147.7	145.6	148.3	1600
2000	159.5	0.0	142.3	142.7	142.4	142.6	142.4	142.1	142.2	142.2	142.1	144.0	142.2	144.5	2000
2500	160.6	0.0	141.1	141.5	141.1	141.6	141.1	141.7	141.6	141.6	141.9	143.4	141.6	144.4	2500
3150	160.5	0.0	139.9	140.6	140.2	141.6	140.7	141.6	139.7	141.6	140.2	142.1	140.9	142.6	3150
4000	157.2	0.0	137.4	138.6	138.6	138.9	138.6	138.6	138.8	138.1	137.6	139.6	138.4	139.3	4000
5000	156.8	0.0	136.6	136.6	137.7	138.7	136.6	138.6	136.4	136.3	137.1	138.6	136.8	137.8	5000
6300	159.5	0.0	141.6	142.7	143.6	150.7	141.1	142.6	139.7	149.4	139.4	155.2	139.0	155.7	6300
8000	155.1	0.0	137.0	139.1	138.0	153.4	137.1	139.6	135.5	152.6	135.1	153.4	137.5	151.6	8000
10000	153.6	0.0	136.4	147.4	137.4	149.5	136.4	141.6	135.6	141.5	137.7	151.9	138.1	152.6	10000
OASPL	153.5	13.8	162.6	160.9	161.8	161.4	162.0	159.6	161.3	160.3	162.0	163.7	162.1	163.1	OASPL

TABULATED 1/3 OCTAVE BAND TRANSDUCER PRESSURE LEVELS

CONFIGURATION S-23

Point Numbers Identified in Appendix A-1
(Use values for transducer shown - disregard other readings)

1/3 Oct Frequency (Hz)	Pt 1 Cold Idle (ng) 1	Pt 1 Cold Idle (use) 2	Pt 2 Idle (ng) 1	Pt 2 Idle (use) 2	Pt 3 Idle (ng) 1	Pt 3 Idle (use) 2	Pt 4 Idle (ng) 1	Pt 4 Idle (use) 2	Pt 181 Cold Appr (ng) 1	Pt 181 Cold Appr (use) 2	Pt 5 Appr (ng) 1	Pt 5 Appr (use) 2	Pt 6 Appr (ng) 1	Pt 6 Appr (use) 2	1/3 Oct Frequency (Hz)
50	130.7	121.9	130.0	122.7	130.7	121.8	130.5	122.1	124.9	125.5	142.1	127.2	142.5	127.0	50
63	131.6	121.0	135.2	124.2	134.4	124.1	135.9	126.3	123.1	129.0	141.9	127.9	141.6	127.3	63
80	130.6	122.1	139.8	131.4	139.2	130.7	135.3	126.5	137.0	128.6	143.8	135.9	144.3	131.4	80
100	132.8	124.3	137.1	129.9	135.5	124.3	136.8	124.6	135.9	127.4	144.4	131.4	144.6	131.1	100
125	147.6	126.1	142.2	127.9	142.3	128.7	145.7	129.7	130.4	128.8	153.6	131.4	152.6	131.4	125
160	147.8	127.9	143.8	128.4	143.2	128.8	144.0	128.3	138.5	130.2	150.5	133.1	150.7	132.9	160
200	142.6	127.4	151.5	134.7	149.6	135.6	142.1	128.9	137.2	131.4	150.4	134.2	150.7	134.1	200
250	141.2	131.8	159.7	140.0	150.9	134.1	140.5	131.6	140.2	133.8	156.0	137.8	156.4	137.6	250
315	140.9	134.9	152.5	143.0	151.2	131.3	149.1	134.1	141.1	138.6	157.2	142.8	157.2	142.9	315
400	140.7	138.2	154.2	141.6	149.5	139.0	147.6	138.1	142.3	134.1	159.7	146.3	159.7	145.4	400
500	140.6	138.2	151.6	138.4	150.9	137.9	149.2	139.0	144.9	134.7	162.3	147.6	163.6	147.0	500
630	139.5	134.9	154.1	139.4	155.1	137.5	155.4	139.9	146.3	138.6	166.6	147.5	161.8	146.8	630
800	139.9	140.7	156.3	142.8	153.3	139.6	153.6	140.8	143.7	140.1	167.7	141.8	166.4	148.7	800
1000	151.6	140.7	157.7	141.9	152.5	140.9	150.8	140.6	141.8	139.1	163.9	150.1	164.2	149.3	1000
1250	153.0	139.9	157.0	142.8	151.9	141.6	150.8	141.2	143.8	143.3	165.6	150.1	166.5	149.2	1250
1600	152.1	142.9	151.8	145.4	151.6	145.1	151.0	145.3	143.4	144.1	164.3	149.2	164.6	146.8	1600
2000	149.5	139.4	152.5	143.3	152.8	143.4	152.4	142.7	145.7	143.1	164.4	147.8	165.0	147.4	2000
2500	151.4	140.4	154.2	142.6	151.0	143.7	151.5	144.0	144.1	140.9	161.5	146.6	162.0	146.0	2500
3150	150.8	142.5	152.9	146.7	152.1	145.6	152.1	144.0	141.4	144.4	158.6	144.0	158.3	144.5	3150
4000	149.9	146.6	150.4	151.8	149.6	148.3	148.6	146.6	136.8	141.7	157.7	151.3	157.3	151.5	4000
5000	147.5	137.6	147.6	143.1	146.2	133.5	145.4	131.6	132.6	131.4	164.1	153.7	165.6	153.9	5000
6300	150.5	141.9	151.4	134.1	150.3	128.2	149.9	128.2	131.9	141.7	156.7	146.4	156.8	150.8	6300
8000	151.2	142.1	151.7	131.4	150.8	128.8	150.9	128.7	128.5	146.8	149.3	139.9	148.9	141.4	8000
10000	143.8	134.9	147.0	135.9	146.2	135.1	146.3	136.9	126.4	142.5	144.7	134.9	145.1	134.7	10000
OASPL	163.2	153.2	166.0	156.2	164.0	154.3	163.3	153.5	154.9	154.7	175.5	160.8	176.0	160.6	OASPL

TABULATED 1/3 OCTAVE BAND TRANSDUCER PRESSURE LEVELS

CONFIGURATION S-23

Point Numbers Identified in Appendix A-1
(Use Values for transducer shown - disregard other readings)

1/3 Oct Frequency (Hz)	Pt7 Appr. (ng) 1	Pt7 Appr. (use) 2	Pt 8 Appr. (ng) 1	Pt 8 Appr. (use) 2	Pt 9 Appr. (ng) 1	Pt 9 Appr. (use) 2	Pt 10 Appr. (ng) 1	Pt 10 Appr. (use) 2	Pt 17 Cold Climb (ng) 1	Pt 17 Cold Climb (use) 2	Pt 14 Climb (ng) 1	Pt 14 Climb (use) 2	1/3 Oct Frequency (Hz)
50	143.0	126.2	143.3	126.5	143.8	127.3	144.7	127.0	144.6	126.4	153.6	126.6	50
63	146.7	126.7	144.1	127.6	141.9	127.9	141.9	129.0	144.2	127.0	150.1	127.1	63
80	144.6	135.2	144.0	135.4	144.7	136.2	146.0	137.5	146.1	132.1	154.3	132.4	80
100	144.6	129.2	144.4	130.9	144.5	131.0	145.2	131.4	149.4	121.4	156.4	134.6	100
125	154.5	131.4	154.1	131.6	151.3	131.8	151.5	132.3	162.2	131.7	158.7	130.4	125
160	151.6	132.5	151.0	132.7	150.3	133.1	150.5	133.4	156.8	131.9	156.8	123.2	160
200	151.0	134.1	150.5	134.4	150.7	134.6	151.7	135.0	150.4	131.2	155.9	134.0	200
250	157.3	137.9	156.9	138.4	157.8	139.9	158.1	140.2	153.2	123.1	157.1	137.6	250
315	156.4	142.5	157.6	142.3	157.5	144.3	158.8	145.2	154.0	139.1	162.6	142.8	315
400	159.4	144.6	160.5	141.3	160.5	147.7	161.6	141.1	159.6	141.4	167.4	145.8	400
500	163.5	146.1	164.2	148.1	164.0	141.9	164.7	146.4	163.9	143.6	164.3	146.8	500
630	169.9	145.9	169.6	147.7	169.9	147.1	170.1	145.4	161.3	141.4	172.6	146.9	630
800	170.8	147.2	168.5	141.7	169.6	141.6	161.9	147.0	170.4	143.9	175.4	146.4	800
1000	164.0	147.7	163.9	150.4	163.9	144.2	164.1	147.6	167.5	142.7	170.4	149.8	1000
1250	166.7	148.2	166.4	150.7	166.2	144.3	166.6	141.3	162.6	144.6	164.6	150.5	1250
1600	164.7	148.3	165.2	150.5	165.1	144.4	165.4	150.1	161.1	144.9	164.7	150.6	1600
2000	164.7	147.2	164.9	150.2	164.5	147.8	164.5	148.5	161.8	143.9	164.9	148.4	2000
2500	162.3	145.5	162.3	150.8	162.4	148.0	162.5	146.3	160.7	142.9	162.7	146.9	2500
3150	157.9	146.3	158.3	152.7	157.6	148.6	157.6	149.2	156.2	146.9	157.6	149.7	3150
4000	157.4	150.3	156.3	149.3	158.1	149.9	156.9	151.9	152.0	144.5	152.1	150.4	4000
5000	163.3	155.1	162.5	139.9	162.9	154.8	163.7	152.6	153.6	134.4	150.6	146.4	5000
6300	152.3	147.5	155.9	132.9	155.6	154.6	157.9	147.5	148.5	134.6	148.8	142.1	6300
8000	147.2	139.5	148.2	137.3	148.2	143.6	148.8	147.6	146.5	130.8	147.1	141.3	8000
10000	143.8	138.4	145.5	131.2	146.0	140.3	146.6	139.9	144.9	137.3	146.6	138.6	10000
OASPL	176.5	160.2	176.7	160.6	176.3	161.5	176.7	160.5	175.7	154.9	174.8	159.9	OASPL

TABULATED 1/3 OCTAVE BAND TRANSDUCER PRESSURE LEVELS

CONFIGURATION S-23

Point Numbers Identified in Appendix A-1
(Use values for transducer shown - disregard other readings)

1/3 Oct Frequency (Hz)	Pt 15 Climb (ng) 1	Pt 15 Climb (use) 2	Pt 16 Climb (ng) 1	Pt 16 Climb (use) 2	Pt 175 Cold T. O. (ng) 1	Pt 175 Cold T. O. (use) 2	Pt 11 T. O. (ng) 1	Pt 11 T. O. (use) 2	Pt 12 T. O. (ng) 1	Pt 12 T. O. (use) 2	Pt 13 T. O. (ng) 1	Pt 13 T. O. (use) 2	1/3 Oct Frequency (Hz)
50	159.2	124.7	153.7	124.8	146.3	127.8	144.3	125.4	143.1	125.4	148.2	126.4	50
63	151.7	127.2	150.1	126.8	147.1	126.7	142.6	125.8	141.2	126.6	144.8	126.4	63
80	155.7	132.2	153.5	133.1	148.0	131.2	145.9	131.7	143.9	131.4	148.6	131.1	80
100	156.6	133.8	154.4	131.0	149.7	131.6	148.6	132.3	147.0	132.4	152.2	135.2	100
125	159.1	130.2	155.0	130.6	150.6	131.3	145.1	129.8	151.7	129.4	154.0	129.5	125
160	158.6	131.8	156.5	132.3	151.1	132.1	152.1	132.0	151.6	132.5	153.7	133.0	160
200	155.9	132.7	154.2	133.5	151.9	131.8	150.7	133.2	148.6	132.3	151.9	133.2	200
250	156.6	134.8	155.6	135.7	154.3	133.5	154.5	135.0	153.1	135.1	155.4	134.5	250
315	161.0	142.4	159.1	141.6	156.3	139.6	155.6	140.2	157.1	140.8	160.4	142.6	315
400	166.1	145.3	162.2	144.3	161.1	141.0	161.3	142.4	162.6	143.3	161.3	145.6	400
500	166.3	141.0	165.7	147.3	165.9	144.3	164.5	145.4	166.0	146.5	164.4	146.1	500
630	172.7	147.6	169.3	147.2	165.9	141.6	170.8	144.1	172.3	145.0	173.0	146.4	630
800	175.6	141.1	171.0	147.7	171.4	144.8	173.8	144.5	174.6	145.9	174.9	145.1	800
1000	169.8	144.7	167.4	148.4	166.2	144.6	169.5	145.3	168.3	148.9	169.3	148.3	1000
1250	163.6	150.7	162.0	149.4	162.7	144.2	165.1	147.3	164.2	148.1	164.8	149.4	1250
1600	164.1	150.2	161.4	149.0	161.3	143.3	164.4	147.2	164.6	147.5	165.6	148.6	1600
2000	163.7	148.9	159.7	148.3	162.6	142.8	166.4	145.9	166.9	145.9	167.3	147.2	2000
2500	162.3	148.0	158.5	147.4	162.6	140.3	164.9	144.6	164.9	142.5	164.4	146.1	2500
3150	156.0	150.2	152.8	149.6	157.2	143.9	157.3	148.2	161.4	147.2	159.2	149.2	3150
4000	150.2	149.9	147.5	150.1	150.3	144.0	154.7	149.9	154.1	147.4	154.9	151.8	4000
5000	147.7	145.2	145.1	144.3	148.9	145.2	152.4	147.4	152.1	148.9	152.8	149.8	5000
6300	146.3	140.4	144.2	137.1	144.1	145.9	150.5	146.2	149.8	153.3	151.3	141.1	6300
8000	144.3	141.4	142.7	140.9	144.0	138.2	148.2	138.6	147.2	145.9	147.1	141.0	8000
10000	143.7	138.5	142.0	137.6	142.1	138.1	147.1	136.2	146.1	136.7	146.6	138.7	10000
OASPL	179.6	159.9	176.1	159.2	176.7	155.3	176.1	157.5	179.2	159.2	179.7	159.2	OASPL

APPENDIX A-3

PRESSURE SPECTRA PLOTS

Machine plots of one-third octave band spectrum levels for H-6 and S-23 pressure transducer signals are contained in this Appendix, together with selected narrowband spectra.

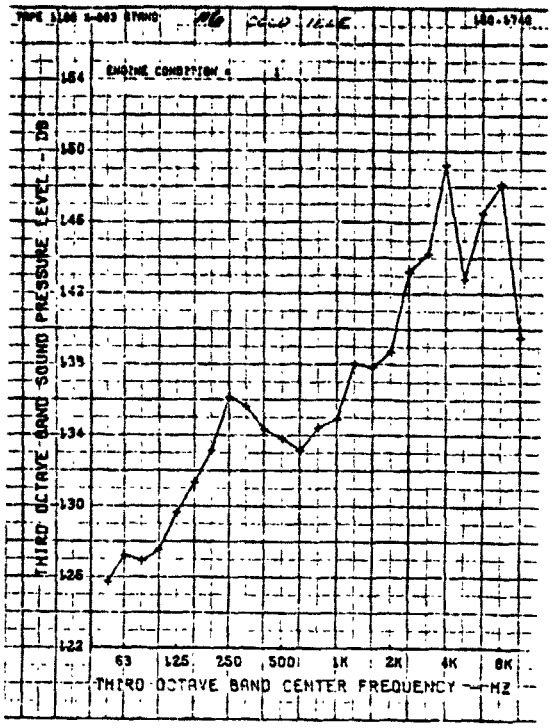
ENGINE CONDITION
THIRD OCTAVE BAND SOUND PRESSURE LEVEL - DB
THIRD OCTAVE BAND CENTER FREQUENCY - HZ
63
125
250
500
1K
2K
4K
8K

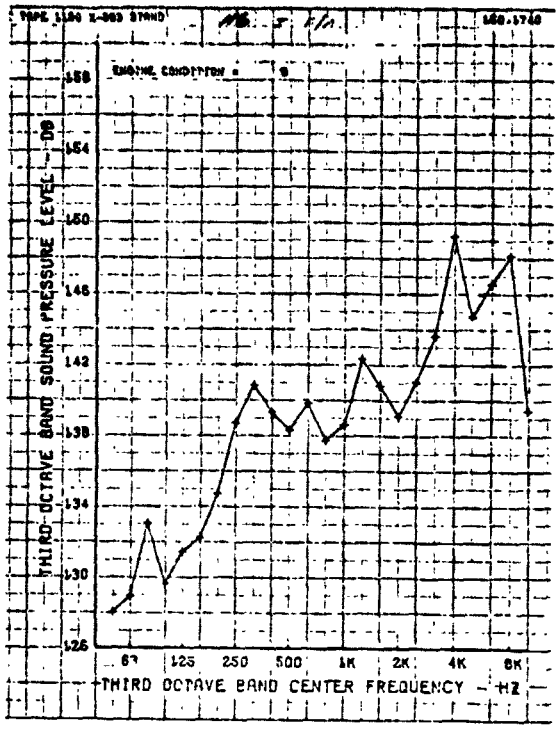
ENGINE CONDITION
THIRD OCTAVE BAND SOUND PRESSURE LEVEL - DB
THIRD OCTAVE BAND CENTER FREQUENCY - HZ
63
125
250
500
1K
2K
4K
8K

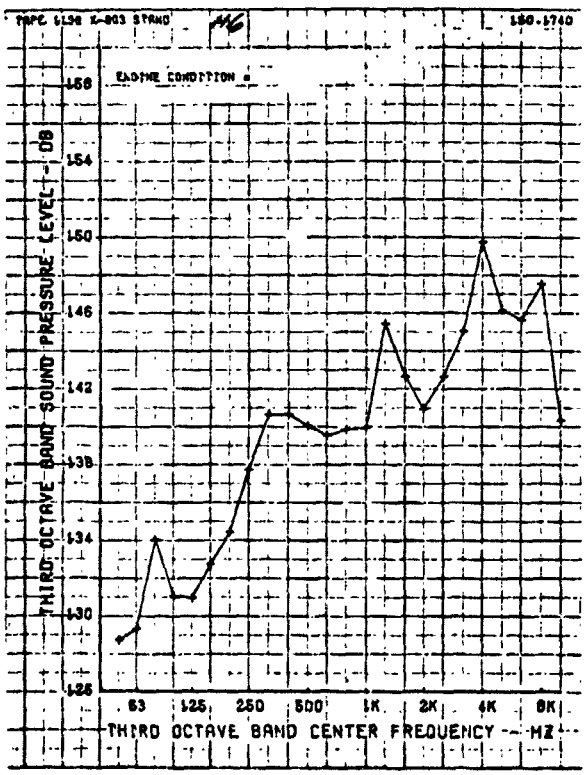
ENGINE CONDITION
THIRD OCTAVE BAND SOUND PRESSURE LEVEL - DB
THIRD OCTAVE BAND CENTER FREQUENCY - HZ
63
125
250
500
1K
2K
4K
8K

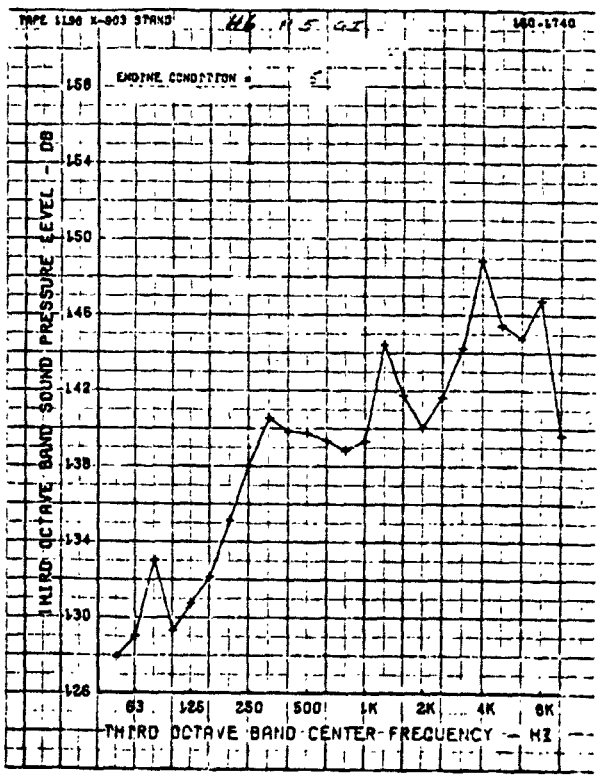
ENGINE CONDITION
THIRD OCTAVE BAND SOUND PRESSURE LEVEL - DB
THIRD OCTAVE BAND CENTER FREQUENCY - HZ
63
125
250
500
1K
2K
4K
8K

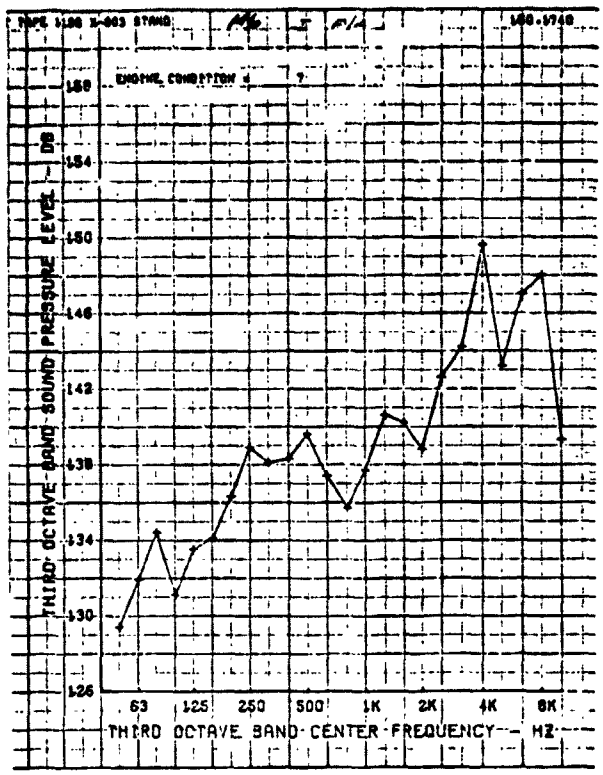
ENGINE CONDITION 7
THIRD OCTAVE BAND SOUND PRESSURE LEVEL — DB
158
154
150
146
142
138
134
126
63
125
250
500
1K
2K
4K
8K
THIRD OCTAVE BAND CENTER FREQUENCY — HZ

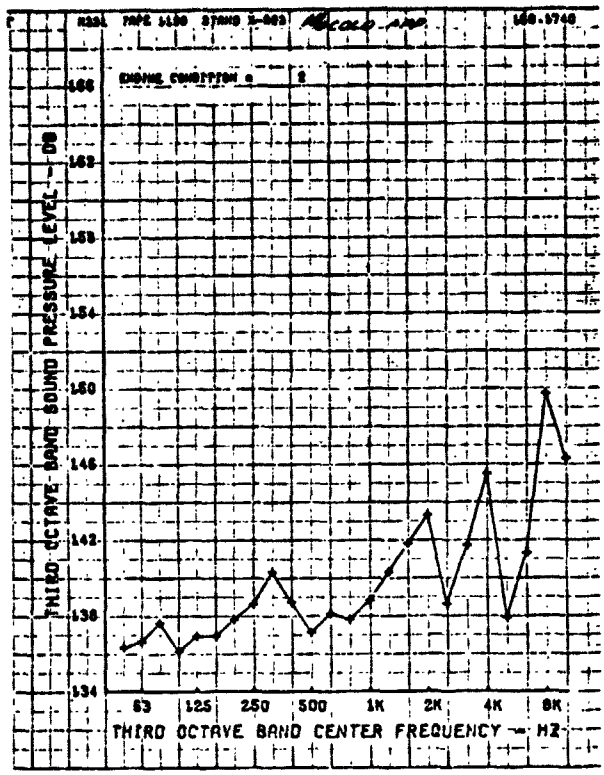
ENGINE CONDITION 2
THIRD OCTAVE BAND SOUND PRESSURE LEVEL — DB
166
162
158
154
150
146
142
138
134
63
125
250
500
1K
2K
4K
8K
THIRD OCTAVE BAND CENTER FREQUENCY — HZ

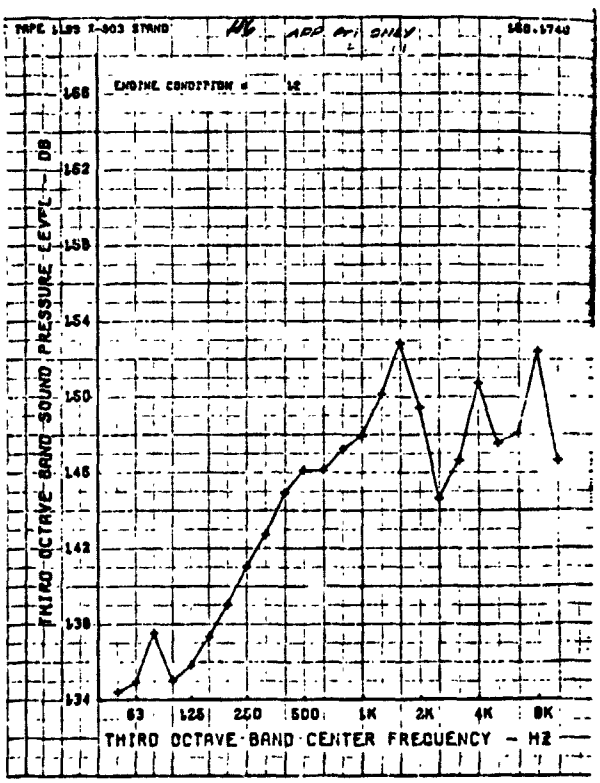
ENGINE CONDITION 12
THIRD OCTAVE BAND SOUND PRESSURE LEVEL — DB
166
162
158
154
150
146
142
138
134
63
125
250
500
1K
2K
4K
8K
THIRD OCTAVE BAND CENTER FREQUENCY — HZ

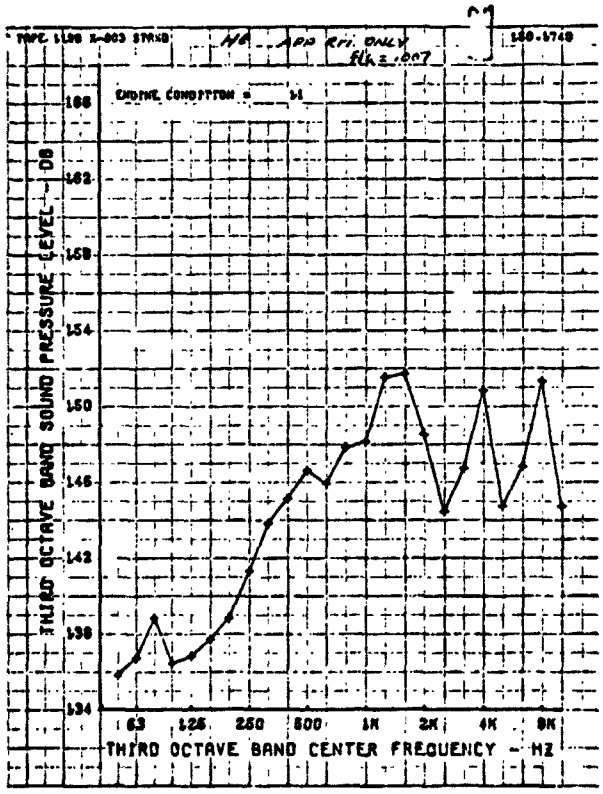
ENGINE CONDITION 11
THIRD OCTAVE BAND SOUND PRESSURE LEVEL — DB
166
162
158
154
150
146
142
138
134
63
125
250
500
1K
2K
4K
8K
THIRD OCTAVE BAND CENTER FREQUENCY — HZ

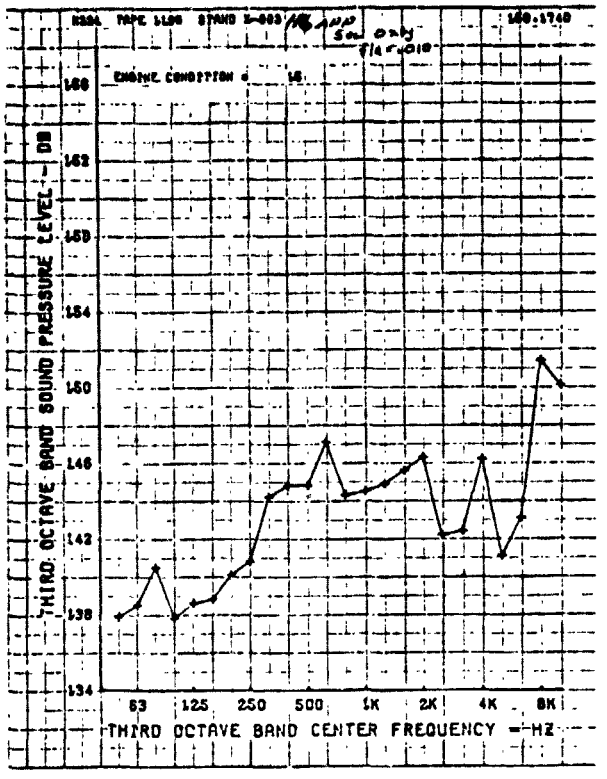
THIRD OCTAVE BAND SOUND PRESSURE LEVEL - DB
THIRD OCTAVE BAND CENTER FREQUENCY - HZ
63 125 250 500 1K 2K 4K 8K

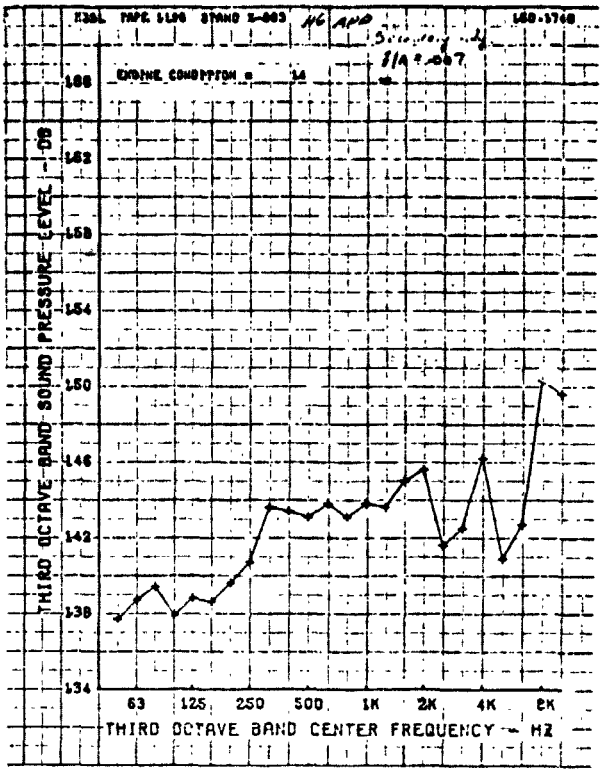
THIRD OCTAVE BAND SOUND PRESSURE LEVEL - DB
THIRD OCTAVE BAND CENTER FREQUENCY - HZ
63 125 250 500 1K 2K 4K 8K

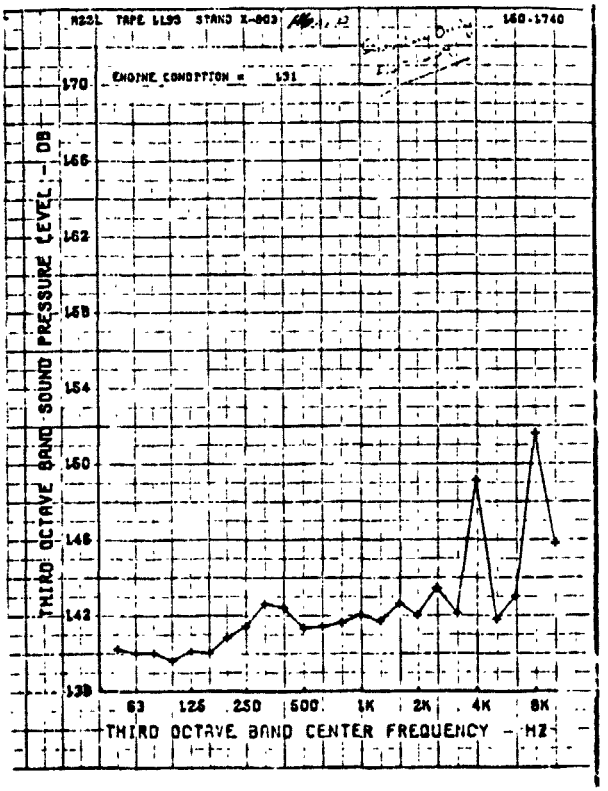
THIRD OCTAVE BAND SOUND PRESSURE LEVEL - DB
THIRD OCTAVE BAND CENTER FREQUENCY - HZ
63 125 250 500 1K 2K 4K 8K

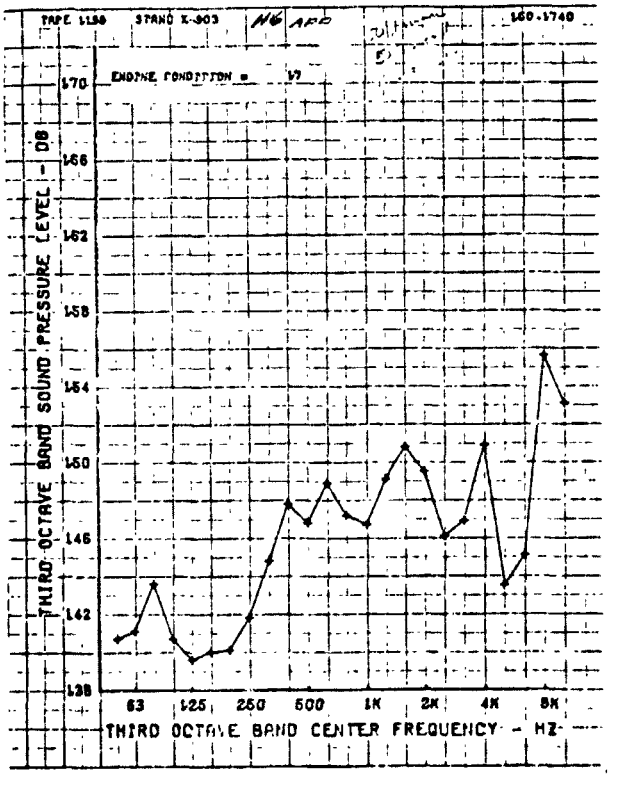
THIRD OCTAVE BAND SOUND PRESSURE LEVEL - DB
THIRD OCTAVE BAND CENTER FREQUENCY - HZ
63 125 250 500 1K 2K 4K 8K

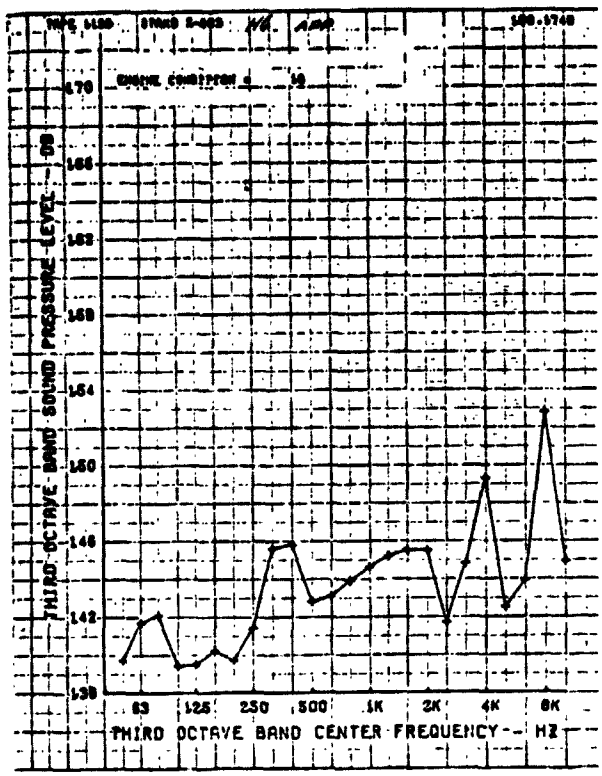
THIRD OCTAVE BAND SOUND PRESSURE LEVEL - DB
THIRD OCTAVE BAND CENTER FREQUENCY - HZ

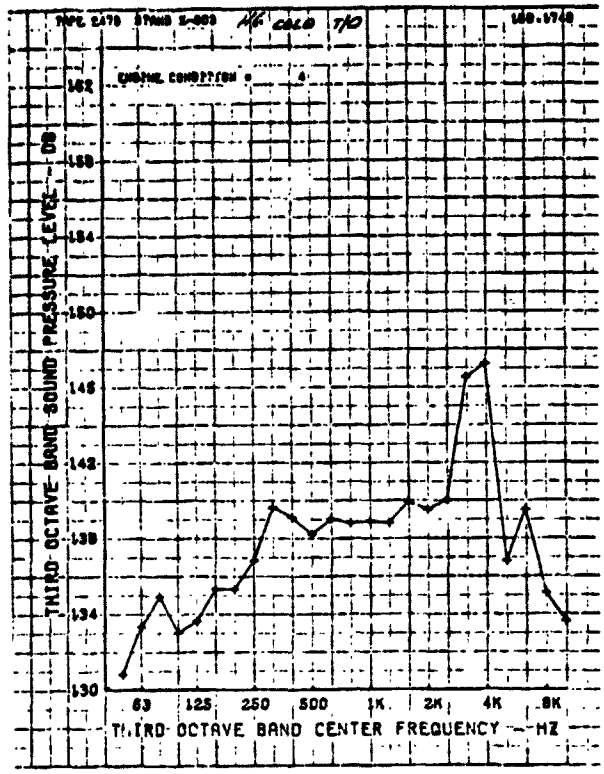
THIRD OCTAVE BAND SOUND PRESSURE LEVEL - DB
THIRD OCTAVE BAND CENTER FREQUENCY - HZ

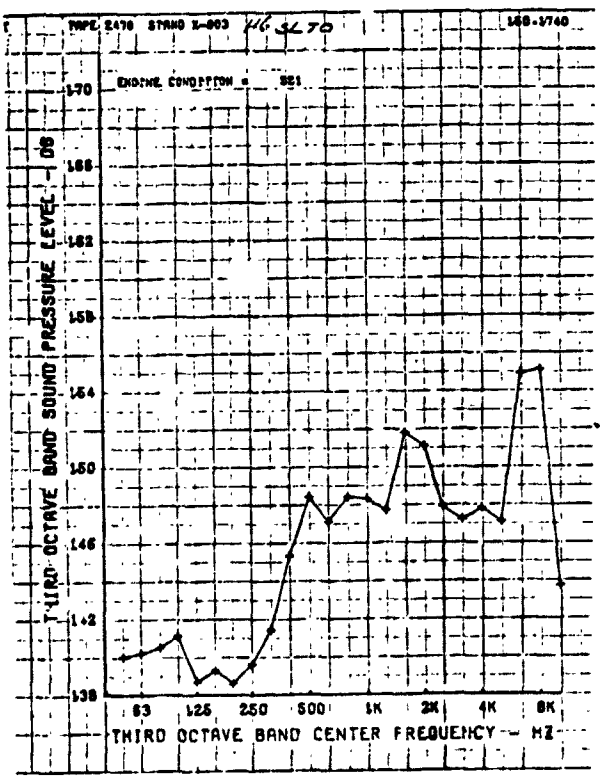
THIRD OCTAVE BAND SOUND PRESSURE LEVEL - DB
THIRD OCTAVE BAND CENTER FREQUENCY - HZ

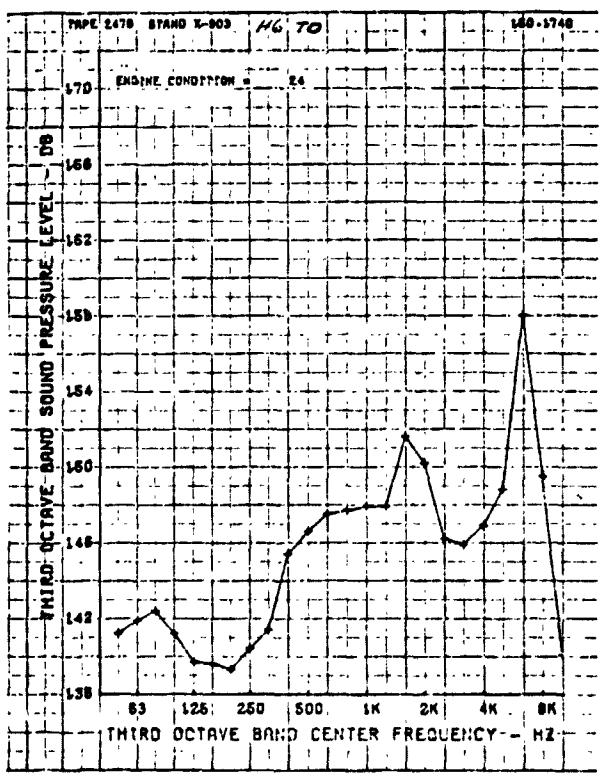
THIRD OCTAVE BAND SOUND PRESSURE LEVEL - DB
THIRD OCTAVE BAND CENTER FREQUENCY - HZ

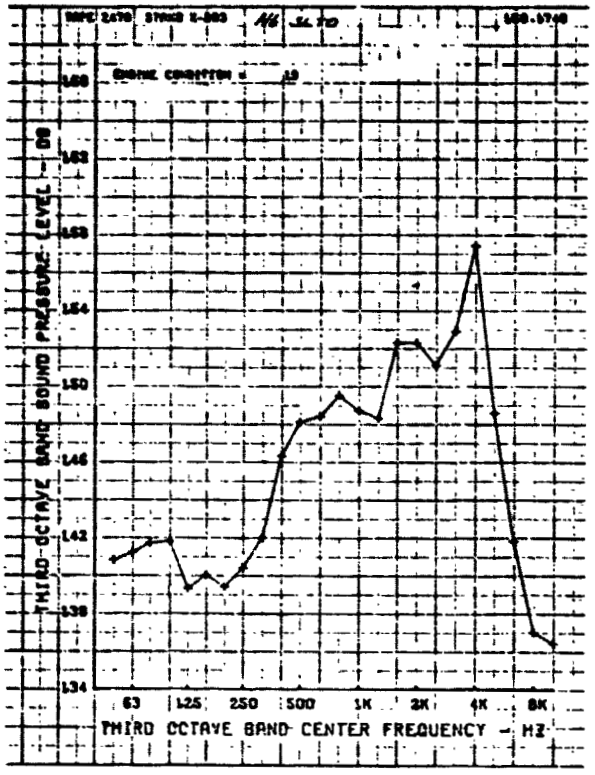

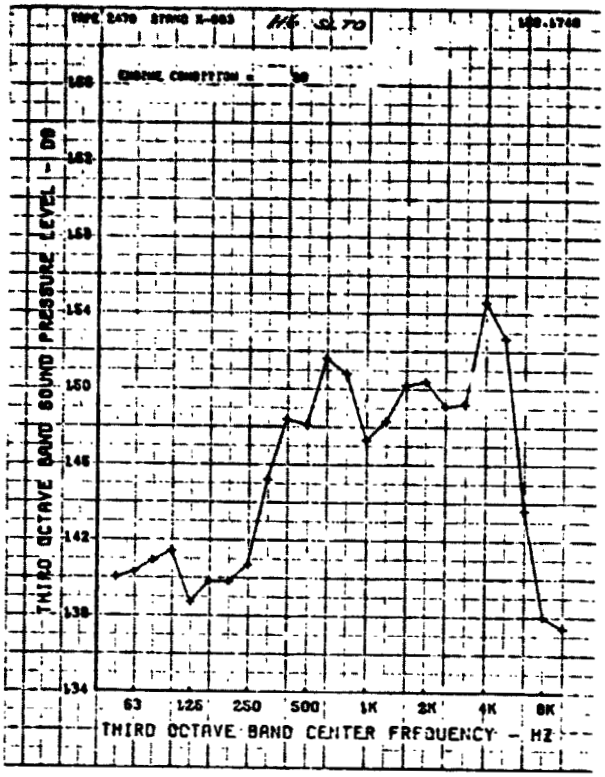

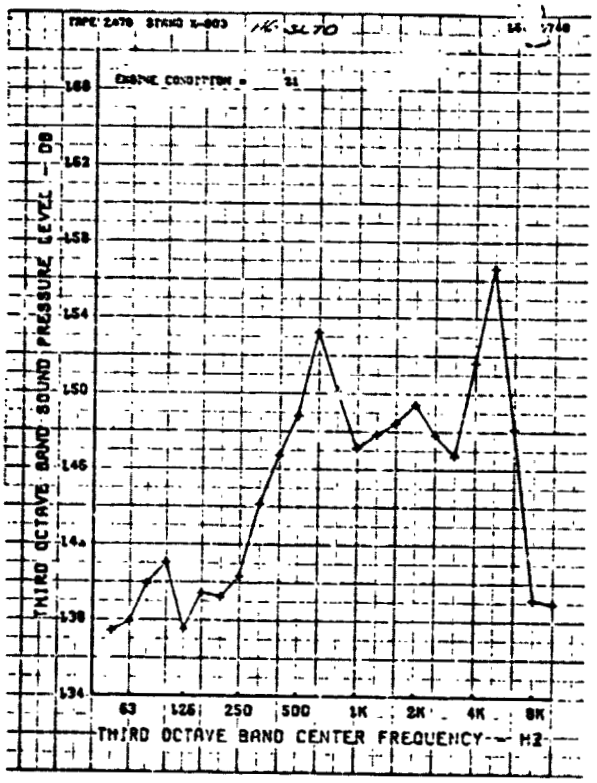

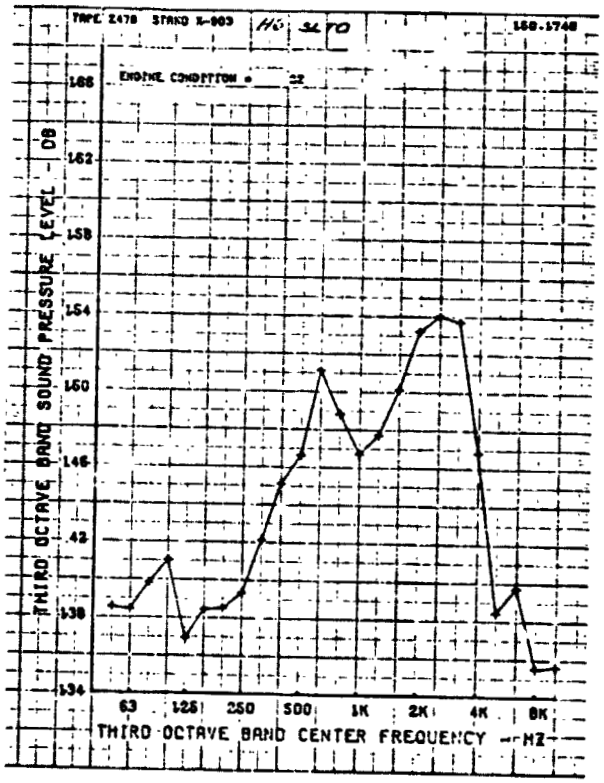

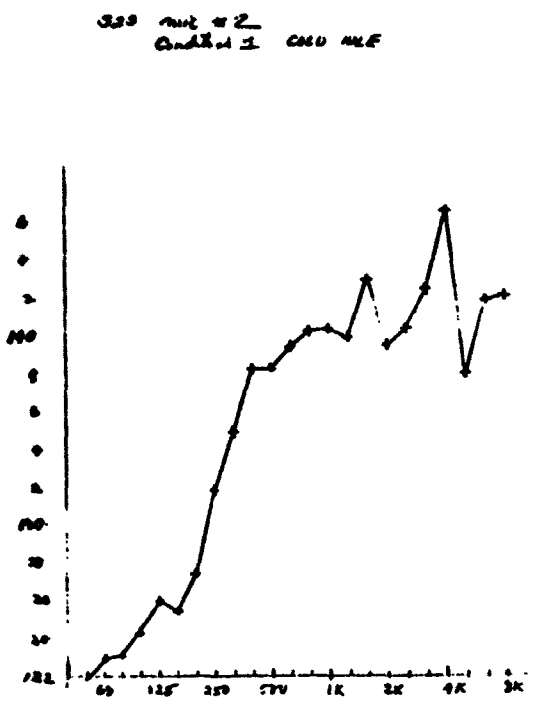
S23 unit #2
Condition 1 COLD MLF

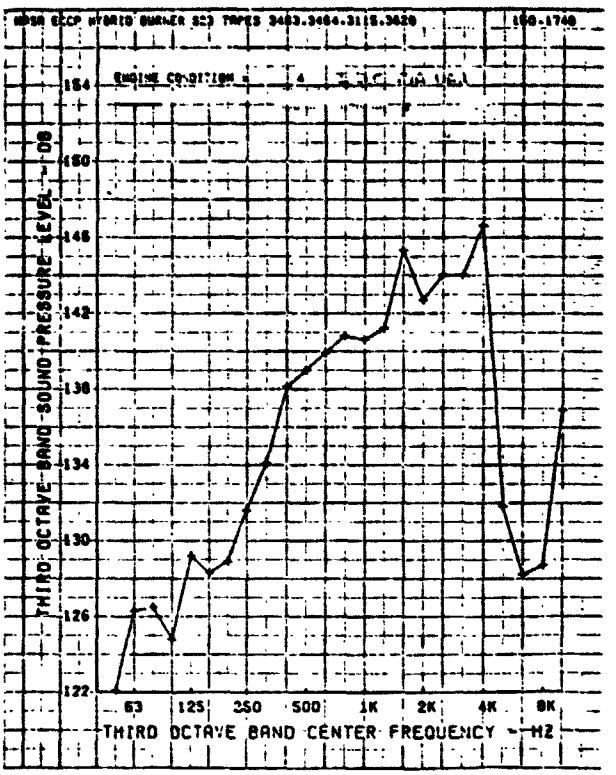
THIRD OCTAVE BAND SOUND PRESSURE LEVEL - DB
THIRD OCTAVE BAND CENTER FREQUENCY - HZ
63 125 250 500 1K 2K 4K 8K

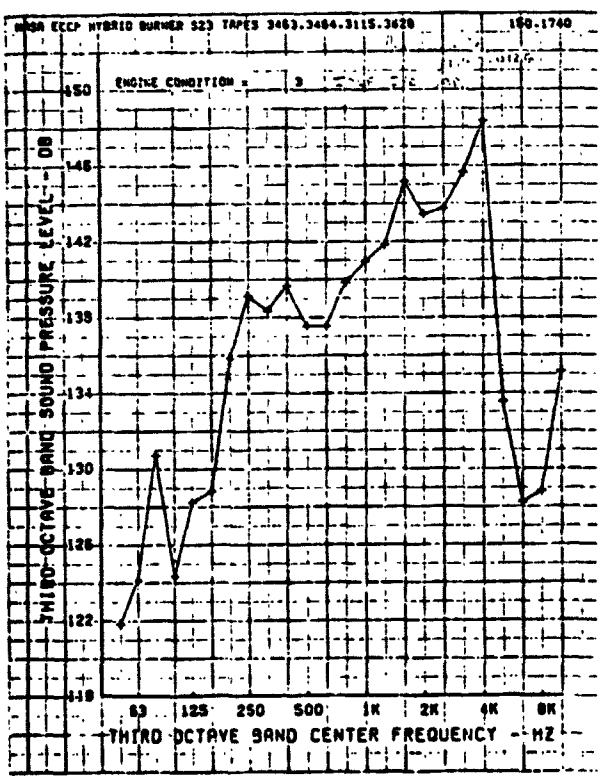
ENGINE CONDITION = 3
THIRD OCTAVE BAND SOUND PRESSURE LEVEL - DB
THIRD OCTAVE BAND CENTER FREQUENCY - HZ
63 125 250 500 1K 2K 4K 8K

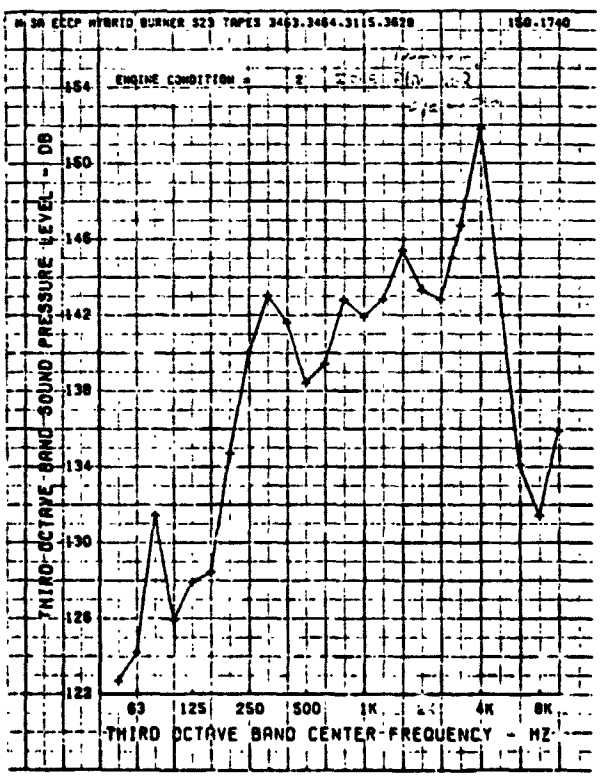
ENGINE CONDITION = 2
THIRD OCTAVE BAND SOUND PRESSURE LEVEL - DB
THIRD OCTAVE BAND CENTER FREQUENCY - HZ
63 125 250 500 1K 2K 4K 8K

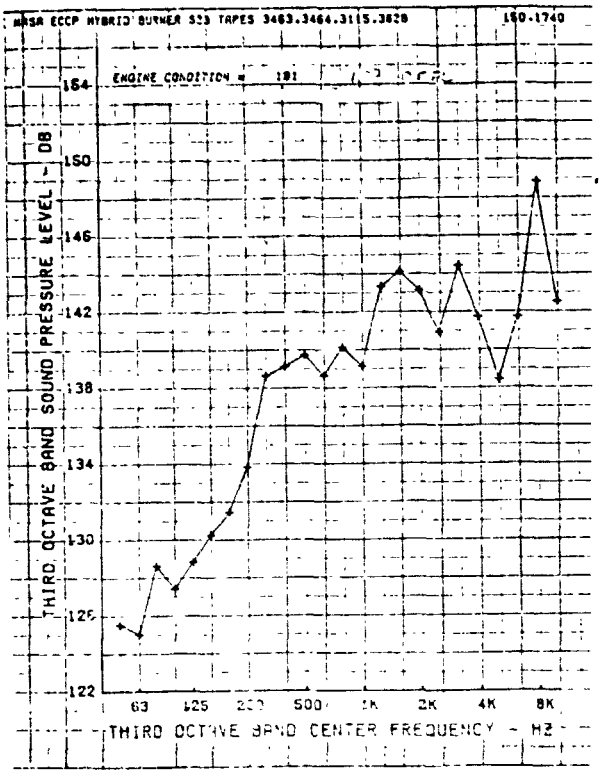
NASA ECCP HYBRID BURNER 523 TAPES 3463.3464.3115.3628
150.1740
ENGINE CONDITION = 181
THIRD OCTAVE BAND SOUND PRESSURE LEVEL - DB
154
150
146
142
138
134
130
126
122
63
125
250
500
1K
2K
4K
8K
THIRD OCTAVE BAND CENTER FREQUENCY - HZ

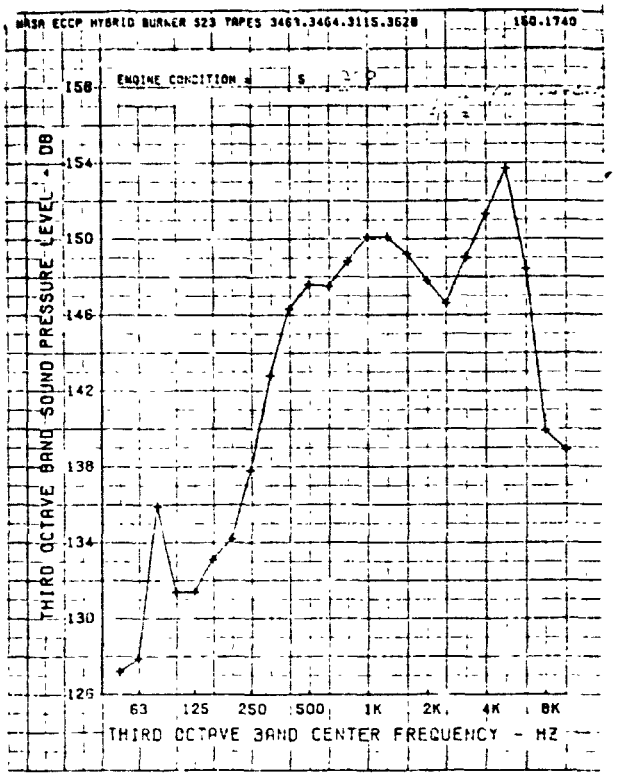
NASA ECCP HYBRID BURNER 523 TAPES 3463.3464.3115.3628
150.1740
ENGINE CONDITION = 5
THIRD OCTAVE BAND SOUND PRESSURE LEVEL - DB
158
154
150
146
142
138
134
130
126
63
125
250
500
1K
2K
4K
8K
THIRD OCTAVE BAND CENTER FREQUENCY - HZ

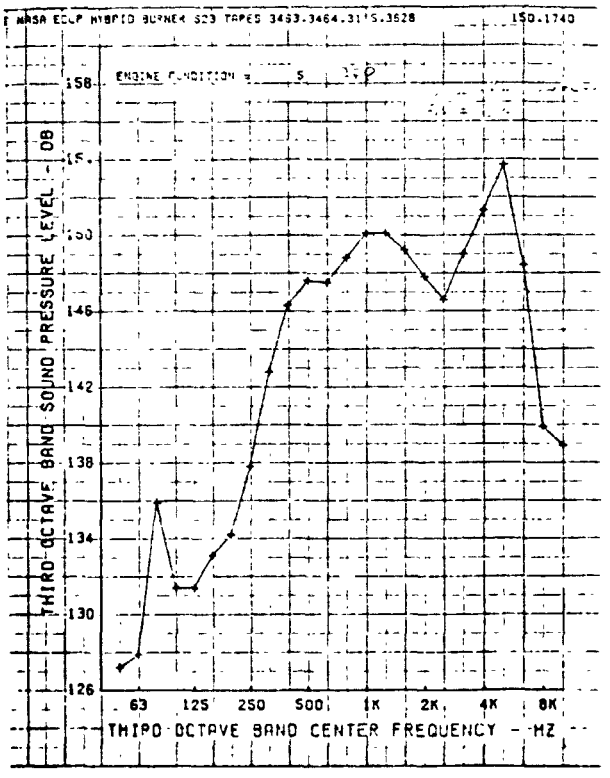
NASA ECCP HYBRID BURNER 523 TAPES 3463.3464.3115.3628
150.1740
ENGINE CONDITION = 5
THIRD OCTAVE BAND SOUND PRESSURE LEVEL - DB
158
154
150
146
142
138
134
130
126
63
125
250
500
1K
2K
4K
8K
THIRD OCTAVE BAND CENTER FREQUENCY - HZ

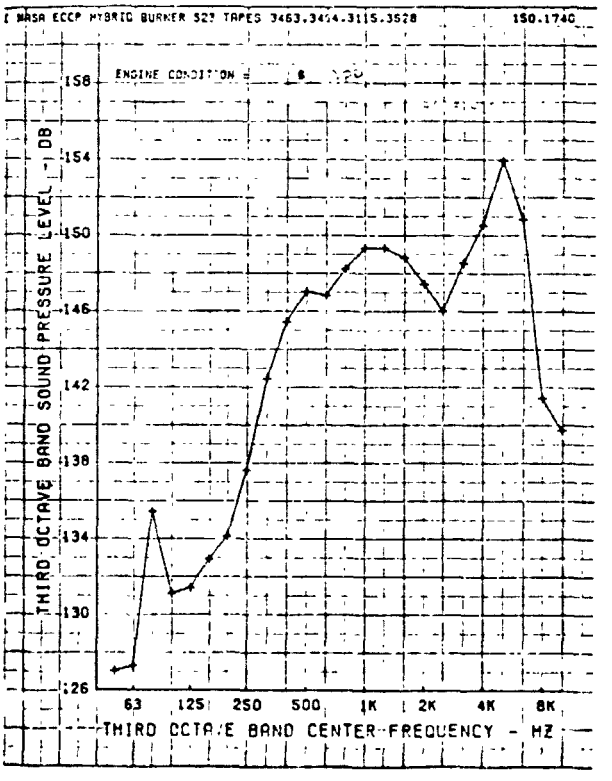
NASA ECCP HYBRID BURNER 523 TAPES 3463.3464.3115.3628
150.1740
ENGINE CONDITION = 6
THIRD OCTAVE BAND SOUND PRESSURE LEVEL - DB
158
154
150
146
142
138
134
130
126
63
125
250
500
1K
2K
4K
8K
THIRD OCTAVE BAND CENTER FREQUENCY - HZ

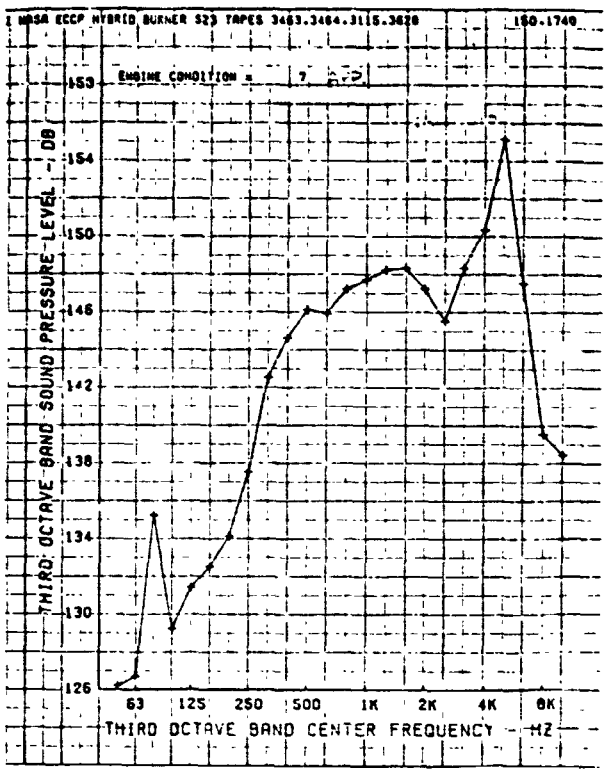
NASA ECCP HYBRID BURNER 523 TAPES 3463.3464.3115.3628
150-1740
ENGINE CONDITION = 7 APP
THIRD OCTAVE BAND SOUND PRESSURE LEVEL - DB
158
154
150
146
142
138
134
130
126
63 125 250 500 1K 2K 4K 8K
THIRD OCTAVE BAND CENTER FREQUENCY - HZ

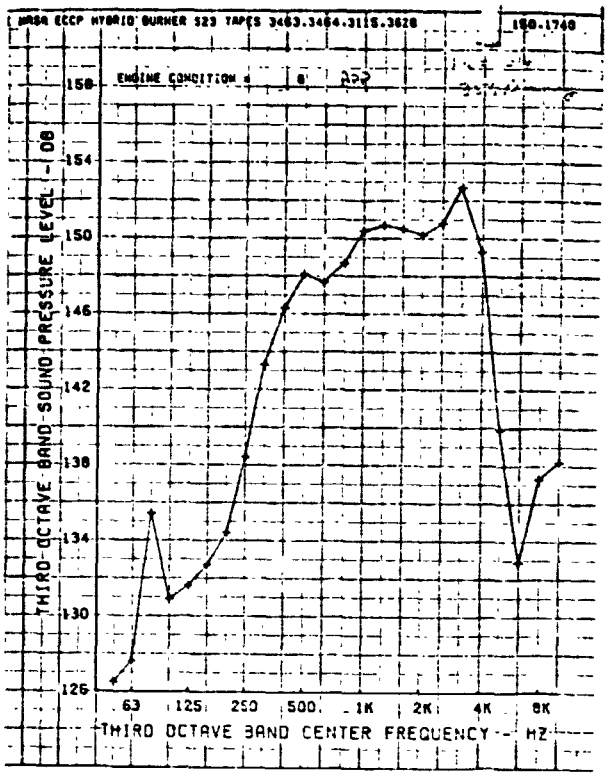
NASA ECCP HYBRID BURNER 523 TAPES 3463.3464.3115.3628
150-1740
ENGINE CONDITION = 8 APP
THIRD OCTAVE BAND SOUND PRESSURE LEVEL - DB
158
154
150
146
142
138
134
130
126
63 125 250 500 1K 2K 4K 8K
THIRD OCTAVE BAND CENTER FREQUENCY - HZ

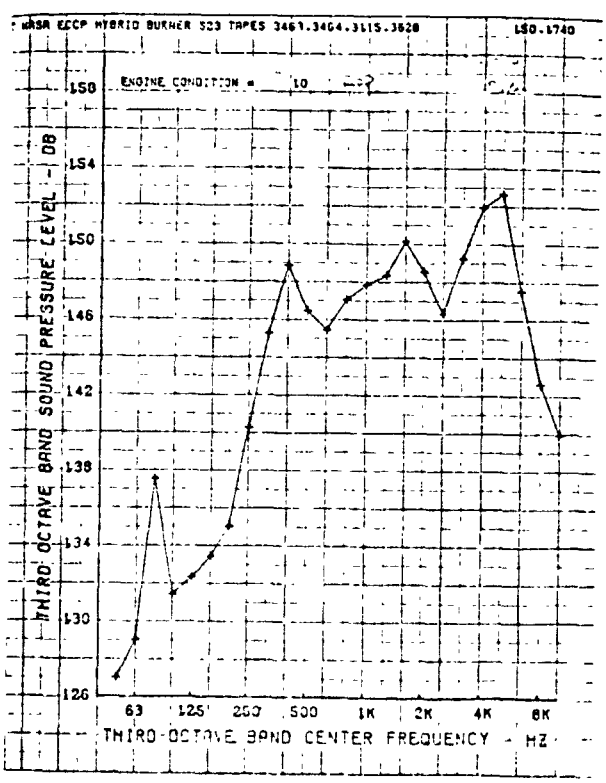
NASA ECCP HYBRID BURNER 523 TAPES 3463.3464.3115.3628
150-1740
ENGINE CONDITION = 10 APP
THIRD OCTAVE BAND SOUND PRESSURE LEVEL - DB
158
154
150
146
142
138
134
130
126
63 125 250 500 1K 2K 4K 8K
THIRD-OCTAVE BAND CENTER FREQUENCY - HZ

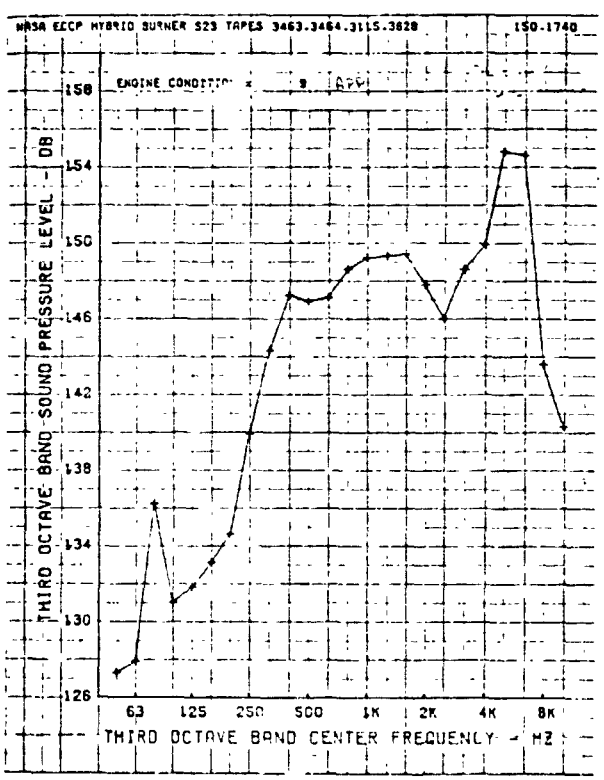
NASA ECCP HYBRID BURNER 523 TAPES 3463.3464.3115.3628
150-1740
ENGINE CONDITION = 9 APP
THIRD OCTAVE BAND SOUND PRESSURE LEVEL - DB
158
154
150
146
142
138
134
130
126
63 125 250 500 1K 2K 4K 8K
THIRD OCTAVE BAND CENTER FREQUENCY - HZ

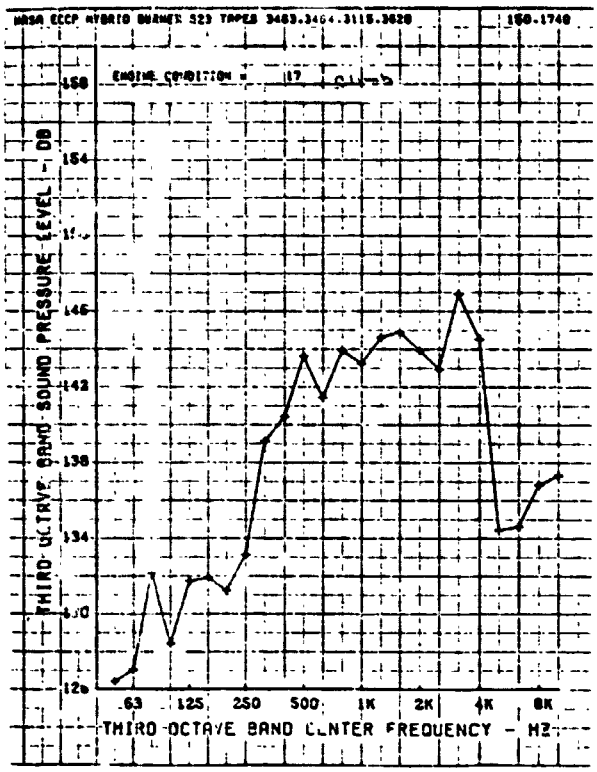

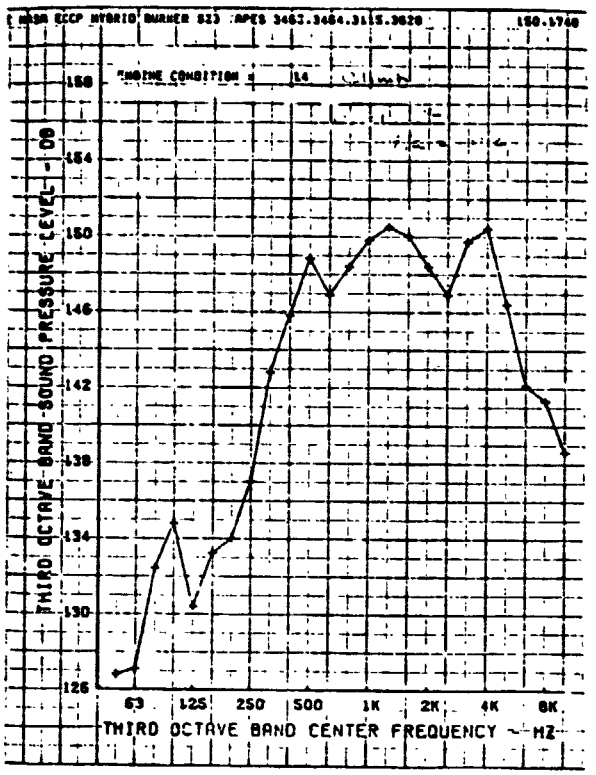

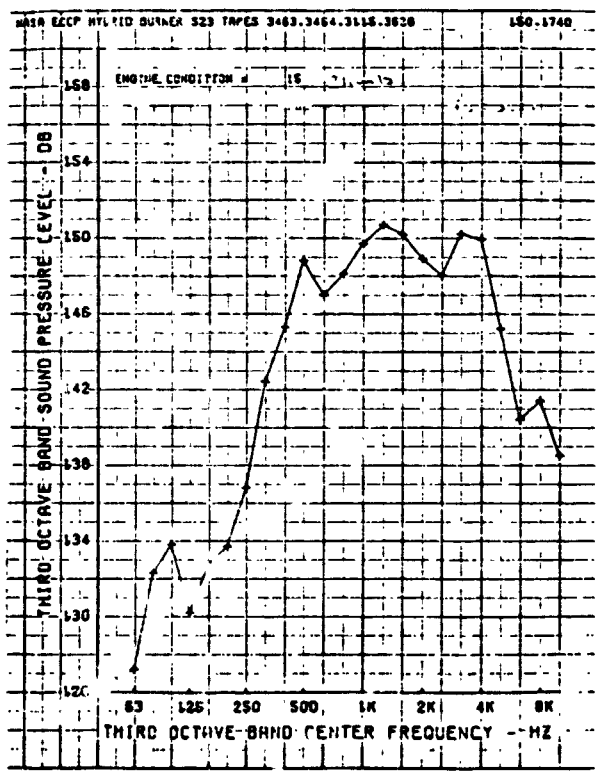

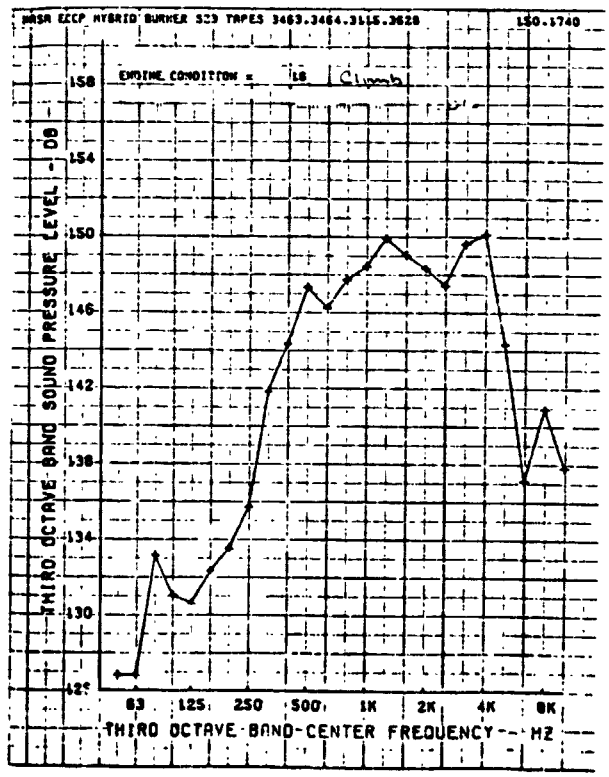

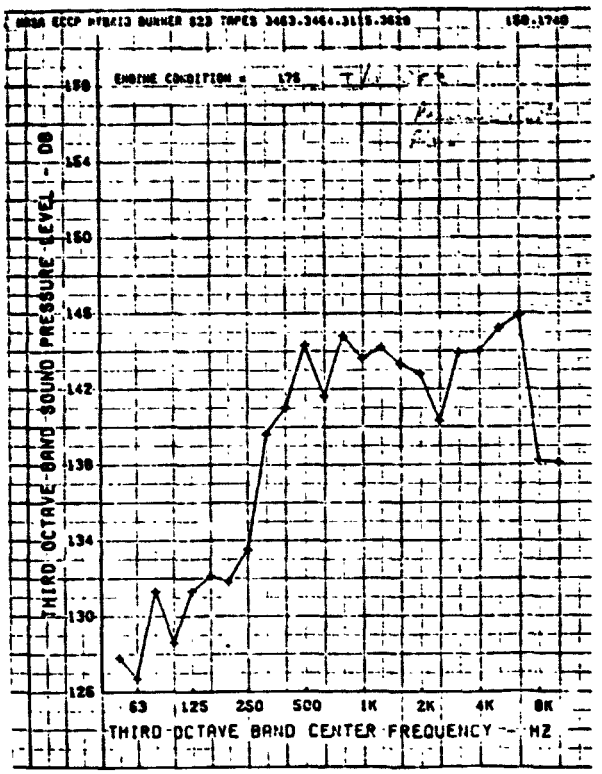
NASA ECCP HYBRID BURNER S23 TAPES 3463.3464.3115.3628
ENGINE CONDITION = 175
THIRD-OCTAVE-BAND SOUND PRESSURE LEVEL - DB
158
154
150
146
142
138
134
130
126
63
125
250
500
1K
2K
4K
8K
THIRD-OCTAVE BAND CENTER FREQUENCY - HZ

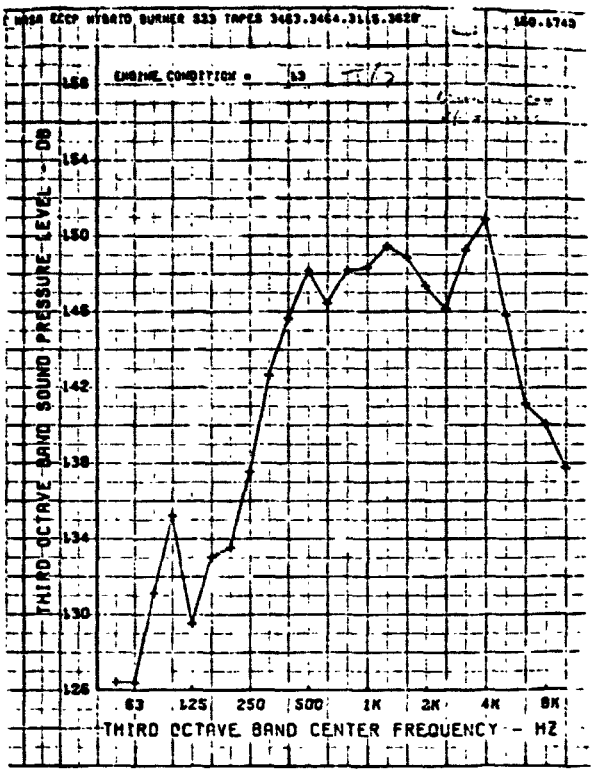
NASA ECCP HYBRID BURNER S23 TAPES 3463.3464.3115.3628
ENGINE CONDITION = 13
THIRD-OCTAVE-BAND SOUND PRESSURE LEVEL - DB
158
154
150
146
142
138
134
130
126
63
125
250
500
1K
2K
4K
8K
THIRD-OCTAVE BAND CENTER FREQUENCY - HZ

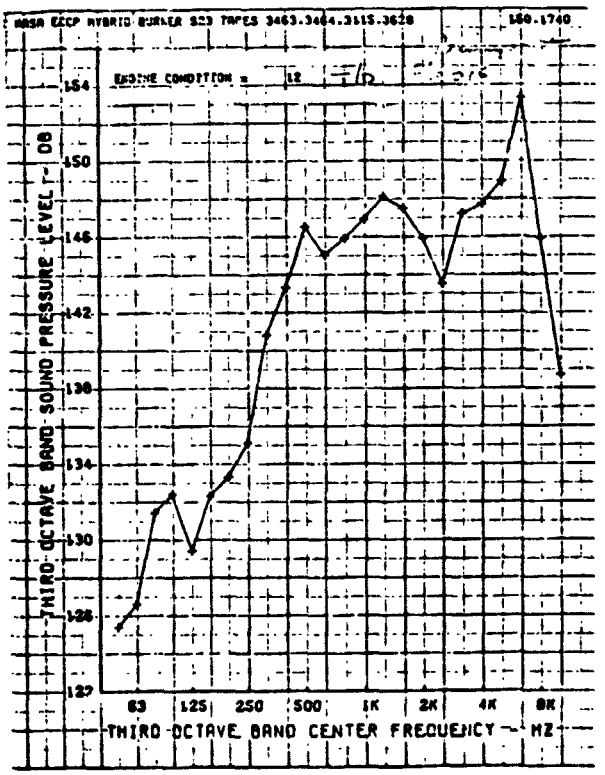
NASA ECCP HYBRID BURNER S23 TAPES 3463.3464.3115.3628
ENGINE CONDITION = 12
THIRD-OCTAVE-BAND SOUND PRESSURE LEVEL - DB
154
150
146
142
138
134
130
126
63
125
250
500
1K
2K
4K
8K
THIRD-OCTAVE BAND CENTER FREQUENCY - HZ

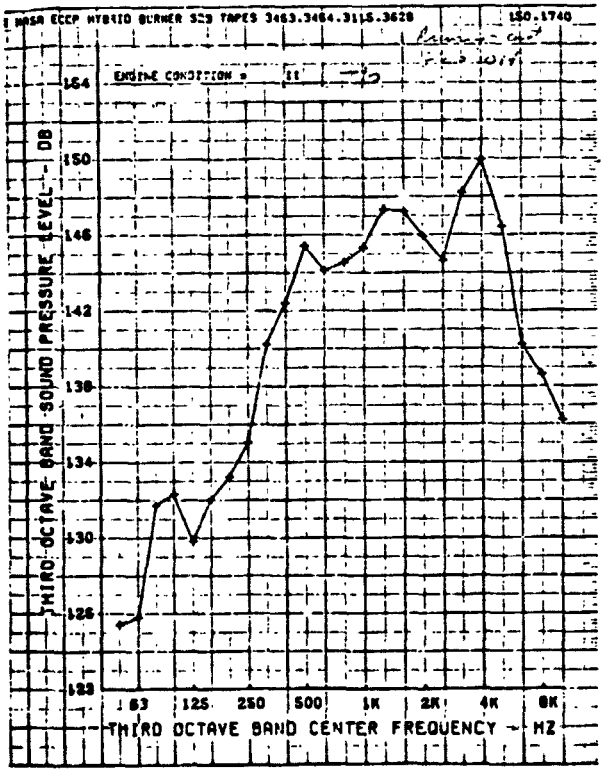
NASA ECCP HYBRID BURNER S23 TAPES 3463.3464.3115.3628
ENGINE CONDITION = 11
THIRD-OCTAVE-BAND SOUND PRESSURE LEVEL - DB
154
150
146
142
138
134
130
126
63
125
250
500
1K
2K
4K
8K
THIRD-OCTAVE BAND CENTER FREQUENCY - HZ

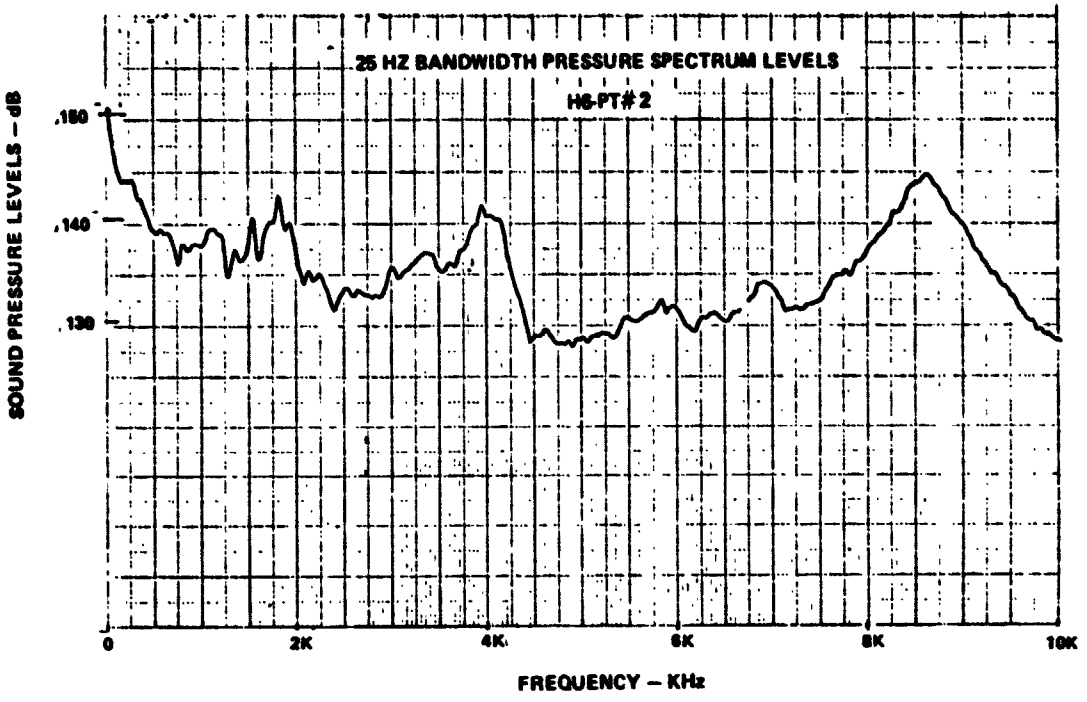
25 HZ BANDWIDTH PRESSURE SPECTRUM LEVELS
HS-PT# 2
SOUND PRESSURE LEVELS – dB
,150
,140
,130
0
2K
4K
6K
8K
10K
FREQUENCY – KHz

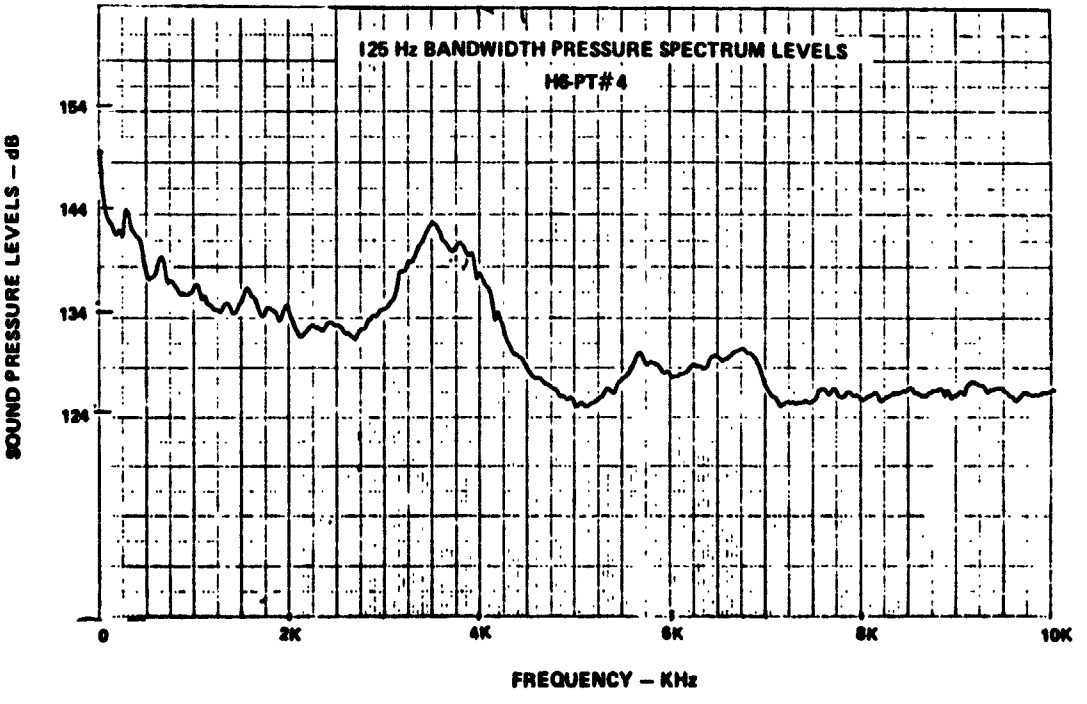
125 Hz BANDWIDTH PRESSURE SPECTRUM LEVELS
HS-PT# 4
SOUND PRESSURE LEVELS – dB
154
144
134
124
0
2K
4K
6K
8K
10K
FREQUENCY – KHz

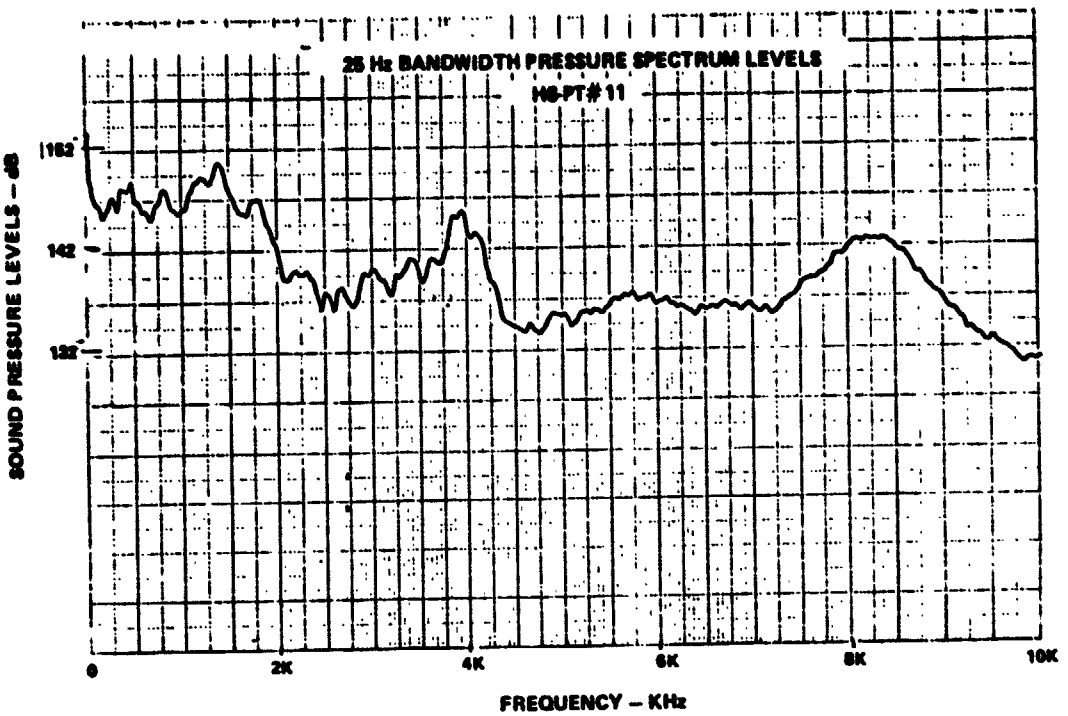
25 Hz BANDWIDTH PRESSURE SPECTRUM LEVELS
H6-PT# 11
SOUND PRESSURE LEVELS – dB
162
142
122
0
2K
4K
6K
8K
10K
FREQUENCY – KHz

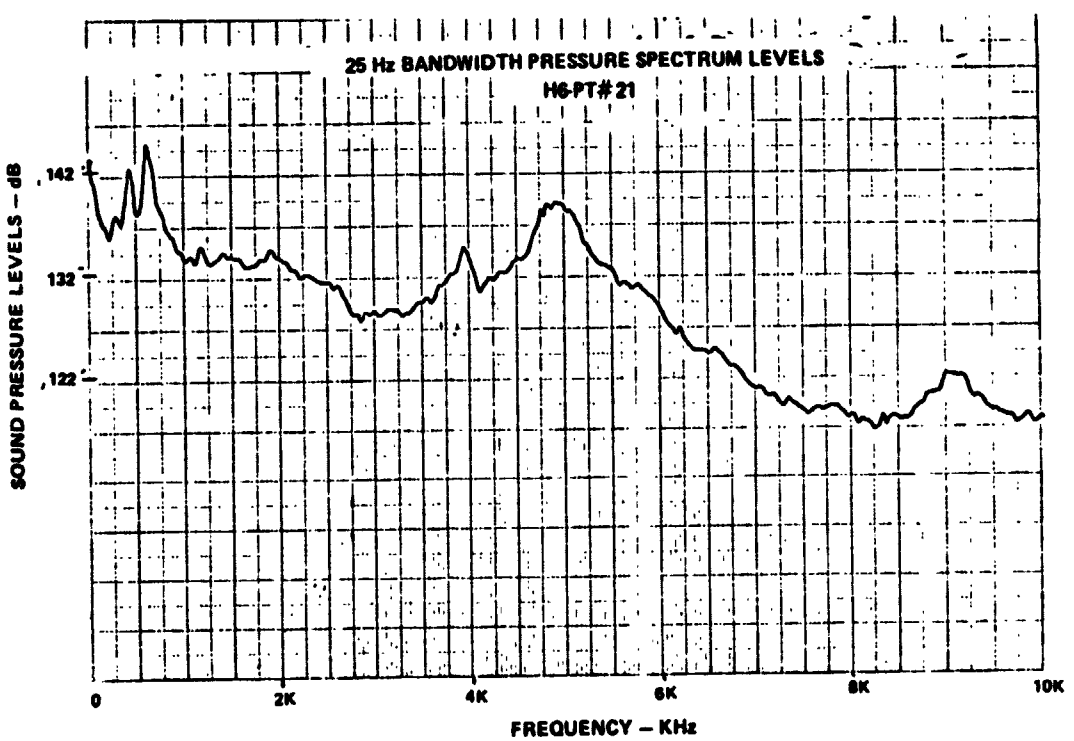
25 Hz BANDWIDTH PRESSURE SPECTRUM LEVELS
H6-PT# 21
SOUND PRESSURE LEVELS – dB
142
132
122
0
2K
4K
6K
8K
10K
FREQUENCY – KHz

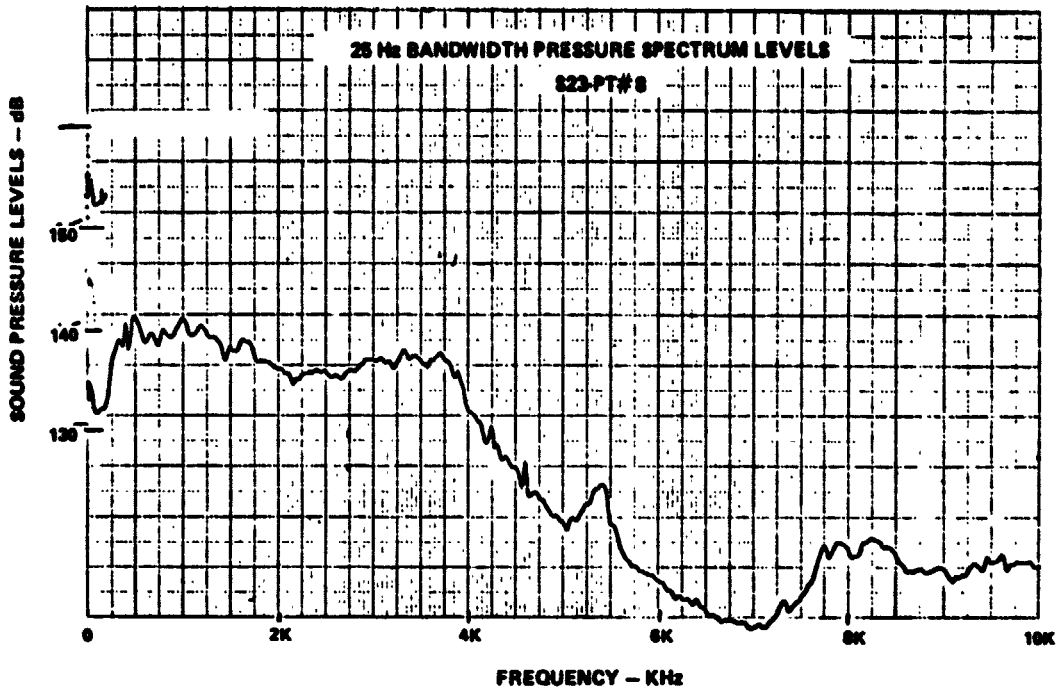
25 Hz BANDWIDTH PRESSURE SPECTRUM LEVELS
S23-PT# 8
SOUND PRESSURE LEVELS – dB
160
140
120
0
2K
4K
6K
8K
10K
FREQUENCY – KHz

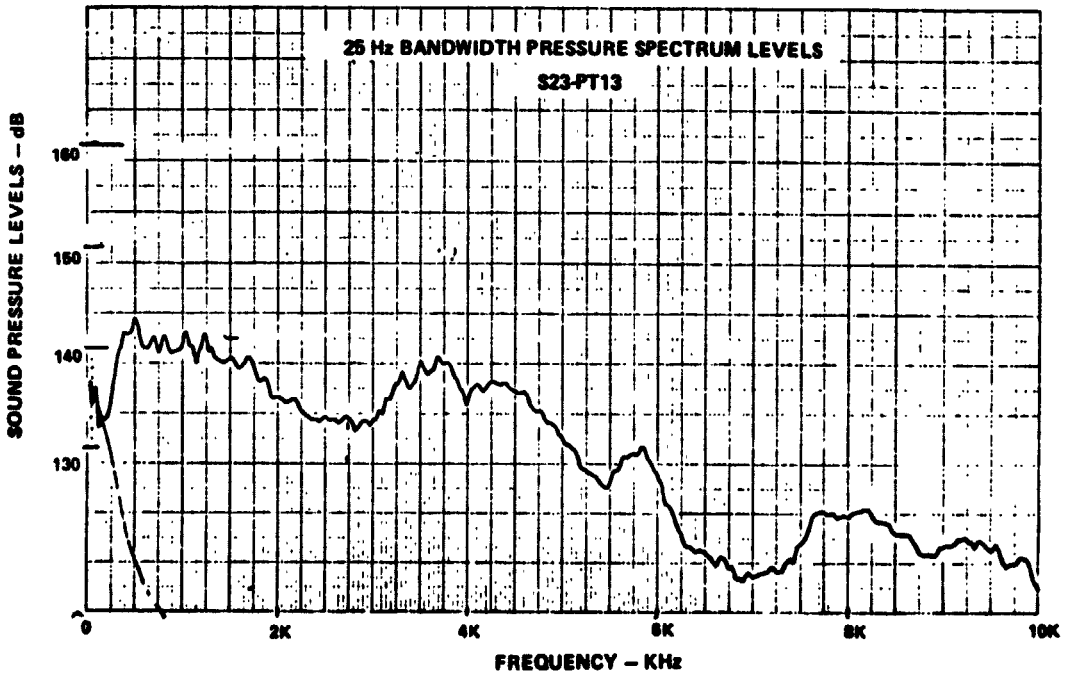
25 Hz BANDWIDTH PRESSURE SPECTRUM LEVELS
S23-PT13
SOUND PRESSURE LEVELS – dB
160
150
140
130
0
2K
4K
6K
8K
10K
FREQUENCY – KHz

APPENDIX A-4

SAMPLE CORRECTED SPECTRA

Curves are presented here showing recorded pressure spectra, corresponding cold flow spectra, and the resulting corrected spectra used in calculating corrected acoustic powerlevels, PWL_{cor}. The method of correction is described in the main text section, Results and Discussion – Pressure Information – Method of Analysis.

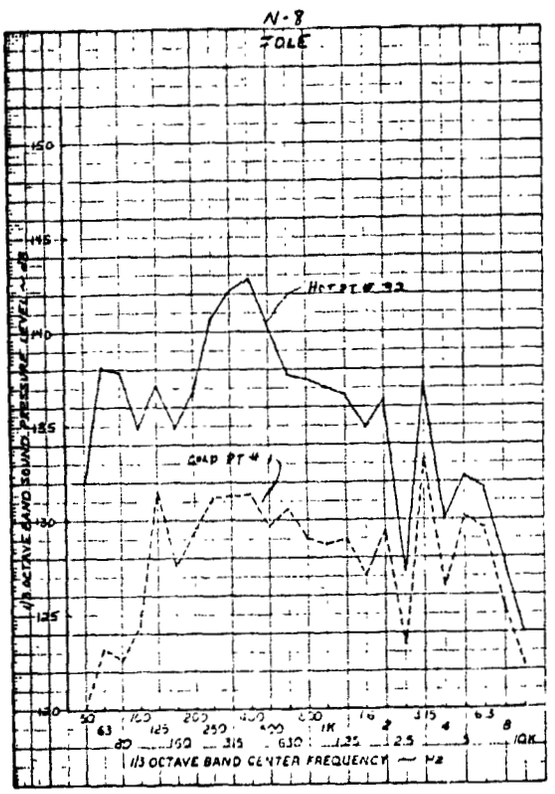

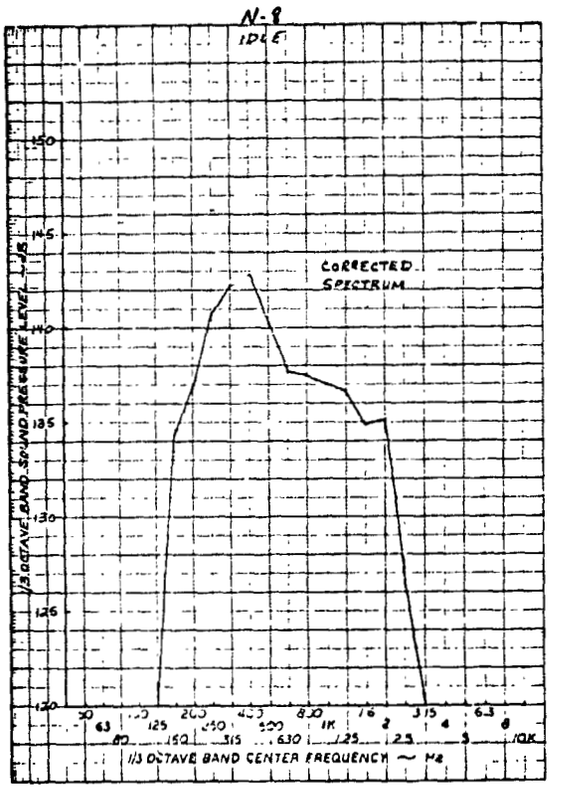

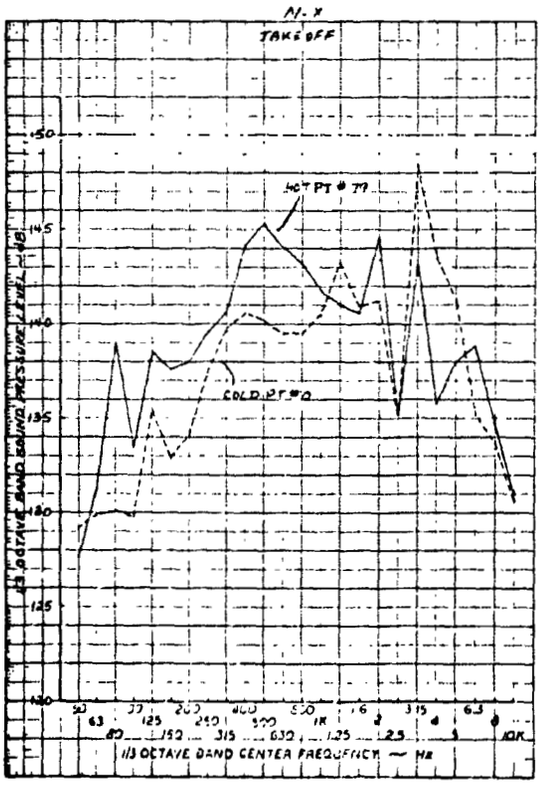

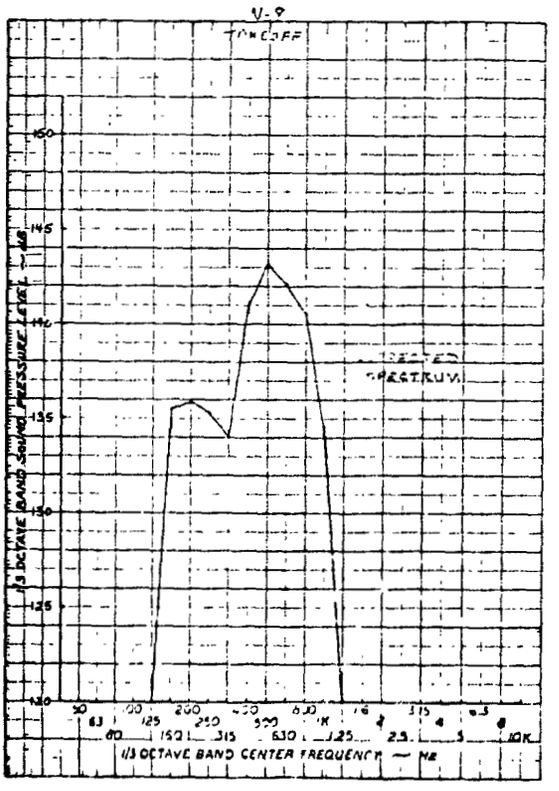

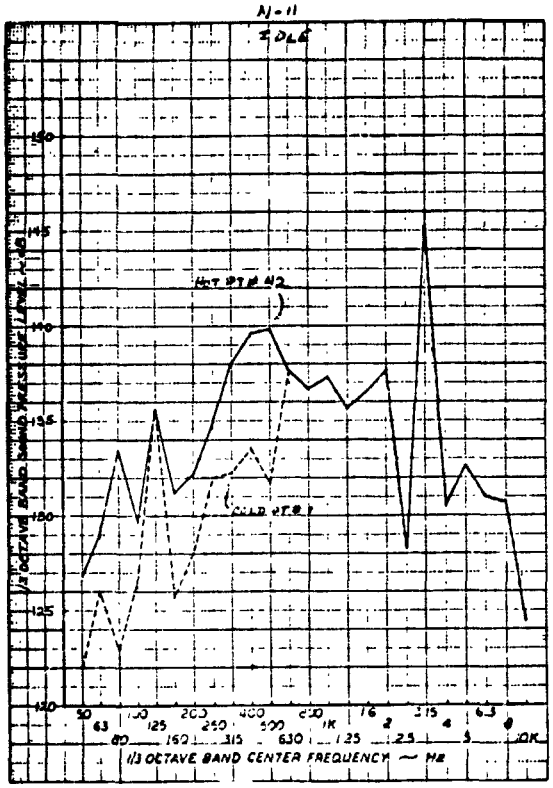
N-11
IDLE
HOT PT # 2
COLD PT # 1
1/3 OCTAVE BAND SOUND PRESSURE LEVEL — dB
1/3 OCTAVE BAND CENTER FREQUENCY — Hz

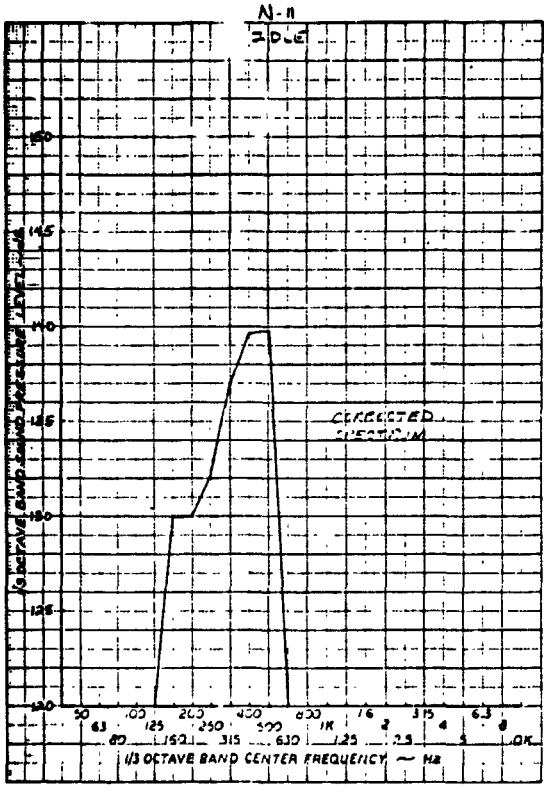
N-11
IDLE
CORRECTED SPECTRUM
1/3 OCTAVE BAND SOUND PRESSURE LEVEL — dB
1/3 OCTAVE BAND CENTER FREQUENCY — Hz


N-11
TAKEOFF
1/3 OCTAVE BAND SOUND PRESSURE LEVEL — dB
1/3 OCTAVE BAND CENTER FREQUENCY — Hz

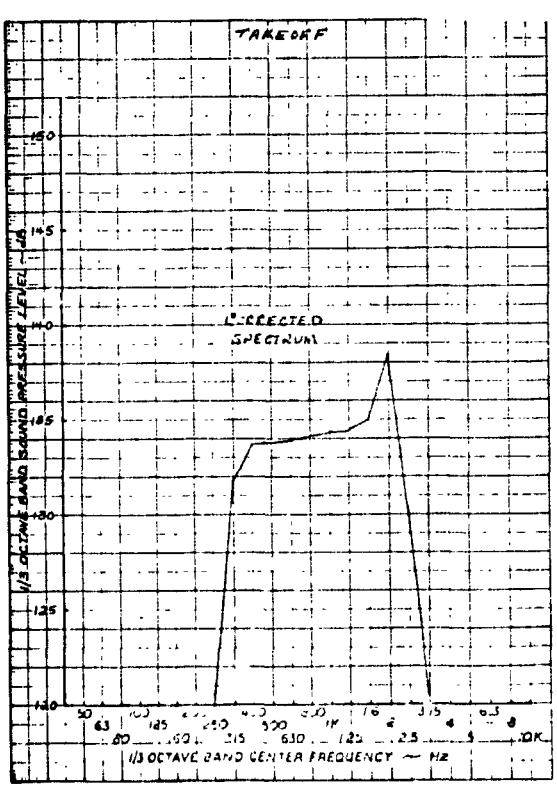
TAKEOFF
CORRECTED SPECTRUM
1/3 OCTAVE BAND SOUND PRESSURE LEVEL — dB
1/3 OCTAVE BAND CENTER FREQUENCY — Hz

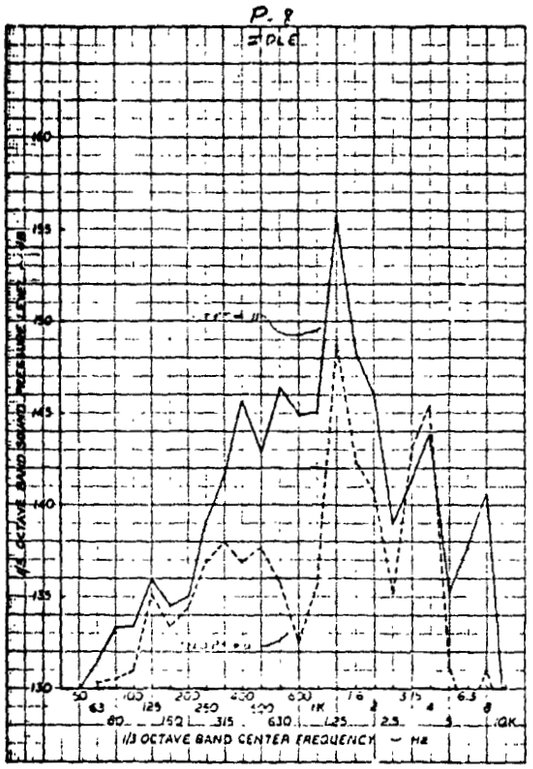
P. 8
IDLE
1/3 OCTAVE BAND SOUND PRESSURE LEVEL ~ dB re 0.0002 μbar
1/3 OCTAVE BAND CENTER FREQUENCY ~ Hz

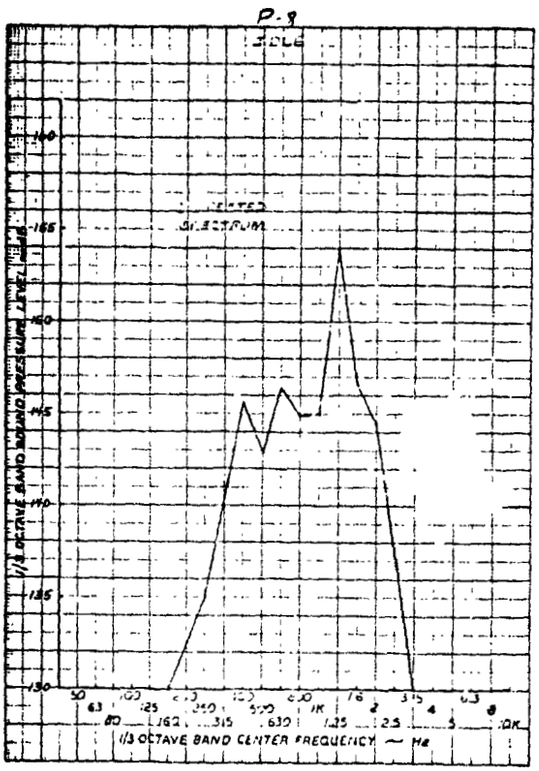
P. 8
IDLE
CORRECTED SPECTRUM
1/3 OCTAVE BAND SOUND PRESSURE LEVEL ~ dB re 0.0002 μbar
1/3 OCTAVE BAND CENTER FREQUENCY ~ Hz

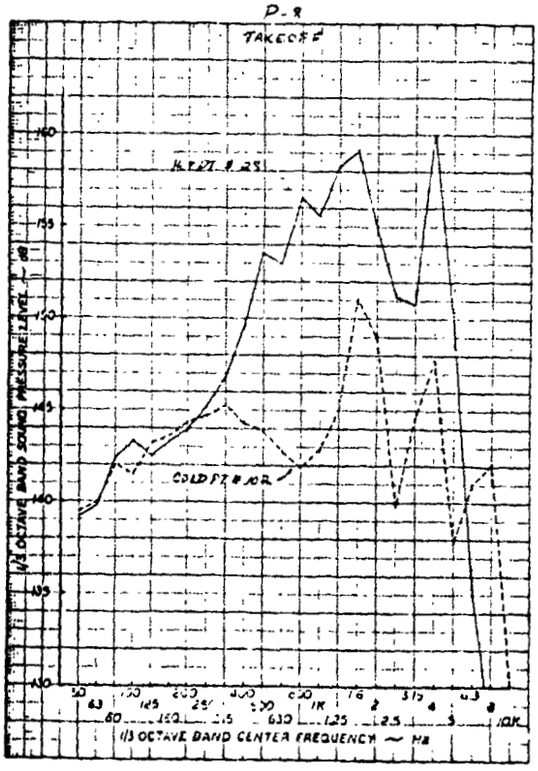
P. 8
TAKEOFF
1/3 OCTAVE BAND SOUND PRESSURE LEVEL ~ dB re 0.0002 μbar
1/3 OCTAVE BAND CENTER FREQUENCY ~ Hz

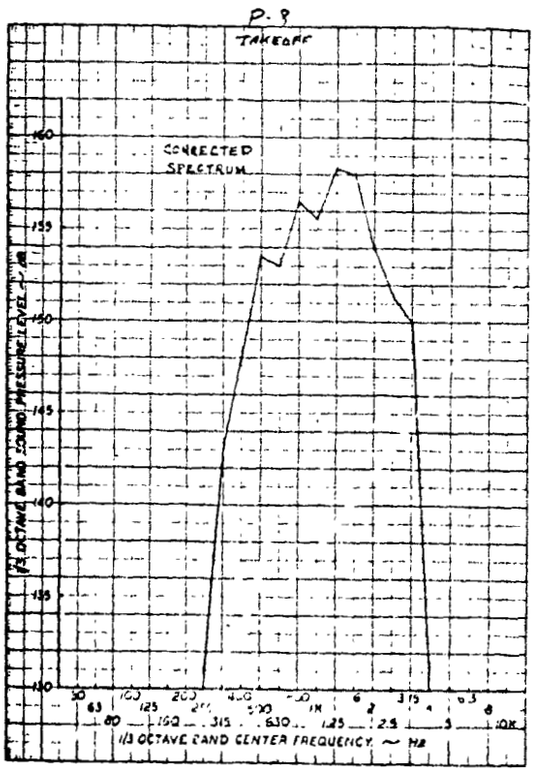
P. 8
TAKEOFF
CORRECTED SPECTRUM
1/3 OCTAVE BAND SOUND PRESSURE LEVEL ~ dB re 0.0002 μbar
1/3 OCTAVE BAND CENTER FREQUENCY ~ Hz

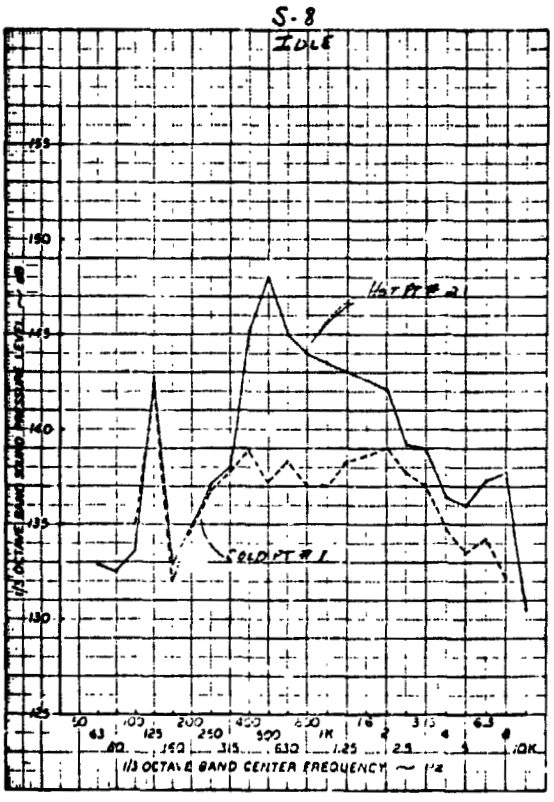
S-8
IDLE
HOT PT # 2
COLD PT # 1
1/3 OCTAVE BAND SOUND PRESSURE LEVEL ~ dB
1/3 OCTAVE BAND CENTER FREQUENCY ~ Hz

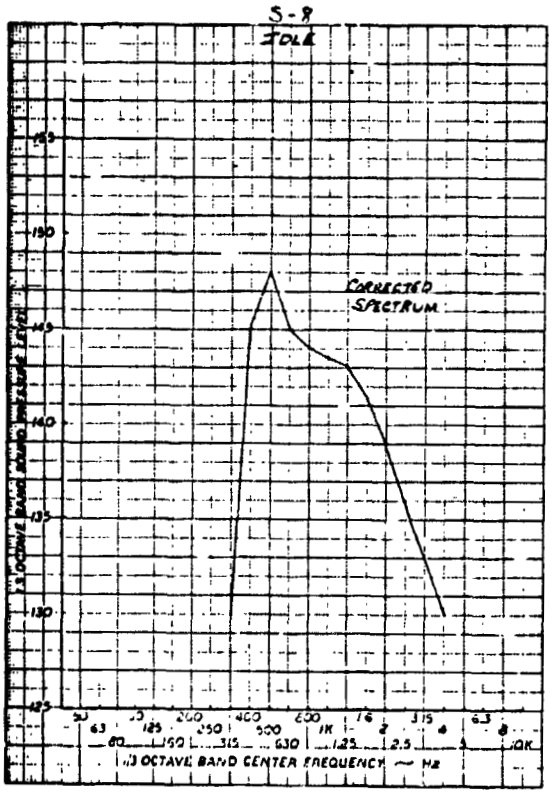
S-8
IDLE
CORRECTED SPECTRUM
1/3 OCTAVE BAND SOUND PRESSURE LEVEL ~ dB
1/3 OCTAVE BAND CENTER FREQUENCY ~ Hz

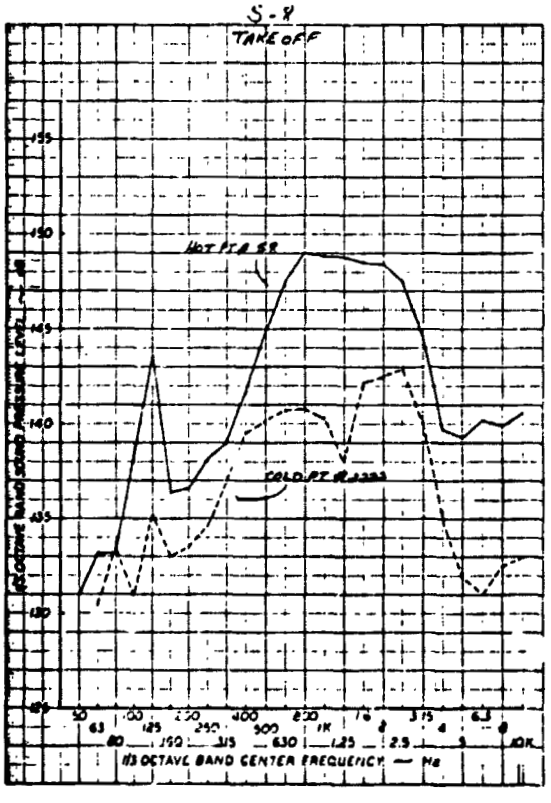
S-8
TAKE OFF
HOT PT # 88
COLD PT # 3333
1/3 OCTAVE BAND SOUND PRESSURE LEVEL ~ dB
1/3 OCTAVE BAND CENTER FREQUENCY ~ Hz

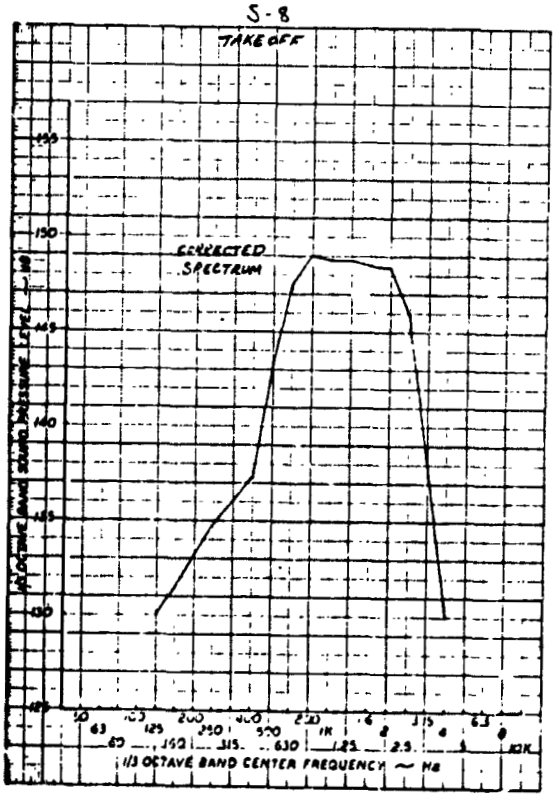
S-8
TAKE OFF
CORRECTED SPECTRUM
1/3 OCTAVE BAND SOUND PRESSURE LEVEL ~ dB
1/3 OCTAVE BAND CENTER FREQUENCY ~ Hz

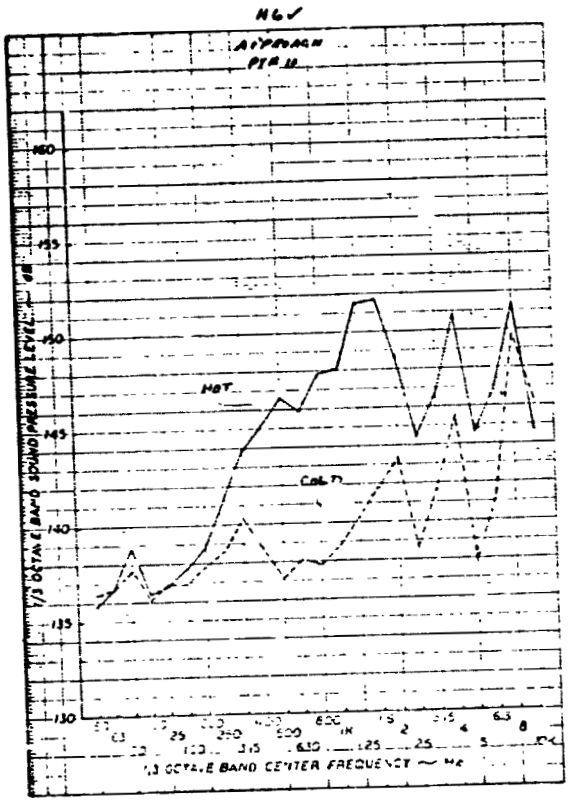

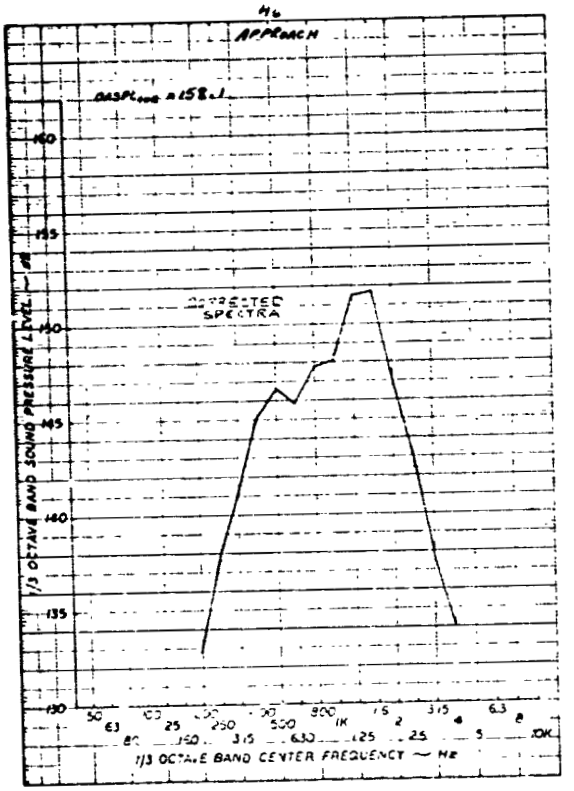

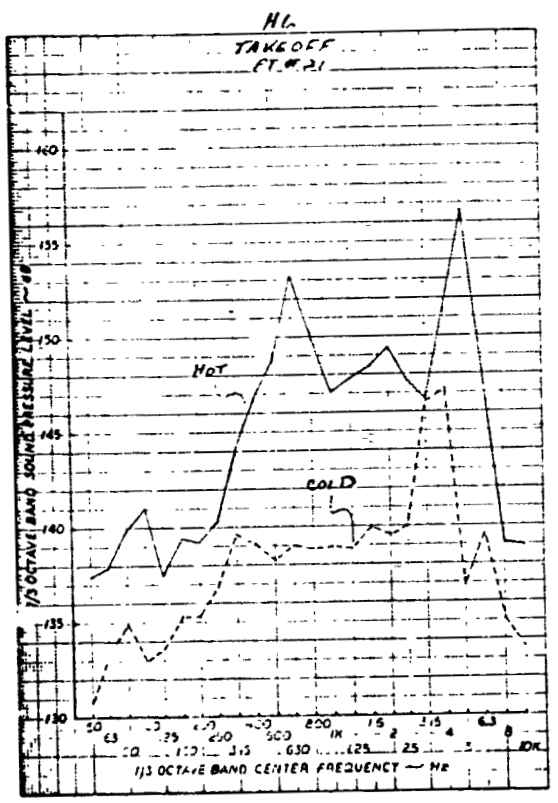

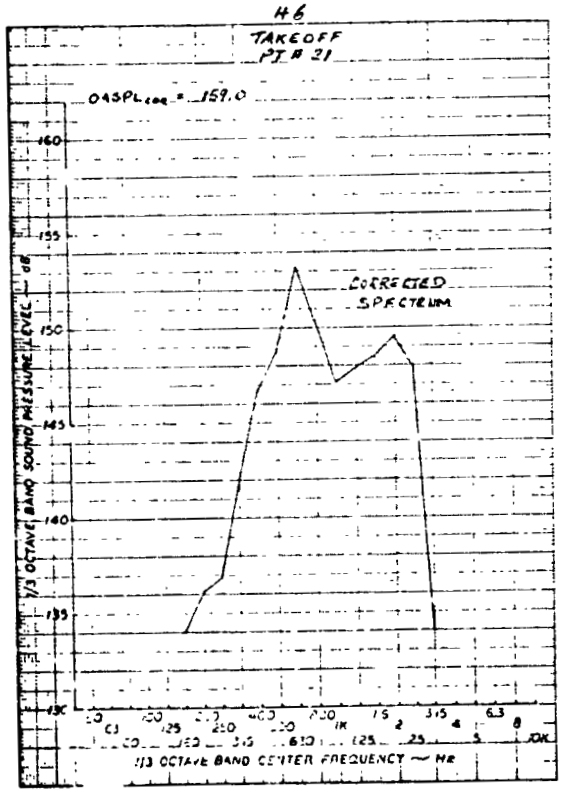


S23
FLYOVER
HOT PT # 8
COLD PT # 121
1/3 OCTAVE BAND SOUND PRESSURE LEVEL — dB
1/3 OCTAVE BAND CENTER FREQUENCY — Hz

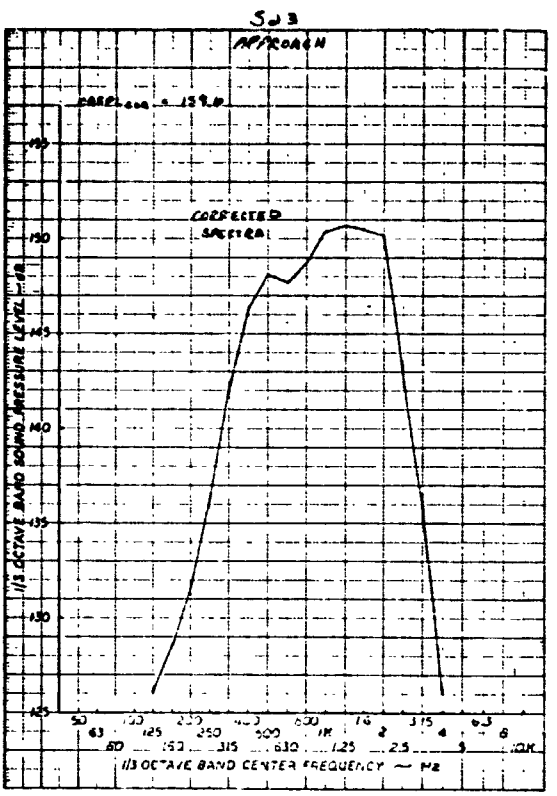
S23
APPROACH
CORRECTED SPECTRA
1/3 OCTAVE BAND SOUND PRESSURE LEVEL — dB
1/3 OCTAVE BAND CENTER FREQUENCY — Hz

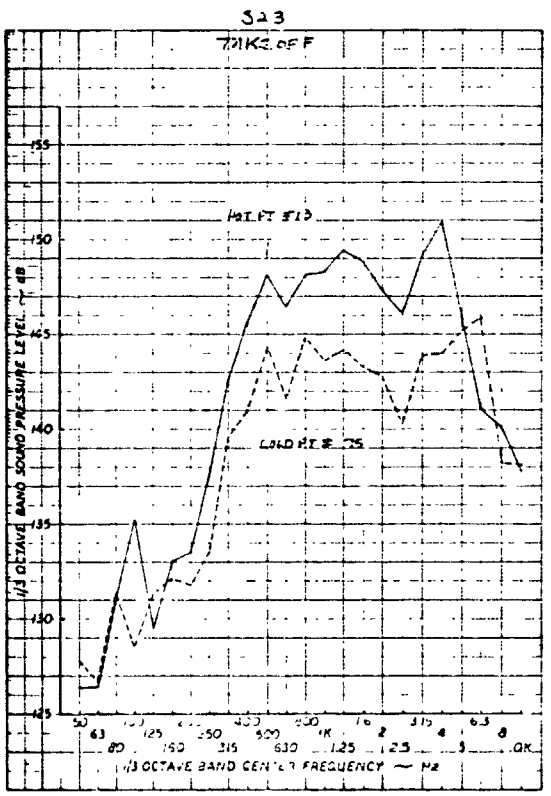
S23
TAKEOFF
HOT PT # 13
COLD PT # 25
1/3 OCTAVE BAND SOUND PRESSURE LEVEL — dB
1/3 OCTAVE BAND CENTER FREQUENCY — Hz

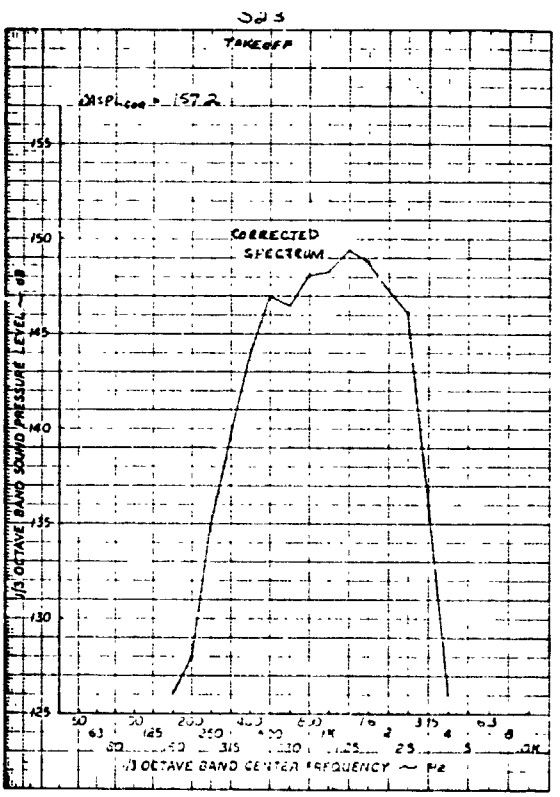
S23
TAKEOFF
CORRECTED SPECTRUM
1/3 OCTAVE BAND SOUND PRESSURE LEVEL — dB
1/3 OCTAVE BAND CENTER FREQUENCY — Hz

APPENDIX B-1

INDIRECT COMBUSTION NOISE THEORY

The following material which concerns the analysis of indirect combustion noise is the basis of the computer program used in the ECCP noise program. This material is an edited version of the paper, "Turbine Noise Due to Turbulence and Temperature Fluctuations", by G. F. Pickett, P&WA Acoustics Group (Reference 7). The paper was presented at the Eighth International Congress on Acoustics, London, England, 23-31 July 1974.

TURBINE NOISE DUE TO TURBULENCE AND TEMPERATURE FLUCTUATIONS

Abstract

In addition to turbomachinery noise generated due to high speed unsteady flows interacting with blades and vanes, significant low frequency noise can be generated by the passage of velocity and temperature "eddies" through large pressure gradients such as exist across turbine blade and vane rows. This noise generating mechanism may contribute to core engine noise observed from high bypass ratio turbofan engines.

An analysis is presented that determines upstream and downstream radiated noise generated by vorticity (turbulence) and entropy (temperature) waves interacting with a blade row simulated by an actuator disc. Radiated noise intensity is found to depend on the change in pressure across the rotor, and the intensity and transverse correlation length scales of the temperature and axial velocity fluctuations. Axial correlation length scales together with the axial convection velocity determine the frequency of noise generated.

Introduction

As fan noise from high bypass ratio turbofan engines is progressively reduced with increased inlet and aft duct treatment, and as jet noise is minimized by appropriate choice of engine cycle and bypass ratio, low frequency core engine noise and high frequency turbine noise become important sources of engine noise. There is now substantial evidence (1, 2) showing that noise from low velocity jets cannot be accounted for by jet noise alone, and that there exist sources of noise upstream of the jet nozzle which contribute significant levels of noise at frequencies generally similar to those produced by jet noise.

Various mechanisms for low frequency core engine noise have been proposed, but, as yet, no definitive tests have been conducted that directly relate core engine noise to one specific dominating mechanism. Following the example of fan noise, it is reasonable to suspect that unsteady flow velocities interacting with blades, vanes, struts and nozzle exit are significant contributors to the overall noise. An additional mechanism exists, however, that involves the large fluctuations in temperature and axial velocity generated in the burner passing through the very large changes in pressure and swirl velocity across successive turbine stages. Physically, acoustic pressure waves and vorticity waves can be generated by this mechanism because axial velocity fluctuations and variations of density due to temperature fluctuations convecting with the fluid, experience abrupt changes as these fluctuations pass through large pressure gradients such as exist across turbine blade rows.

In this paper, an analysis is presented that involves the solution of the three-dimensional linearized equations of continuity, momentum, energy, state and second law of thermodynamics. These equations are solved in conjunction with the satisfaction of appropriate steady and unsteady jump conditions across a vane or blade row that is modeled as an actuator disc.

The general analysis includes noise generation due to fluctuating lift and drag forces at the disc in addition to the noise generated by fluctuating temperatures and velocities convecting through the disc.

Total noise estimates from all the blade rows of the turbine that contribute significantly are calculated by assuming that no coupling exists between the blade and vane rows. Under certain conditions Cumpsty and Marble (3) found that the coupling could be important and the present model will need to be extended to include this effect. An additional effect that could significantly change the frequency distribution and sound power levels from any core engine noise mechanism is the duct exit impedance. This impedance has been shown (4,5) to be large for low frequencies and to change with flow speed through the duct exit. The effect of the detailed flow at the tailpipe lip on the impedance has not, to the author's knowledge, been considered in any analysis, but it probably does change the impedance at the duct exit. If this latter effect is significant, it should be expected that factors such as forward speed, fan duct geometry and split or common flow nozzle, will affect levels of core engine noise.

ANALYSIS

Analytical Model

The method considers small unsteady perturbations of the mean flow through an "actuator disc" blade or vane row that represents either a turbine rotor or nozzle guide vane stage. The analysis also accounts for the large changes in mean stream flow variables that are not only an inherent design feature of turbine stages, but also a key factor in the noise generating mechanism considered in this paper.

Consider a cascade as shown in Figure 1, where the turbulent velocity superimposed on the mainstream flow $\underline{U}_1(\underline{x}, t)$ entering the cascade is $\underline{u}_{c_1}(\underline{x}, t)$ and where temperature fluctuations $\theta_{c_1}(\underline{x}, t)$ convecting with the mean stream are superimposed on the upstream ambient temperature θ_{0_1}. In the Appendix it is shown how these perturbations convecting through an actuator disc representation of the cascade, together with fluctuating lift and drag forces at the cascade give rise to acoustic waves. Neglecting the noise due to unsteady lift and drag at the cascade, which has been considered in a separate paper (6), the expression for upstream and downstream acoustic pressure waves due only to temperature and axial velocity fluctuations traversing the cascade reduces to:

$$p_{p_i}(\omega, k_y, k_z) = \frac{A_{2i}\,\Delta P}{\Delta A}\,\theta_{c_1}(\omega, k_y, k_z) + \left[\frac{A_{2i}\,\overline{\rho_0}\,(U_1^2 - U_2^2)}{U_1}\right.$$

$$\left. A_{1i}\left\{\frac{\overline{\rho_0 U}\,k_x^{(c)}}{\rho_{0_2}}\,\Delta\rho_0 + \rho_{0_1}\,k_y\,\Delta V\right\}\right]\frac{u_{c_1}(\omega, k_y, k_z)}{\Delta A}\,, \qquad (1)$$

where i = 1 and 2 represent upstream and downstream respectively and where the acoustic waves and the temperature and inflow turbulence are related in frequency and wave number space. The values A_{ij} (i, j = 1 2) and ΔA are written out in full in the Supplement of this Appendix and other terms are as described in the Notation.

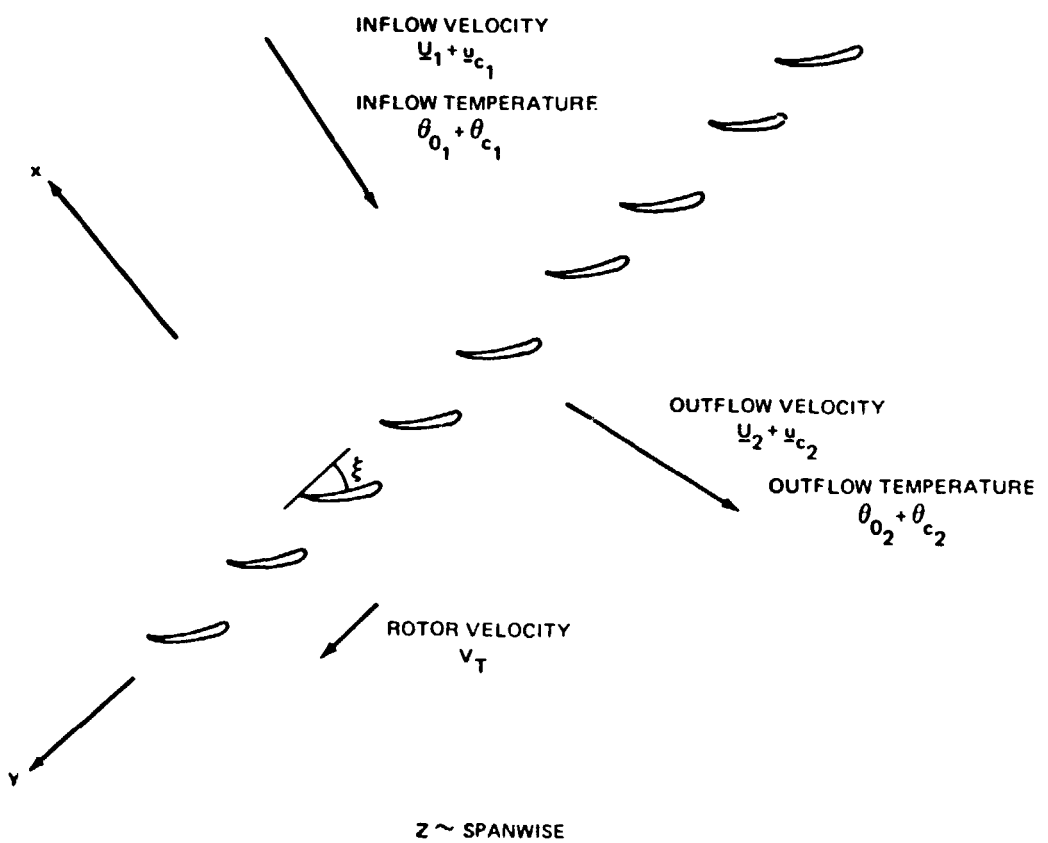

Figure 1 *Cascade Representation of Turbine Blade or Vane Row*

The upstream and downstream acoustic pressure spectra can be calculated from equation (1) by forming the product of the acoustic pressure wave in frequency/wave number space with its appropriate complex conjugate $p^*(\omega, k_y, k_z)$. The resulting spectra will be seen to depend not only on the spectra of the inflowing temperature $|\theta_{c_1}(\omega, k_y, k_z)|^2$ and axial velocity fluctuations $|u_{c_1}(\omega, k_y, k_z)|^2$, but also on terms coupling these fluctuations, $\theta_c u^*_{c_1}$ and $\theta^*_c u_{c_1}$. Once the pressure spectra are known, the upstream and downstream acoustic intensity radiating per unit area can be calculated from equations (A30) and (A31) in the Appendix by summing over those wave numbers which give rise to propagating acoustic modes.

From the form of equation (1), it can be seen that noise is generated by temperature fluctuations only when there is a non zero pressure change across the actuator disc and by axial velocity fluctuations when there are non zero changes in either density, mean swirl velocity or mean axial velocity across the disc. In order to derive the complete noise field due to these mechanisms, the fluctuating axial velocity and temperature spectra in frequency/wave number space and the cross spectra between axial velocity and temperature fluctuations are required. Because of the difficulty involved in providing appropriate inputs, only the noise due to convecting temperature fluctuations traversing the actuator disc will be considered in this paper. Although the noise due to other terms may not be negligible, they would exhibit results having properties similar to those that will be brought out by considering only the noise due to convecting temperature fluctuations. In most cases, this mechanism probably dominates that due to axial velocity fluctuations because, in general, turbine stages are designed with very large pressure drops and changes in mean swirl velocity, but only relatively small density and mean axial velocity changes which make the first two terms in the square bracket of equation (1) small. The term containing the large swirl velocity term, however, is multiplied by the circumferential wave number k_y. Since the mechanism being considered is essentially a low frequency noise generator, only the plane wave mode (i.e., $k_y = 0$) propagates over the lower end of the frequency range of interest in low frequency core noise. In this range, no contribution can be made by the term involving large swirl velocity changes.

Considering, therefore, only noise due to convecting temperature fluctuations, the upstream and downstream pressure spectra become.

$$|p_{p_i}(\omega, k_y, k_z)|^2 = \left(\frac{A_{2i}\,\Delta P}{\Delta A\,\theta_0}\right)^2 |\theta_{c_1}(\omega, k_y, k_z)|^2 \quad i = 1, 2 \qquad (2)$$

Thus, for a specified frequency/wave number spectrum of the convecting temperature fluctuations at the actuator disc, the upstream and downstream acoustic intensity flux due to these fluctuations traversing the disc can be calculated.

Representation of Fluctuating Temperature Input

In order to make the infinite two-dimensional actuator disc of Figure (1) be a more realistic representation of a turbine stage, the disc is taken to reflect the azimuthal 2π radian periodicity inherent in actual rotor or stator stages. The temperature distortion entering the actuator disc representation of a turbine blade row is thus taken to be repetitive over a period of one circumference.

In addition, the temperature distortion is assumed "frozen" as it convects through the actuator disc and to have a cross correlation in a coordinate system moving with the free stream of the form

$$R_\theta (x', y', z') = \overline{\theta_c^2} \exp - \left\{ \frac{x'^2}{L_x^2} + \frac{y'^2}{L_y^2} + \frac{z'^2}{L_z^2} \right\}, \qquad (3)$$

where (x', y', z') represents the separation distance between two reference points, L_x, L_y and L_z are representative of the axial, circumferential and spanwise correlation length scales of the convected temperature distortion and $\overline{\theta^2}$ is the mean square intensity.

Applying the condition of periodicity over the range $2\pi r$ (where r is representative of the radius of the turbine stage) and assuming that L_y is much smaller than one circumference, the cross correlation of the temperature distortion can be written as a Fourier series in y' as

$$R_\theta (y', z', \tau) = \overline{\theta_c^2} \sum_{j=-\infty}^{\infty} A_j (z', \tau)\, e^{\frac{ij y'}{r}},$$

where

$$A_j (z', \tau) = \frac{1}{2\pi r}\, e^{-\left\{ \frac{z'^2}{L_z^2} + \frac{U_1^2 \tau^2}{L_x^2} \right\}} \int_{-\pi r}^{\pi r} e^{-\frac{y'^2}{L_y^2}}\, e^{-\frac{ij y'}{r}}\, dy',$$

and x' has been replaced by $U_1 \tau$.

Since $L_y << 2\pi r$, the limits of integration can be extended to infinity permitting the above to be evaluated as

$$R(y', z', \tau) = \frac{\pi^{1/2} L_y}{2\pi r} \overline{\theta_c^2} \; e^{-\frac{z'^2}{L_z^2}} \; e^{-\frac{U_1^2 \tau^2}{L_x^2}} \sum_{j=-\infty}^{\infty} e^{-\frac{j^2 L_y^2}{4r^2}} \; e^{\frac{ijy}{r}} \qquad (4)$$

The spectrum of the inflow temperature distortion is then readily calculated by Fourier transforming in space and time, so that

$$|\theta(\omega, k_y, k_z)|^2 = \frac{L_x L_y L_z \overline{\theta_c^2}}{8\pi^{3/2} U_1 r} \; e^{-\frac{1}{4}\left[\frac{\omega^2 L_x^2}{U^2} + k_z^2 L_z^2\right]}$$

$$\sum_{j=-\infty}^{\infty} e^{-\frac{j^2 L_y^2}{4r^2}} \; \delta\left(k_y - \frac{j}{r}\right). \qquad (5)$$

From the form of this equation, the following non-dimensional parameters (denoted by primes) are suggested:

$$L_x' = \frac{L_x}{r} \qquad L_y' = \frac{L_y}{r} \qquad L_z' = \frac{L_z}{r}$$

$$\omega' = \frac{r\omega}{U_1} \qquad k_y' = r k_y \qquad k_z' = r k_z \qquad \overline{\theta_c'^2} = \frac{\overline{\theta_c^2}}{\theta_0^2}$$

Thus, in non-dimensional parameters,

$$|\theta(\omega, k_y, k_z)|^2 = \frac{\theta_0^2 r^3}{U_1 \, 8\pi^{3/2}} \overline{\theta'^2_c} \; H(\omega', k_y', k_z') \qquad (6)$$

where

$$H(\omega', k_y', k_z') = L_x' L_y' L_z' \; e^{-\frac{1}{4}(\omega'^2 L_x'^2 + k_z'^2 L_z'^2)} \sum_{j=-\infty}^{\infty} e^{-\frac{1}{4} j^2 L_y'^2} \; \delta(k_y' - j) \qquad (7)$$

Results and Discussion

The overall sound power radiated to the far field due to convecting temperature fluctuations interacting with turbine blade rows can be obtained by substituting equations (6, 7) for the temperature distortion in equation (2) to obtain the acoustic pressure spectrum and then applying equations (A30) and (A31) of the Appendix to determine the acoustic intensity flux.

If the radiated intensity integrated over the non-dimensional frequency band $[\omega_1', \omega_2']$ is written in terms of non-dimensional parameters, equation (A31) for the upstream (i = 1) and downstream (i = 2) acoustic intensity flux becomes:

$$\left[I_{x_i}\right]_{\omega_1'}^{\omega_2'} = \frac{(\Delta P)^2}{8\pi^{3/2}\rho_{o_i} a_i} \overline{\theta'^2}_{c_i} \int_{\omega_1'}^{\omega_2'} \int_{k_{z_i}^{(1)'}}^{k_{z_i}^{(2)'}} \int_{k_{y_i}^{(1)'}}^{k_{y_i}^{(2)'}} H R_i B_{3i}^2 \, d\omega' \, dk_z' \, dk_y', \quad (8)$$

where

$$k_{y_i}^{(j)'} = M_{x_i} \omega' \left[\frac{-M_{y_i} + (-1)^j \sqrt{1-M_{x_i}^2}}{1 - M_{x_i}^2 - M_{y_i}^2}\right],$$

$$k_{z_i}^{(j)'} = \frac{(-1)^j M_{x_i} \omega'}{\sqrt{1 - M_{x_i}^2 - M_{y_i}^2}},$$

i, j = 1, 2

In this equation, the triple integral is non-dimensional since the terms retained in the integral are the non-dimensional input temperature distortion $H(\omega', k_y', k_z')$, the non-dimensional radiation factor $R_i(\omega', k_y', k_z')$ and the term $B_{i3}(\omega', k_y', k_z')$, which relates the temperature spectrum to the acoustic pressure spectrum. The non-dimensional limits of integration over the wave numbers are obtained from the Appendix and are such as to only account for the propagating acoustic modes that are generated.

In order to determine the general properties of this result the triple integral is evaluated numerically to account for a wide variety of operating conditions. It is constructive, however, to consider first a particular approximate case, valid at low frequencies, that can be written out explicitly.

Since the temperatures in the turbine are very high, the speed of sound is as much as twice that of the ambient speed of sound and the flow is characterized by relatively low Mach numbers. The wave number limits of integration in such cases reduce approximately to $\pm \omega' M_{x_i}$. Now, if only very low frequencies are considered, so that $|\text{Max}(k'_y)| = |\omega' M_{x_i}| < 1$, only the circumferential mode $k'_y = 0$ can propagate and only the $j = 0$ term in equation (7) contributes to the total. Also, at low frequencies there is only a small range of k_z's that give rise to propagating modes (i.e., $|k_z| < |\omega' M_{x_i}|$). Over this range, H, R_i and B_{i3} vary only slightly and equation (8) simplifies including the expression for H from (7) to:

$$\left[I_{x_i}\right]_{\omega'_1}^{\omega'_2} = \frac{(\Delta P)^2 \quad \overline{\theta'^2_{c_i}}}{8\pi^{3/2} \rho_{0_i} \; a_i} \int_{\omega'_1}^{\omega'_2} < R_i >< B_{i3}^2 > L'_x \; L'_y \; L'_z \; 2\omega' M_{x_i}$$

$$e^{-\frac{1}{4}\omega'^2 \; L_x'^2} \; d\omega', \qquad (9)$$

where $< R_i >$ and $< B_{i3}^2 >$ are averages of R_i and B_{i3}^2 over the k_z range of integration. This equation is reduced further, since for plane wave modes R_i and B_{i3} are independent of ω'. Taking these terms outside of the integral and integrating with respect to ω', the following limiting form of the intensity results for the case of low frequencies:

$$\left[I_{x_i}\right]_{\omega'_1}^{\omega'_2} = - \frac{M_{x_i} (\Delta P)^2}{2\pi^{3/2} \rho_{0_i} \; a_i} \overline{\theta'^2_{c_i}} < R_i >< B_{i3}^2 > \frac{L'_y \; L'_z}{L'_x}$$

$$\left[e^{-\frac{1}{4} L_x'^2 \omega'^2} \right]_{\omega'_1}^{\omega'_2} \qquad (10)$$

If, as is usually the case, the change in axial velocity and speed of sound across a stage is relatively small compared with the change in static pressure and swirl velocity, $< R_i >$ and $< B_{13} >$ can be much simplified. Using bars where appropriate to denote average values across the stage, the downstream values R_2 and B_{23} are as follows:

$$R_2 = (1 - M_{x_2})^2$$

$$B_{23} = \frac{-(1 + \overline{M}_x)}{2 + \dfrac{\Delta P}{\overline{\rho}_0 \, \overline{a}^2} \, \overline{M}_x}.$$

Since, for consideration of low frequency core noise, only the downstream radiated wave is directly important, only the downstream intensity flux is written out in its approximate form. Thus,

$$\left[I_{x_2} \right]_{\omega_1'}^{\omega_2'} = - \frac{(\Delta P)^2}{2 \pi^{3/2} \, \rho_{0_2} a_2} \, \overline{\theta'^2_{c_1}} \, \frac{(1 - M_{x_2})^2 \, (1 + \overline{M}_x)^2}{\left\{ 2 + \dfrac{\Delta P}{\overline{\rho}_0 \, \overline{a}^2} \, \overline{M}_x \right\}^2} \, M_{x_2} \, \frac{L_y' \, L_z'}{L_x'}$$

$$\left[e^{-\frac{1}{4} L_x'^2 \, \omega'^2} \right]_{\omega_1'}^{\omega_2'}$$

or, since $\overline{M}_x^2 \ll 1$ and $\dfrac{\Delta P}{\rho_0 \, \overline{a}^2} \, \overline{M}_x \ll 1$ for most turbine blade or vane rows,

$$\left[I_{x_2} \right]_{\omega_1'}^{\omega_2'} = - \frac{(\Delta P)^2}{8 \pi^{3/2} \, \rho_{0_2} a_2} \, \overline{\theta'^2_{c_1}} \, M_{x_2} \, \frac{L_y' \, L_z'}{I_x'} \left[e^{-\frac{1}{4} L_x'^2 \, \omega'^2} \right]_{\omega_1'}^{\omega_2'} \qquad (11)$$

The peak acoustic intensity can be determined by differentiating the integrand of equation (9) with respect to ω' and equating to zero. It is found to occur when $\omega'_m = \sqrt{2}/L'_x$. If this frequency satisfies the condition $\omega' M_x < 1$, the peak radiated acoustic intensity in a bandwidth given by $[\omega'_m - \Delta\omega', \omega'_m + \Delta\omega']$ is, so long as $\Delta\omega' << \omega'_m$,

$$\left[I_{x_2} \right]_{\omega'_m - \Delta\omega'}^{\omega'_m + \Delta\omega'} = \frac{1}{\sqrt{3}\, 2\pi^3 e} M_{x_2} \frac{(\Delta P)^2}{\rho_{0_2} a_2} \overline{\theta'^2_{c_1}} L'_y L'_z \Delta\omega' \qquad (12)$$

From this approximate analysis, it can be inferred that for cases where the noise due to convecting temperature fluctuations is predominantly propagated in the plane wave mode, the acoustic intensity flux within a fixed bandwidth is proportional to the turbine stage operating parameters $(\Delta P)^2$, M_{x_2}, the mean square intensity of the temperature fluctuations, and the transverse "correlation area" of these fluctuations. The axial length scale does not, therefore, contribute in such cases to the peak intensity on a fixed bandwidth basis. Together with the axial velocity, however, it does fix the frequency at which peak noise occurs.

The range of validity of these particular results can be demonstrated by calculating a range of cases using numerical integration of the triple integral of equation (8). For example, the narrowband spectra of noise due to temperature fluctuations of fixed intensity and transverse length scale passing through the first row of exit nozzle guide vanes on a JT3D engine operating at a typical approach speed is shown in Figure 2 for a range of axial length scales. Also shown are some results for the low frequency approximation given by equation (12). It can be seen that the larger axial length scales generate approximately equal levels of peak noise at low frequencies and are reasonably well represented by the approximate form of equation (12). As the length scale decreases, noise is generated over a wider frequency range with slightly higher peak values and the approximation is seen to be inaccurate. The changes in peak level and spectrum shape for axial length scales less than about 0.4 of a radius are due to noise propagating in acoustic modes other than the plane wave mode.

The effect of varying transverse length scale for constant intensity temperature fluctuations is shown in Figure 3. The peak one-third octave band power level is plotted aginst L'_y (which is taken equal to L'_z for comparison purposes) for three non-dimensional axial length scales at the same operating conditions as used in the previous figure. It can be seen that at the lower non-dimensional transverse length scales, the power level increases directly with the transverse correlation area and then deviates below this dependence at higher values of L'_y and L'_z. This effect is due to the propagation of higher circumferential modes and is seen to be slightly more pronounced for the smaller axial length scales which generate peak noise at higher frequencies. The dependence of peak one-third octave band power levels on the transverse correlation area of the temperature fluctuations is thus a reasonable approximation over a reasonable range of transverse and axial length scales. As shown earlier, however, inaccuracies will be encountered if cases with transverse length scales on the order of a radius are considered and where in addition the axial length scale is less than 0.4 of a radius.

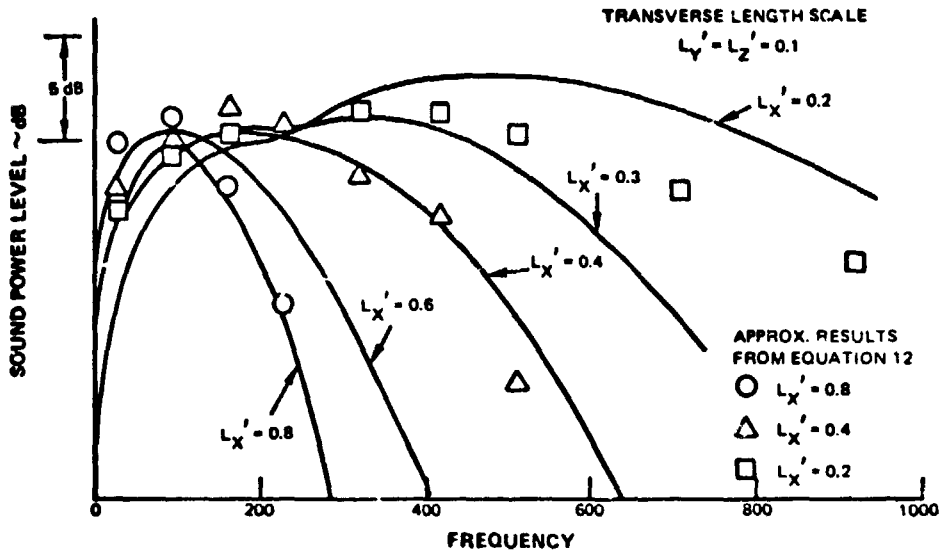

Figure 2 *Narrow Band (32Hz) Acoustic Power Spectra as a Function of Axial Length Scale (JT3D First Nozzle Guide Vane) Approach, 77% Design Speed*

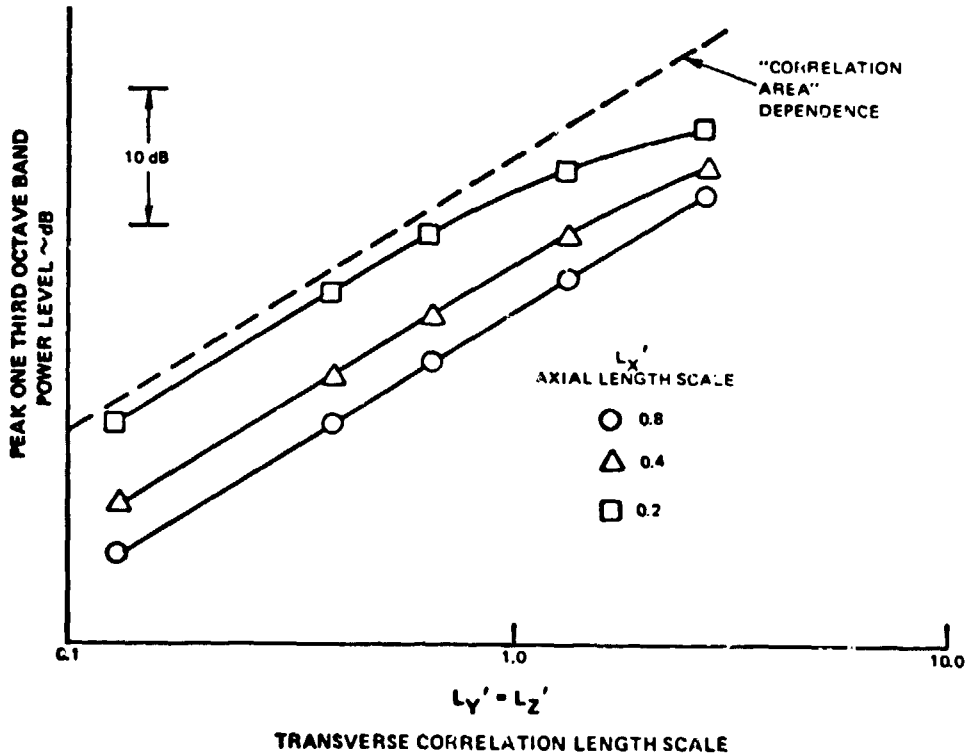

Figure 3 *Dependence of Peak One-Third Octave Band Noise on Transverse Length Scale (JT3D First Nozzle Guide Vane) Approach, 77% Design Speed*

References:

1. Bushell, K. W., "A Survey of Low Velocity and Coaxial Jet Noise with Application to Prediction", JSV 17(2), 1971.

2. Gerend, R. P.; Kumasaka, H. P. and Roundhill, J. P., "Core Engine Noise", presented at AIAA Aero-Acoustics Conference, Seattle, Washington, October, 1973.

3. Cumpsty, N. A. and Marble, F. E., "The Generation of Noise by the Fluctuations in Gas Temperature into a Turbine", University of Cambridge Report No. CUED/A TURBO/TR 57, 1974.

4. Mani, R., "Refraction of Acoustic Duct Waveguide Modes by Exhaust Jets", Q. of App. Math., January, 1973.

5. Lee, B. H. K. and Jones, D. J., "Transmission of Upstream Sound through a Subsonic Jet", Presented at AIAA 6th Fluid and Plasma Dynamics Conference, July, 1973.

6. Pickett, G.F., "Effect of Non-Uniform Inflow On Fan Noise," Presented at Spring Meeting of Acoustical Society of America, New York City, April 1974.

Notation

a	=	speed of sound
b	=	half blade chord
c_v	=	coefficient of expension at constant volume
c_p	=	coefficient of expansion at constant pressure
B	=	number of rotor blades
B_{i3}	=	amplitude of acoustic pressure due to temperature fluctuations passing through turbine blade row
D	=	drag force
f	=	cyclic frequency
F	=	lift force
$\underline{F}$	=	force vector
$H(\omega' k'_y k'_z)$	=	non-dimensional spectrum of $\theta(\omega', k'_y, k'_z)$
$H(x)$	=	Heaviside function
i	=	$\sqrt{-1}$
$\underline{I}$	=	acoustic intensity vector
j	=	harmonic of inflow temperature distortion
k	=	wave number vector (k_x, k_y, k_z)
L	=	length scales (L_x, L_y, L_z) of temperature fluctuations
M	=	Mach number
p	=	acoustic pressure
P	=	steady state pressure
r	=	representative radius of turbine stage
$R_\theta(y', z', \tau)$	=	cross-correlation function of temperature fluctuations
R_l	=	radiation factor
s	=	unsteady entropy
t	=	time
$\underline{u}$	=	unsteady velocity vector (u, v, w)
$\underline{U}$	=	steady state velocity vector (U, V. W)
V_T	=	rotor tip speed
x	=	axial coordinate
y	=	circumferential coordinate
z	=	spanwise coordinate
α_i	=	$\underline{U}_i \cdot \underline{k} - \omega$
γ	=	ratio of specific heats
δ	=	delta function
ξ	=	stagger angle of blades
ρ	=	density
θ	=	temperature
ω	=	frequency, radians per sec
τ	=	time displacement
ψ	=	phase angle
Ω_i	=	$M_{y_i} k_y + M_{z_i} k_z - \omega/a_i$

Subscripts

0	=	steady state
1	=	upstream
2	=	downstream
c	=	convected wave
i	=	integer
p	=	acoustic (pressure) wave
x	=	axial component
y	=	circumferential component
z	=	spanwise component

Superscripts

c	=	convective wave
p	=	pressure wave
1	=	lower cutoff value
2	=	upper cutoff value
i	=	integer
'	=	non-dimensional for dependent variables
'	=	displacements of independent variables x', y', z'.

Non-Dimensional Variables

L_x'	=	L_x/r
L_y'	=	L_y/r
L_z'	=	L_z/r
k_y'	=	rk_y
k_z'	=	rk_z
$\overline{\theta_c'^2}$	=	$\overline{\theta_c^2}/0_0^2$
ω'	=	$\frac{\omega r}{U_1}$

SUPPLEMENT

DERIVATION OF CONDITIONS FOR THE PROPAGATION OF ACOUSTIC, VORTICITY AND ENTROPY WAVES, AND THE JUMP CONDITIONS ACROSS AN ACTUATOR DISC

Using the notation illustrated in Figure 1 where small unsteady velocity components $\underline{u} = (u, v, w)$ are superimposed on a steady and constant velocity field $\underline{U} = (U, V, W)$ relative to the stationary coordinate system $\underline{x} = (x, y, z)$, the linearized equations for continuity, momentum (Navier-Stokes) and energy are, neglecting viscous and heat conduction effects:

$$\frac{\partial \rho}{\partial t} + (\underline{U} \cdot \underline{\nabla})\, \rho + \rho_o\, (\underline{\nabla} \cdot \underline{u}) = 0, \tag{A1}$$

$$\rho_o \frac{\partial \underline{u}}{\partial t} + \rho_o\, (\underline{U} \cdot \underline{\nabla})\, \underline{u} + \underline{\nabla} p = \rho_o \underline{F}, \tag{A2}$$

$$\frac{\partial s}{\partial t} + (\underline{U} \cdot \underline{\nabla})\, s = 0. \tag{A3}$$

In these equations, p, ρ and s are the perturbation pressure, density and entropy respectively, and ρ_o and $\rho_o \underline{F}$ are the ambient density and fluctuating force per unit volume applied at the cascade. In addition, the linearized equations of state and second law of thermodynamics can be written as:

$$\rho - \frac{\rho_o}{P} p + \frac{\rho_o}{\theta_o} \theta = 0, \tag{A4}$$

$$s + \frac{R}{P} p - \frac{c_p}{\theta_o} \theta = 0, \tag{A5}$$

where P is the ambient pressure, θ_o the ambient temperature R the gas constant c_p the coefficient of thermal expansion at constant pressure and θ the perturbation temperature.

If the rotor is represented by an actuator disc at the x = 0 plane, and if the flow variables are assumed to have the form $\rho\,(\underline{x}, t) = \rho\,(\underline{k}, \omega)\, e^{i(\underline{k} \cdot \underline{x} - \omega t)}$ etc., equations (A1) - (A3) become, away from the rotor plane x = 0, (where F = 0), and dividing by $e^{i(\underline{k} \cdot \underline{x} - \omega t)}$:

$$\begin{aligned} &(\underline{U} \cdot \underline{k} - \omega)\, \rho + \rho_o\, (\underline{u} \cdot \underline{k}) = 0, \\ &(\underline{U} \cdot \underline{k} - \omega)\, \underline{u} + \frac{\underline{k}}{\rho_o} p = 0, \\ &(\underline{U} \cdot \underline{k} - \omega)\, s = 0. \end{aligned} \tag{A6}$$

Equations (A4) and (A5) remain of the same form where, without ambiguity, all dependent variables are functions in wave number/frequency space.

The seven equations given by (A4) to A6) represent a linear set of homogeneous equations in seven unknowns. The condition for a non-trivial solution of this set of equations is that the determinant formed by a matrix representation of these equations be zero. This condition is satisfied when

$$(\underline{U} \cdot \underline{k} - \omega)^3 \left[|\underline{k}|^2 - \frac{(\underline{U} \cdot \underline{k} - \omega)^2}{a^2} \right] = 0, \tag{A7}$$

where $\left(\frac{\gamma P}{\rho_o}\right)^{1/2}$ is replaced by the speed of sound a.

Inspection of this equation shows it to be a 5th order polynomial in k_x, one root of which is a triple root given by $\underline{U} \cdot \underline{k} - \omega = 0$, or

$$k_x^{(c)} = \frac{\omega - Vk_y - Wk_z}{U}, \tag{A8}$$

where the superscript (c) is used because it can be seen that the form given for k_x gives rise to a wave convecting downstream with the mean flow. Substitution of this form for k_x into equations (A4) - (A6) yields the following relations for variables convecting with the mainstream:

$$\begin{aligned} p_c &= 0 \\ u_c k_x^{(c)} + v_c k_y + w_c k_z &= 0 \\ s_c &= s_{c_1} \\ \theta_c &= \frac{\theta_o s_{c_1}}{\gamma c_v} \\ \rho_c &= \frac{\rho_o}{\gamma c_v} s_{c_1}, \end{aligned} \tag{A9}$$

where s_{c_1} represents any constant entropy waves that may exist convecting downstream to the rotor plane.

Waves of this type represent vorticity and entropy waves propagating with no associated pressure fluctuations and with phase velocities equal to the component of the mainstream velocity in a direction normal to the wave front. The wave defined by equations in (A9) thus represents a spatial vorticity and entropy distribution that is convected downstream with the mainstream flow.

The remaining two roc's give rise to upsteam and downstream acoustic waves (denoted by subscripts 1 and 2 respectively).

$$k_{x_1}^{(p)} = \frac{M_{x_1}\Omega_1 + \sqrt{\Omega_1^2 - (1 - M_{x_1}^2)(k_y^2 + k_z^2)}}{(1 - M_{x_1}^2)}$$

$$k_{x_2}^{(p)} = \frac{M_{x_2}\Omega_1 - \sqrt{\Omega_1^2 - (1 - M_{x_2}^2)(k_y^2 + k_z^2)}}{(1 - M_{x_2}^2)}$$

where $\Omega_i = M_{y_i} k_y + M_{z_i} k_z - \omega/a_i$

and $\frac{1}{a_i}(U_i, V_i, W_i) = (M_{x_i}, M_{y_i}, M_{z_i})$ for $i = 1, 2$.

Substitution of the results in equations (A4) - (A6) yield the following relationship that relate all acoustic perturbation variables in terms of acoustic pressure:

$$\begin{aligned}
u_{p_i} &= \frac{-k_{x_i}^{(p)}}{\rho_o(\underline{U}_i \cdot \underline{k} - \omega)} p_{p_i} \\
v_{p_i} &= \frac{-k_y}{\rho_o(\underline{U}_i \cdot \underline{k} - \omega)} p_{p_i} \\
w_{p_i} &= \frac{-k_z}{\rho_o(\underline{U}_i \cdot \underline{k} - \omega)} p_{p_i} \\
\rho_{p_i} &= \frac{1}{a_i^2} p_{p_i} \\
\theta_{p_i} &= \frac{\theta_o}{P}\left(\frac{\gamma-1}{\gamma}\right) p_{p_i}.
\end{aligned} \qquad \text{(A11)}$$

where i = 1 and 2 refer to upstream and downstream regions respectively.

It has been shown that in the absence of conductivity, the unsteady flow field away from the rotor cascade, can be represented by upstream and downstream propagating acoustic waves and vorticity and entropy waves convecting with the mainstream flow. In order to see how sound can be generated as vorticity and entropy waves interact with the rotor, it is necessary to satisfy steady and unsteady jump conditions across the rotor disc. Fluctuations in force are experienced at the rotor due to the unsteady flow causing variations in lift on the blades and this gives rise to one source of acoustic waves. Additional noise is generated, however due to entropy and vorticity waves experiencing a rapid change in static pressure across the rotor. The appropriate jump conditions are now derived and will be applied to the present problem where convected and acoustic waves are present both upstream and downstream of the rotor.

Steady Flow Jump Conditions

Using the same notation as in Figure 1, with the cascade plane being represented by an actuator disc at x = 0, and with upstream and downstream flow variables represented by subscripts 1 and 2 respectively. The steady equations of continuity and momentum for a flow through the actuator disc are:

$$\underline{\nabla} \cdot (\rho_o \underline{U}) = 0, \tag{A12}$$

$$\rho_o (\underline{U} \cdot \underline{\nabla}) \underline{U} + \underline{\nabla} P = \rho_o \underline{F}_o \delta (x) \tag{A13}$$

where $\rho_o \underline{F}$ is now the steady force per unit area at the actuator disc.

Integrating equation (A12) across the disc from $-\epsilon$ to ϵ and considering the limit as $\epsilon \to o$, it is easily seen that only terms that contain variables differentiated by x need to be retained. Thus

$$\lim_{\epsilon \to o} \int_{-\epsilon}^{\epsilon} \frac{\partial}{\partial x} (\rho_o U)\, dx = 0,$$

where upon

$$\rho_{o_1} U_1 = \rho_{o_2} U_2 \tag{A14}$$

Similarly, the x component of equation (A13) becomes

$$\lim_{\epsilon \to o} \int_{-\epsilon}^{\epsilon} \left\{ \rho_o U \frac{\partial U}{\partial x} + \frac{\partial P}{\partial x} \right\} dx = \overline{\rho_o} (F_o \cos \xi + D_o \sin \xi) \tag{A15}$$

where F_o and D_o represent the steady lift and the drag at the cascade respectively. The lift is taken in the direction normal to the airfoils of the cascade and D_o, the drag, is taken in the direction parallel to the airfoils. Also the bar notation as in $\overline{\rho_o}$ represents the average of the upstream and downstream values i.e. $\overline{\rho_o} = \frac{1}{2}(\rho_{o_1} + \rho_{o_2})$

In order to integrate across the singularity at the rotor plane, it is expedient to express both the upstream and downstream variables within one function by use of the Heaviside (or step) function. In this way, the axial mean stream velocity and its derivative are represented throughout all space respecively as

$$U(x) = U_1 H(x) + U_2 [1 - H(x)],$$

$$\frac{\partial U}{\partial x}(x) = (U_1 - U_2) \frac{\partial H}{\partial x} = \Delta U \, \delta(x),$$

where $(U_1 - U_2)$ is replaced by ΔU and the fact that the differential of a Heaviside function with its argument is a delta function of that argument is applied. This technique is applied throughout this appendix, but in particular, equation (A15) becomes:

$$\overline{\rho_o U} \, \Delta U + \Delta P = -\overline{\rho_o} (F_o \cos \xi + D_o \sin \xi). \tag{A16}$$

Similarly the y and z components of (A13) reduce to

$$\overline{\rho_o U} \, \Delta V = -\overline{\rho_o} [F_o \sin \xi + D_o \cos \xi], \tag{A17}$$

$$\Delta W = 0 \tag{A18}$$

Unsteady Flow Jump Conditions

Integrating the unsteady lineraized equation of continuity as given by equations (A1) across the x = 0 plane from $-\epsilon$ to ϵ yields, as before,

$$\lim_{\epsilon \to o} \int_{-\epsilon}^{\epsilon} \frac{\partial}{\partial x} (\rho U + \rho_o u) \, dx = 0,$$

i.e. $\rho_1 U_1 - \rho_2 U_2 + \rho_{o_1} u_1 - \rho_{o_2} u_2 = 0.$

The x component of the unsteady momentum equation, equation (A2) is integrated in the same way across the actuator disc.

$$\lim_{\epsilon \to o} \int_{-\epsilon}^{\epsilon} \left\{ \rho U \frac{\partial U}{\partial x} + \rho_o U \frac{\partial u}{\partial x} + \rho_o u \frac{\partial U}{\partial x} + \frac{\partial p}{\partial x} \right\} dx = \int_{-\epsilon}^{\epsilon} \rho_o (F \cos \xi - D \sin \xi)\, \delta(x)\, dx$$

$$+ \int_{-\epsilon}^{\epsilon} \rho (F_o \cos \xi - D_o \sin \xi)\, \delta(x)\, dx$$

where $\rho_o F$ and $\rho_o D$ represents the fluctuating lift and drag per unit area at the cascade in the directions normal to and along the airfoil respectively (as shown in Figure 2).

Using the same methods as with the steady flow jump conditions, this equation can be reorganized so that

$$\lim_{\epsilon \to o} \int_{-\epsilon}^{\epsilon} \left\{ \rho U \Delta U \delta(x) + \rho_o u \Delta U \delta(x) \right\} dx + [\rho_o U u]_{-\epsilon}^{\epsilon} - \int_{-\epsilon}^{\epsilon} \left\{ u \rho_o \Delta U + u U \Delta \rho_o \right\} \delta(x)\, dx$$

$$+ [p]_{-\epsilon}^{\epsilon} = \overline{\rho_o} (F \cos \xi - D \sin \xi) + \bar{\rho} (F_o \cos \xi - D_o \sin \xi),$$

whereupon,

$$\overline{\rho U} \Delta U + \rho_{o_1} U_1 u_1 - \rho_{o_2} U_2 u_2 - \overline{uU}\, \Delta \rho_o + \Delta p$$

$$= \overline{\rho_o} (F \cos \xi - D \sin \xi) + \bar{\rho} (F_o \cos \xi - D_o \sin \xi). \qquad \text{(A20)}$$

The y and z components of the unsteady momentum equations can be considered in a similar manner reducing with help from the steady jump conditions to:

$$\Delta V (\overline{\rho U} + \overline{\rho_o u}) + \rho_{o_1} U_1 v_1 - \rho_{o_2} U_2 v_2 - \overline{\rho_o v}\, \Delta U - \overline{vU}\, \Delta \rho_o = -\bar{\rho}_o (F \sin \xi + D \cos \xi)$$

$$- \bar{\rho} (F_o \sin \xi + D_o \cos \xi), \qquad \text{(A21)}$$

$$\rho_{o_1} U_1 w_1 - \rho_{o_2} U_2 w_2 - \overline{\rho_o w}\, \Delta U - \overline{Uw}\, \Delta \rho_o = 0. \qquad \text{(A22)}$$

Application of Jump Conditions Across the Rotor Disc

It is assumed that vorticity and entropy waves convecting with the mainstream exist both upstream and downstream of the rotor and that the only source of acoustic waves is at the rotor. If the subscripts p and c for the unsteady variables indicate that the variables are due to acoustic pressure waves or convected waves respectively, and if as before the subscripts 1 and 2 denote upstream and downstream respectively, the upstream and downstream variables take on the form

$$\rho_1 = \rho_{p_1} + \rho_{c_1}$$

$$\rho_2 = \rho_{p_2} + \rho_{c_2}$$

with similar expressions for the other variables.

Substitution of these expressions in the unsteady jump condition for continuity (A19):

$$(\rho_{p_1} + \rho_{c_1})\, U_1 - (\rho_{p_2} + \rho_{c_2})\, U_2 + \rho_{o_1}\,(u_{p_1} + u_{c_1}) - \rho_{o_2}(u_{p_2} + u_{c_2}) = 0.$$

Applying the relations in (A9) and A11) this equation can be written relating the upstream and downstream pressure waves as follows:

$$\left(\frac{p_{p_1}}{a_1^2} - \frac{\rho_{o_1} s_1}{\gamma c_v}\right) U_1 - \left(\frac{p_{p_2}}{a_2^2} - \frac{\rho_{o_2} s_1}{\gamma c_v}\right) U_2 + \rho_{o_1}\left(\frac{-k_{x_1}^{(p)}}{\rho_{o_1}\alpha_1}\, p_{p_1} + \rho_{o_1} u_{c_1}\right)$$

$$-\rho_{o_2}\left(\frac{-k_{x_2}^{(p)}}{\rho_{o_2}\alpha_2}\right) - \rho_{o_2} u_{c_2} = 0,$$

where $\alpha_i = \underline{U}_i \cdot \underline{k}^{(p)} - \omega$

Further reduction using the steady continuity conditions and reorganizing,

$$\left[\frac{U_1}{a_1^2} - \frac{k_{x_1}^{(p)}}{\alpha_1}\right] p_{p_1} - \left[\frac{U_2}{a_2^2} - \frac{k_{x_2}^{(p)}}{\alpha_2}\right] p_{p_2} = \rho_{o_2} u_{c_2} - \rho_{o_1} u_{c_1}. \qquad \text{(A23)}$$

In like manner, the jump condition for the x-component of momentum, equation (A20) becomes, using the notation introduced earlier in this appendix:

$$\tfrac{1}{2}\left[U_1(\rho_{p_1}+\rho_{c_1}) + U_2(\rho_{p_2}+\rho_{c_2})\right]\Delta U + \rho_{o_1} U_1 (u_{p_1}+u_{c_1}) - \rho_{o_2} U_2 (u_{p_2}+u_{c_2}) -$$

$$\tfrac{1}{2}\left[U_1(u_{p_1}+u_{c_1}) + U_2(u_{p_2}+u_{c_2})\right]\Delta\rho_o$$

$$+\Delta p_p = \overline{\rho_o}\,(F\cos\xi - D\sin\xi) + (\overline{\rho_p}+\overline{\rho_c})\,(F_o\cos\xi - D_o\sin\xi)$$

Using the equations (A9 and (A11) as before, together with the jump condition for the x-component of the steady momentum equation, it can be shown that this equation reduces to:

$$\left[1 - \frac{\tfrac{1}{2}\Delta P}{\overline{\rho_o}\,a_1^2} + \frac{\tfrac{1}{4}\rho_{o_2}(\Delta U)^2}{\overline{\rho_o}\,a_1^2} - \frac{\overline{\rho_o}\,U_1\,k_{x_1}^{(p)}}{\rho_{o_1}\alpha_1}\right] p_{p_1} - \left[1 + \frac{\tfrac{1}{2}\Delta P}{\overline{\rho_o}\,a_2^2} + \frac{\tfrac{1}{4}\rho_{o_1}(\Delta U)^2}{\overline{\rho_o}\,a_2^2} - \frac{\overline{\rho_o}\,U_2\,k_{x_2}^{(p)}}{\rho_{o_2}\alpha_2}\right] p_{p_2}$$

$$= \overline{\rho_o}\,(F\cos\xi - D\sin\xi) - \Delta P\,\frac{s_1}{\gamma c_v} - \overline{\rho_o}\,U_1\,u_{c_1} + \overline{\rho_o}\,U_2\,u_{c_2} \qquad \text{(A24)}$$

The jump condition for the y-component of momentum (equation A23) can be obtained using similar methods. Thus

$$\left[\tfrac{1}{2}\Delta V\left\{\frac{\tfrac{1}{2}\rho_{o_2}\Delta U}{\overline{\rho_o}\,a_1^2} - \frac{k_{x_1}^{(p)}}{\alpha_1}\right\} - \frac{\tfrac{1}{2}k_y}{\alpha_1\rho_{o_1}}\left\{\rho_{o_1}U_2 + \rho_{o_2}U_1\right\}\right] p_{p_1} - \left[\tfrac{1}{2}\Delta V\left\{\frac{\tfrac{1}{2}\rho_{o_1}\Delta U}{\overline{\rho_o}\,a_2^2} - \frac{k_{x_2}^{(p)}}{\alpha_2}\right\}\right.$$

$$\left. - \frac{\tfrac{1}{2}k_y}{\alpha_2\rho_{o_2}}\left\{\rho_{o_1}U_2 + \rho_{o_2}U_1\right\}\right] p_{p_2}$$

$$= \overline{\rho_o}\,(F\sin\xi + D\cos\xi) - \tfrac{1}{2}\Delta V\left[\rho_{o_1}u_{c_1} + \rho_{o_2}u_{c_2}\right] - \tfrac{1}{2}\left\{\rho_{o_1}U_2 + \rho_{o_2}U_1\right\}(v_{c_1} - v_{c_2}) \qquad \text{(A25)}$$

and the z-component of momentum (equation A22) becomes:

$$-\frac{k_z}{\rho_{o_1}\alpha_1}\,p_{p_1} + \frac{k_z}{\rho_{o_2}\alpha_2}\,p_{p_2} = w_{c_2} - w_{c_1} \qquad \text{(A26)}$$

Now, the term u_{c_2} can be eliminated between equations (A23) and (A24) yielding an equation relating the up and downstream acoustic waves of the form

$$A_{11}\, p_{p_1} + A_{12}\, p_{p_2} = \overline{\rho_o}\,(F\cos\xi - D\sin\xi) - \Delta P\,\frac{S_1}{\gamma c_v} - \overline{\rho_o}(U_1^2 - U_2^2)\,\frac{u_{c_1}}{U_1}, \quad \text{(A27)}$$

where

$$A_{11} = 1 - \frac{\tfrac{1}{2}\Delta P}{\overline{\rho_o} a_1^2} + \frac{\tfrac{1}{4}\rho_{o_2}(\Delta U)^2}{\overline{\rho_o} a_1^2} + \frac{\overline{\rho_o} k_{x_1}^{(p)}}{\rho_{o_1} U_1 \alpha_1}(U_2^2 - U_1^2) - \frac{\overline{\rho_o} U_1 U_2}{\rho_{o_2} a_1^2}$$

$$A_{12} = -\left\{1 + \frac{\tfrac{1}{2}\Delta P}{\overline{\rho_o} a_2^2} + \tfrac{1}{4}\frac{\rho_{o_1}(\Delta U)^2}{\overline{\rho_o} a_2^2} - \frac{\overline{\rho_o} U_2^2}{\rho_{o_2} a_2^2}\right\}$$

A second relationship between the up and downstream pressure waves can be obtained by substituting for u_{c_2}, v_{c_2} and w_{c_2} from equations (A23) (A25) and (A26) respectively in the second equation from (A9). Thus:

$$A_{21}\, p_{p_1} + A_{22}\, p_{p_2} = \overline{\rho_o}\, k_y\,(F\sin\xi + D\cos\xi)$$

$$- [\tfrac{1}{2}(\rho_{o_1} U_2 + \rho_{o_2} U_1)\frac{k_x^{(c)}}{\rho_{o_2}}\,\Delta\rho_o + \rho_{o_1} k_y\,\Delta V]\, u_{c_1} \quad \text{(A28)}$$

where

$$A_{21} = \frac{\tfrac{1}{2} k_x^{(c)}}{\rho_{o_2}}(\rho_{o_1} U_2 + \rho_{o_2} U_1)\left(\frac{U_1}{a_1^2} - \frac{k_{x_1}^{(p)}}{\alpha_1}\right) + \tfrac{1}{2}\Delta V k_y\left(\frac{\tfrac{1}{2}(\rho_{o_1} U_2 + \rho_{o_2} U_1)}{\overline{\rho}\, a_1^2} - \frac{2k_{x_1}^{(p)}}{\alpha_1}\right)$$

$$- \frac{\tfrac{1}{2}(\rho_{o_1} U_2 + \rho_{o_2} U_1)}{\rho_{o_1}\alpha_1}(k_y^2 + k_z^2),$$

$$A_{22} = -\frac{\tfrac{1}{2} k_x^{(c)}}{\rho_{o_2}}(\rho_{o_1} U_2 + \rho_{o_2} U_1)\left(\frac{U_2}{a_2^2} - \frac{k_{x_2}^{(p)}}{\alpha_2}\right) - \frac{\tfrac{1}{2}\Delta V k_y \rho_{o_2} U_2}{\overline{\rho_o}\, a_2^2}$$

$$+ \frac{\tfrac{1}{2}(\rho_{o_1} U_2 + \rho_{o_2} U_1)}{\rho_{o_2}\alpha_2}(k_y^2 + K_z^2).$$

So long as the determinant ($A_{11}\ A_{22} - A_{12}\ A_{21}$) is non-zero, a solution for the upstream and downstream pressure waves can be obtained in the form:

$$p_{p_i} = B_{1i}\ (\overline{\rho_o}\ F) + B_{2i}\ (\overline{\rho_o}\ D) + B_{3i}\ \frac{\Delta P}{\theta_o}\ \theta_{c_1} + B_{4i}\ \rho_{o_1} U_1 u_{c_1},\ i = 1, 2 \qquad \text{(A29)}$$

where the non-dimensional coefficients B_{ji} are readily determined and the normalized upstream temperature fluctuation convecting with the main stream has replaced $\frac{s_{c_1}}{\gamma c_v}$ by using equation (A9).

It can be seen that acoustic waves are generated not only by fluctuating lift and drag at the rotor, but also by entropy (temperature) waves and the axial component of inflow velocity distortion as they experience a change in mean stream flow conditions across the rotor. The fluctuating lift and drag forces are moving with the blades of the rotor and generally generate high and low frequency noise depending on the velocity fluctuations giving rise to the fluctuating angle of attack at the blades. The noise generated by temperature and axial velocity fluctuations, which is the main concern of this paper, will generally be of low frequency and only significant when large changes in pressure, density and mean axial velocity are experienced across the rotor.

Upstream and Downstream Radiated Acoustic Intensity Flux

Once the Fourier transform of a pressure wave $p\ (\omega,\ k_y, k_z)$ is known in a constant moving medium, the acoustic intensity flux vector can be derived by applying the work of Bloklintsev. Thus,

$$\underline{I}\ (\omega, k_y, k_z) = \frac{|p(\omega, k_y, k_z)|^2}{\rho_o\ a}\ \cdot \frac{(\underline{U} + a\underline{n})}{a - \underline{U} \cdot \underline{\nabla}\psi}$$

where $\underline{I}$ is a vector giving the magnitude and direction of acoustic intensity at frequency ω and in wave numbers k_y and k_z, and where $\underline{n}$ is the vector normal to the wave front, and where the pressure waves have space-time dependence of the form $e^{i(\omega t - \frac{\omega}{c}\psi)}$.
For a typical rotor situation where the mean radial velocity is essentially zero (except of course for leaned blades or vanes) the upstream and downstream intensity flux per unit area radiated by a pressure wave is calculated from

$$I_{x_i}(\omega, k_y, k_z) = \frac{|p(\omega, k_y, k_z)|^2}{\rho_{o_i} a_i}\ R_i\ (\omega, k_y, k_z) \qquad i = 1, 2.$$

where the non-dimensional $R_i(\omega, k_y, k_z)$ is given by:

$$R_i = (-1)^{i+1} \left[\frac{M_{x_i} + \dfrac{k_{x_i}^{(p)}}{\sqrt{k_{x_i}^{(p)} + k_y^2 + k_z^2}}}{1 - \dfrac{M_{x_i} k_{x_i}^{(p)} + M_{y_i} k_y}{\dfrac{\omega}{a_i}}} \right] \qquad \text{(A30)}$$

In order to derive the acoustic intensity flux at a given frequency and for all wave numbers, I_{x_i} and I_{x_2} have to be summed over all applicable k_y and k_z and the solution doubled to account for an additional set of pressure waves of the form $p = p(-k_y, -k_z, -\omega)\, e^{-i(\underline{k}\cdot\underline{x} - \omega t)}$

The applicable range of k_y and k_z correspond to those wave numbers that give rise to propagating as opposed to decaying acoustic waves. The condition for propagation is that $k_{x_1}^{(p)}$ and $k_{x_2}^{(p)}$ are real. Thus, the upstream and downstream acoustic intensity flux per unit area at frequency ω is calculated from:

$$I_{x_i}(\omega) = 2 \int_{k_{z_i}^{(1)}}^{k_{z_i}^{(2)}} \int_{k_{y_i}^{(1)}}^{k_{y_i}^{(2)}} I_{x_i}(\omega, k_y, k_z)\, dk_y\, dk_z$$

where

$$k_{y_i}^{(j)} = \frac{-M_{y_i} \dfrac{\omega}{a_i} + (-1)^j \sqrt{\left(\dfrac{\omega}{a_i}\right)^2 M_{y_i}^2 + (1 - M_{x_i}^2 - M_{y_i}^2)\left(\dfrac{\omega}{a_i}\right)^2}}{(1 - M_{x_i}^2 - M_{y_i}^2)} \qquad \text{(A31)}$$

$$k_{z_i}^{(j)} = \frac{(-1)^j \left(\dfrac{\omega}{a_i}\right)}{\sqrt{1 - M_{x_i}^2 - M_{y_i}^2}} \qquad j, i = 1, 2.$$

The numerical calculation of these integrals is reasonably straightforward except for the fact that the determinant ($A_{11}\ A_{22} - A_{12}\ A_{21}$) goes to zero at the limits of integration. In this event, the upstream and downstream radiating pressure tend to infinity giving rise to a singularity in the integral of the form 1/x which is non-integrable. This limitation in the analysis is common to many solutions of linear systems that do not contain damping due to either dissipative or non-linear terms. Recognizing the fact that these infinities do not occur in reality, and that in many cases of interest, the bulk of the radiated energy is concentrated in modes not immediately at or next to cutoff, no serious error is introduced in the integration.

APPENDIX B-2

THERMOCOUPLE VOLTAGE SPECTRA

One-third octave band spectrum levels of compensated thermocouple voltage are presented for thermocouple elements identified by the following code:

THERMOCOUPLE IDENTIFICATION CODE

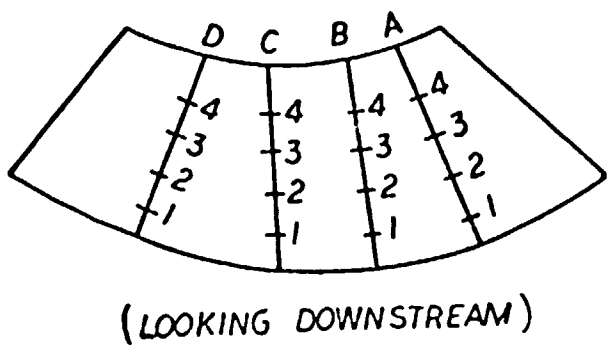

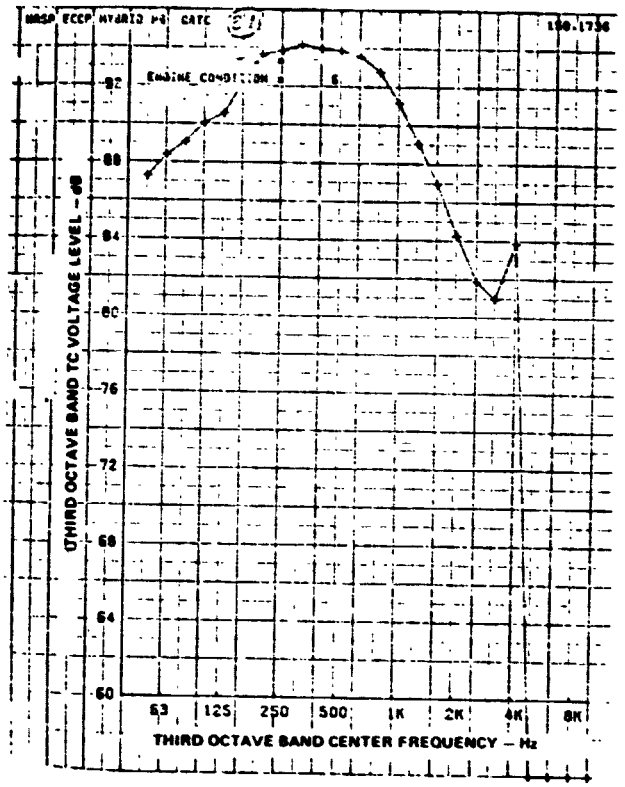

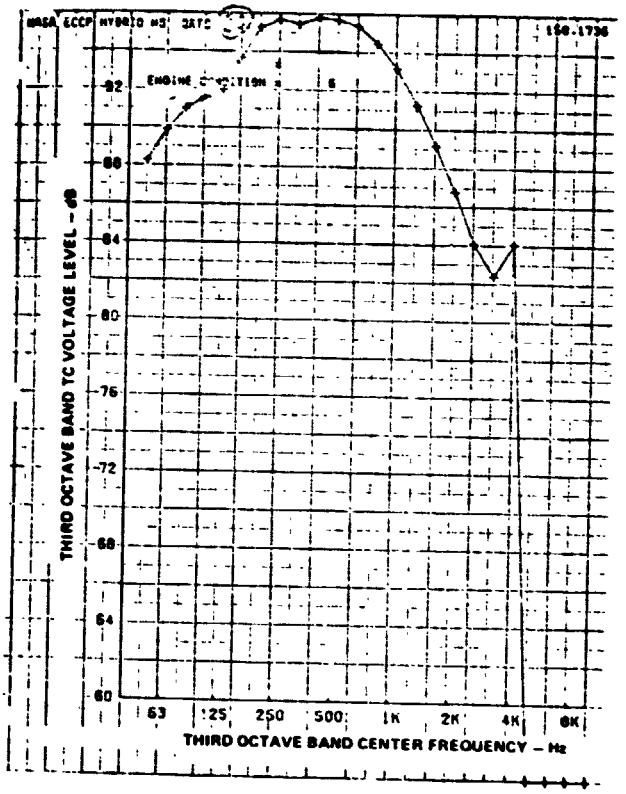

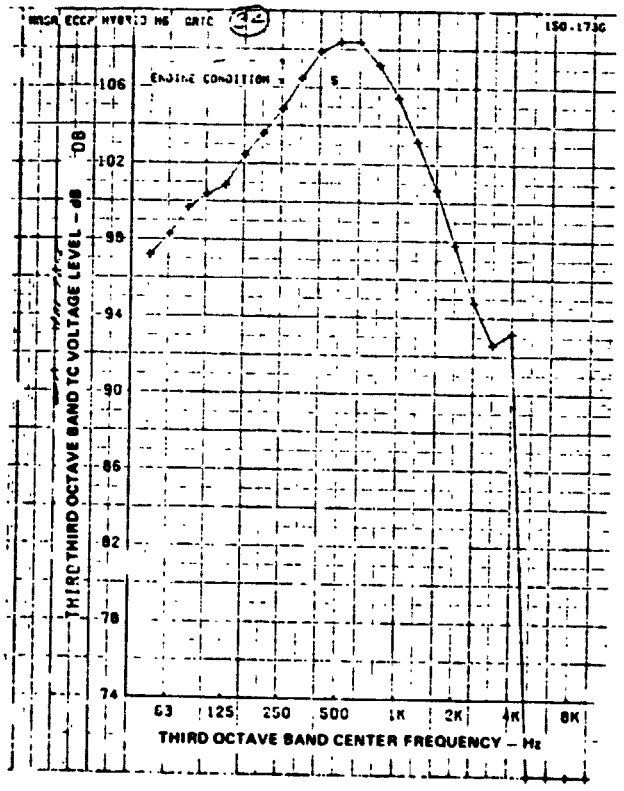

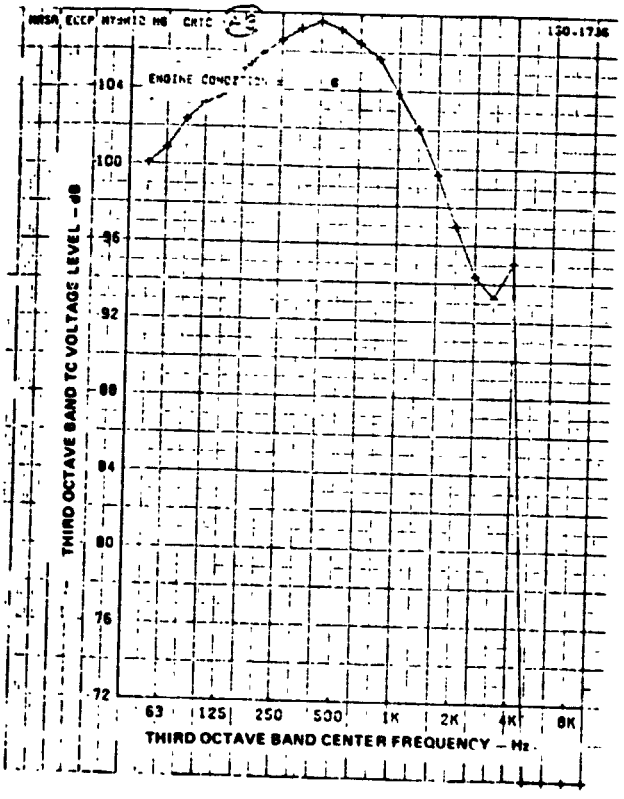

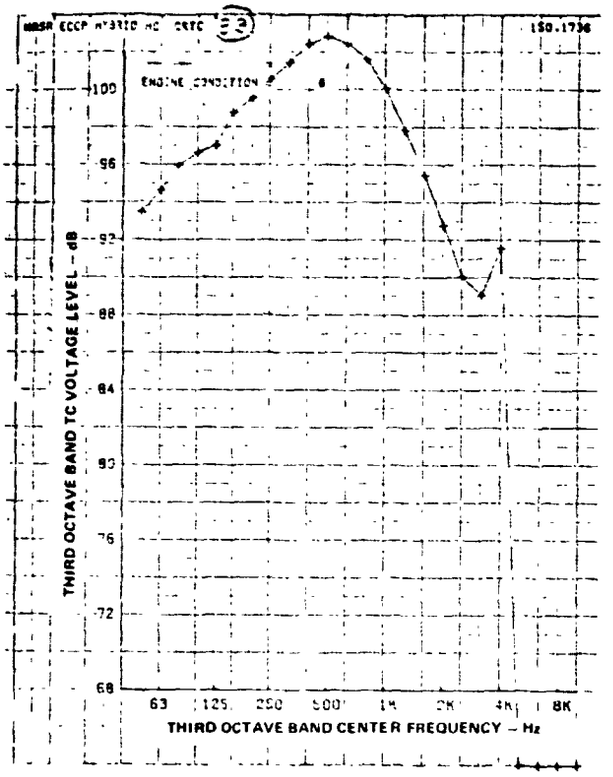
ENGINE CONDITION
THIRD OCTAVE BAND TC VOLTAGE LEVEL – dB
THIRD OCTAVE BAND CENTER FREQUENCY – Hz
63
125
250
500
1K
2K
4K
8K

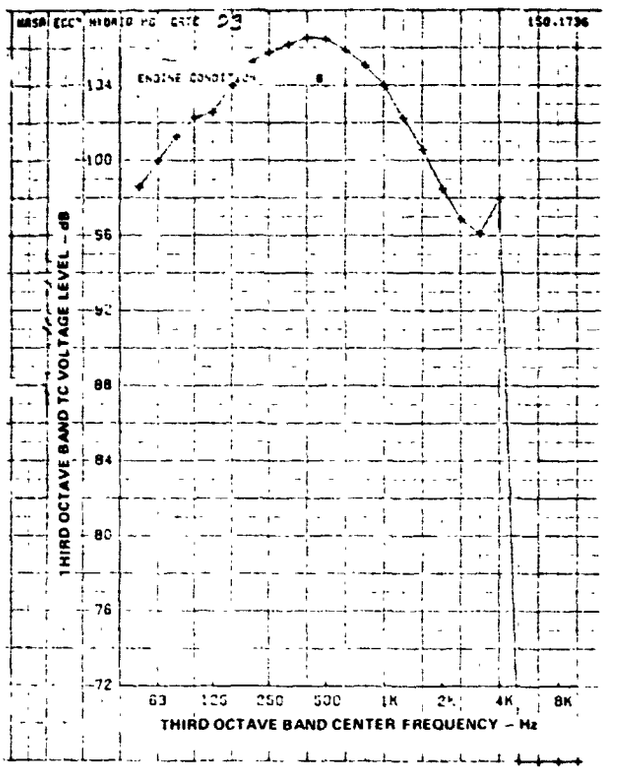
ENGINE CONDITION
THIRD OCTAVE BAND TC VOLTAGE LEVEL – dB
THIRD OCTAVE BAND CENTER FREQUENCY – Hz
63
125
250
500
1K
2K
4K
8K

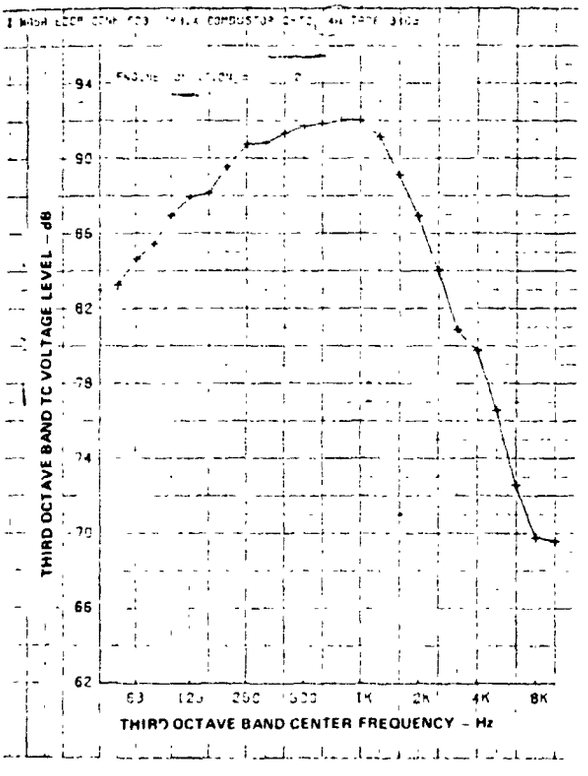
THIRD OCTAVE BAND TC VOLTAGE LEVEL – dB
THIRD OCTAVE BAND CENTER FREQUENCY – Hz
63
125
250
500
1K
2K
4K
8K

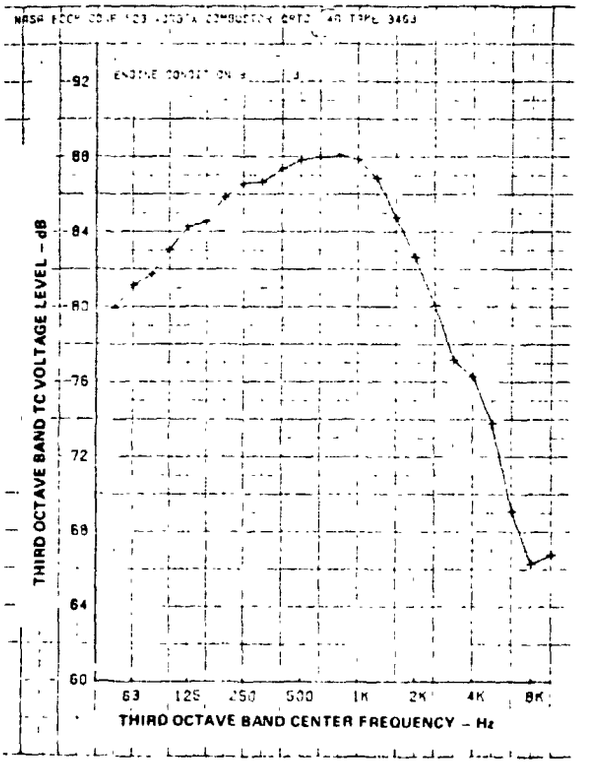
THIRD OCTAVE BAND TC VOLTAGE LEVEL – dB
THIRD OCTAVE BAND CENTER FREQUENCY – Hz
63
125
250
500
1K
2K
4K
8K

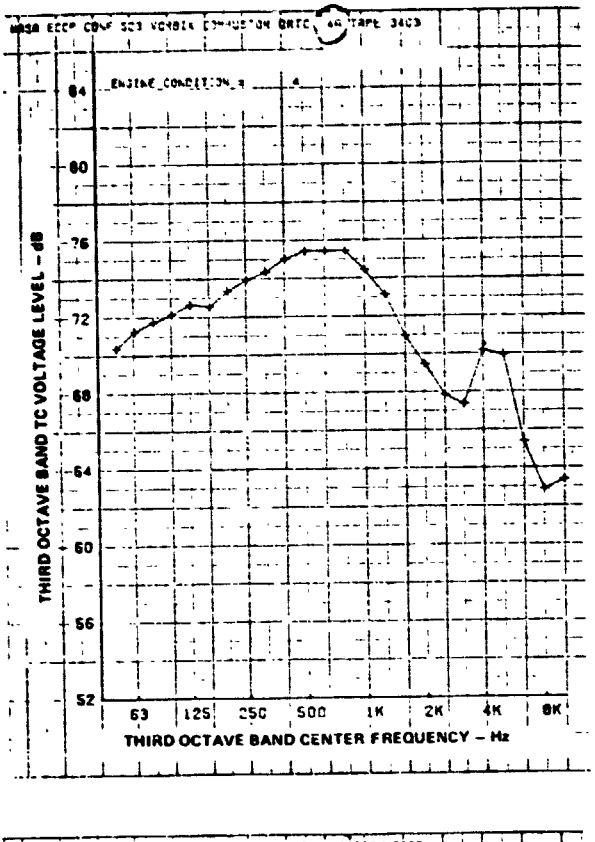
THIRD OCTAVE BAND TC VOLTAGE LEVEL – dB
THIRD OCTAVE BAND CENTER FREQUENCY – Hz
63
125
250
500
1K
2K
4K
8K

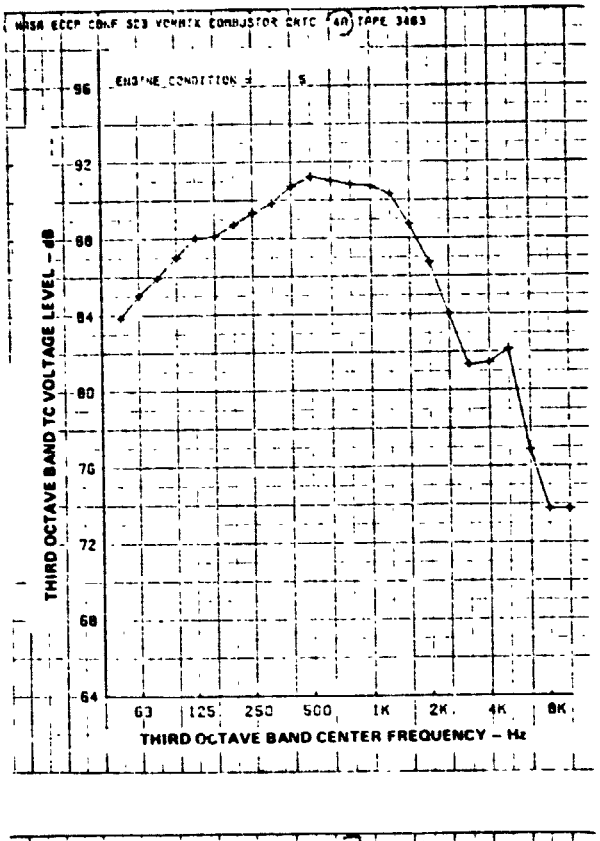
THIRD OCTAVE BAND TC VOLTAGE LEVEL – dB
THIRD OCTAVE BAND CENTER FREQUENCY – Hz
63
125
250
500
1K
2K
4K
8K

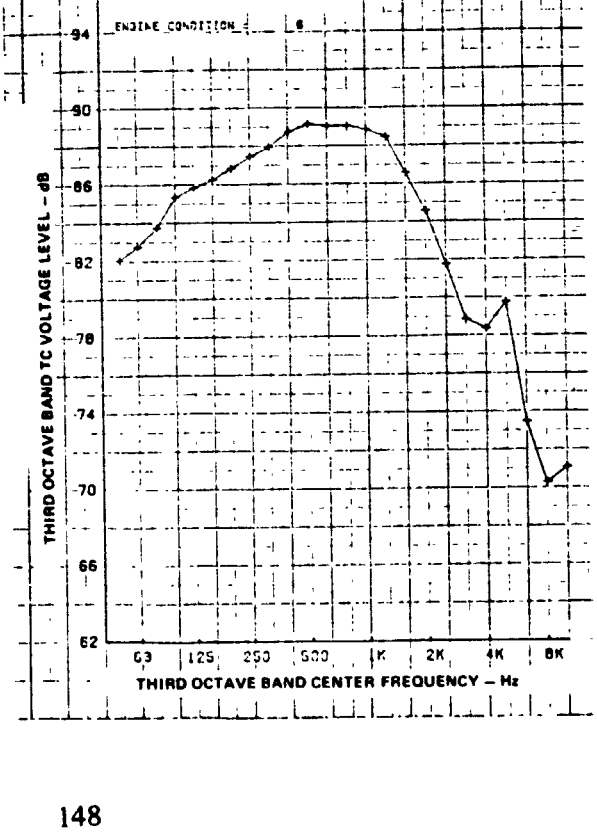
THIRD OCTAVE BAND TC VOLTAGE LEVEL – dB
THIRD OCTAVE BAND CENTER FREQUENCY – Hz
63
125
250
500
1K
2K
4K
8K

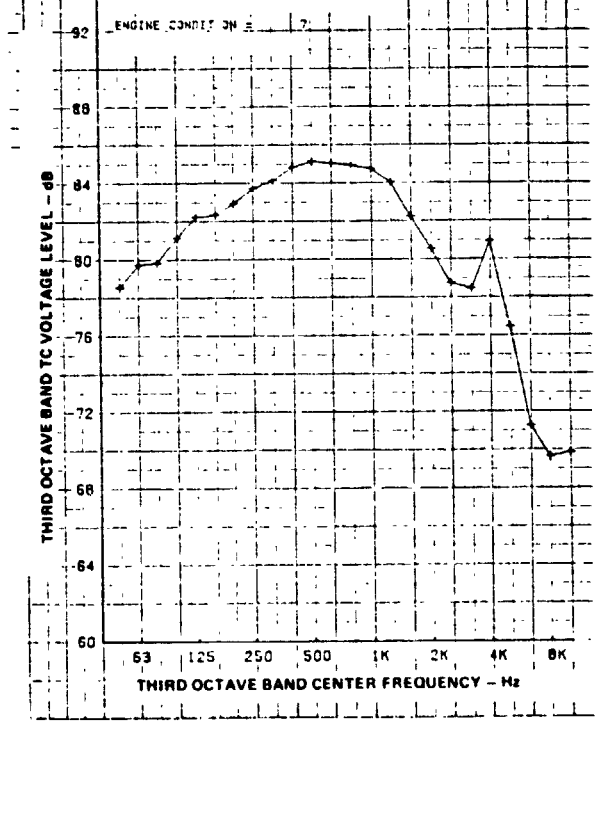
THIRD OCTAVE BAND TC VOLTAGE LEVEL – dB
THIRD OCTAVE BAND CENTER FREQUENCY – Hz
63
125
250
500
1K
2K
4K
8K

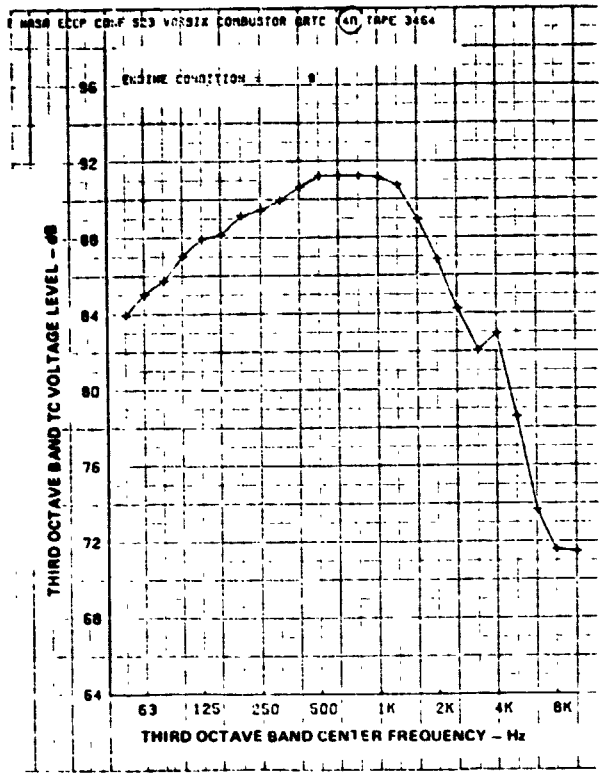
ENGINE CONDITION = 9
THIRD OCTAVE BAND TC VOLTAGE LEVEL – dB
96
92
88
84
80
76
72
68
64
63
125
250
500
1K
2K
4K
8K
THIRD OCTAVE BAND CENTER FREQUENCY – Hz

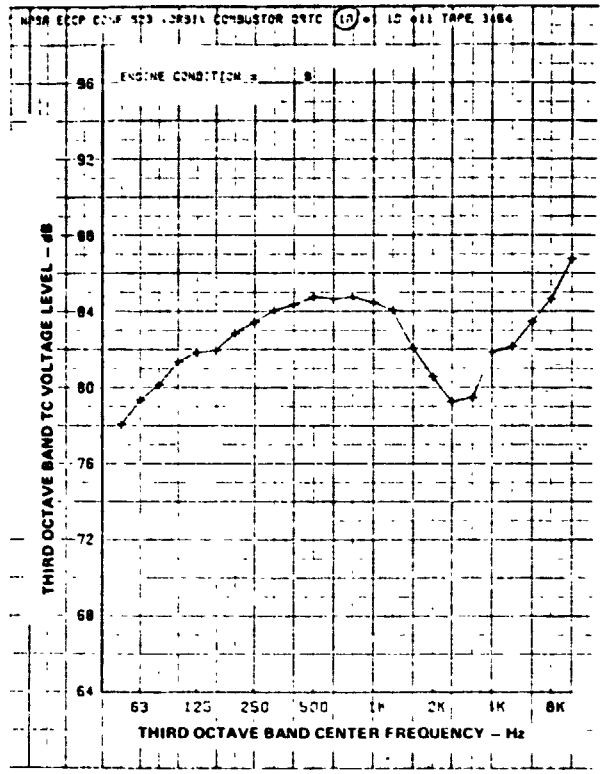
ENGINE CONDITION = 9
THIRD OCTAVE BAND TC VOLTAGE LEVEL – dB
96
92
88
84
80
76
72
68
64
63
125
250
500
1K
2K
4K
8K
THIRD OCTAVE BAND CENTER FREQUENCY – Hz

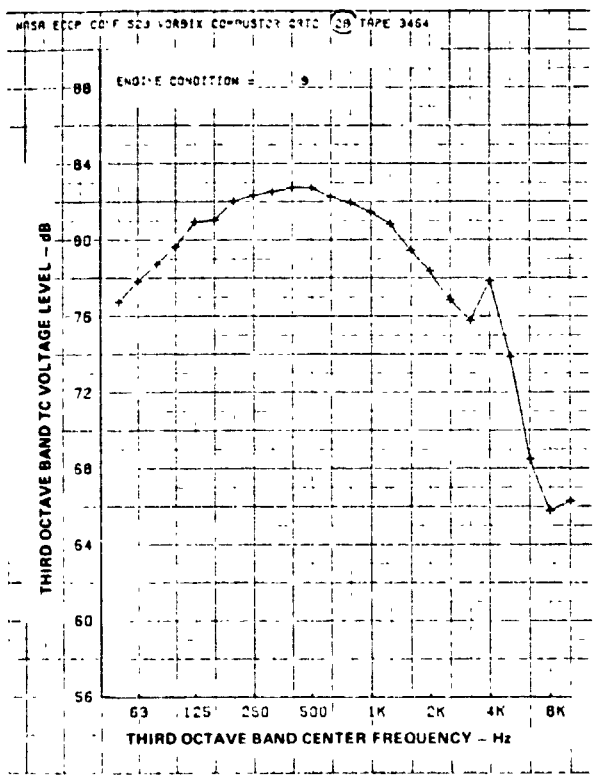
ENGINE CONDITION = 9
THIRD OCTAVE BAND TC VOLTAGE LEVEL – dB
88
84
80
76
72
68
64
60
56
63
125
250
500
1K
2K
4K
8K
THIRD OCTAVE BAND CENTER FREQUENCY – Hz

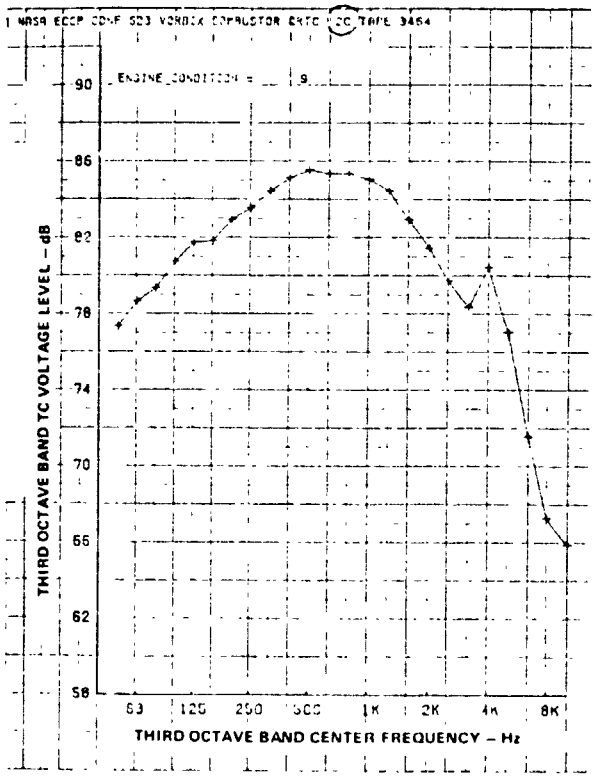
ENGINE CONDITION = 9
THIRD OCTAVE BAND TC VOLTAGE LEVEL – dB
90
86
82
78
74
70
66
62
58
63
125
250
500
1K
2K
4K
8K
THIRD OCTAVE BAND CENTER FREQUENCY – Hz

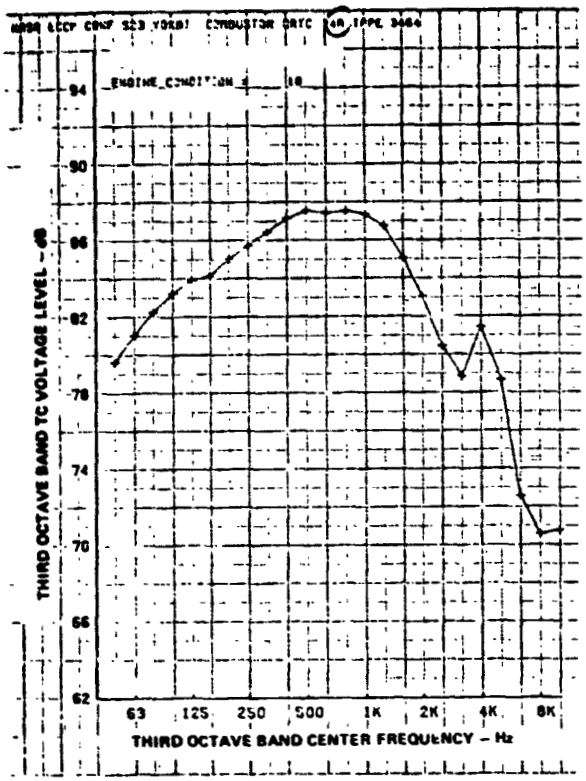

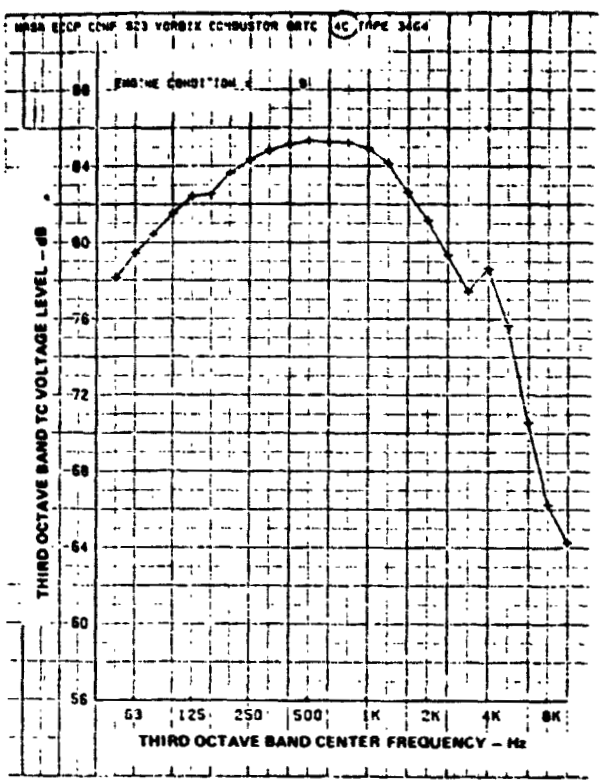

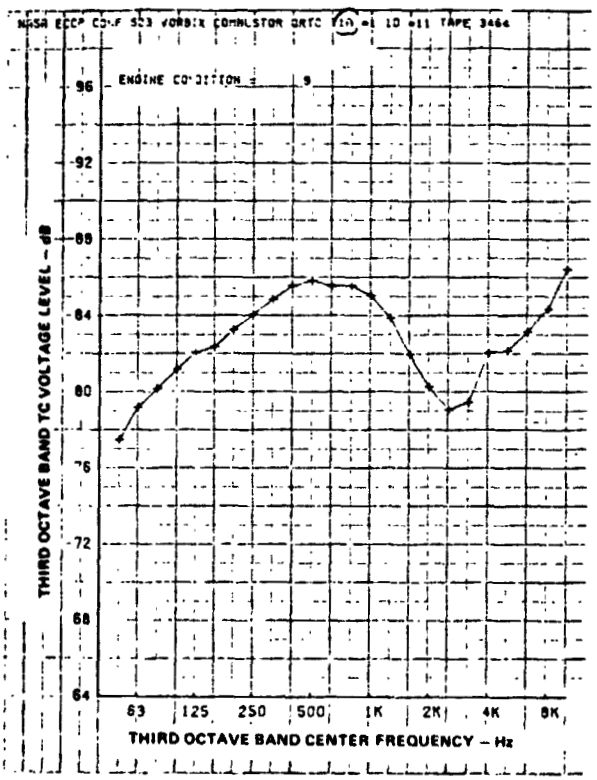

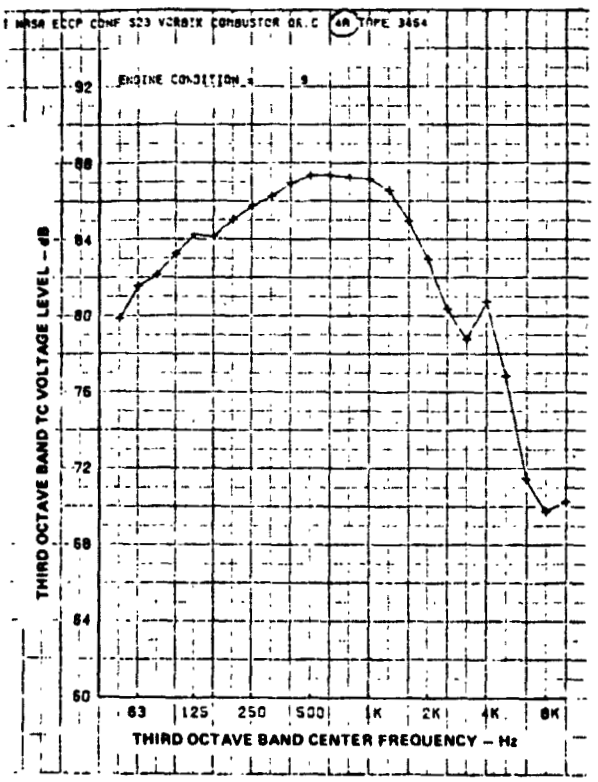

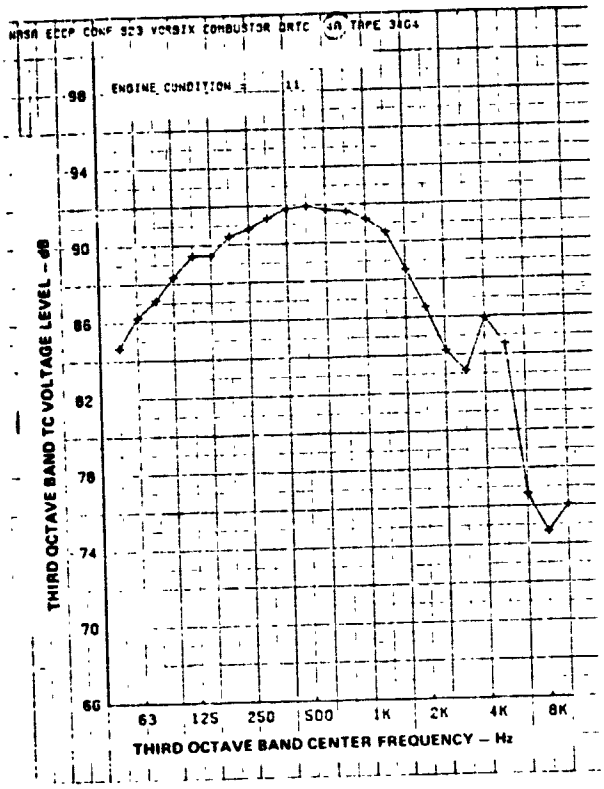
ENGINE CONDITION = 11
THIRD OCTAVE BAND TC VOLTAGE LEVEL – dB
98
94
90
86
82
78
74
70
66
63
125
250
500
1K
2K
4K
8K
THIRD OCTAVE BAND CENTER FREQUENCY – Hz

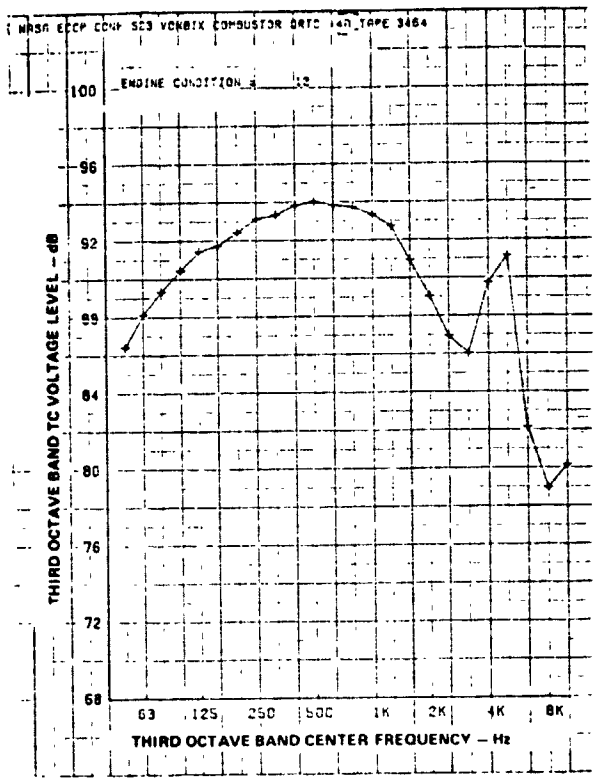
ENGINE CONDITION = 12
THIRD OCTAVE BAND TC VOLTAGE LEVEL – dB
100
96
92
88
84
80
76
72
68
63
125
250
500
1K
2K
4K
8K
THIRD OCTAVE BAND CENTER FREQUENCY – Hz

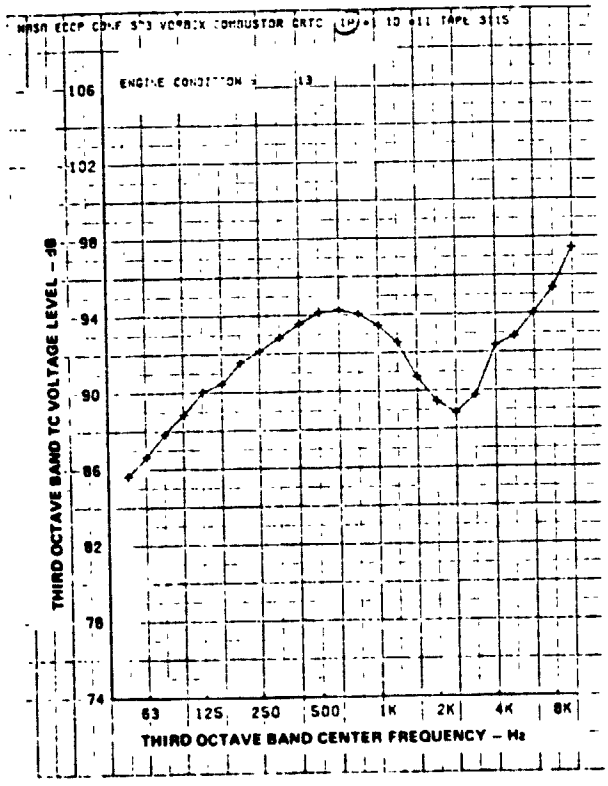
ENGINE CONDITION = 13
THIRD OCTAVE BAND TC VOLTAGE LEVEL – dB
106
102
98
94
90
86
82
78
74
63
125
250
500
1K
2K
4K
8K
THIRD OCTAVE BAND CENTER FREQUENCY – Hz

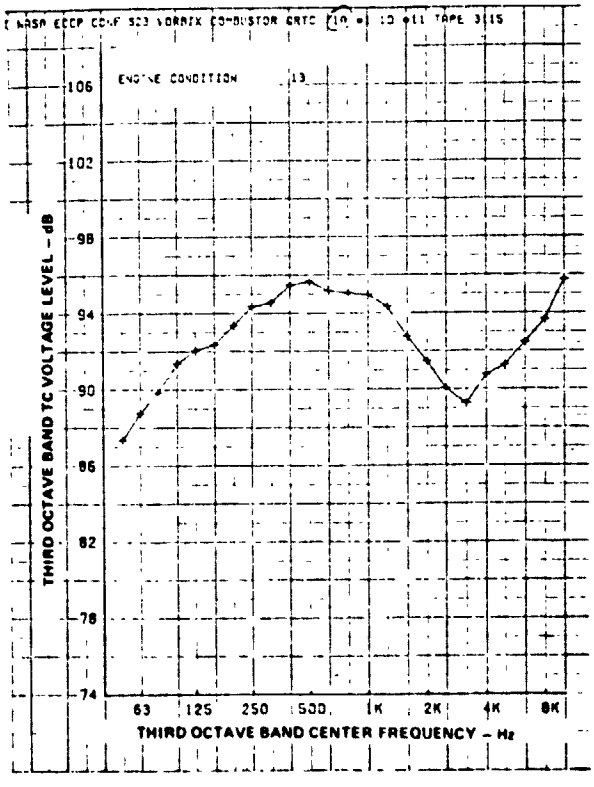
ENGINE CONDITION 13
THIRD OCTAVE BAND TC VOLTAGE LEVEL – dB
106
102
98
94
90
86
82
78
74
63
125
250
500
1K
2K
4K
8K
THIRD OCTAVE BAND CENTER FREQUENCY – Hz

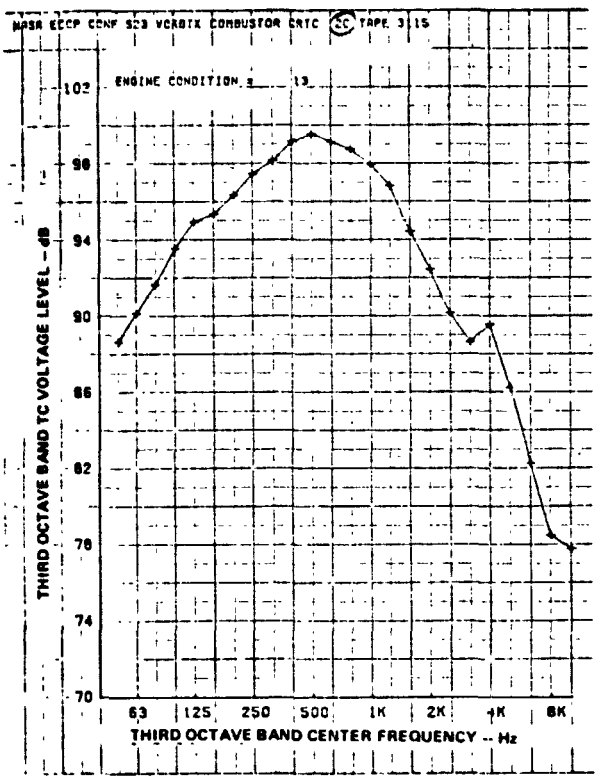
NASA ECCP CONF 523 VORBIX COMBUSTOR ORTC 3C TAPE 3 15
ENGINE CONDITION # 13
THIRD OCTAVE BAND TC VOLTAGE LEVEL – dB
102
98
94
90
86
82
78
74
70
63
125
250
500
1K
2K
4K
8K
THIRD OCTAVE BAND CENTER FREQUENCY – Hz

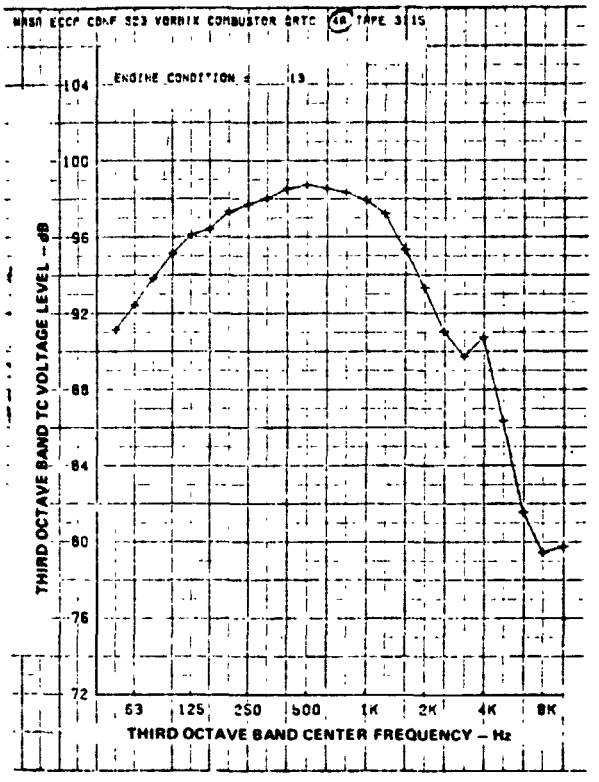
NASA ECCP CONF 523 VORBIX COMBUSTOR ORTC 4R TAPE 3 15
ENGINE CONDITION # 13
THIRD OCTAVE BAND TC VOLTAGE LEVEL – dB
104
100
96
92
88
84
80
76
72
63
125
250
500
1K
2K
4K
8K
THIRD OCTAVE BAND CENTER FREQUENCY – Hz

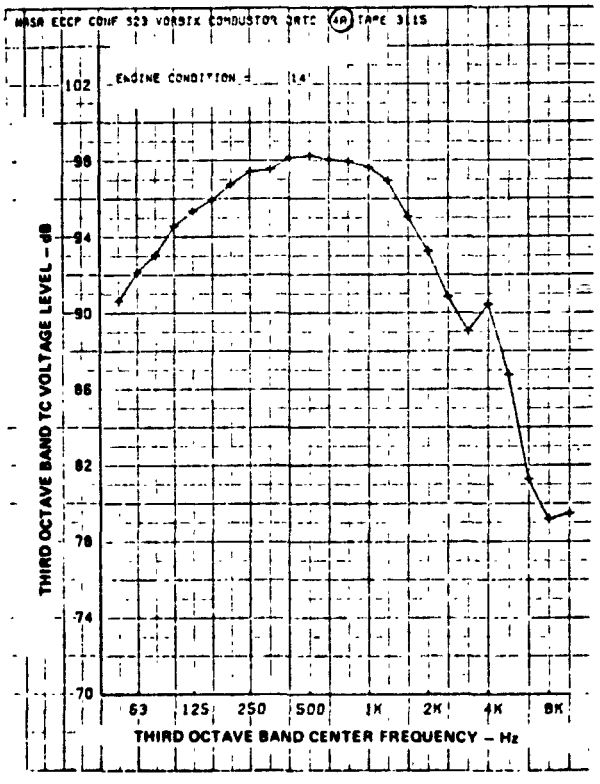
NASA ECCP CONF 523 VORBIX COMBUSTOR ORTC 4R TAPE 3 15
ENGINE CONDITION # 14
THIRD OCTAVE BAND TC VOLTAGE LEVEL – dB
102
98
94
90
86
82
78
74
70
63
125
250
500
1K
2K
4K
8K
THIRD OCTAVE BAND CENTER FREQUENCY – Hz

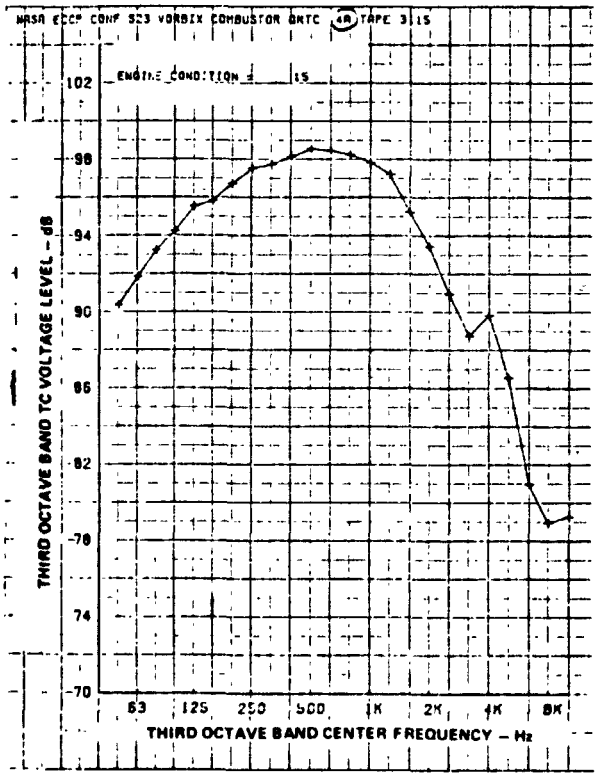
NASA ECCP CONF 523 VORBIX COMBUSTOR ORTC 4R TAPE 3 15
ENGINE CONDITION # 15
THIRD OCTAVE BAND TC VOLTAGE LEVEL – dB
102
98
94
90
86
82
78
74
70
63
125
250
500
1K
2K
4K
8K
THIRD OCTAVE BAND CENTER FREQUENCY – Hz

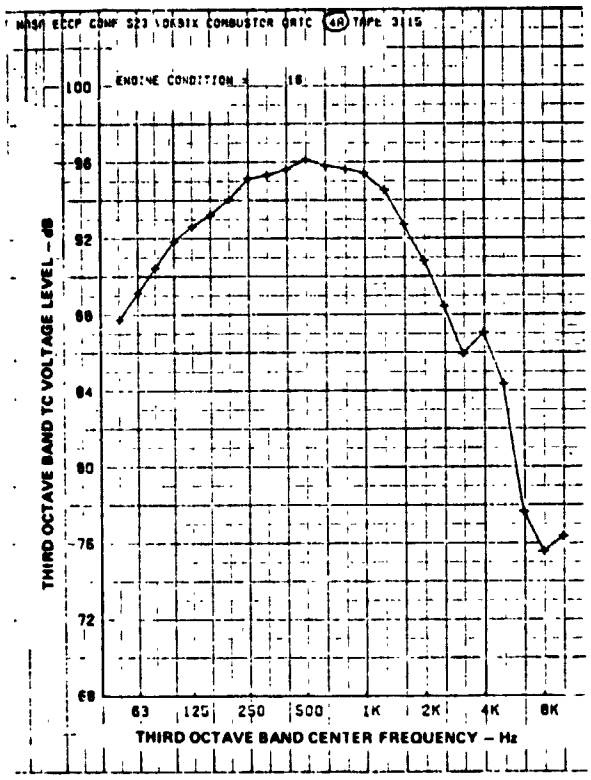
NASA ECCP COMP S23 \ DK31X COMBUSTOR ORTC (4R) TAPE 3115
ENGINE CONDITION 16.
100
96
92
88
84
80
76
72
68
THIRD OCTAVE BAND TC VOLTAGE LEVEL – dB
63
125
250
500
1K
2K
4K
8K
THIRD OCTAVE BAND CENTER FREQUENCY – Hz

APPENDIX B-3

THERMOCOUPLE CORRELOGRAMS

Normalized auto and cross correlation function machine plots are presented in this Appendix. The relevant transducer locations are illustrated on each plot. Selected cross-correlations between thermocouple elements and wall pressure transducers are also included.

THERMOCOUPLE IDENTIFICATION CODE

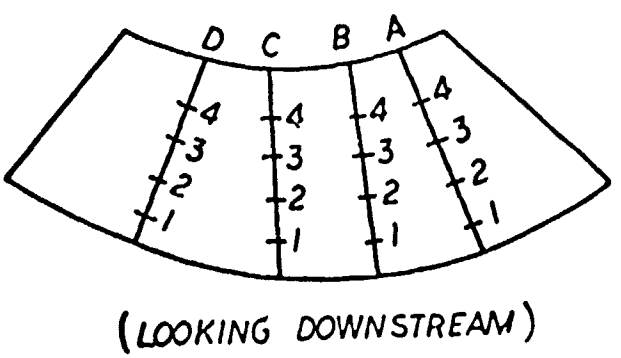

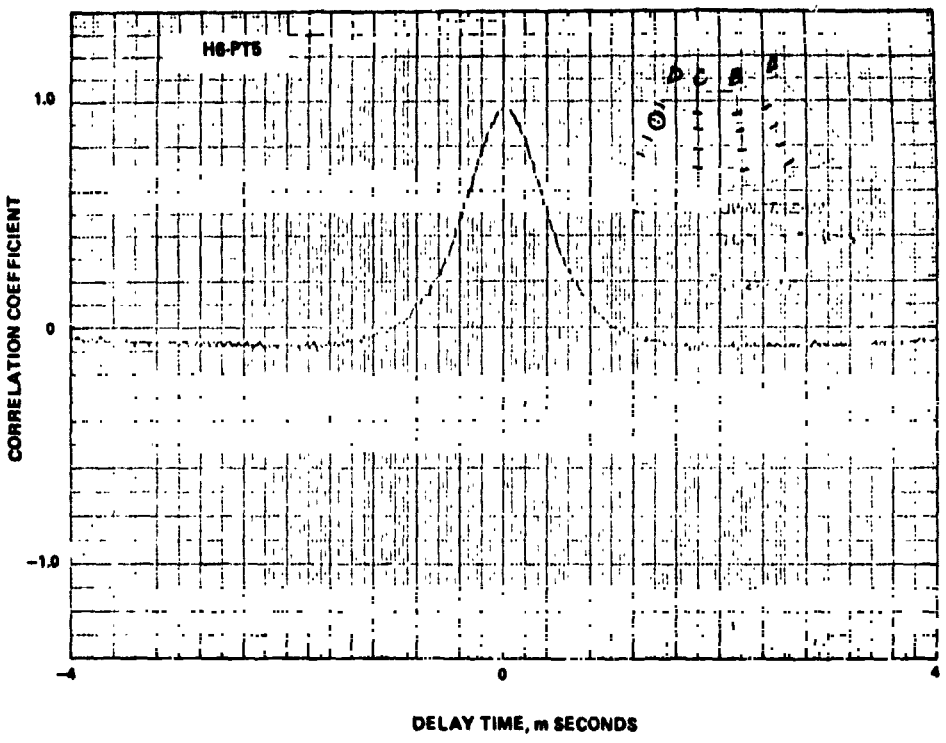

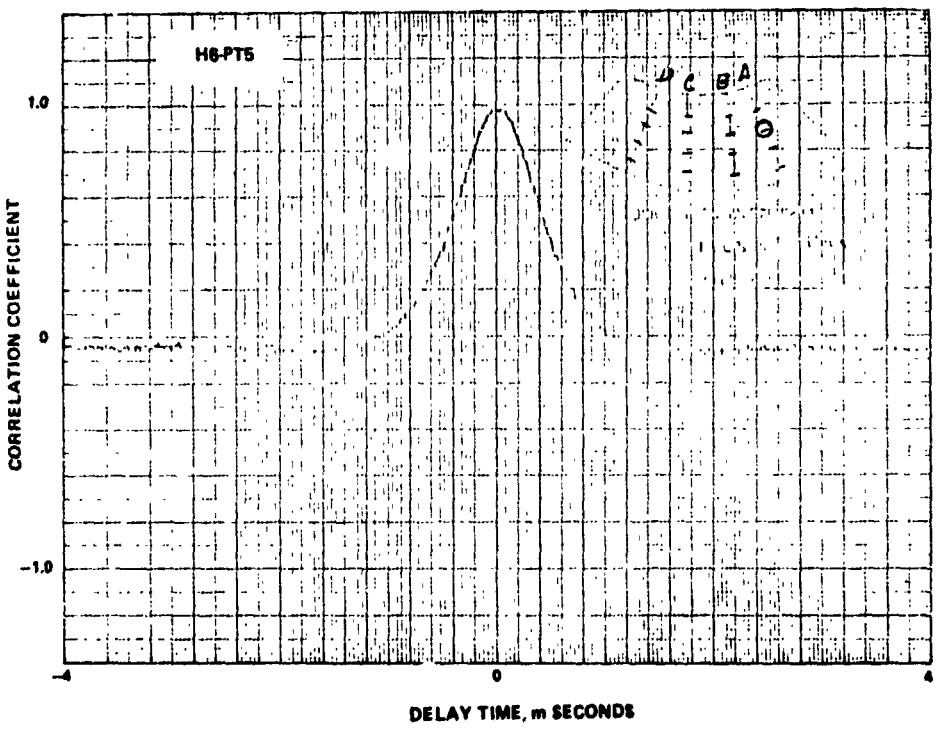

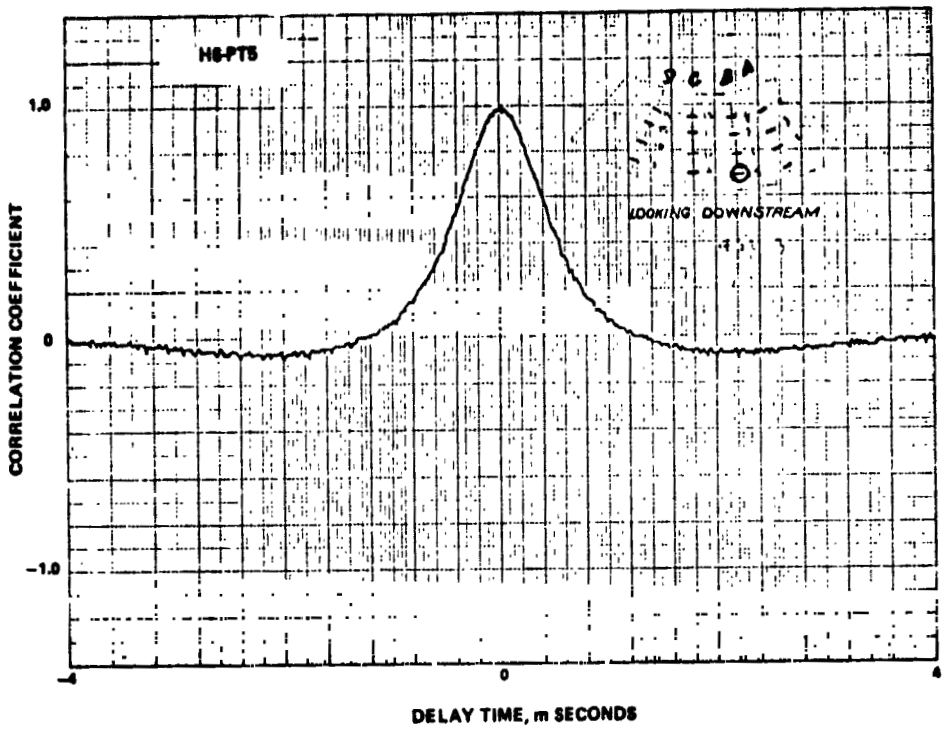
H6-PT5
1.0
0
-1.0
CORRELATION COEFFICIENT
LOOKING DOWNSTREAM
-4
0
4
DELAY TIME, m SECONDS

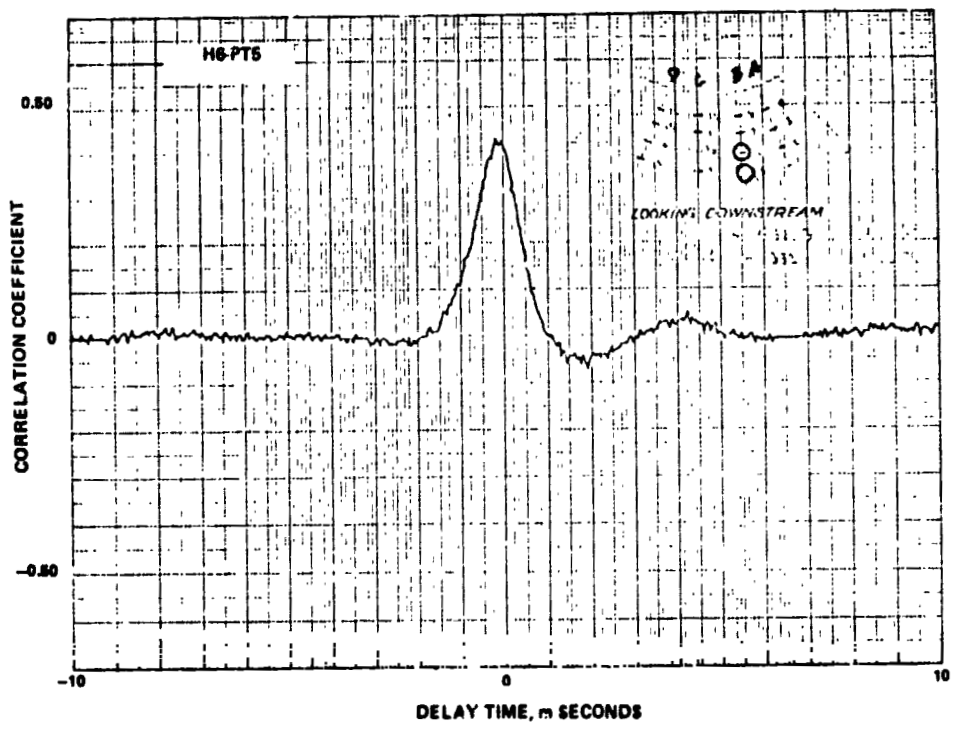
H6-PT5
0.50
0
-0.50
CORRELATION COEFFICIENT
LOOKING DOWNSTREAM
-10
0
10
DELAY TIME, m SECONDS

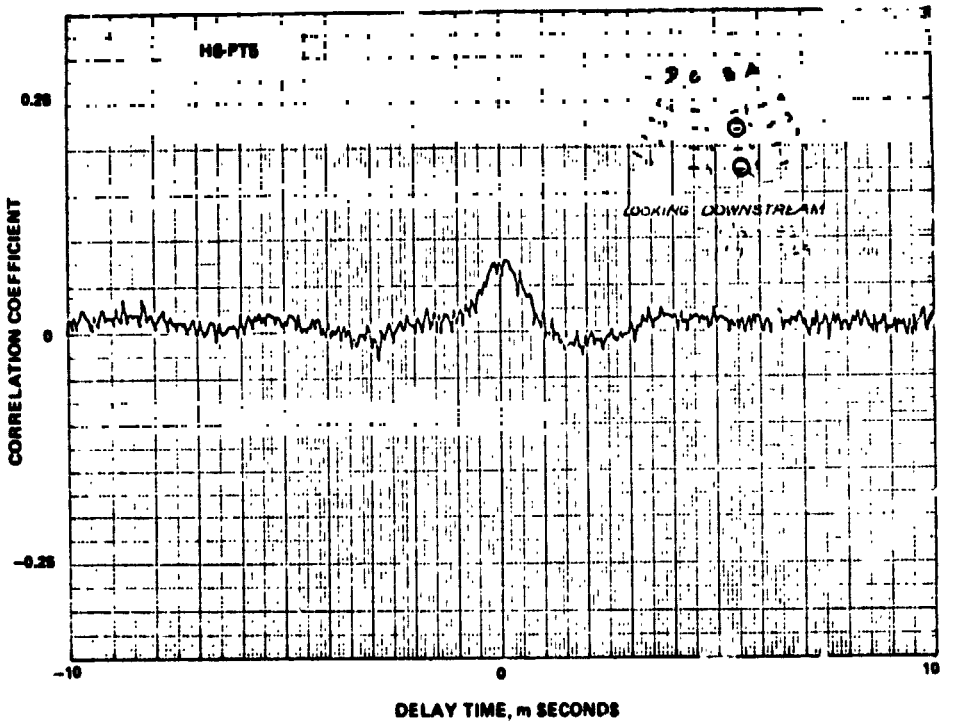
H6-PT5
0.25
0
-0.25
CORRELATION COEFFICIENT
LOOKING DOWNSTREAM
-10
0
10
DELAY TIME, m SECONDS

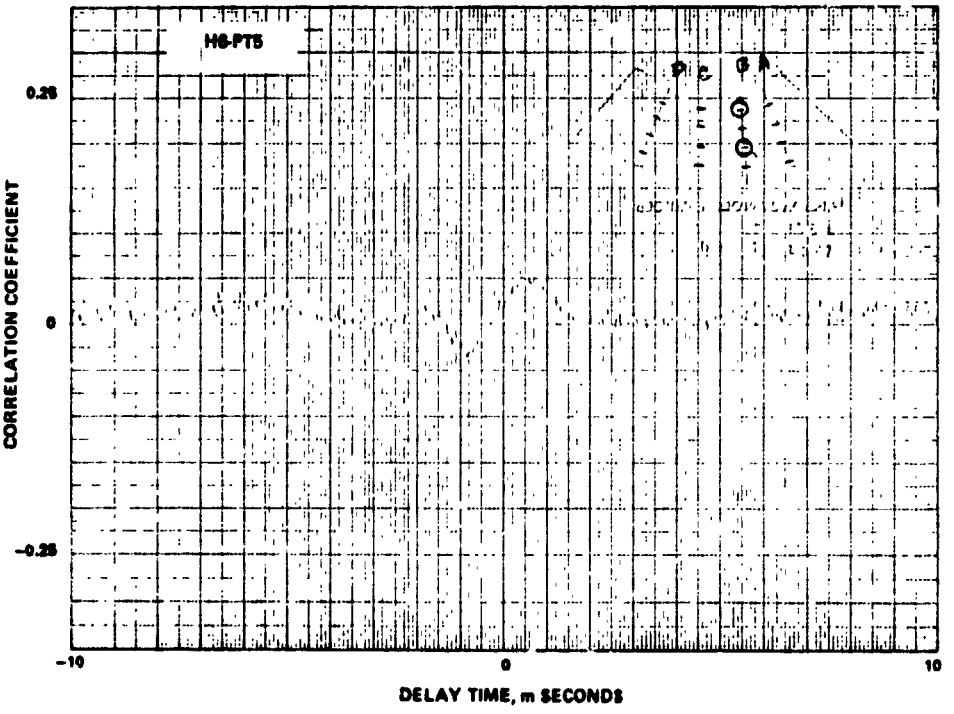
H6-PT5
0.25
0
-0.25
CORRELATION COEFFICIENT
-10
0
10
DELAY TIME, m SECONDS

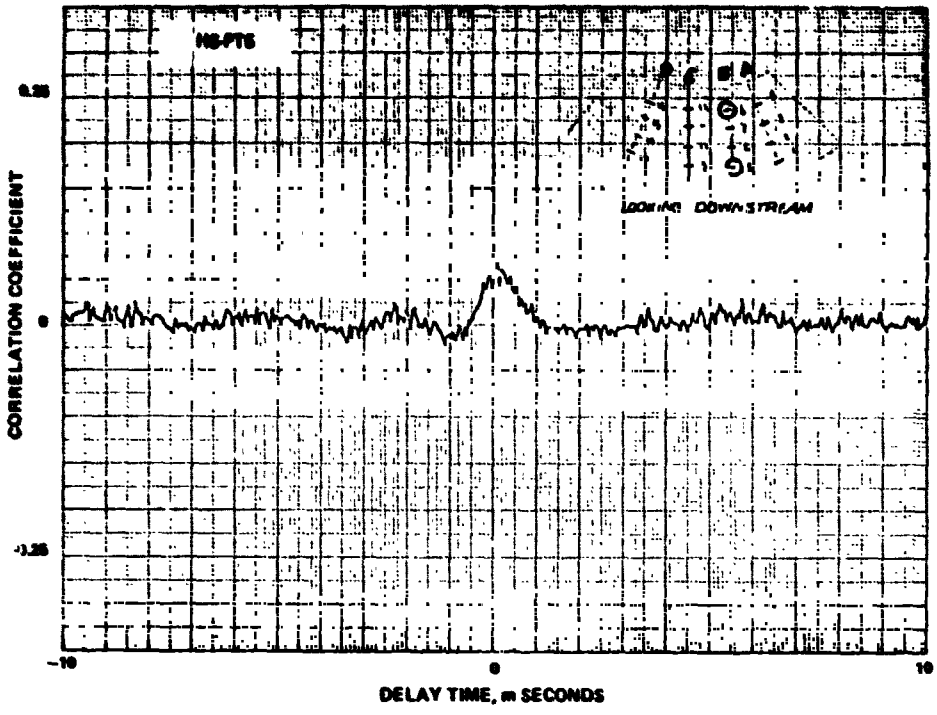

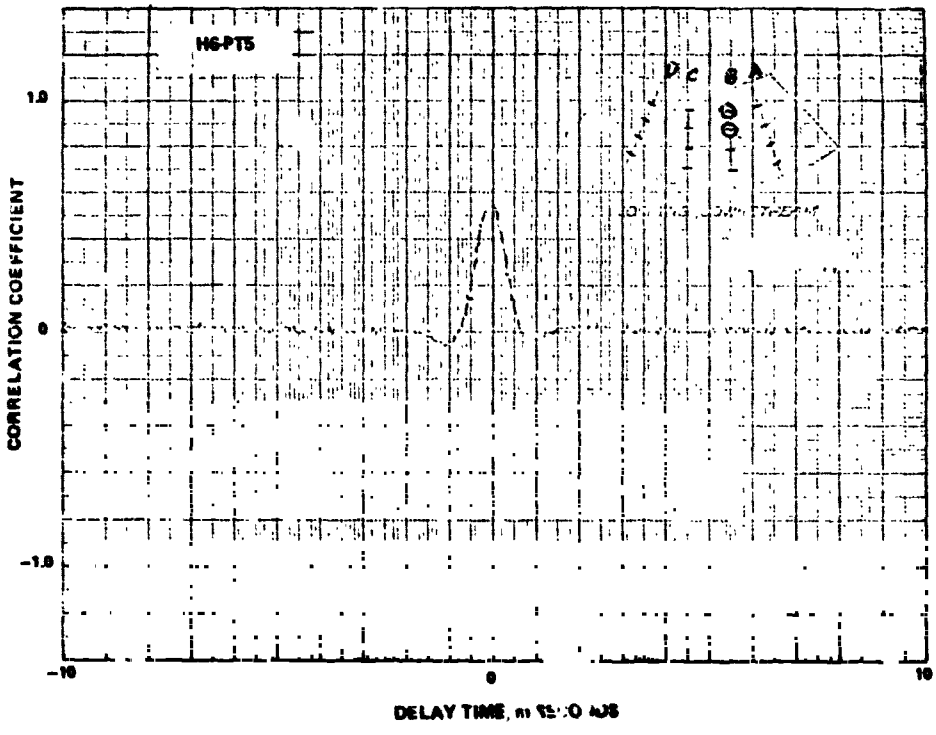

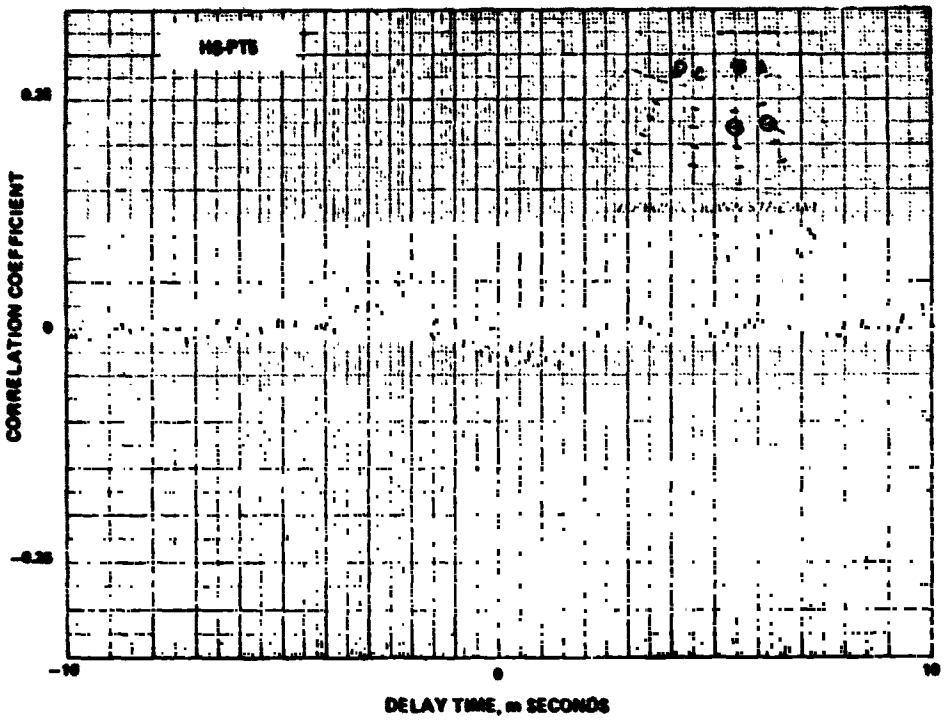
HG-PT5
0.25
0
-0.25
CORRELATION COEFFICIENT
-10
0
10
DELAY TIME, m SECONDS

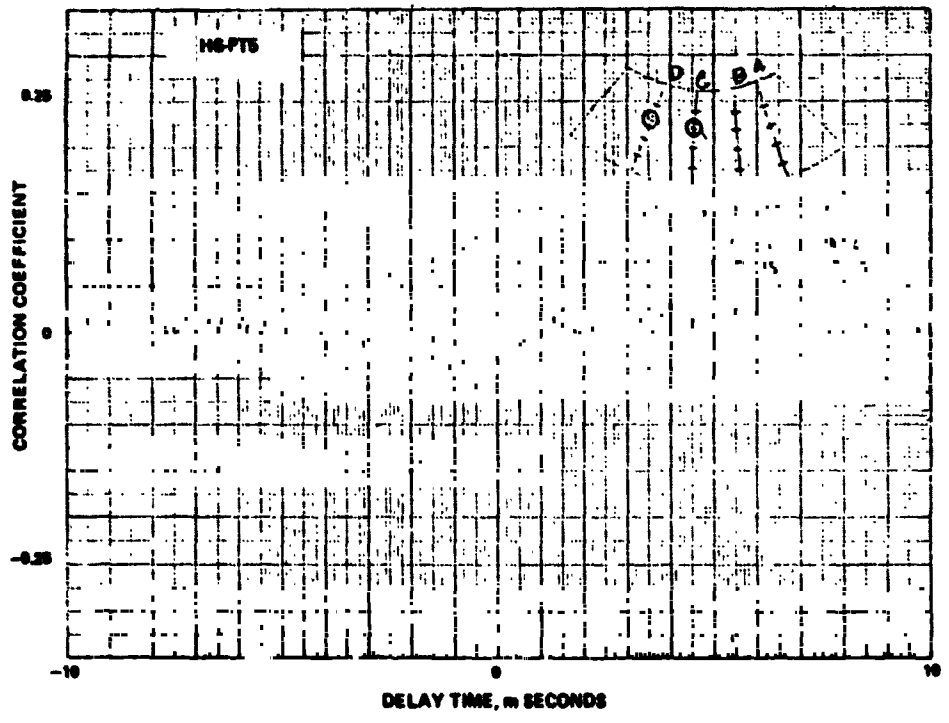
HG-PT5
0.25
0
-0.25
CORRELATION COEFFICIENT
-10
0
10
DELAY TIME, m SECONDS

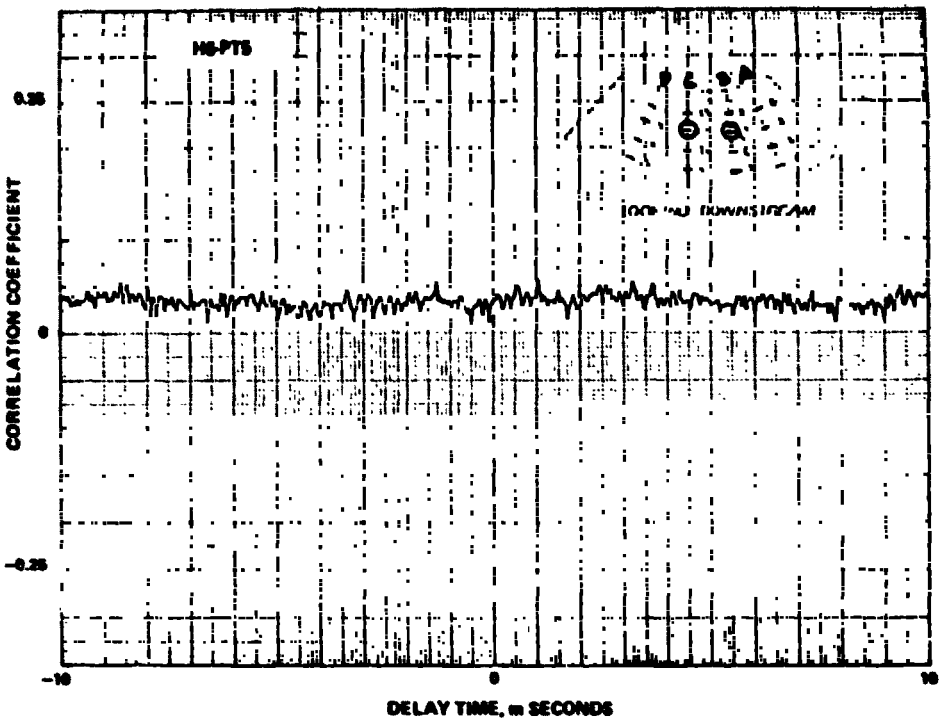
HS-PTS
CORRELATION COEFFICIENT
0.25
0
-0.25
-10
0
10
DELAY TIME, m SECONDS

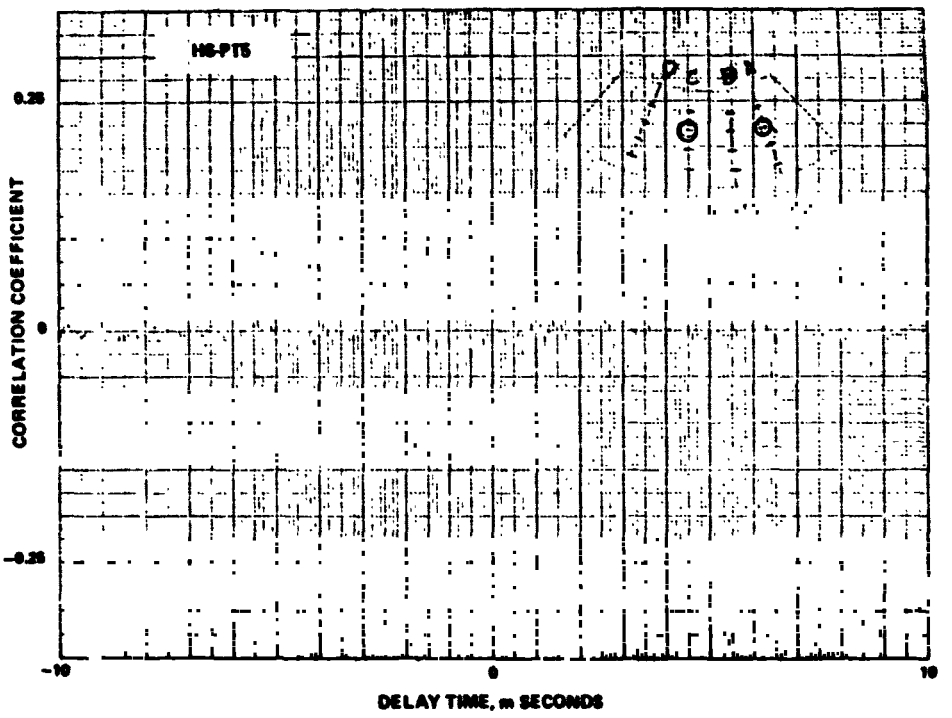
HS-PTS
CORRELATION COEFFICIENT
0.25
0
-0.25
-10
0
10
DELAY TIME, m SECONDS

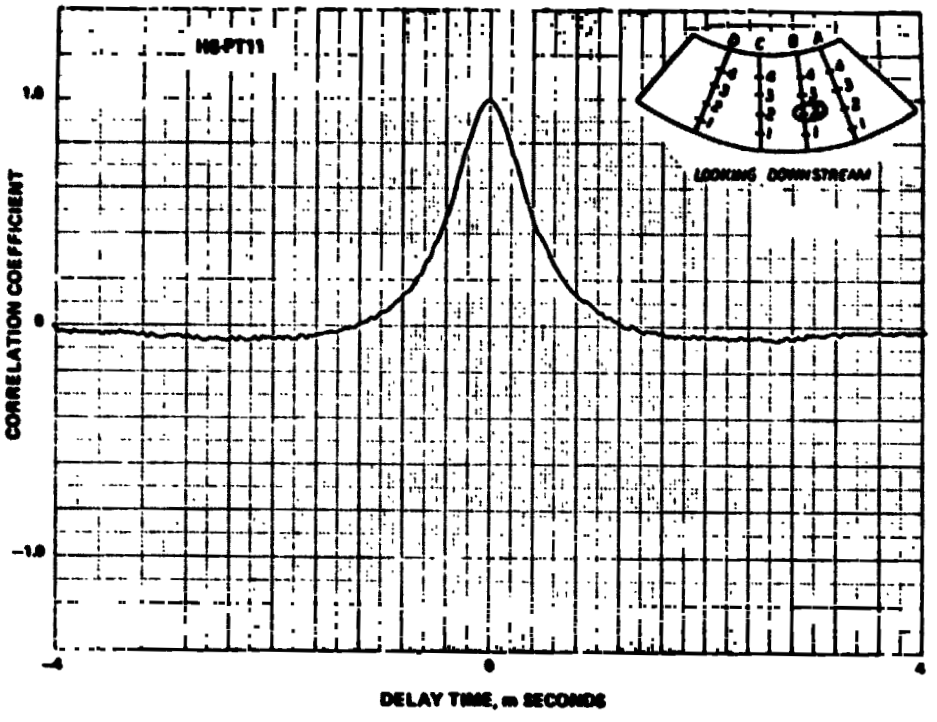
HS-PT11
D C B A
LOOKING DOWNSTREAM
CORRELATION COEFFICIENT
1.0
0
-1.0
-4
0
4
DELAY TIME, m SECONDS

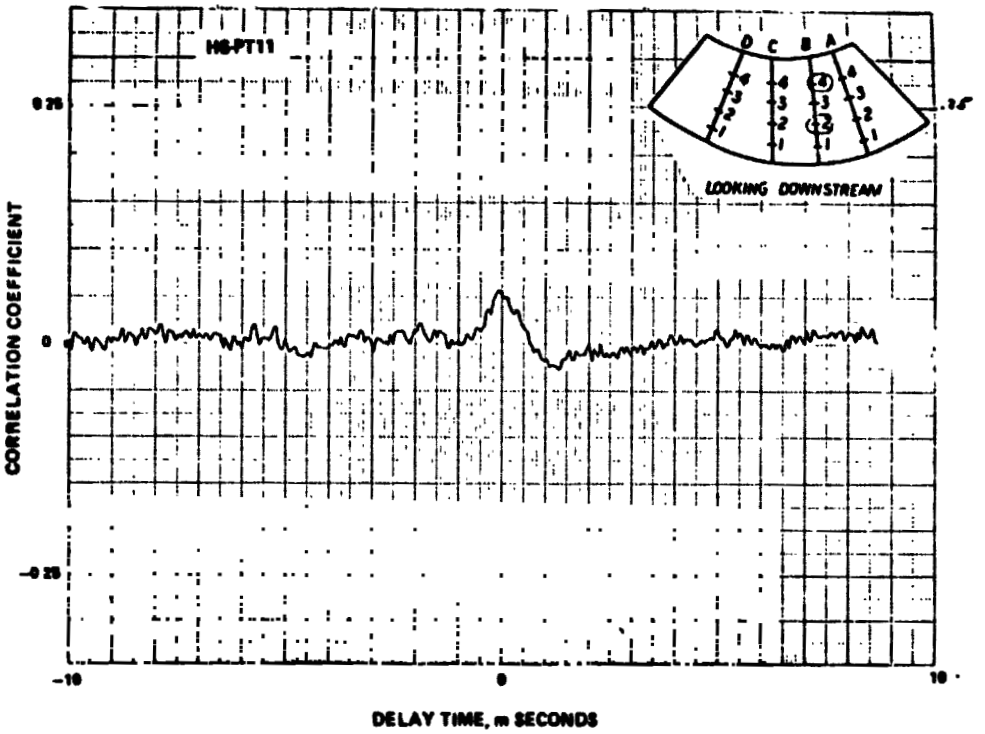
HS-PT11
D C B A
LOOKING DOWNSTREAM
CORRELATION COEFFICIENT
0.25
0
-0.25
-10
0
10
DELAY TIME, m SECONDS

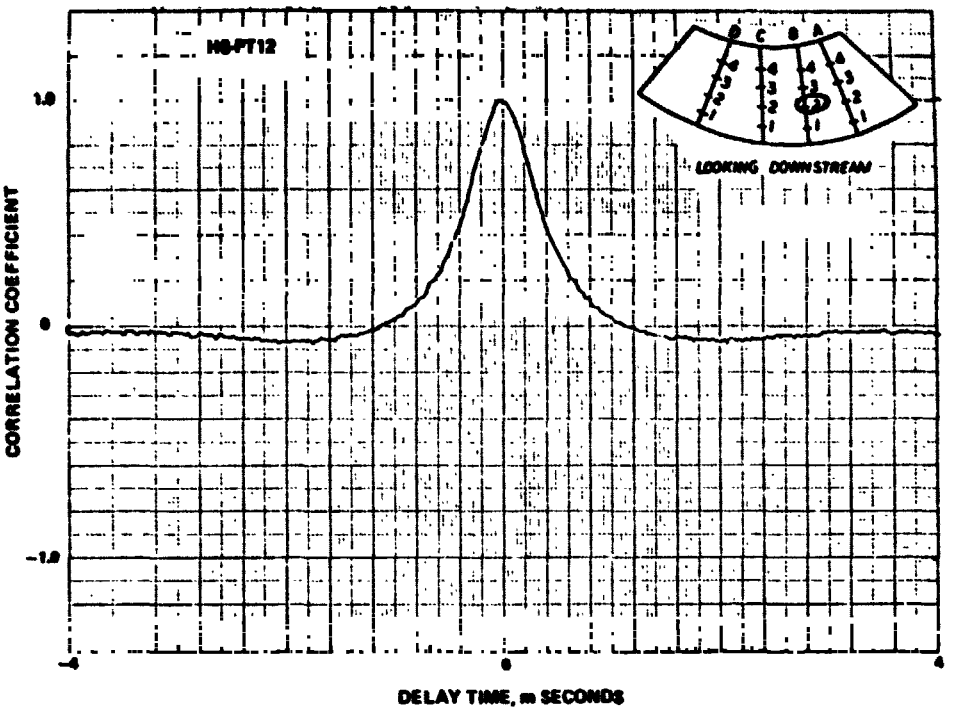
HS-PT12
1.0
0
-1.0
CORRELATION COEFFICIENT
-4
0
4
DELAY TIME, m SECONDS
D C B A
LOOKING DOWNSTREAM

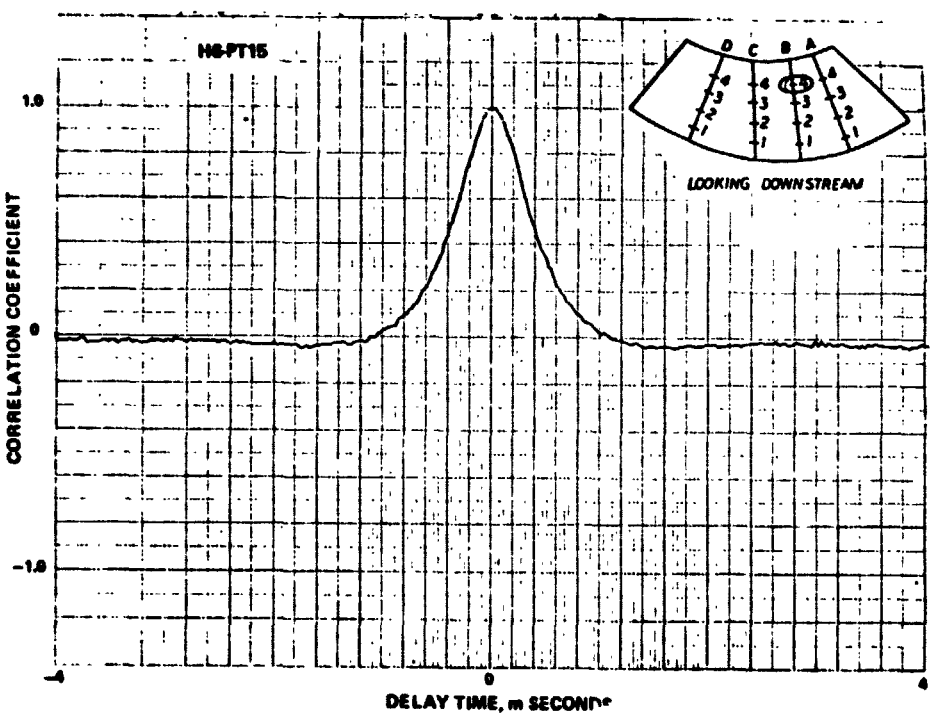
HS-PT15
1.0
0
-1.0
CORRELATION COEFFICIENT
-4
0
4
DELAY TIME, m SECONDS
D C B A
LOOKING DOWNSTREAM

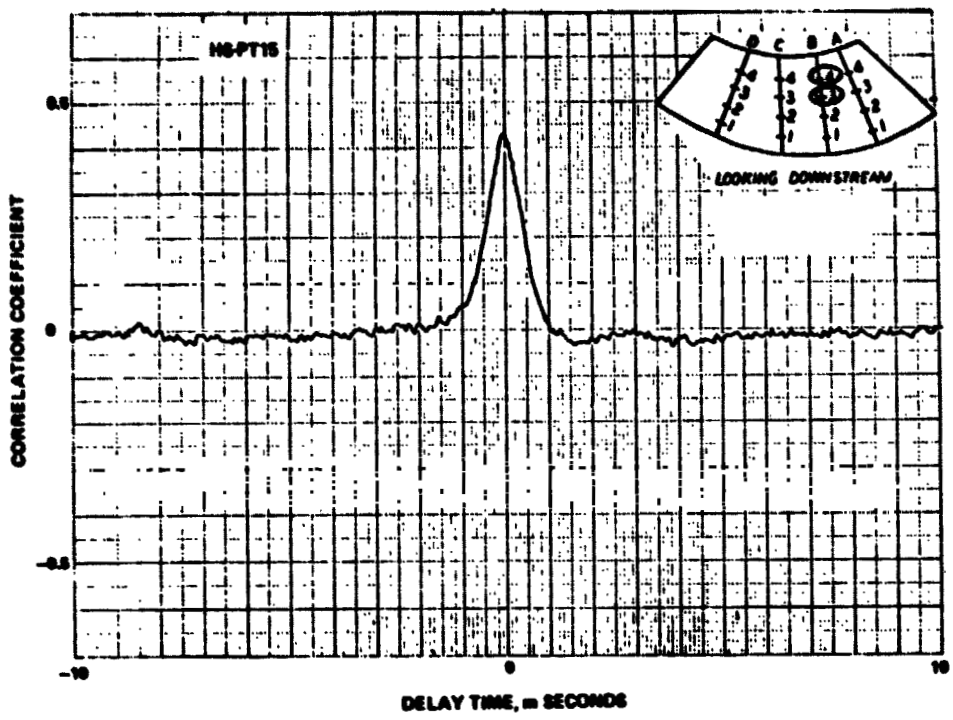
HS-PT15
CORRELATION COEFFICIENT
0.5
0
-0.5
-10
0
10
DELAY TIME, m SECONDS
D C B A
LOOKING DOWNSTREAM

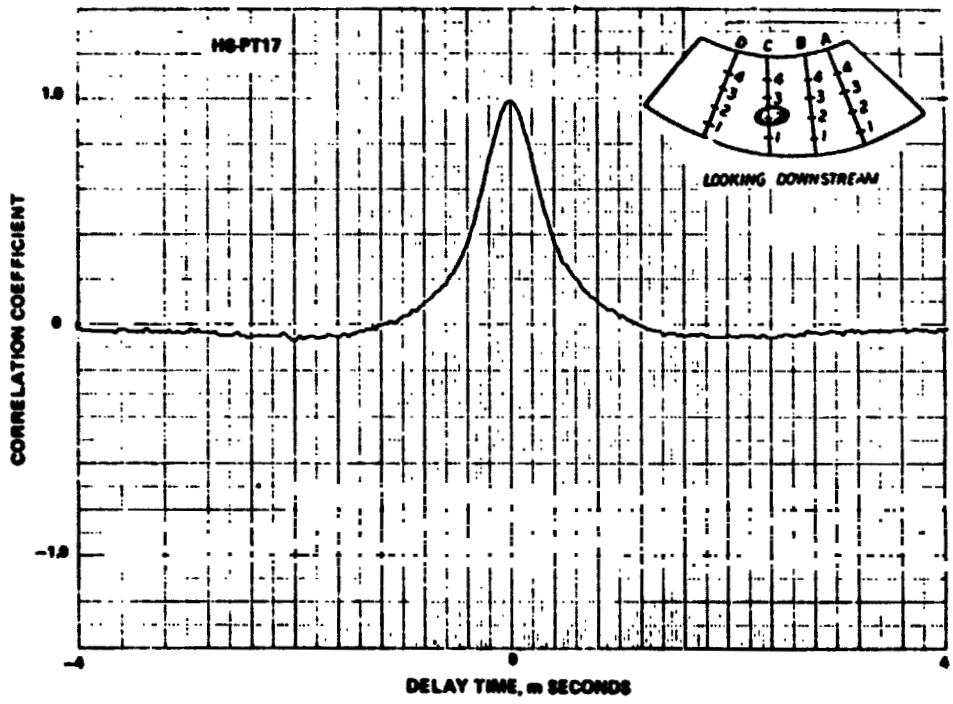
HS-PT17
CORRELATION COEFFICIENT
1.0
0
-1.0
-4
0
4
DELAY TIME, m SECONDS
D C B A
LOOKING DOWNSTREAM

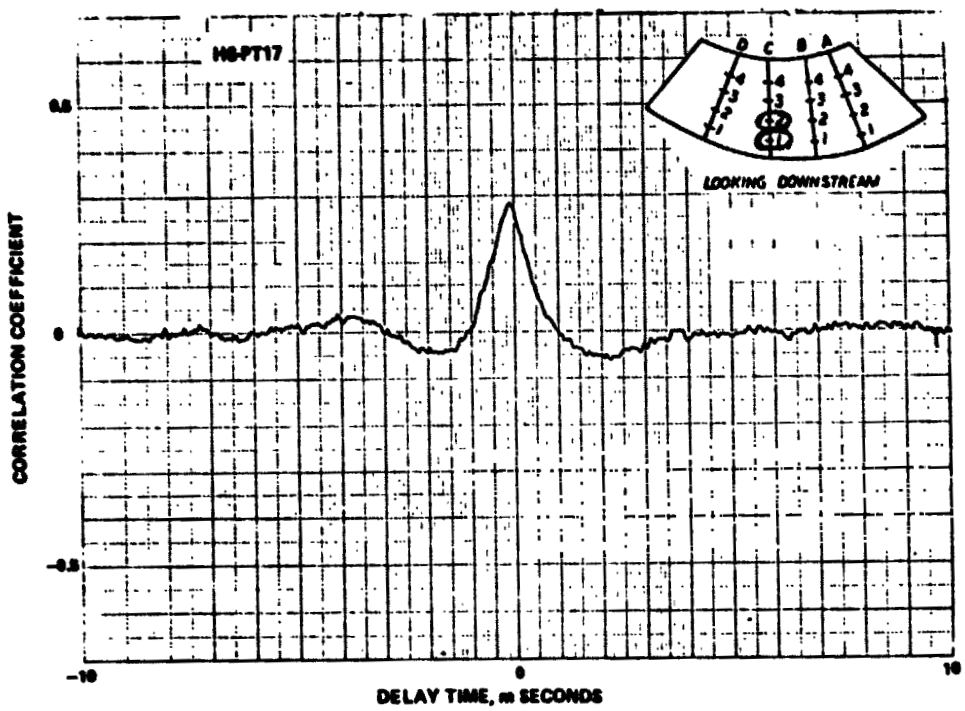
HS-PT17
0.5
0
-0.5
CORRELATION COEFFICIENT
-10
0
10
DELAY TIME, m SECONDS
D C B A
LOOKING DOWNSTREAM

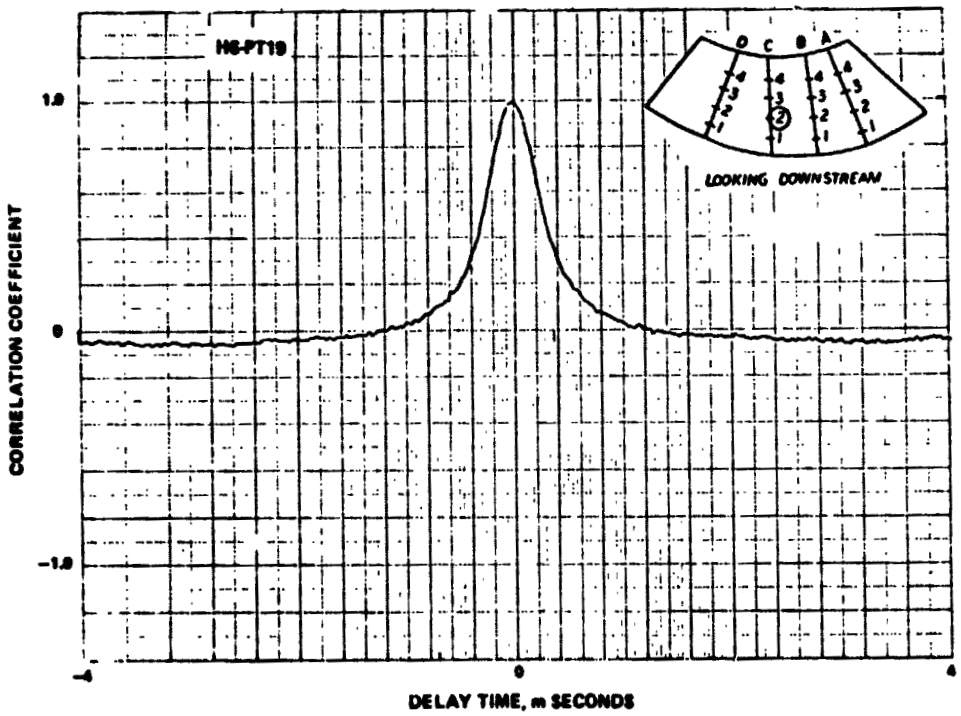
HS-PT19
1.0
0
-1.0
CORRELATION COEFFICIENT
-4
0
4
DELAY TIME, m SECONDS
D C B A
LOOKING DOWNSTREAM

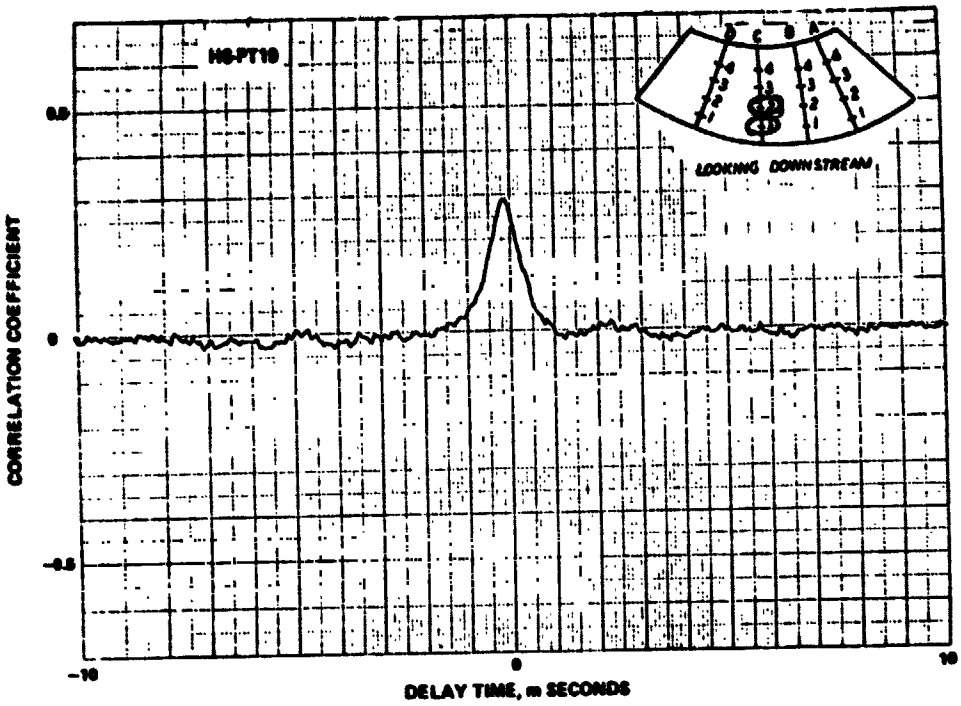
H6-PT10
D C B A
LOOKING DOWNSTREAM
CORRELATION COEFFICIENT
0.5
0
-0.5
-10
0
10
DELAY TIME, m SECONDS

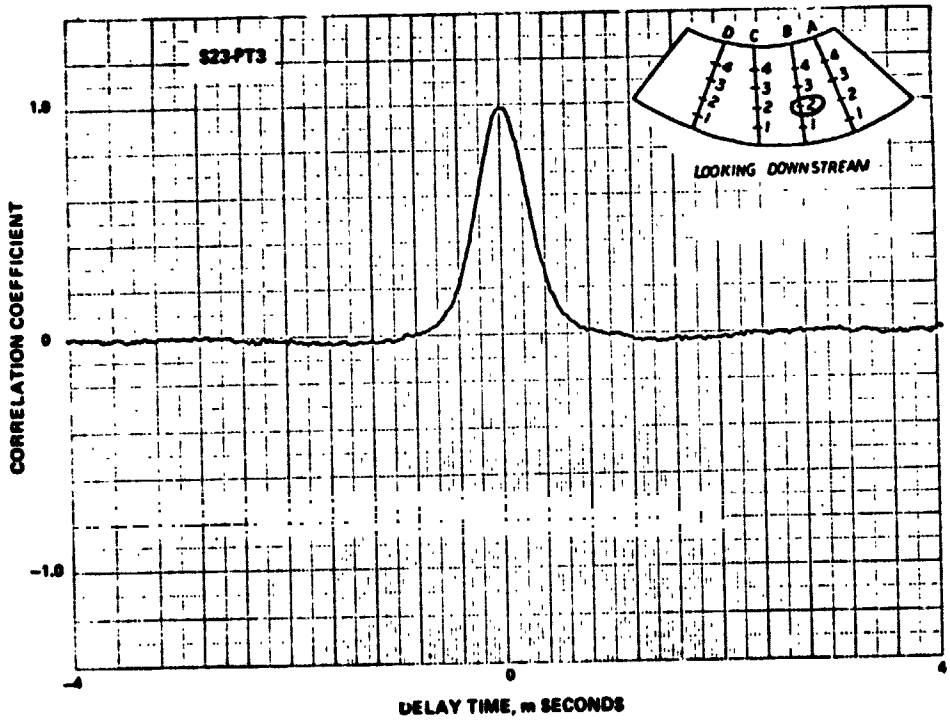
S23-PT3
D C B A
LOOKING DOWNSTREAM
CORRELATION COEFFICIENT
1.0
0
-1.0
-4
0
4
DELAY TIME, m SECONDS

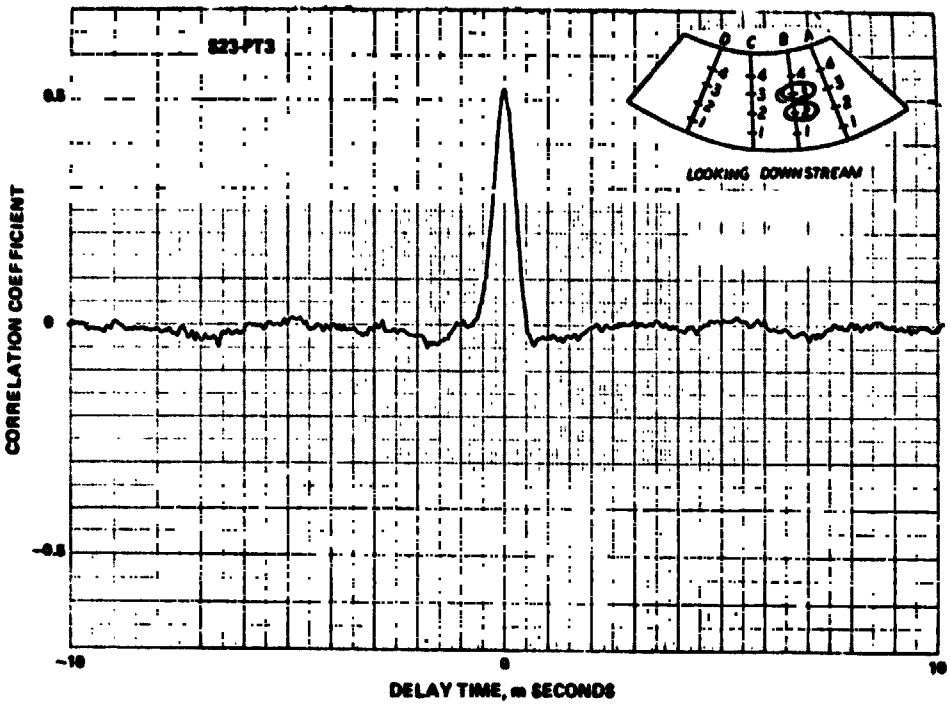

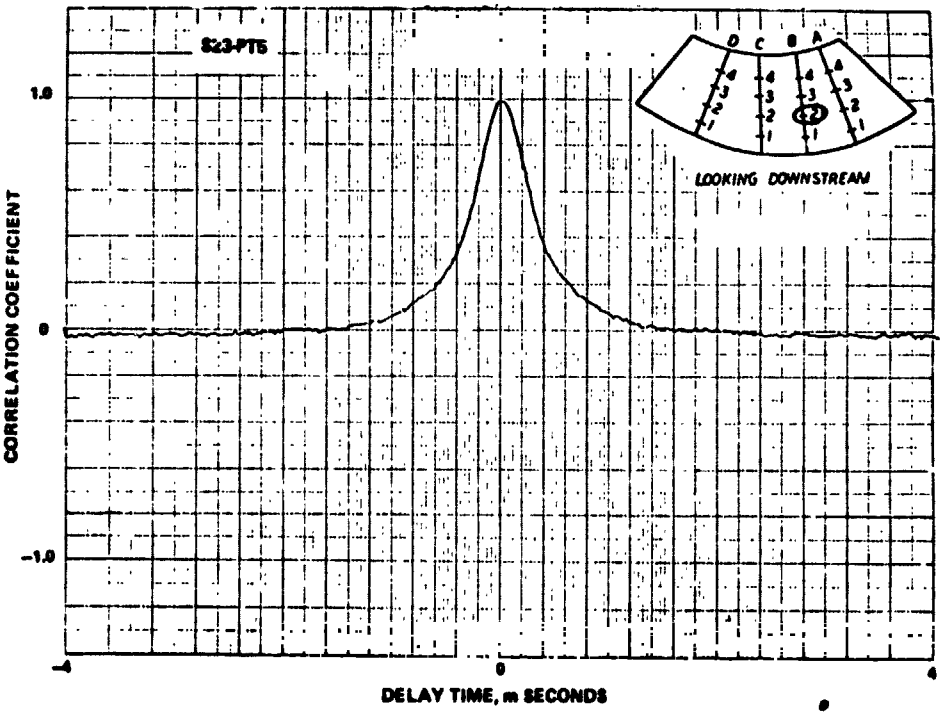

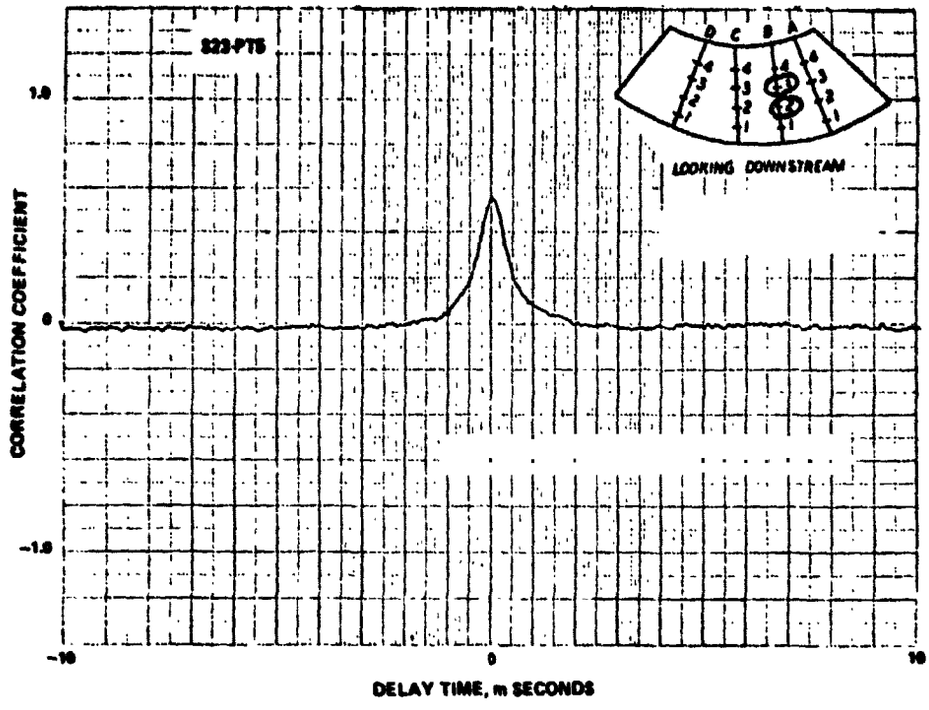
S23-PT5
D C B A
LOOKING DOWNSTREAM
CORRELATION COEFFICIENT
1.0
0
-1.0
-10
0
10
DELAY TIME, m SECONDS

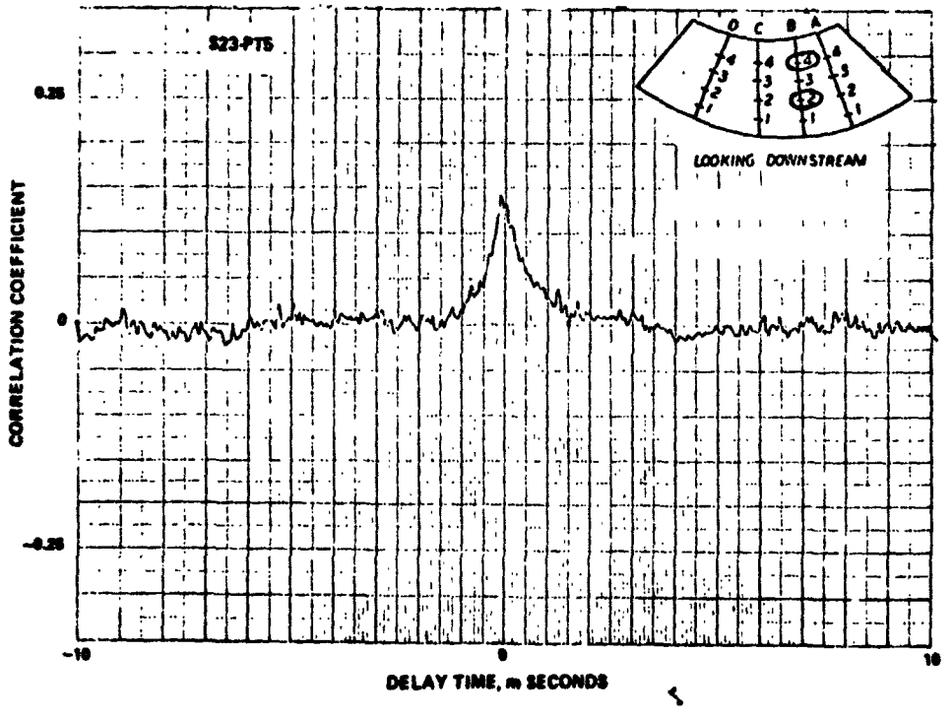
S23-PT5
D C B A
LOOKING DOWNSTREAM
CORRELATION COEFFICIENT
0.25
0
-0.25
-10
0
10
DELAY TIME, m SECONDS

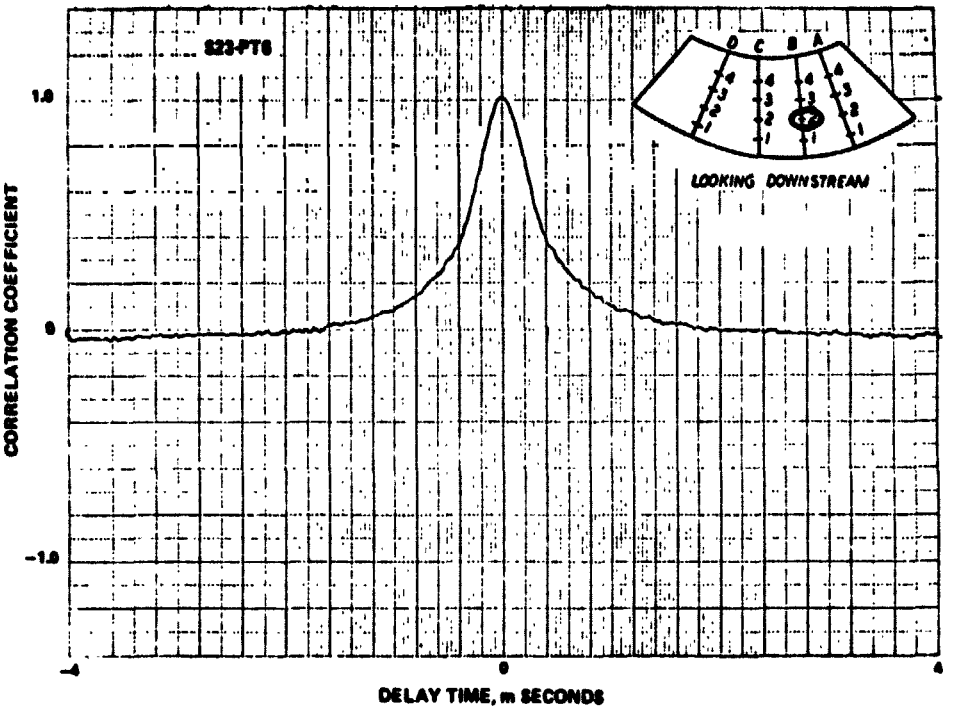
S23-PT6
1.0
0
-1.0
CORRELATION COEFFICIENT
-4
0
4
DELAY TIME, m SECONDS
D C B A
LOOKING DOWNSTREAM

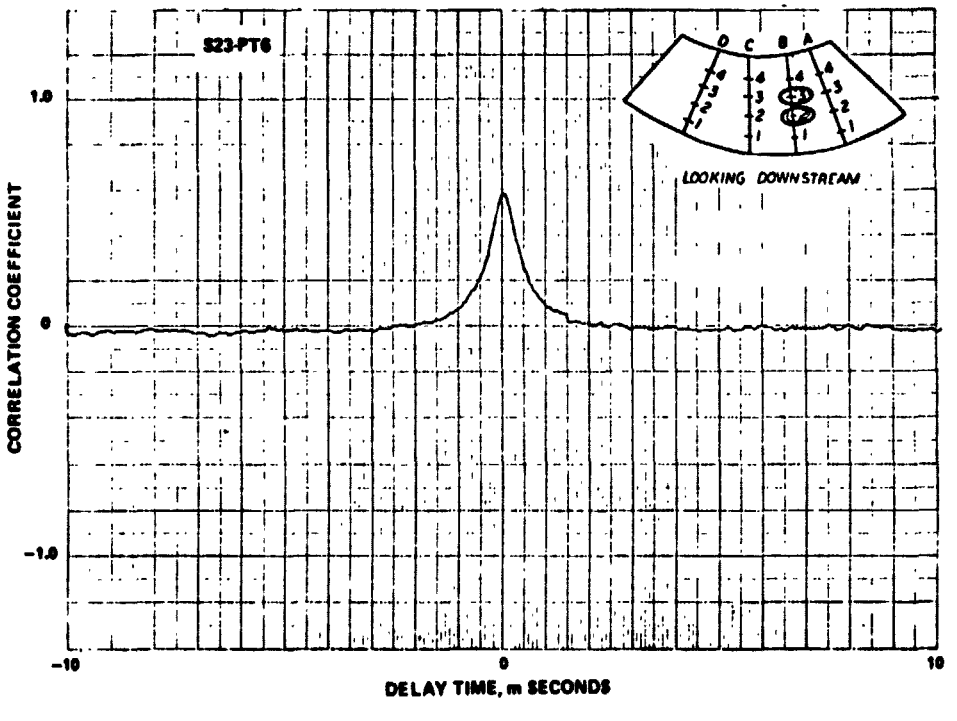
S23-PT6
1.0
0
-1.0
CORRELATION COEFFICIENT
-10
0
10
DELAY TIME, m SECONDS
D C B A
LOOKING DOWNSTREAM

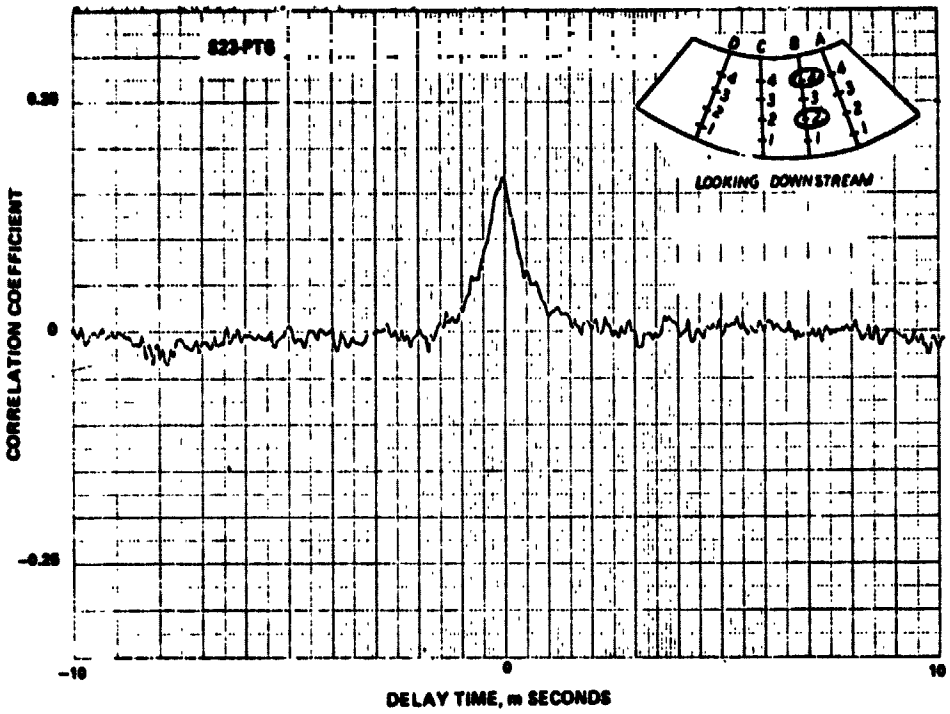
S23-PT6
D C B A
LOOKING DOWNSTREAM
0.25
0
-0.25
CORRELATION COEFFICIENT
-10
0
10
DELAY TIME, m SECONDS

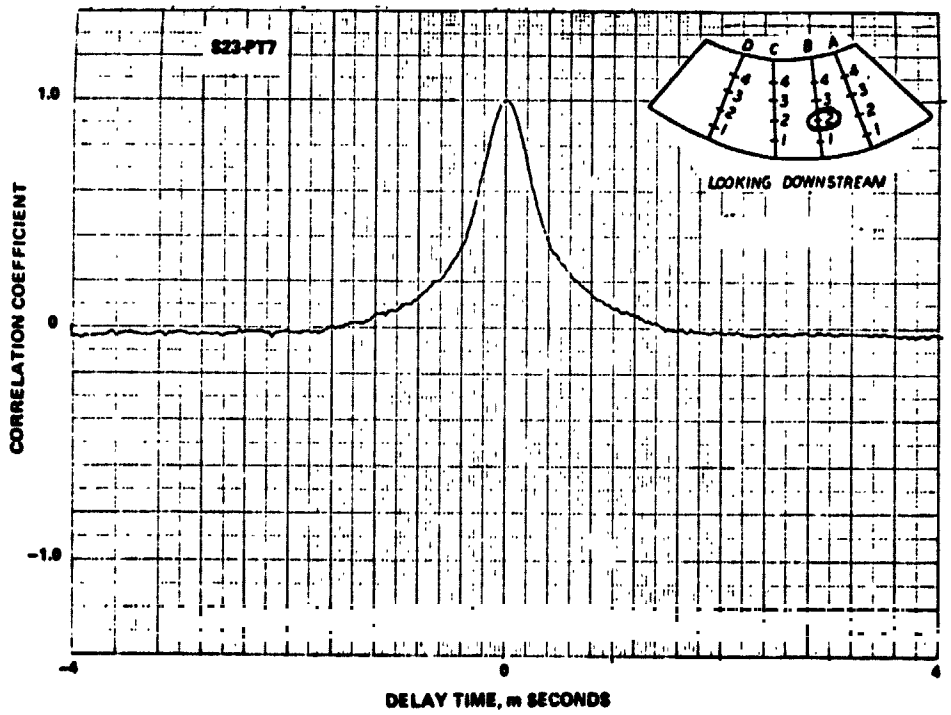
S23-PT7
D C B A
LOOKING DOWNSTREAM
1.0
0
-1.0
CORRELATION COEFFICIENT
-4
0
4
DELAY TIME, m SECONDS

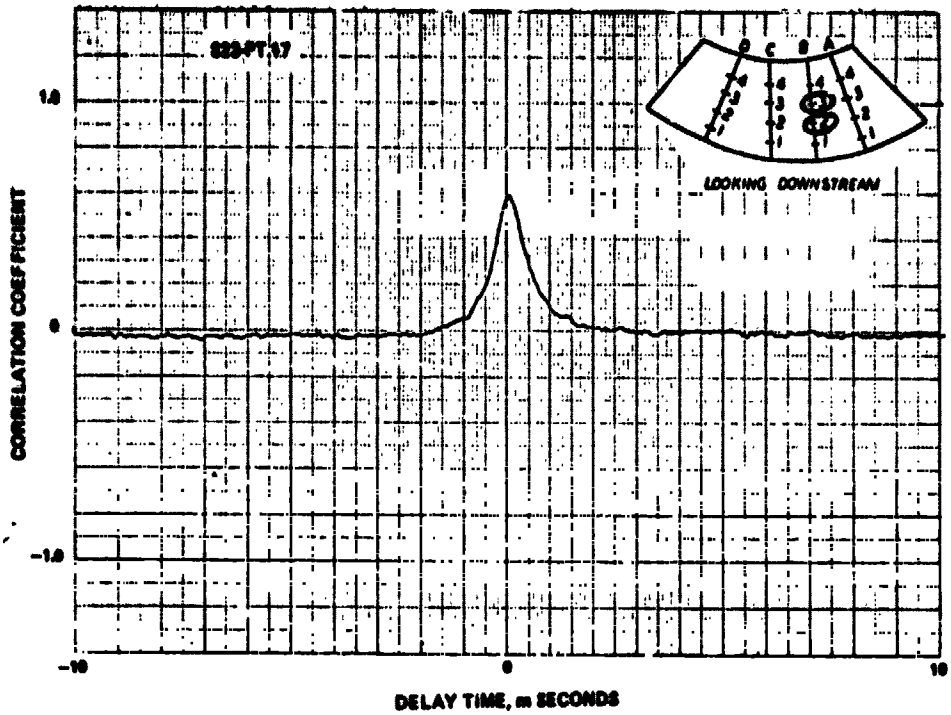
S23-PT17
D C B A
LOOKING DOWNSTREAM
1.0
0
-1.0
CORRELATION COEFFICIENT
-10
0
10
DELAY TIME, m SECONDS

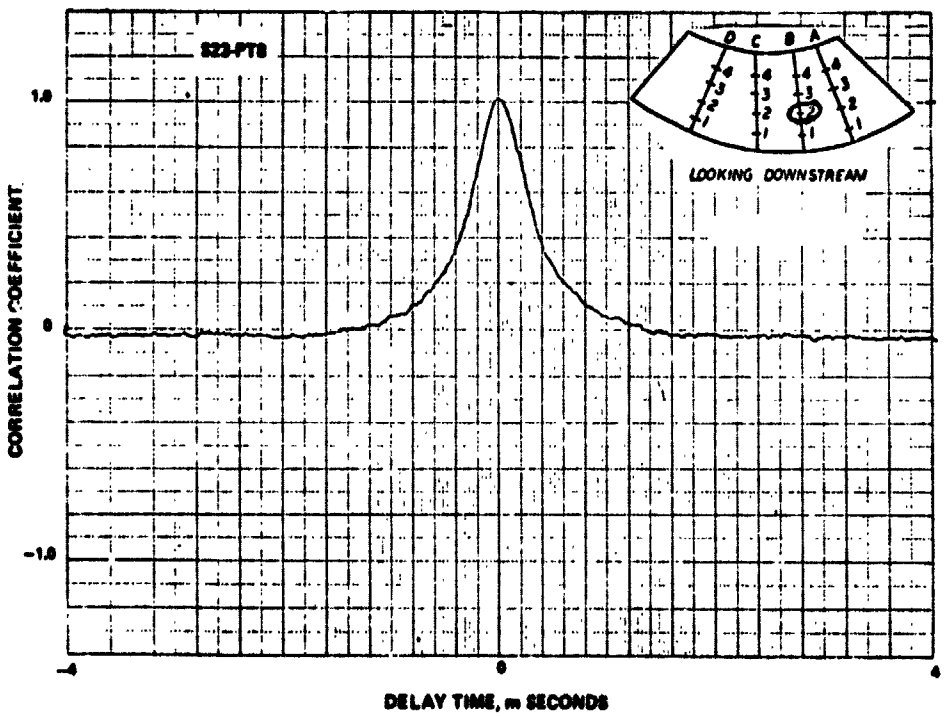
S23-PT8
D C B A
LOOKING DOWNSTREAM
1.0
0
-1.0
CORRELATION COEFFICIENT
-4
0
4
DELAY TIME, m SECONDS

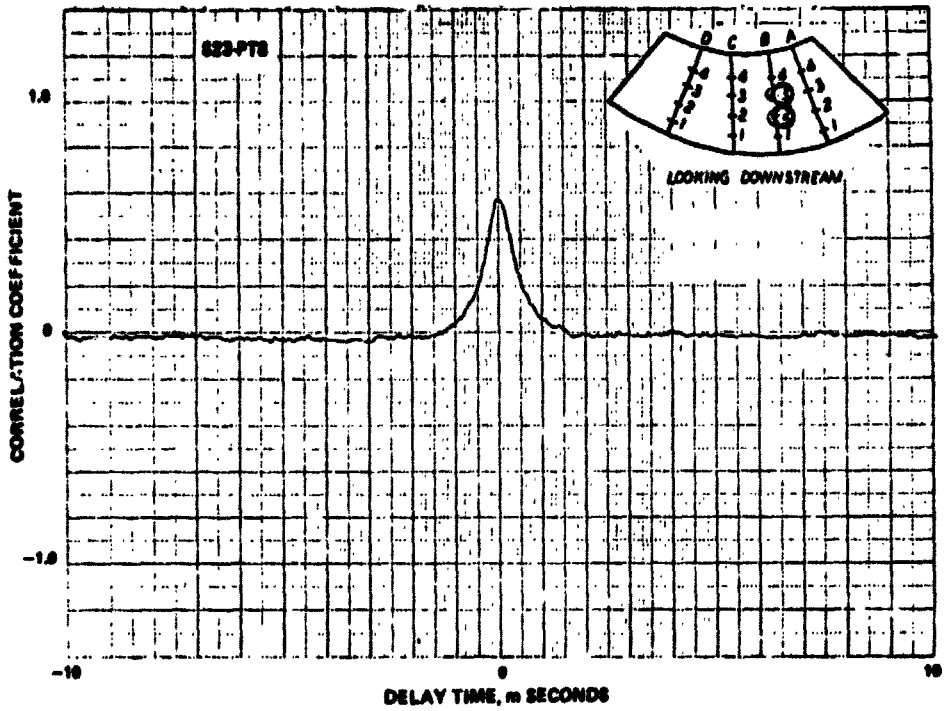
S23-PT8
D C B A
LOOKING DOWNSTREAM
1.0
0
-1.0
CORRELATION COEFFICIENT
-10
0
10
DELAY TIME, m SECONDS

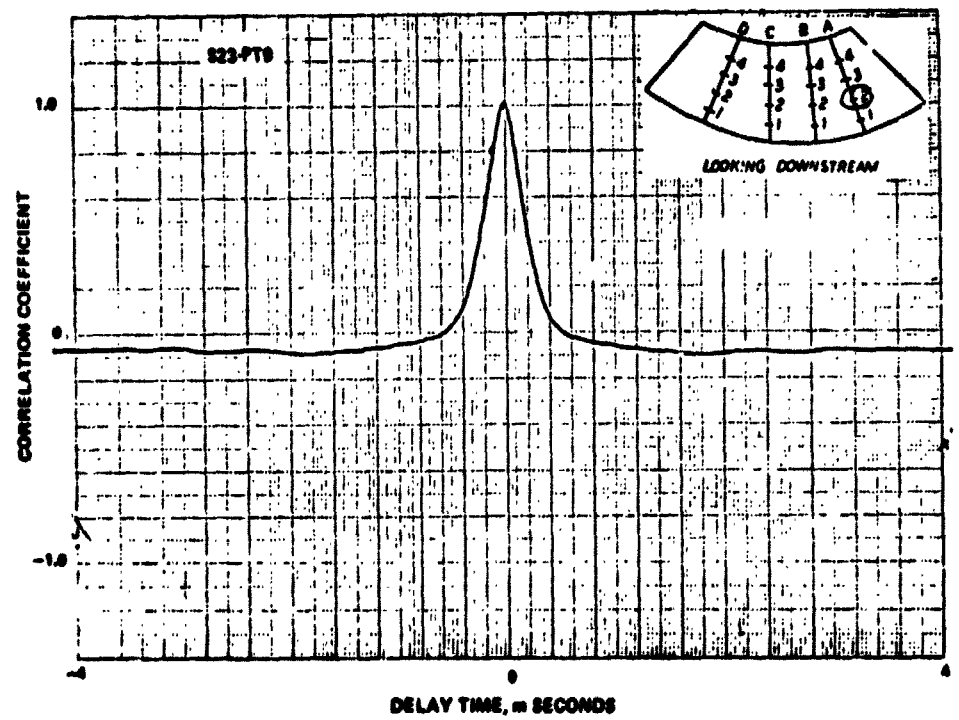
S23-PT8
D C B A
LOOKING DOWNSTREAM
1.0
0
-1.0
CORRELATION COEFFICIENT
-4
0
4
DELAY TIME, m SECONDS

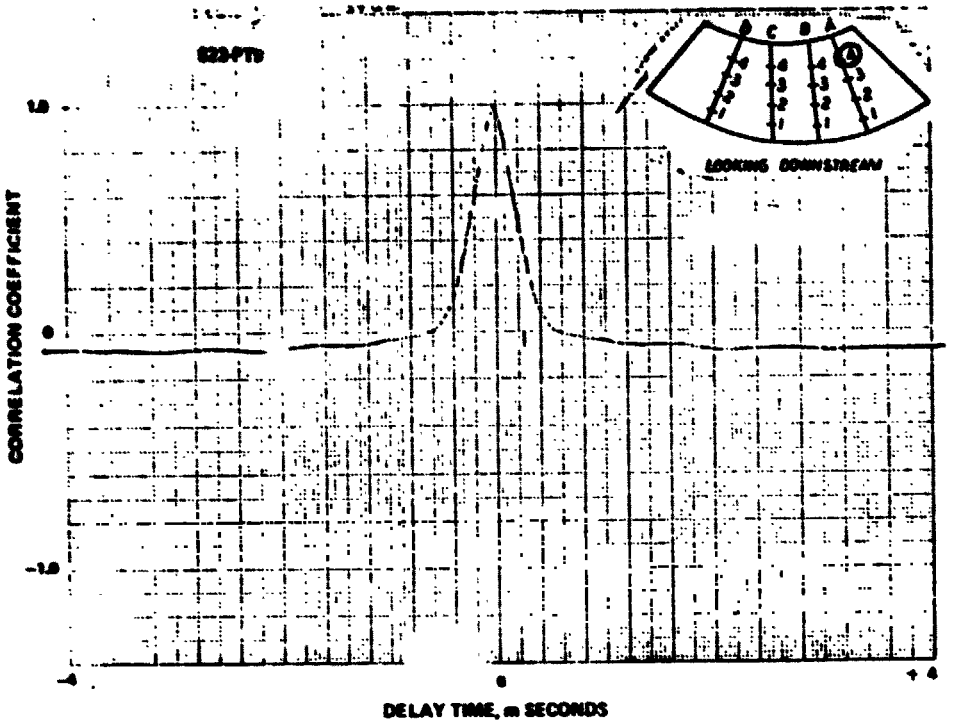

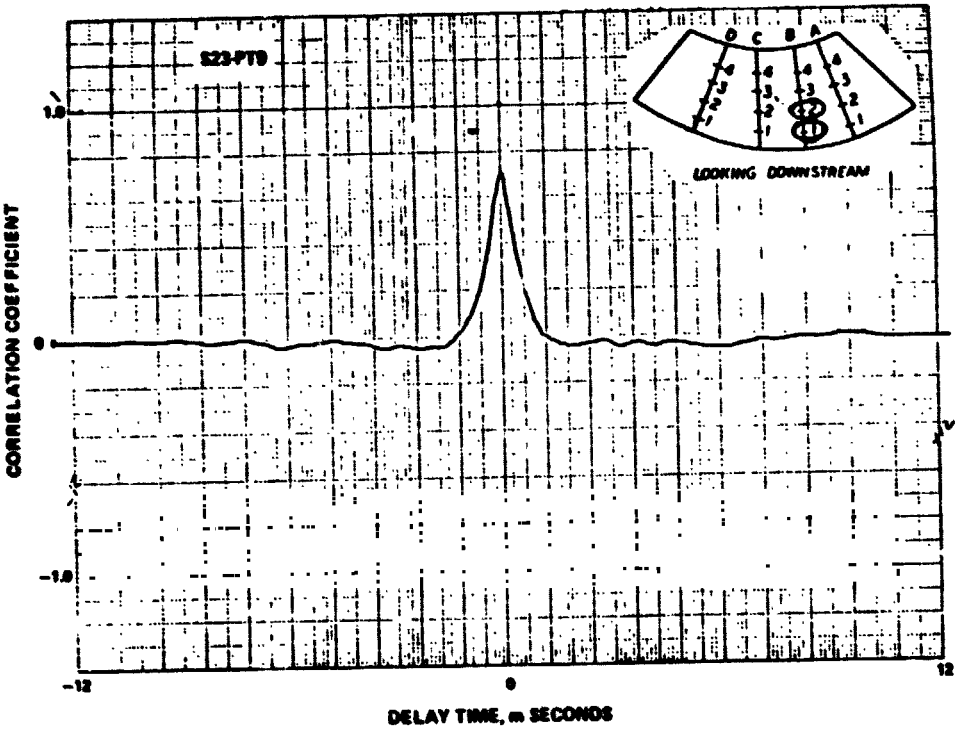

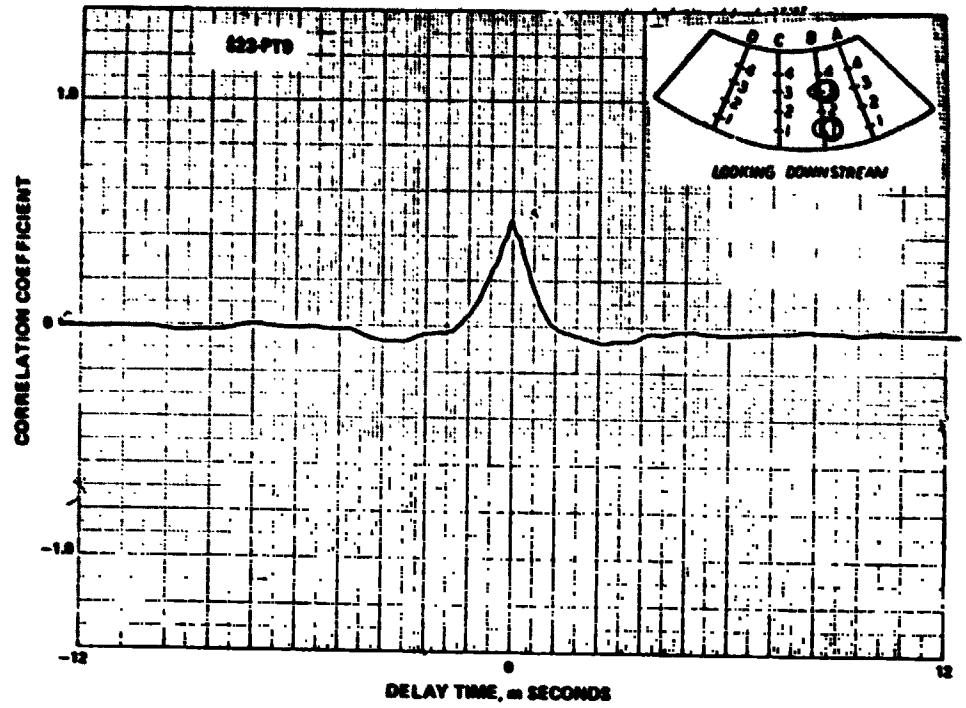
S22-PT9
1.0
0
-1.0
-12
0
12
CORRELATION COEFFICIENT
DELAY TIME, m SECONDS
D C B A
LOOKING DOWNSTREAM

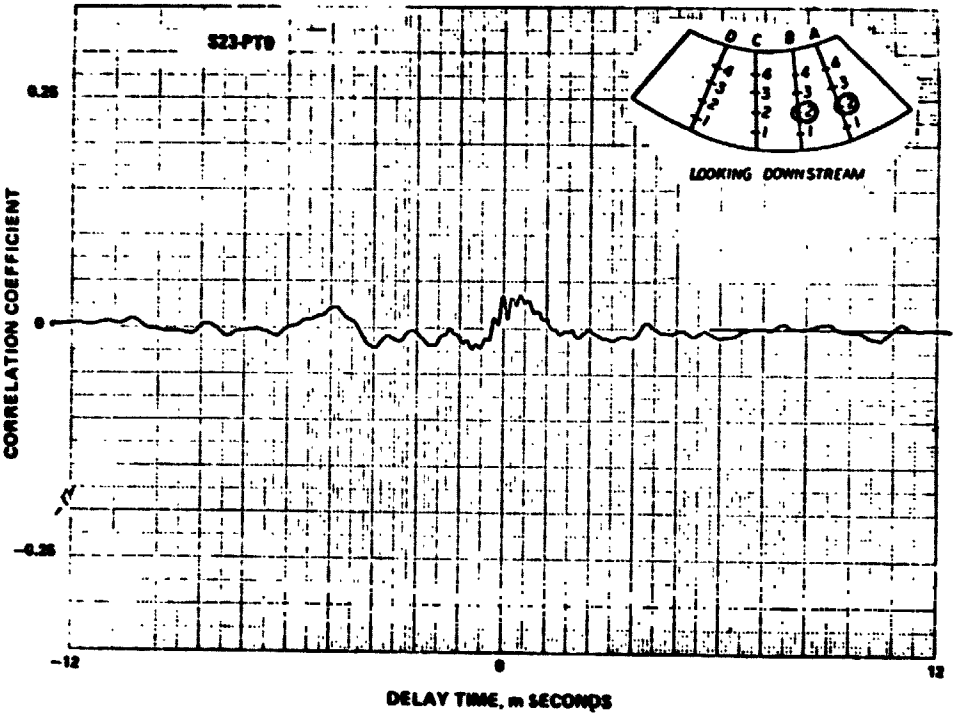
S23-PT9
0.25
0
-0.25
-12
0
12
CORRELATION COEFFICIENT
DELAY TIME, m SECONDS
D C B A
LOOKING DOWNSTREAM

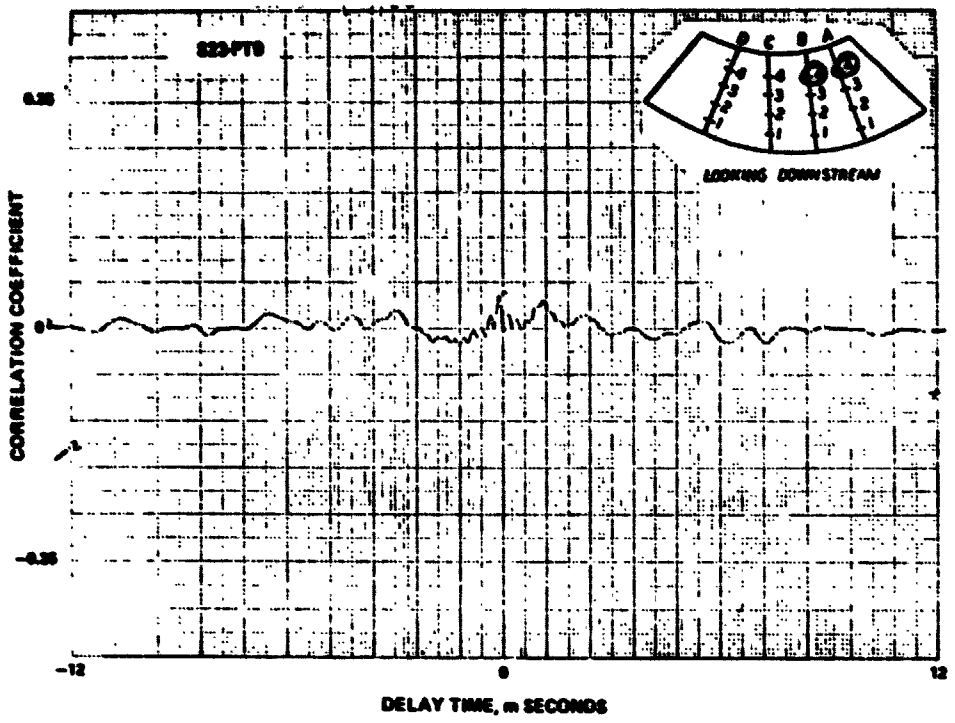
S23-PT9
D C B A
LOOKING DOWNSTREAM
CORRELATION COEFFICIENT
0.35
0
-0.35
-12
0
12
DELAY TIME, m SECONDS

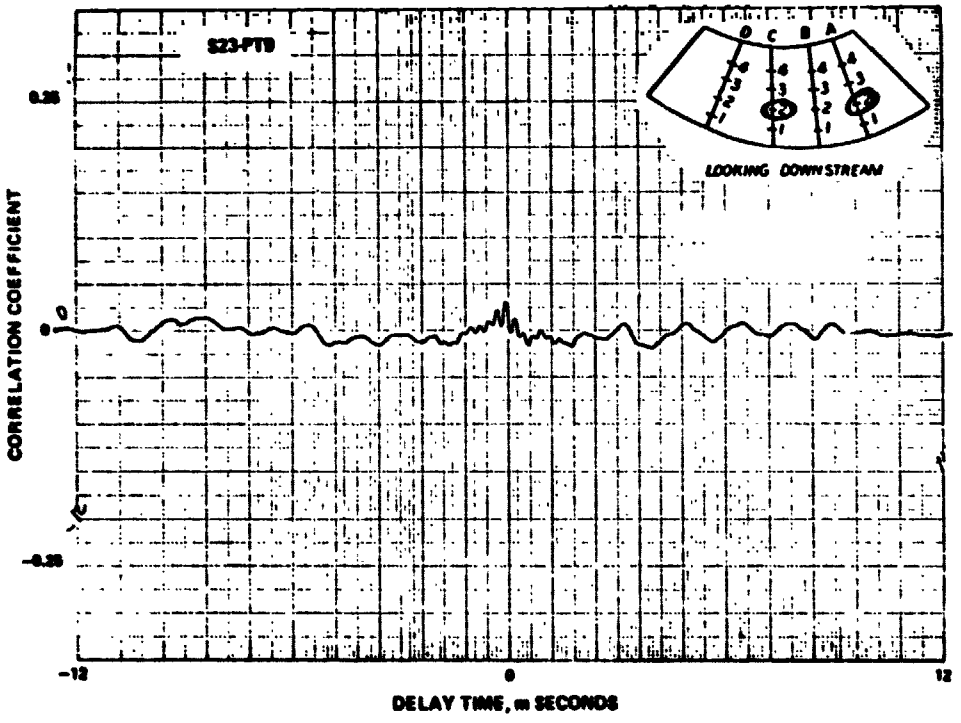
S23-PT9
D C B A
LOOKING DOWNSTREAM
CORRELATION COEFFICIENT
0.35
0
-0.35
-12
0
12
DELAY TIME, m SECONDS

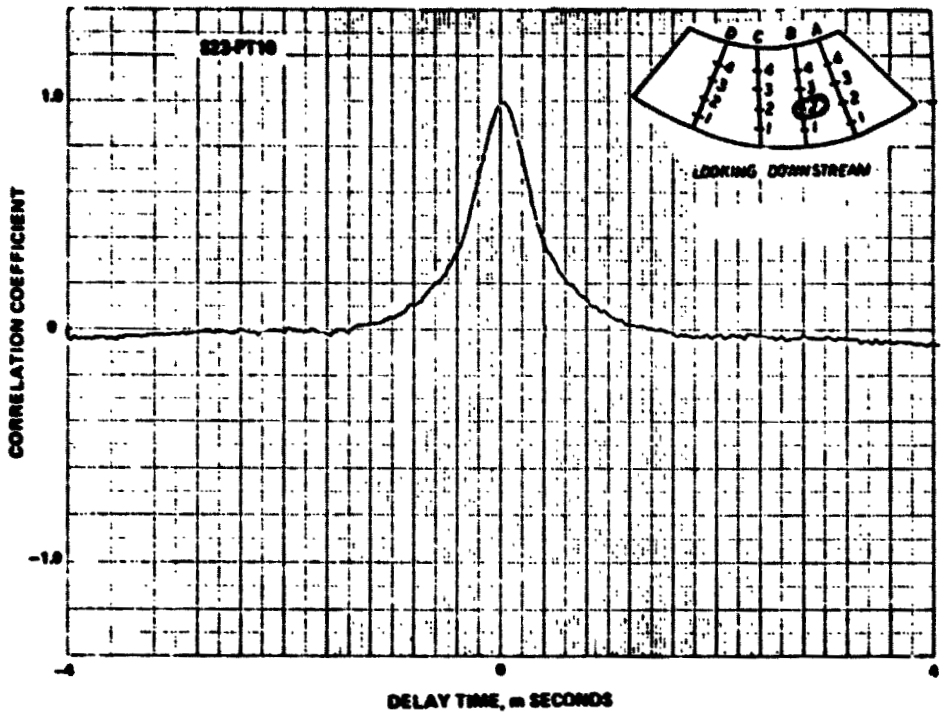
S23-PT10
CORRELATION COEFFICIENT
1.0
0
-1.0
-4
0
4
DELAY TIME, m SECONDS
D C B A
LOOKING DOWNSTREAM

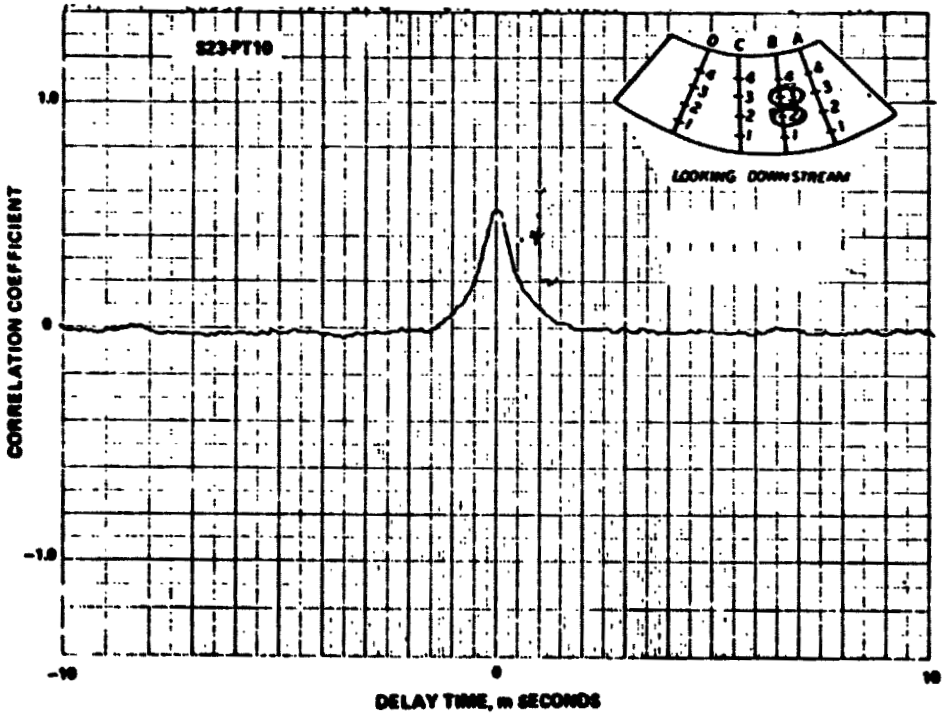
S23-PT10
CORRELATION COEFFICIENT
1.0
0
-1.0
-10
0
10
DELAY TIME, m SECONDS
D C B A
LOOKING DOWNSTREAM

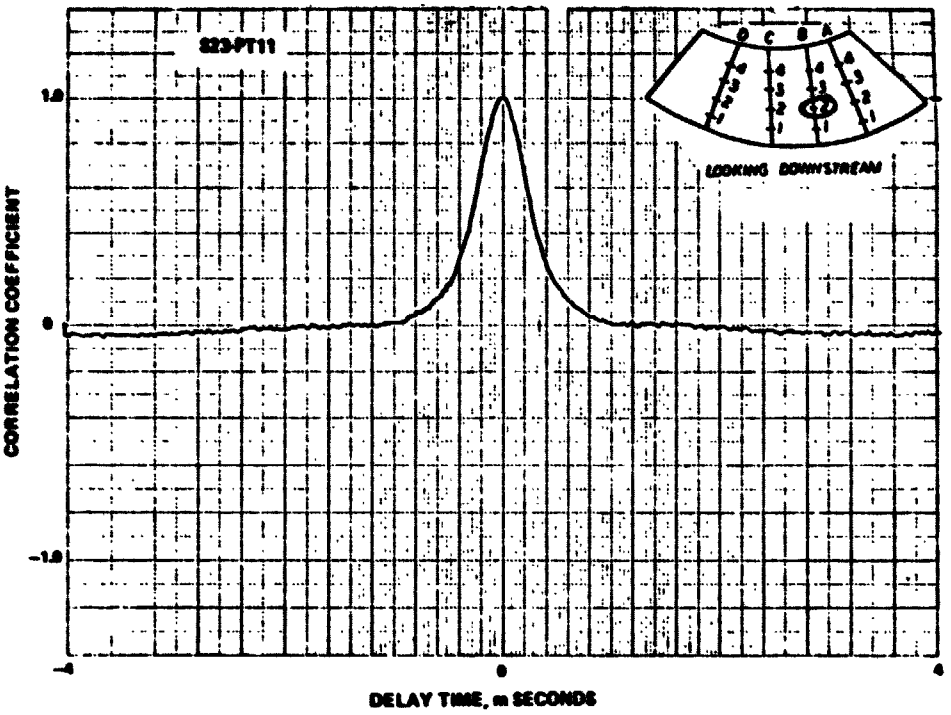

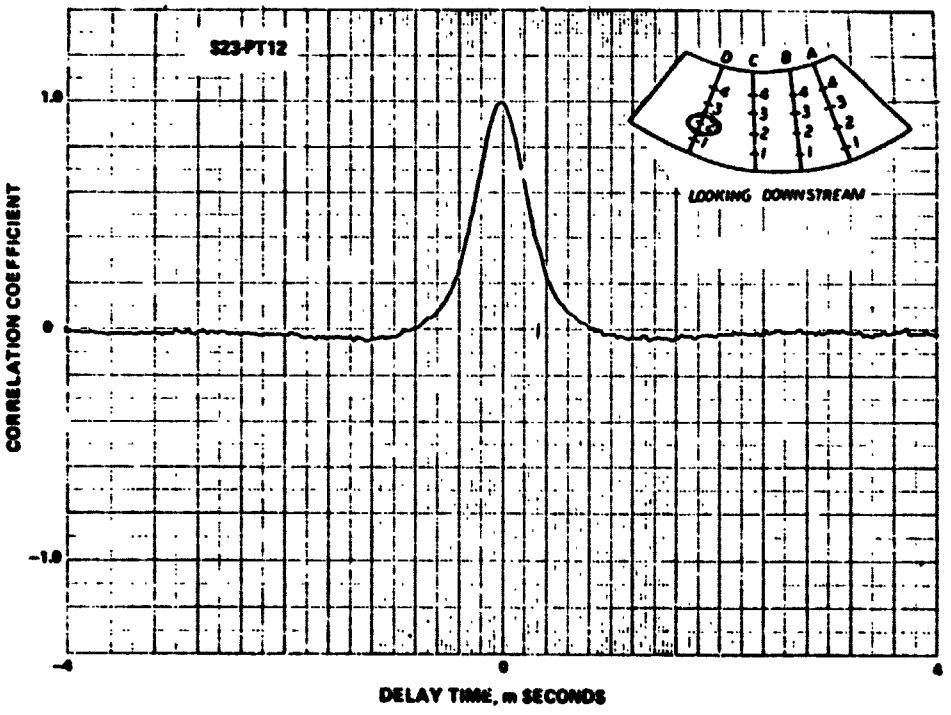

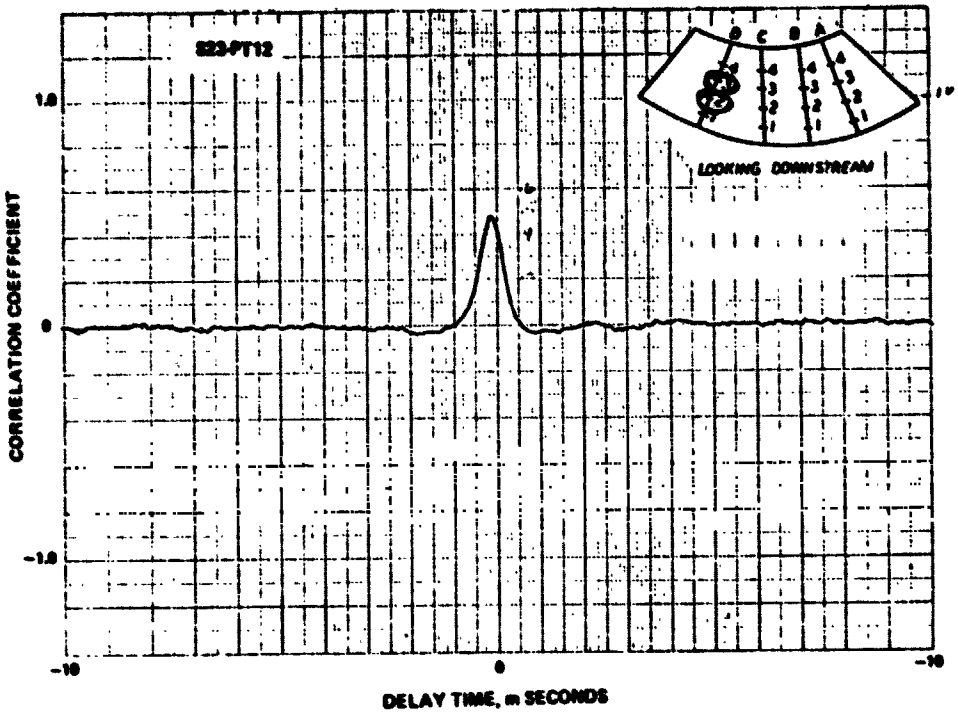
S23-PT12
1.0
0
-1.0
CORRELATION COEFFICIENT
-10
0
-10
DELAY TIME, m SECONDS
D C B A
LOOKING DOWNSTREAM

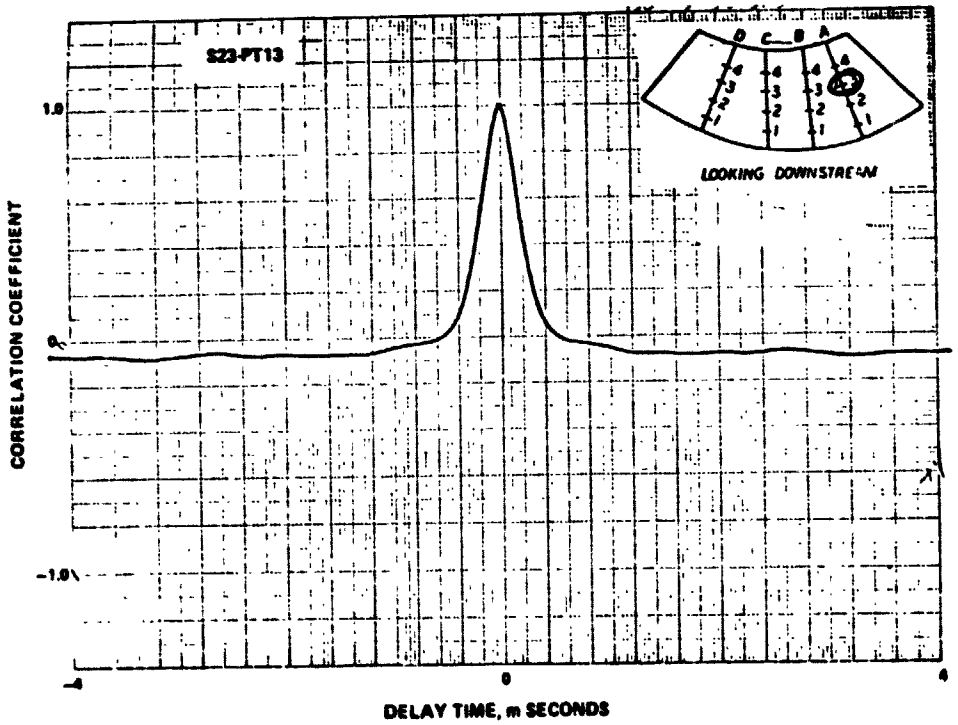
S23-PT13
1.0
0
-1.0
CORRELATION COEFFICIENT
-4
0
4
DELAY TIME, m SECONDS
D C B A
LOOKING DOWNSTREAM

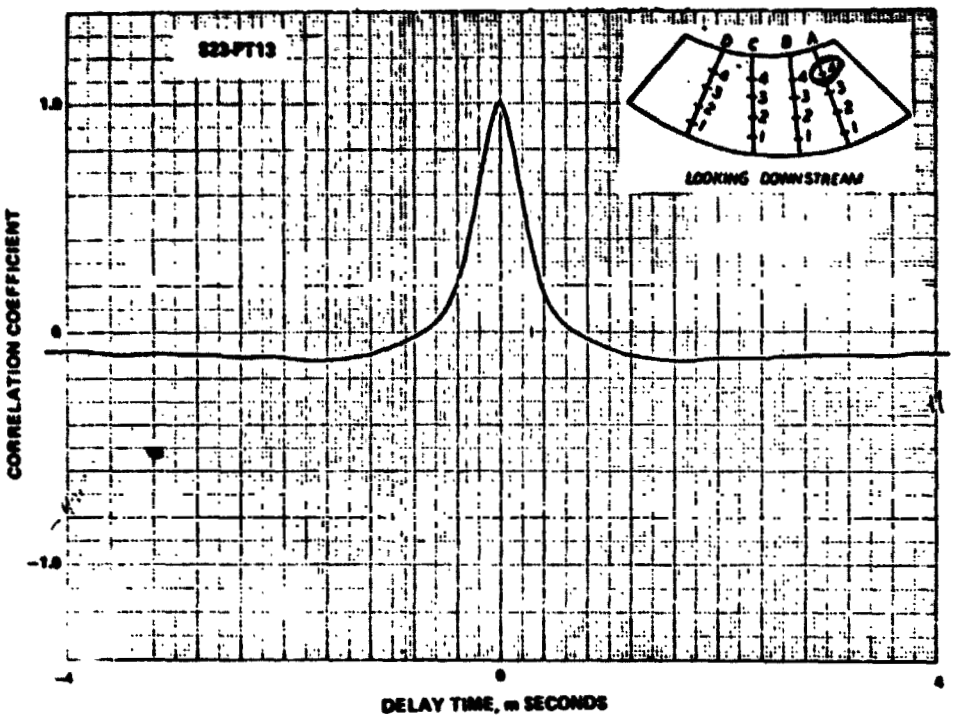
823-PT13
D C B A
LOOKING DOWNSTREAM
CORRELATION COEFFICIENT
1.0
0
-1.0
-4
0
4
DELAY TIME, m SECONDS

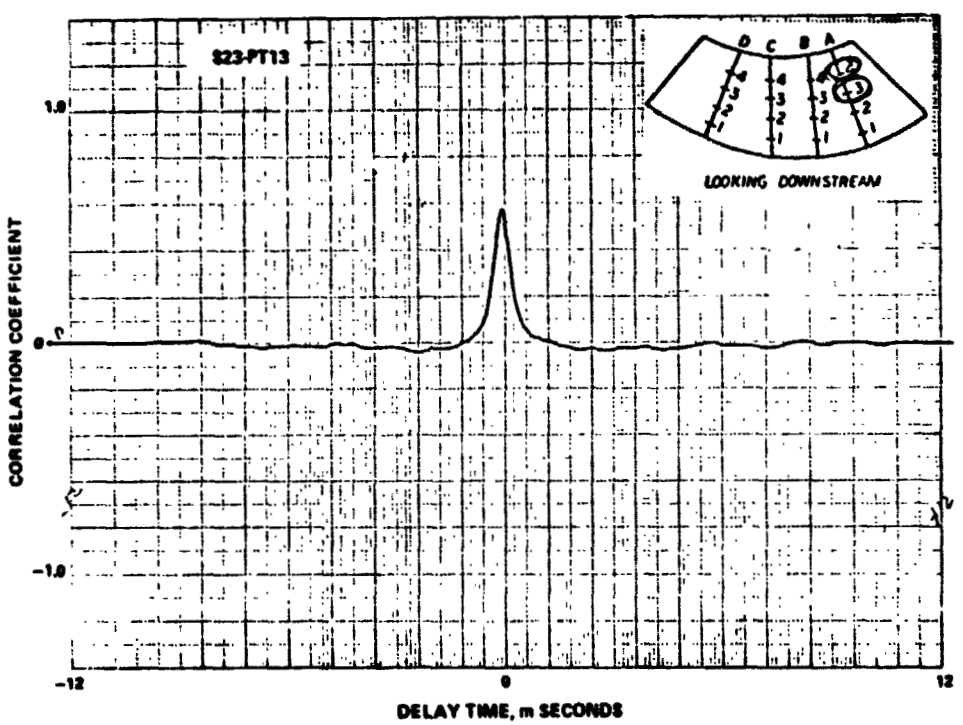
823-PT13
D C B A
LOOKING DOWNSTREAM
CORRELATION COEFFICIENT
1.0
0
-1.0
-12
0
12
DELAY TIME, m SECONDS

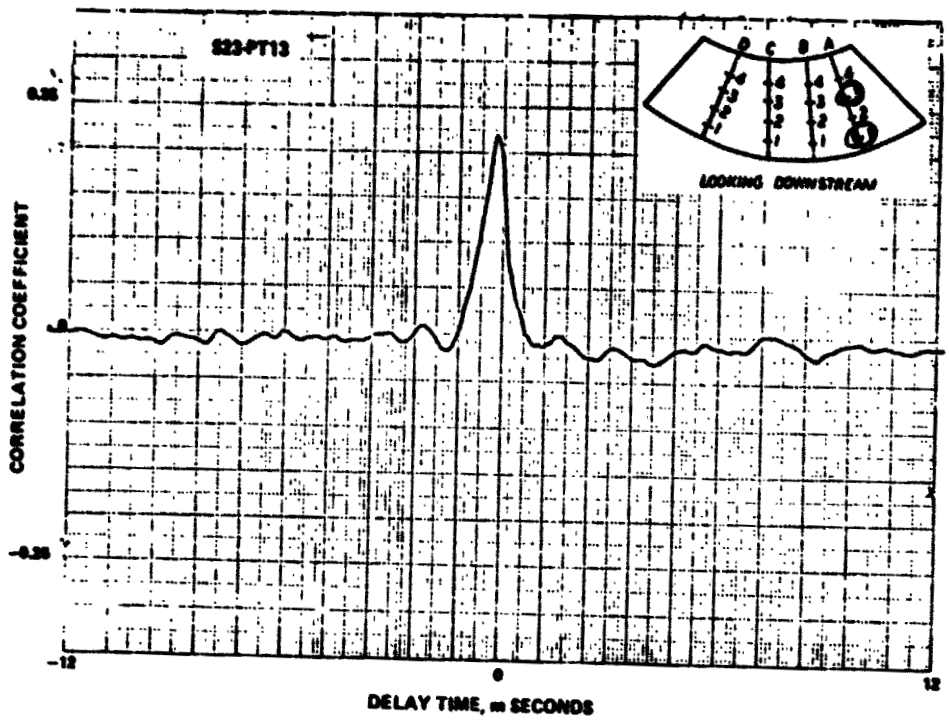

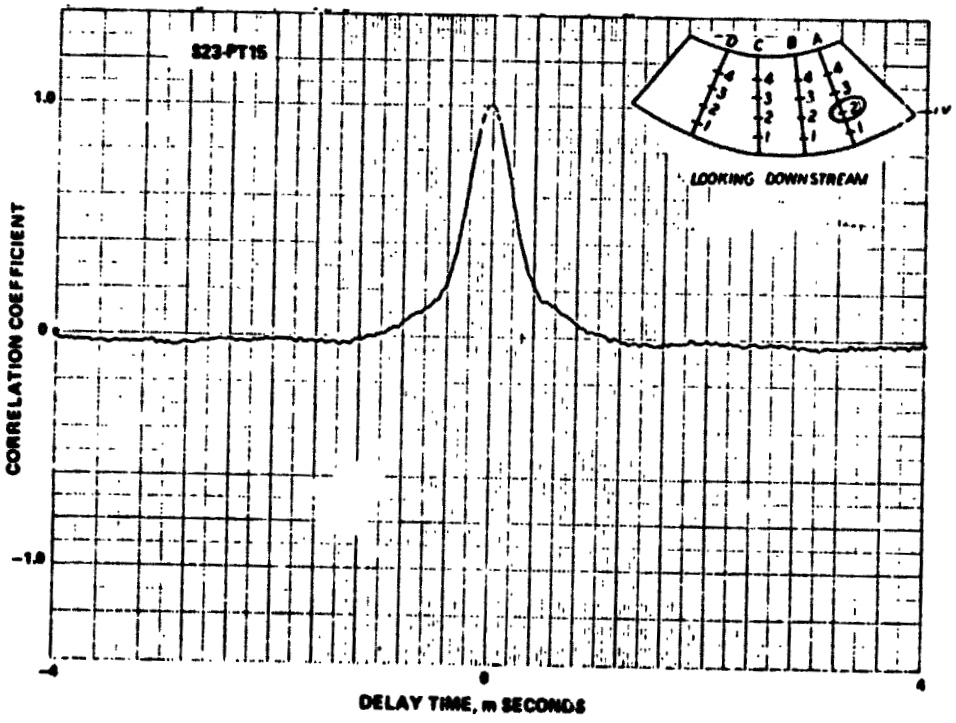

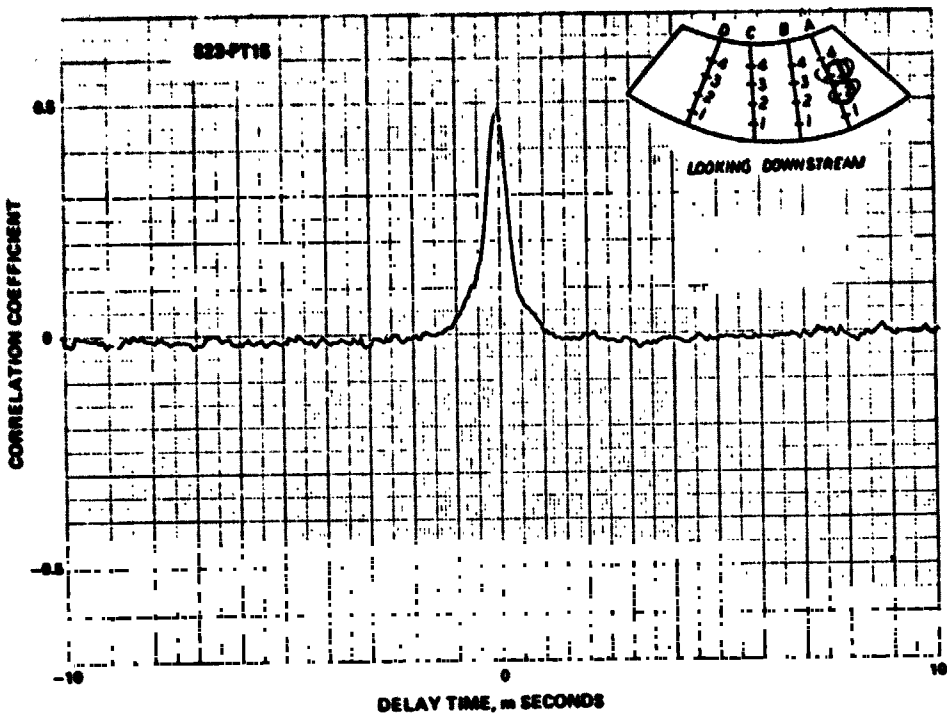
S23-PT15
D C B A
LOOKING DOWNSTREAM
CORRELATION COEFFICIENT
0.5
0
-0.5
-10
0
10
DELAY TIME, m SECONDS

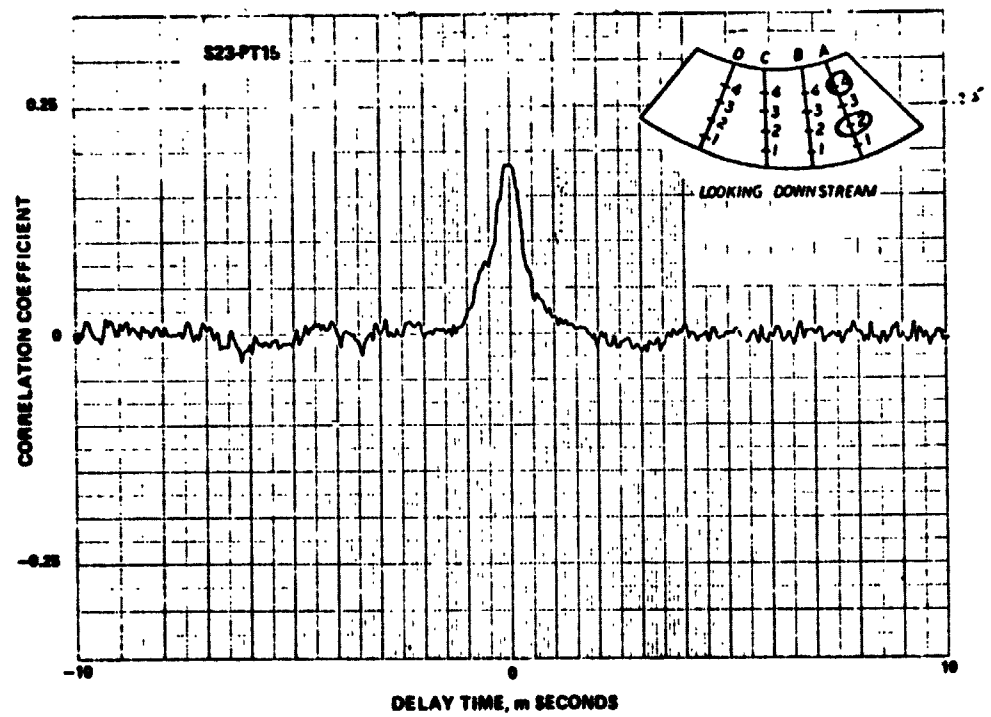
S23-PT15
D C B A
LOOKING DOWNSTREAM
CORRELATION COEFFICIENT
0.25
0
-0.25
-10
0
10
DELAY TIME, m SECONDS

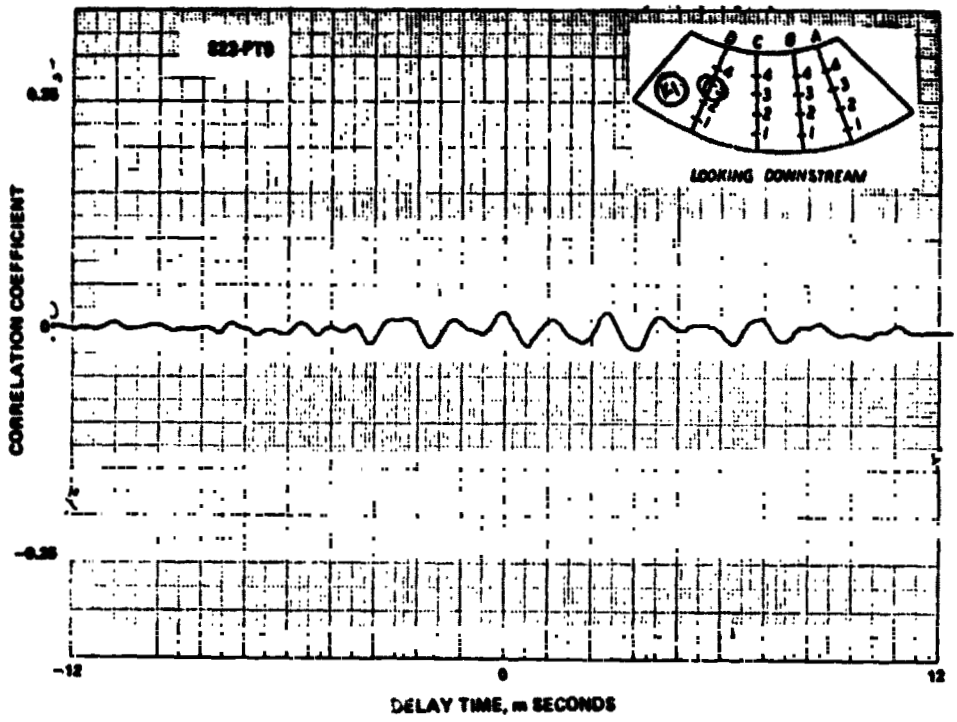

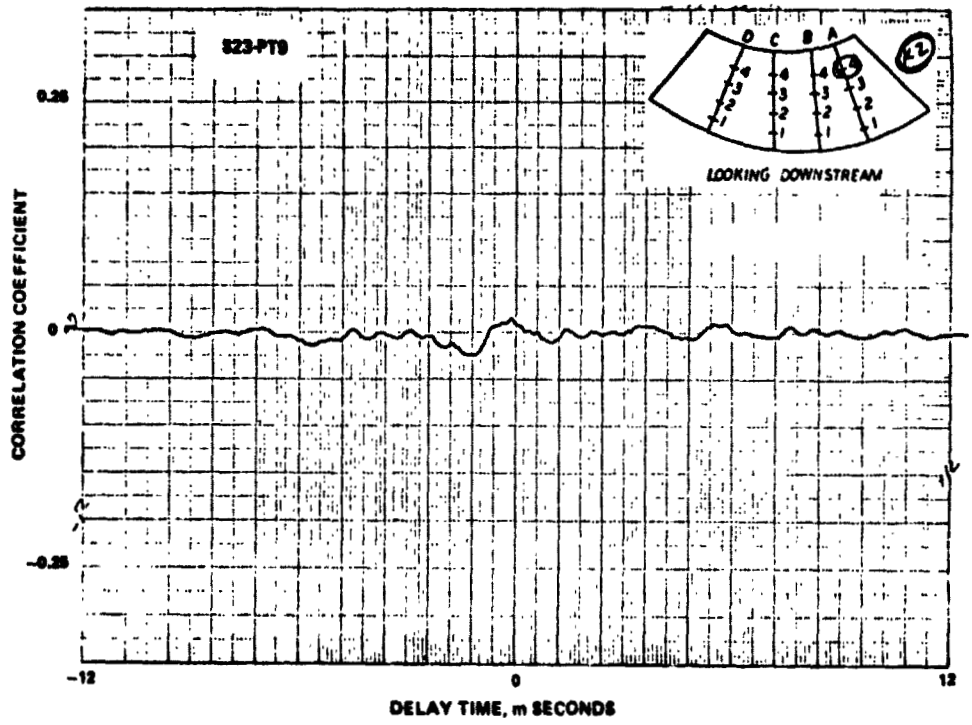

PRESSURE – TEMPERATURE CORRELATIONS

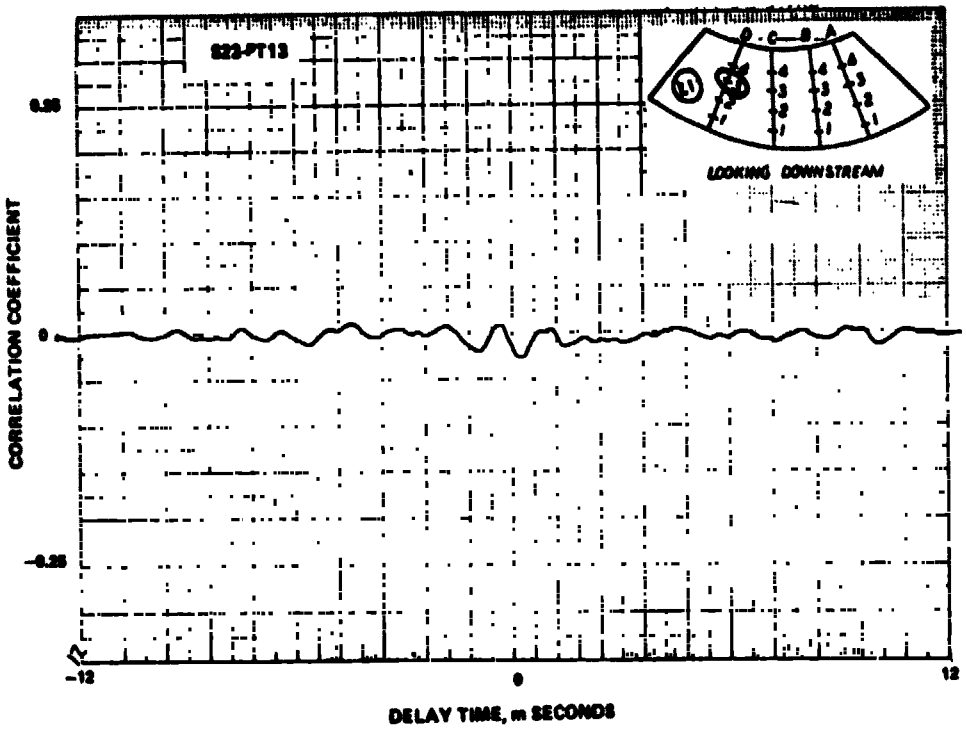

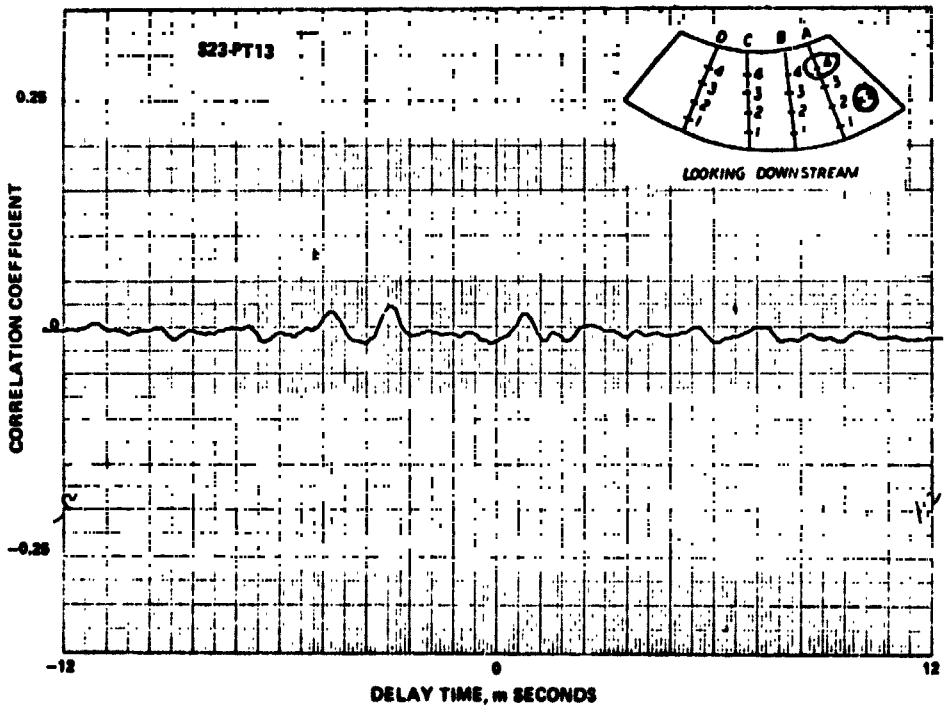

PRESSURE – TEMPERATURE CORRELATIONS